Enhancing the performance of silicon photonic biosensors for clinical applications

Shon Schmidt

A dissertation
submitted in partial fulfillment of the
requirements for the degree of

Doctor of Philosophy

University of Washington

2016

Reading Committee:

Daniel Ratner, Chair

Prof. Karl Bohringer

Prof. Barry Lutz

Program Authorized to Offer Degree:
Department of Bioengineering, University of Washington

University of Washington

Abstract

Enhancing the performance of silicon photonic biosensors for clinical applications

Shon Schmidt

Chair of the Supervisory Committee:
Associate Professor Daniel Ratner
Dept. of Bioengineering (Advisor)

Silicon photonic biosensors have the potential to transform medical diagnostics and healthcare delivery. Hundreds of these nano-scale sensors can be integrated onto a single millimeter-sized silicon substrate and fabricated in foundries to achieve economies of scale similar to modern day computer chips. These refractive index sensors operate using near-infrared light that propagates through nano-scale silicon wires. A portion of the light resides outside the waveguide interacting with biomolecules on the waveguide's surface, altering the refractive index sensed by the light. While silicon photonic biosensors have demonstrated performances approaching today's gold-standard diagnostic, the enzyme-linked immunosorbent assay (ELISA), improving their performance expands their use for applications requiring enhanced sensitivities and detection limits.

This dissertation describes efforts to develop biosensors with enhanced performance beyond what today's commercially available silicon photonic platforms can achieve. In addition, system level simplifications involving capillary-driven networks and new clinically-relevant assays that expand its diagnostic use are demonstrated as well. These achievements were accomplished by improving the bulk and surface sensitivity, detection limit, and quality factor of transverse electric (TE) and transverse magnetic (TM) mode resonators in various waveguide topologies. Specifically, TM mode microring resonators, microdisk resonators, thin waveguide resonators, and sub-wavelength grating microring resonators that provide

an order of magnitude sensitivity improvement over today's commercially available ring resonators are presented. Furthermore, the use of novel TE mode slot-waveguide, TM mode strip waveguide, and suspended waveguide Bragg gratings which facilitate higher sensitivities and lower detection limits for biosensing applications are described. The detection of antibodies in undiluted human using porous membranes instead of pumps and flow cells is shown to achieve similar performnance while reducing overall system complexity. Finally, the comparative performance of red blood cell phenotyping and the detection of hemagglutinins in undiluted human plasma is demonstrated using TE and TM mode ring resonators. These significant accomplishments enable new biosensing applications ranging from small molecule detection to cell phenotyping with performance beyond what is possible with today's commercially available platforms.

TABLE OF CONTENTS

LIST OF FIGURES

GLOSSARY

BSA: Bovin Serum Albumin

DBM: decibel-milliwatt

DUV: Deep ultra-violet

ER: Extinction ratio

FDTD: Finite-difference time domain

ELISA: Enzyme-linked immunosorbent assay

FSR: Free spectral range

FWHM: Full width at half maximum

GDS: Graphic Database System

GUI: Graphical user interface

IFA: Immunofluorescent assay

ILOD: Intrinsic limit of detection

IVD: In vitro diagnostic

MEMS: Microelectromechanical systems

MPW: Multi project wafer

MRR: Micro ring resonator

MW: Molecular weight

NW: Nanowire

PBS: Phosphate buffered saline

PDMS: Polydimethylsiloxane

POC: Point-of-care

POCT: Point-of-care test

PTFE: Polytetrafluoroethylene

RBC: Red blood cell

RI: Refractive index

RIU: Refractive index unit

SA: Streptavidin

SLOD: System limit of detection

SPR: Surface plasmon resonance

SOI: Silicon-on-Insulator

SWG: Sub-wavelength grating

TE: Transverse electric

TM: Transverse magnetic

UI: User interface

ACKNOWLEDGMENTS

I would like to thank my committee, Prof. Bohringer, Prof. Chrostowski, Prof. Lutz, and Prof. Ratner for the opportunity to learn a new field mid-career. I appreciate the guidance, advice, and training on how to think as a scientist and ask better questions about my own research. And to my advisor and mentor, Prof. Daniel Ratner, for guiding me through this process and obtaining the required funding for my research. I am especially grateful for the freedom to explore entrepreneurship during my time in school. This experience has been invaluable.

I cannot express enough appreciation for my family's support and encouragement throughout this journey. Specifically, to my parents, Dr. Daniel and Susan Schmidt, for relocating and living close by to care for our every need and their grandchildren. And to my siblings, Dr. Nicole Schmidt, Maj. James Schmidt, and Mrs. Jessica Hebebrand, and my extended family, Dr. Hyatt Moore IV and Stephen Svoboda, for their guidance and help proof-reading manuscripts. A special thanks to Hyatt for all the chats on software architecture as I developed the probe station software. I'm also grateful to Mr. and Mrs. Hyatt Moore III for their support, encouragement, and nurturing of Cambria, my long-suffering wife. Most of all, I appreciate the love and support of my wife, Cambria, and our three sons, Jamison, Kaden, and Ashton. I apologize for all those evenings and weekends I spent in the lab or hid away to write and study. Your patience and support has been humbling and I am looking forward to resuming a more normal life with you.

A special thanks is deserved to both Christian Redd and Jonas Flueckiger. Both are good friends and helped tremendously throughout grad school. Christian spent countless hours helping me prepare for exams and reading manuscripts. Jonas enabled much of my

research through his own projects building novel biosensors. I have been truly blessed by their collaboration.

I would like to thank colleagues at the University of Washington for their help and support. I appreciate the advice, wet-lab training, and assay development provided by Dr. Jing Shang, Dr. Jim Kirk, and Dr. Jeff Chamberlain. A special thanks to the undergraduates I had the privilege of interacting with during my tenure: Andrew Millspaugh, Pavel Kulik and Vince Wu, for their contributions to the software development; Alex Wang, for his mechanical prototypes; and Alissa Bleem, for her help with the paper fluidic concepts. Finally, to the summer students: Matt Doerfler, Emily Thompson, and Victor Bass, for their help with instrument drivers and the GUI for the probe station software. I'm grateful to Josh Buser in Prof. Yager's lab for his collaboration on the paper fluidics project and to Hal Holmes for his help regenerating chips so I had ample replicates for my experiments. I'd like to express my gratitude to Dr. Michael Khbeis, Dr. Andrew Lingley, Duane Irish, and Rick Bojko at the Washington Nanofabrication Facility (WNF) for the ebeam fabrication and CYTOP cladding services they provided.

I would also like to acknowledge colleagues at the University of British Columbia for providing the silicon photonic biosensors for my research; Dr. Samantha Grist, Dr. Valentina Donzella, and Dr. Sahba Talebi Fard, for the disk, sub-wavelength grating, and thin waveguide ring resonators; and to Prof. Nicholas Jaeger, for the use of his laser at the University of Washington. It was instrumental in my research. Finally, none of this would be possible without financial support provided by the Washington Royalty Research Fund and National Science Foundation.

DEDICATION

To my parents, Dan and Susan, who gave so I would gain. To Cambria, my wife and life-long friend, whose support and belief enabled this dream. And to my sons Jamison Drake, Kaden Christian and Ashton Daniel. May your life be filled with an insatiable curiosity for a deeper understanding of this wonderfully mysterious world. Soli Deo gloria.

Chapter 1
INTRODUCTION

1.1 Healthcare transformation

Diagnostics will play a significant role in the healthcare transformation currently underway in the United States. Areas where their impact will be significant include healthcare delivery, wellness and prevention, and personalized medicine. The shift away from established fee-for-service payment structures towards capitated contracts with Accountable Care Organizations (ACOs) is catalyzing new delivery models and technology integration. There are a growing number of non-physician workers administering healthcare, especially primary care, under the supervision of a medical doctor (MD). Diagnostic technologies in the point-of-care setting can help accommodate the training gap and can improve work flows and efficiencies. On-the-spot testing allows treatment plans to be administered without the delay imposed by sending samples for out-of-house testing.

1.2 Diagnostics

In vitro diagnostics (IVDs) are performed on samples taken from bodily fluids, primarily blood and urine. IVDs have become ubiquitous in modern medicine with clinical applications ranging from pathogen identification to blood typing. Most sophisticated IVD tests requiring high sensitivity and specificity involve expensive bench-top instruments, consume expensive reagents, and are performed in a centralized hospital laboratory setting by highly trained operators. For detecting proteins and small molecules, the enzyme-linked immunosorbent assay (ELISA) remains a gold-standard widely in use today. While it is highly sensitive ($\sim$1 pM or 1-2 pg/mL), it is also costly ($300 - $650 per panel), time consuming (1-3 hours per

run), requires secondary colorimetric or chemiluminescent amplification (additional process steps), and is burdened by complex logistics when performed in centralized laboratories [1–4].

By contrast, point-of-care (POC) diagnostics are a subset of IVDs that can be performed at the patient's bedside, in the doctor's office, or at home [5, 6]. The nascent emergence of ACOs is catalyzing a growing interest in POC diagnostics to improve healthcare delivery [7]. In 2011, POC diagnostic tests (POCT) comprised the largest share of the IVD market, with over-the-counter and hospital POC sales of over US$15 billion, or 30% of the IVD market [8]. POCTs are very cost effective as they impact ≈70% of all health care decisions yet only account for ≈4% of total healthcare spending [9]. The most common POCT include blood glucose monitoring, pregnancy tests, cholesterol monitoring, and infectious disease detection, including HIV. Advances in science and technology continue to expand POCT into applications currently performed by conventional IVD in the hospital setting [10]. By improving the testing efficiency, cost, and portability of IVDs, POC tests benefit the patient, provider, and healthcare system as a whole allowing responsive clinical interventions to be provided on the spot. However, not all POCTs achieve performance similar to laboratory-based instrumentation and some may require greater sensitivity [11]. Therefore, the primary motivation behind my research includes developing technologies that allow diagnostic tests currently confined to a laboratory into the POC setting where their impact can be broadly realized. Specifically, my efforts have focused on enhancing the performance of silicon photonic biosensors for clinical applications.

1.3 Silicon photonic biosenors

Silicon photonics is an emerging chip-based technology that shows promise for biosensing applications [12–17]. The silicon on insulator (SOI) platform is compatible with standard CMOS fabrication processes as well, facilitating manufacturing at the economies of scale offered by today's foundries. As near-infrared light propagates through nano-scale silicon wires on the chip, a portion of the light's electric resides outside the waveguide and is sensitive to refractive index changes in the cladding. This electric field, called an evanescent field,

decays exponentially with distance away from the surface of the waveguide. Because of this overlap with the cladding material, the propagation properties, namely the effective index, are sensitive to small index perturbations in the cladding, which makes them ideal candidates for quantifying molecular binding events. For easy read-out, most silicon photonic biosensor utilize a resonant optical cavity, in which the change in surface chemistry is correlated to a shift in resonance wavelength. A number of different configurations have been proposed including ring resonators [18–20], disk resonators [21], and photonic crystals [22].

Table 1.1 lists the performance of recently reported foundry-compatible silicon photonic biosensors. Many different sensor types have been developed for both silicon and silicon nitride substrates resulting in a range of performance metrics (Quality factor, sensitivity, etc.). While some were evaluated using clinically relevant assays, most devices employ established chemistries, like biotin/streptavidin systems that provide high binding affinities, to demonstrate their biosensing capability. While these experiments show their potential, they do not reflect the complexity of a biological matrix or the sensor's performance under such conditions. Therefore, the sensors developed as part of this dissertation research are demonstrated with either a model biological sandwich assay (e.g.: antibody/antigen with amplification) or in human samples such as blood.

Arlett *et al.* recently reviewed many state-of-the-art microelectromechanical (MEMS) based biosensors and compared their performance to an ELISA [1]. Figure 1.1 highlights a portion of their analysis including SPR, silicon nano-wires, and silicon photonics. Silicon photonic sensors have achieved sensitivity ranges within current envelopes for making clinical judgments using label-free sensing in complex media (≈10 ng/mL)[12, 40]. They can achieve detection limits similar to the ELISA (sub-pg/mL or sub-pM) by employing a secondary amplification step while still offering advantages over their mechanical and electrical biosensor counterparts as shown in Fig. 1.1 [1, 41, 42]. Also, silicon photonic devices are not susceptible to mechanical force under normal microfluidic flow, electromagnetic interference, nor the electrical conduction of the analyte media. Additionally, silicon photonic biosensors offer the advantage of real-time monitoring of kinetic binding interactions.

Table 1.1: Comparison of silicon photonic biosensors

Type	Mode	Material	S [nm/RIU]	Q	DL	Assay	Ref
Multiplexed ring	TE	Si	54	>40k	1.6 - 39 ng/mL	Ebola, Dengue	[23]
Ring	TE	Si	54	43k	1.5 pg/mm^2	Biotin-Streptavidin	[24, 25]
Ring	TE	Si	54	>40k		PSA, AFP, CEA, TNF-α, IL-8	[26]
Porous ring	TE	Si	380	10,000	4 pm/nM	DNA	[27]
Slot ring	TE	SiN	141	1300	50 ng/mL	PSA	[28]
Slot ring	TE	Si	298		$4.2 \cdot 10^{-5}$ RIU	Biotin-Avidin	[29]
Ring	RE	Si		20k	10 ng/mL	Biotin-Avidin	[30]
Ring	TE	Si	70	20,000	10 ng/ml	Biotin-Streptavadin	[19]
Slot Ring	TE	Si_3N_4	246		$5 \cdot 10^{-6}$ RIU 0.9 pg/mm^2	Glutaraldehyde-antiBSA	[31]
Ring	TE	Si		24,000	33 pM and 1.4 nM	IgE and Thrombin	[32]
Ring	TM	Si		12,000	10nM	ssDNA	[33]
Ring	TE	Si_3N_4	110			BSA	[34]
Slot Ring	TE	Si_3N_4	212		28 pg/mm^2	Anti-BSA	[35]
Slot microdisk	TM	SiNx		7,000	30 ng/mL	Biotin-Streptavadin	[36]
Photonic crystal microcavity	TE	Si	70	5,300	50 fM	Avidin/biotin	[37]
Crystal ring slot	TE	Si	160	11,500	$8.75x10^{-5}$ RIU		[38]
Triple ring and disk		Si on polymer	1,000	67,000			[39]

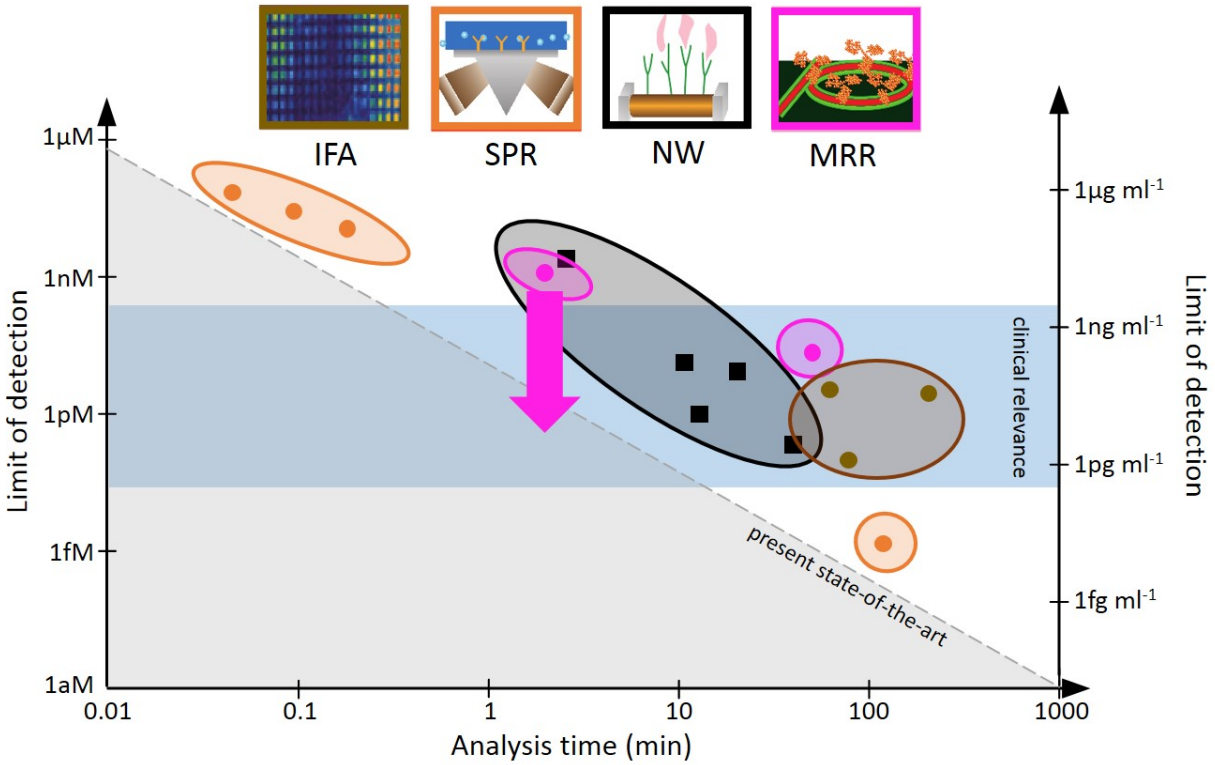

Adapted from: Arlett, J., Myers, E. & Roukes, M. Comparative advantages of mechanical biosensors. Nature nanotechnology **6**, 203-215 (2011).

Figure 1.1: The left vertical axis represents the detection limit (moles/L) while the right vertical axis represents the equivalent g/mL for different kinds of MEMS biosensors for PSA (34 kDa), a model target antigen. Note that both axes are logarithmic. The bottom axis represents the analysis time. Devices on the right hand side offer greater sensitivities at expense of analysis time. The gray dashed line represents the limits of the current state-of-the-art. The pink, circled dots represent the performance of silicon photonic micro ring resonators (MRR) shown compared to surface plasmon resonance (SPR), silicon nano-wire (NW), and the ELISA, or immunofluorescent assay (IFA). The light blue region in the center of the plot represents clinically relevant sensitivities. The pink downward arrow represents our research objectives: to increase the performance of silicon photonic biosensors to achieve clinically relevant sensitivities without amplification and for short analysis time.

Silicon photonic biosensors have demonstrated the detection of proteins [43, 44], nucleic acids [45], viruses [46], and bacteria [47]. Yet, commercially available silicon photonic biosensor platforms still require secondary amplification for some diagnostic assays [43]. For example, the diagnostic level of significance for the prostate-specific antigen (PSA) in human plasma is ≈4 ng/mL (120 pM). Kirk *et al.* recently reported that they could only achieve a detection limit of ≈10 ng/mL for the label-free detection of streptavidin (spiked into undiluted human plasma) using DpC polymer-coated biosensors on a commercially-available silicon photonic platform [40]. To achieve clinically relevant performance for an expanded set of diagnostic assays, sensitivity needs to be enhanced. While the overall system performance is not solely determined by the sensor alone, enhancing a sensor's native sensitivity and detection limit will help expand the platform's capability for applications as well.

Adoption of the silicon photonic biosensor platform beyond centralized laboratories into point-of-care settings will require many optimizations, including: miniaturization and cost reduction of platform components such as the laser source, optical couplers, detectors, electronic read-out, and control circuity. Microfluidic integration must be considered too as analyte delivery to the sensing region impacts overall performance. Integrating sophisticated microfluidic systems that prepare samples, sequence reagents, and store waste would simplify operation and any required user interaction. To that end, integrating porous membranes that obviate the need for pumps, gaskets, or flow cells would greatly advance the platform towards point-of-care diagnostic applications.

1.4 Research aims

This dissertation describes my efforts to improve the native performance of silicon photonic biosensors by an order of magnitude over today's commercial platforms [25] and demonstrate system optimizations and assays that expand their use in clinically-relevant applications. These objectives are achieved through four specific aims:

1. Tools that expedite biosensor development and automate characterization

2. Devices with an order of magnitude performance enhancement over today's sensors

3. System simplification through porous membrane integration

4. Serologic phenotyping of human blood samples using developed components

The next sections detail each aim, stating the problem addressed, the experimental approach employed, the results achieved, and the significance and broader impact of these accomplishments.

1.4.1 Aim 1: Tools that expedite biosensor development and automate characterization

A high barrier exists in developing silicon photonic biosensors. Many aspects of the design process can be improved. For example, fabrication via foundry processes takes many months while ebeam lithography can produce prototypes in a few hours. Testing devices is time consuming. Manually performing assays for many biosensors is arduous, especially when reagent sequencing is required. Automating the testing of devices and prototyping designs using fast-turn ebeam lithography would greatly improve the development efficiency. Chapter 3 describes efforts to create a probe station that automates the testing and characterization of silicon photonic biosensors. Through collaboration with Prof. Chrostowski's students at the University of British Columbia, a process design kit (PDK), which includes a chip-framework and cells that reduce design risk and facilitate efficient registration and test setup, is also developed and characterized.

The system was built using closed-loop stages with sub-micron resolution and includes a custom application that interfaces with the various equipment. The software implements unique algorithms that help find first light quickly and conduct multi step biological assays. The probe station software has been open sourced on GitHub [48] to help lower the barrier for other research groups. The platform is currently in use at more than a dozen sites across different countries and has helped generate scores of publications [49], including those in this dissertation. In addition, an Internet-based silicon photonic design course

uses the automated probe station to assess students' designs [50]. A description of these efforts and observed biosensing performance of the test setup has recently been submitted for peer-reviewed publication [51]. It has also been discussed in a book [52] and presented at conferences [20].

1.4.2 Aim 2: Devices with an order of magnitude performance enhancement

Silicon photonic sensors have achieved sensitivities approaching clinically-relevant thresholds for label-free sensing in complex media (≈10 ng/mL) [26, 40, 43, 53, 54]. Yet today's commercially available silicon photonic biosensor systems still require secondary amplification for detection of extremely low concentrations[24]. Achieving sensitivities at pg/mL levels or lower for label-free, silicon photonic sensors suitable for high-volume fabrication would greatly expand their potential as a label-free diagnostic device. Therefore, in collaboration with the Chrostowski group at the University of British Columbia, eighteen novel sensors were designed, fabricated, characterized, and assessed in a biological environment.

Sensors are described in chapter 4 and include topologies such as ring and disk resonators and Bragg gratings realized in different waveguide geometries (ultra-thin silicon) and configurations (slot, strip, rib, and suspended-waveguides) for both transverse electric (TE) magnetic (TM) modes. Devices that operate at 1310 nm wavelengths, where absorptive losses to water are reduced by an order of magnitude, achieved detection limits beyond what is possible by their 1550 nm counterparts. While most devices have been described and published [20, 21, 55–59], some have recently been submitted for publication [60–63]. Ultra-thin waveguide resonators employing TE and TM modes as well as suspended waveguide Bragg gratings were explored. 1310 nm wavelength sensors were also designed and demonstrated improved detection limits beyond what their 1550 nm counterparts can achieve. These efforts resulted in novel sensors that offer an approximately 10x sensitivity improvement over commercially-available platforms [25] and a provisional patent filing for the sub-wavelength grating ring biosensor [64]. Performance metrics of all investigated sensors are listed in Table 4.3 and will enable new clinical diagnostic applications requiring performance beyond what

can be achieved with silicon photonic systems today.

1.4.3 Aim 3: System simplification through porous membrane integration

With silicon photonic biosensors approaching clinically-relevant performance, focus has shifted towards lab-on-chip systems with integrated fluidics, lasers, detectors, and electronic read-out. While a few groups have already demonstrated on-chip lasers and detectors [42, 65, 66], most fluidic solutions still require flow cells, gaskets, and external pumps to sequence reagents across the sensors [25, 67]. Replacing these components with porous membranes that sequence reagents using capillary action would reduce cost and system complexity. Therefore, porous membrane networks integrated with silicon photonic biosensors were investigated, characterized, and demonstrated for alloantibody detection in undiluted human plasma.

Chapter 5 describes how porous membranes were designed and tuned to achieve similar performance as their conventional counterparts (gaskets, flow cells, and pumps). Assays employing both fluid network types were performed and results confirmed our hypothesis that porous membranes can replace conventional fluid networks without compromising overall performance. These efforts resulted in a provisional patent filing and first of their kind demonstration that simplifies silicon photonic lab-on-chip systems for clinically-relevant biosensing applications [68]. A manuscript has been prepared and submitted to a peer-reviewed journal for publication [68, 69].

1.4.4 Aim 4: Serologic phenotyping of human blood samples using developed components

Silicon photonic biosensors have yet to be demonstrated for blood typing, a diagnostic test routinely performed for transfusion medicine. In 2013, more than 14 million units of whole blood were collected for transfusions [70]. Every unit underwent screening to determine the blood group (A, B, AB, O, and Rh) compatibility between the donor and recipient. Tube-based agglutination assays remain the gold-standard [71] and are performed by specially-trained technicians in well-equipped laboratories. A portable diagnostic capable of typing

and pathogen screening could improve work flows and minimize errors, which account for ≈25% of fatalities in transfusion medicine [72].

Chapter 6 describes the use of silicon photonic ring resonators for red blood phenotyping (direct typing) as well as alloantibody detection (indirect typing) in undiluted human plasma. The chapter describes how custom TE and TM mode ring resonators are characterized and functionalized using streptavidin/biotin conjugation chemistries for both direct and indirect typing. Since the TE and TM mode rings were subjected to patient samples simultaneously, differences in the observed resonant wavelength shifts provide insight into the thickness of adsorbed protein layers. This work expands the repertoire of clinical assays demonstrated on the silicon photonic biosensor platform. And when combined with previous demonstrations of multiplexed analytes and pathogen detection, these results helps realize the goal of a single lab-on-chip system capable of blood typing outside the laboratory setting. A manuscript has been prepared and submitted to a peer-reviewed journal for publication [73].

1.5 Document organization

The next chapter provides a brief background on the history of biosensors, theory of operation for silicon photonic biosensors, mechanisms that facilitate capillary driven flow in porous membranes, and an overview on blood group systems and how they are determined using today's diagnostic methods. Chapter 3 describes the tools that enabled the development and characterization of sensors described in Chapter 4. Chapter 5 discusses system optimizations that eliminate the needs for external pumps and flow cells while Chapter 6 demonstrates blood typing using sensors developed as part of this work. The dissertation concludes with a brief summary of accomplishments (Section 7.3.1), published works (Section 7.3.2), and suggestions on future work (Section 7.2) to continue evolving the silicon photonic biosensor platform towards commercial diagnostic applications.

Chapter 2

BACKGROUND

2.1 Biosensors

The field of biosensing has experienced phenomenal growth over the past 30 years with 5000 papers published on biosensing in 2011 alone, an increase from just 100 manuscripts on the subject in 1985 [74]. Biosensors are a foundational element of diagnostics but also in molecular research and assay development. For the scope of this dissertation, the term *biosensor* is used to describe a device functionalized with molecules specific to a biological target that can translate their capture into a detectable signal. Readout formats vary by sensor, but popular ones include a visual color change (colorimetric), a fluorescence, or an electronic signal (voltage or current change).

2.1.1 Origins

Leland C. Clark was the first to detail the concept of a biosensor in his 1962 seminal work describing an electrode system for continuous glucose monitoring [75]. He showed how an electrode response could be sped up by employing an enzymatic reaction that converted glucose into gluconic acid (via glucose-oxidase), causing a detectable and quantifiable change in pH. While foundational for modern day glucose meters, Clark speculated that electrochemical detection could be used for a broad range of bio analytical applications. While not directly enzyme-based, Clark's accomplishments along with advances in manufacturing and chemistry have created an over-the-counter diagnostic market in excess of US$13 billion per year including tests such as pregnancy, HIV and drug tests [74].

2.1.2 Optical sensors

Optical biosensors use light (or electromagnetic waves) and affinity molecules to detect target analytes. The two most popular optical label-free sensors include surface plasmon resonance (SPR)[76–79] and silicon photonic biosensors[41, 42]. SPR utilizes a plasmon wave traveling along a metal-solution interface to detect molecular binding.

Surface plasmon resonant sensors

SPR sensors were pioneered by Ingemar Lundström's group at Linköping University more than two decades after Clark's publication [80] and were transformational in that they allowed real-time monitoring of molecular binding events. Lundström's sensor utilized surface plasmon resonance (SPR) to measure molecular absorption to a gold surface. A surface plasmon is created when incident photons (or light) oscillate conduction-band electrons at a glass/metal interface. The resonant condition is met when the incident photon frequency matches the natural oscillation of surface electrons (against the restoring force imposed by positive nuclei). Light at the resonant condition is absorbed and not reflected back to the detector (attenuated-signal SPR). Adsorbing biomolecules on the surface alter resonant conditions which are then detected and quantified.

While the method by which a surface plasmon operates was initially suggested by Kretschmann in 1971, biomolecular detection was not demonstrated until 1983 [81], resulting in the formation of a Swedish company called Pharmacia Biosensor in 1986. The venture later became Biacore in 1990 which was acquired by GE in 2006 for US$390 million. While achieving impressive sensitivities of 10^{-5} to 10^{-7} RIU ($\sim$1 fg/mL for proteins) [76, 78, 82], SPR's specialized metal-plated chips and bench-top instrumentation limit its potential beyond research settings (the unit RIU stands for refractive index unit). While effort has been invested into developing a field-deployable instrument based on Texas Instruments' Spreeta sensing chips [83], SPR has not gained traction as a standard POC diagnostic platform and its market remains relatively modest at US$100 million per annum.

Silicon nanophotonics

Nanophotonics describes the nascent scientific field examining how light with wavelengths between 300 nm and 2 µm interact with structures at sub-wavelength scales. Even at these scales light can be confined given a refractive index contrast and guided on a planar photonic chip. Silicon is transparent to near infrared (NIR) wavelengths and has been widely adopted for use in datacom applications mainly due to the compatibility with advanced lithography techniques developed for CMOS foundries, that enable precise fabrication of sub-wavelength structures en-mass at economies-of-scale.

The origins of silicon photonics can be traced back to the pioneering works of Soref and Pertermann in silicon waveguides during the mid-1980's [84, 85]. Since then, significant investments by industry and governments have accelerated its use in data communications [86] while attracting tremendous attention as a promising platform technology for biosensing applications as well [12, 23]. Its combination of excellent material properties (high contrast index), ultra-compact device footprint, established surface modification techniques [87], and fabrication compatibility with existing complementary metal-oxide semiconductor (CMOS) foundries [88] uniquely position it to become a diagnostic platform with ELISA-like performance [25].

2.1.3 Label vs. label-free

An important distinction in biosensing is whether or not an assay was performed labeled or label-free as shown in Fig. 2.1. In a labeled assay, quantitative signal enhancement can be achieved through the binding of an additional molecule to the immobilized target, as shown in Fig. 2.1a. This labeling process, also referred to as secondary amplification, can achieve sub-pg/mL sensitivities [3, 43] and provides additional specificity confirmation. Yet, amplification comes with trade-offs: it may limit multiplexing, does not allow for real-time kinetic monitoring of the target analyte, consumes additional reagents, and requires additional time and steps.

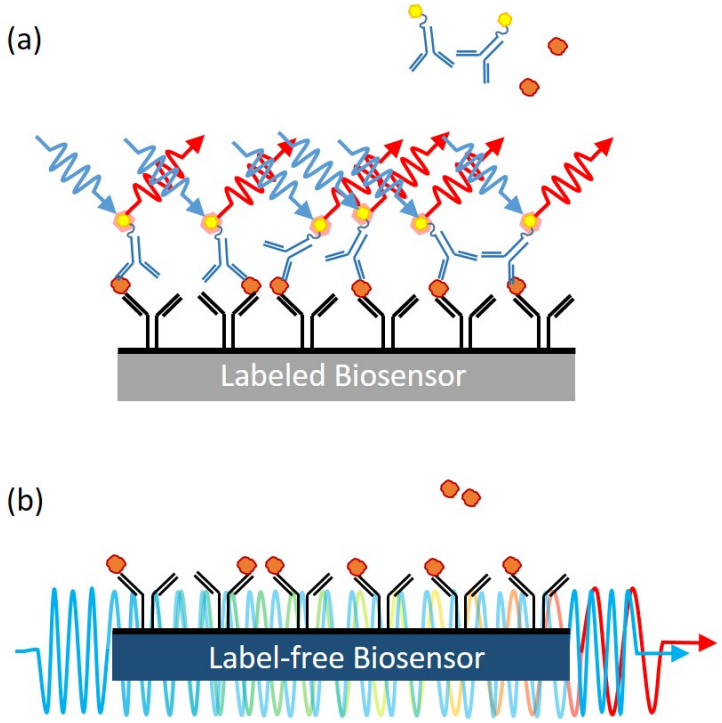

Figure 2.1: (a) Schematic representation of a biological stack-up for labeled assays, or tests involving secondary amplification. Biomolecules, such as antibodies with a florescent tag, bind to the immobilized target analyte and provide signal amplification when stimulated. (b) Schematic representation of a label-free biosensor. The sensor continuously monitors the surface and detects any additional bound mass from the captured target.

Label-free methods have emerged as a potential way to avoid possible structural and functional alterations of target molecules while providing acceptable sensitivity and selectivity. While label-free sensors also rely on immobilized bio receptor molecules with affinities to the target analyte, they do not require an additional label or amplification. The sensor translates the binding of the target into a measurable output signal, as shown in Fig. 2.1b. Label-free systems facilitate real-time kinetic monitoring and the rapid quantification of multiplexed titers [12, 89]. They simplify required assay steps, reduce reagent consumption, and enable high multiplexing in a single fluidic channel. Drawbacks include biological noise resulting

from non-specific binding and the lack of two compounded events that improve specificity (binding of both the target and label).

While silicon photonic biosensors have achieved impressive biosensing results, mainstream sensors often require label-based signal amplification for detection of extremely low concentrations [90]. Achieving sensitivities at pg/mL levels or lower with label-free silicon photonic sensors suitable for high-volume fabrication would greatly expand their clinical diagnostic potential as a label-free diagnostic device.

2.1.4 Sensitivity vs. specificity

The performance of a diagnostic test is determined by its sensitivity and specificity. Tests with high sensitivity and specificity are desirable. Sensitivity typically refers to the smallest amount of the target (concentration) that can be detected reliably. In this dissertation, the term detection limit will be used to describe the smallest detectable amount of the target analyte. Throughout this dissertation, the term sensitivity describes the optical sensor's response to refractive index changes (caused by bound mass on the sensor). We further distinguish between bulk and surface sensitivity. Bulk sensitivity refers to the sensor's response to a uniform change in the cladding whereas surface sensitivity refers to the sensor's response to biomolecular interactions at the sensor's surface, e.g. the adsorption of a thin layer of a protein. The 'cladding' refers to the aqueous environment that surrounds the sensor. The detection limit is described in terms of the sensor itself (intrinsic limit of detection, or iLoD) and the overall system (system limit of detection, or sLoD). The sLoD determines the noise floor and concentration limit of the system for diagnostic applications.

Specificity refers to the cross-reactivity of the surface chemistries to off target molecules. It largely depends on the fidelity of the capture molecule but is impacted by fouling and non-specific interactions. Fouling, which is the adsorption or binding of off-target molecules to the sensor's surface impact the detection limit. Surface modifications that resist fouling while providing robust conjugation elements for capture molecules have been employed to improve both the specificity and sensitivity of a system as described in Sec. 2.4. Finally, secondary

antibodies that bind to captured target molecules can further improve both sensitivity and specificity. The additional bound mass increases the sensor's signal while the biological specificity of the recognition element provides additional certainty and confidence in the presence of the bound target. Assays used to assess the biosensing performance of sensors developed as part of this work employ secondary amplification as described in Sec. 4.2.1.

2.2 Silicon photonic biosensors

Silicon photonic biosensors are chip-based devices that exploit the electric field distribution of light confined in a waveguide to sense biomolecular interactions on the surface of the waveguide. A portion of the light's electrical field exists outside the waveguide as an evanescent field and detects molecular binding events on the waveguide's surface as shown in Fig. 2.2a and Fig. 2.2b. Silicon photonic biosensors utilize optical resonant structures that are sensitive to changes in the refractive index in the evanescent field region [91]. When the target analyte binds to chemistries on the waveguide's surface, the accumulated mass changes the refractive index (RI) perturbing the evanescent field. This perturbation changes the sensor's resonant wavelength, indicating the presence of a bound analyte as shown in Fig. 2.2b.

Table 1.1 lists the performance of recently reported foundry-compatible silicon photonic biosensors. Many different sensor types have been developed for both silicon and silicon nitride substrates resulting in a range of performance metrics (Quality factor, sensitivity, and detection limit). While some were evaluated using clinically relevant assays, most devices employ established chemistries, like biotin-streptavidin systems, that provide high binding affinities, to demonstrate their biosensing capability. While these experiments show their potential, they do not reflect the complexity of a biological matrix or the sensor's performance under such conditions. Therefore, the sensors developed as part of this dissertation research are demonstrated with either a model biological sandwich assay (e.g.: antibody/antigen with amplification) or in human samples such as blood.

Although the main focus of the work presented here is primarily on experimental results

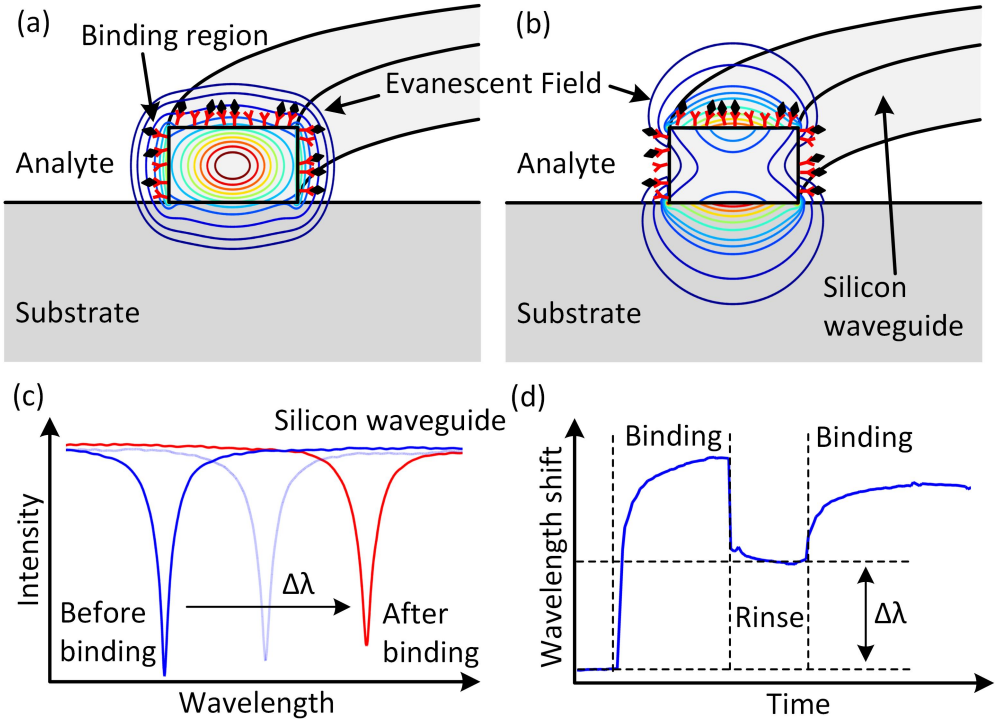

Figure 2.2: Operating principle for a silicon photonic biosensor. A portion of the optical mode exists outside the waveguide as an evanescent field and is sensitive to biological binding events on the waveguide's surface (orange region). (a) Mode profile for the fundamental TE mode. (b) Mode profile for the fundamental TM mode. (c) Analyte binding on a resonator structure increases the effective index (n_{eff}) resulting in a resonant wavelength shift, $\Delta\lambda$. (d) Sensogram of a biological assay where the shift of the resonant wavelength is recorded as function of time.

and the subsequent analysis, a theoretical understanding and derivation of simplified analytical solutions for silicon photonic waveguides and biosensors is key for optimizing and comparing sensors developed and characterized as part of this research project. The next section begins with the fundamental principles of light propagation in 2D silicon structures that are important for the waveguide structures used in the biosensors. Furthermore, the

performance metrics used for comparative analysis are described. The section concludes with design considerations for optical biosensors.

2.2.1 Waveguide fundamentals

A dielectric structure that is able to confine and guide an electromagnetic wave is referred to as a waveguide [92]. One such example is the optical fiber used in Internet data communications which has a core material with a high refractive index difference compared to its cladding, confining the light by total internal reflections (TIR). A similar principle extends to rectangular silicon wires, or waveguides, on a buried-oxide substrate [86]. Due to the fabrication processes utilized, these waveguides have a rectangular cross section and are typically realized in silicon-on-insulator (SOI) wafers. Figure 2.3 shows a 2D cross-section representing a silicon photonic waveguide.

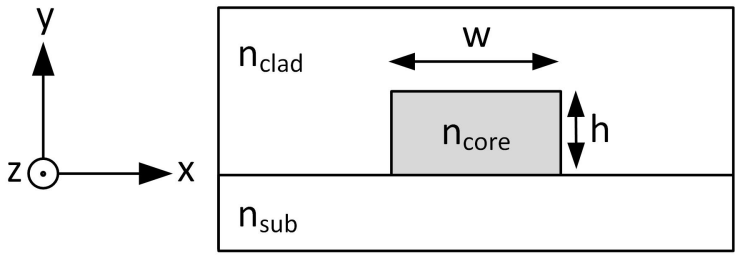

Figure 2.3: Schematic of a waveguide cross section with lateral mode confinement.

For the purpose of this dissertation, the substrate (n_{sub}) is a 2-3 µm-thick oxide layer on a 750 µm-thick silicon wafer. Waveguides (n_{core}) are etched into a 220 nm thick silicon layer grown onto the oxide layer with a width (w) and thickness (h), as shown in Fig. 2.3. Further etching can reduce the core thickness. Foundries typically standardize on 220 nm, 150 nm, and 90 nm thick cores [52]. The width can be of any dimension within the constraints of the process. When the light is confined in two directions (x and y axis), the light travels in the z direction (out of page as shown in Fig. 2.3) and assumes an electric field distribution

dependent on the waveguide's geometry, wavelength, polarization, and refractive index of the different materials. The resulting electric field distribution $\mathbf{E}_m(x, y)$ is referred to as *mode*. Due to translational invariance in x and y, the modal fields can be expressed as:

$$\mathbf{E}_m(x, y, z) = \mathbf{E}_m(x, y)e^{i(\omega t - \beta_m z)}, \tag{2.1a}$$

$$\mathbf{H}_m(x, y, z) = \mathbf{H}_m(x, y)e^{i(\omega t - \beta_m z)}, \tag{2.1b}$$

where β_m is called the propagation constant or eigenvalue of the mth mode. Waveguide modes can be regarded as transverse resonances of the field in a waveguide.

Modes

Waveguide modes are important to biosensing applications as they define the amount of electric field overlap with the biological sample, ultimately determining the sensitivity (see Sec. 2.2.1). Depending on the core's dimensions and the index contrast with the cladding, an optical waveguide will only support a discrete number of modes. The mode with the highest effective refractive index, n_{eff}, is typically assigned the lowest mode number, i.e., $m = 1$. A waveguide allowing only one optical mode is referred to as *single mode* and the term *multi mode* is used for waveguides that support more than one mode. Smaller waveguides typically support fewer modes, whereas larger waveguides support multiple modes.

Analytical solutions to mode profiles $\mathbf{E}_m(x, y)$ and $\mathbf{H}_m(x, y)$ for a rectangular cross section (e.g. Fig. 2.3) do not exist, therefore, they must be determined numerically. The mode solver used herein (by Lumerical Solutions Inc [93]) uses a finite difference technique in the frequency domain based on an algorithm proposed by Zhu and Brown [94]. The mode shape in a waveguide is determined by the wavelength, polarization of the light, and material properties (i.e. the refractive indexes of the core, n_{core}, the substrate n_{sub}, and the cladding n_{clad}). A large portion of the research effort described in this dissertation was focused on optimizing waveguide geometries to improve sensing performance. In this case, optimized waveguides may be different depending on the application. For example, a mode that sup-

ports fields that extend further from the waveguide surface may be useful for detecting large molecules and cells, whereas modes that confine their modal field close to the surface could be advantageous for sensing small particles and analytes.

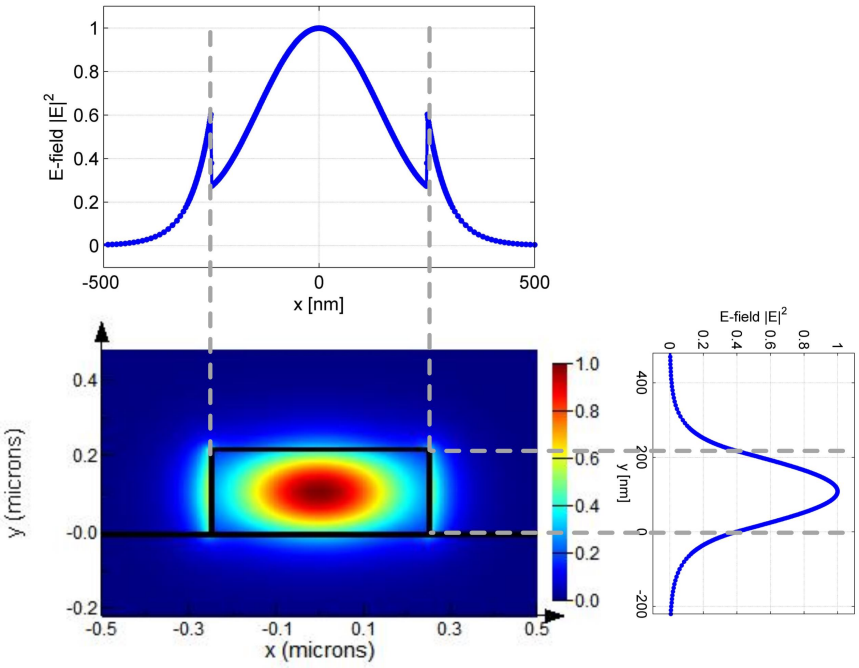

Figure 2.4: TE mode profile for a waveguide with thickness $t = 220$ nm and width $w = 500$ nm. The electric field is plotted at $x = 0$ nm and $y = 110$ nm for the vertical and horizontal line plot, respectively.

Figure 2.4 shows the field distribution of a TE mode for a silicon waveguide with thickness $t = 220$ nm and width $w = 500$ nm at a wavelength of $\lambda = 1550$ nm. The guiding structure consists of a silicon core (with $n_{core} = n_{Si} = 3.45$) on a silicon oxide substrate (with $n_{sub} = n_{SiO_2} = 1.44$) and water (with $n_{clad} = n_{H2O} = 1.33$) as cladding material, as most analytes of interest are in aqueous solution. The confinement factor is $\Gamma_{TE} = 0.78$. Similar to the equation for the confinement factor (Eq. 2.2), the fraction of the electric field (mode) propagating in the substrate and the cladding can be calculated. Doing so reveals that

10% travels in the substrate and 12% in the cladding. This has important implications for biosensing applications where we aim to maximize the overlap between the analyte and electric field.

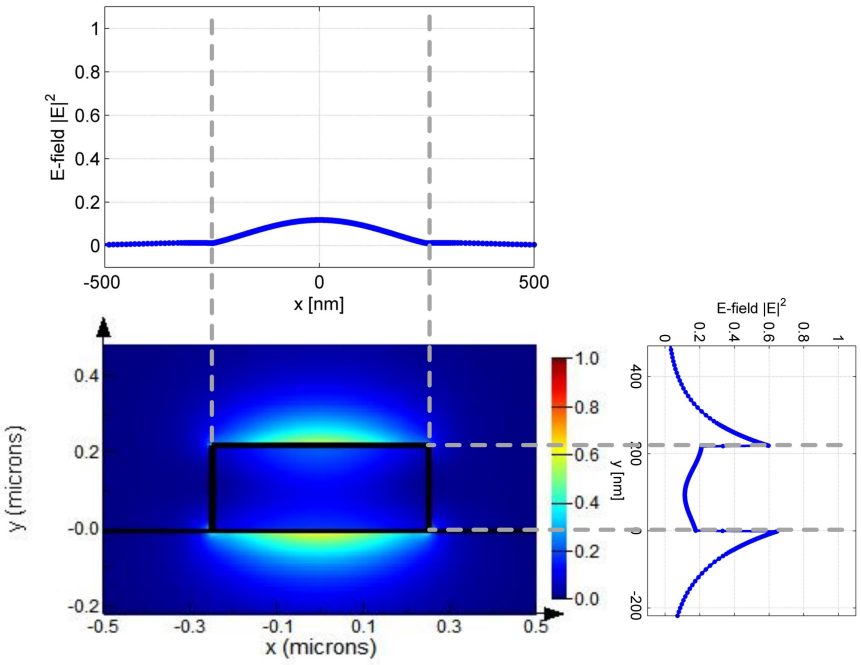

Figure 2.5: TM mode profile for a waveguide with thickness $t = 220$ nm and width $w = 500$ nm. The electric field is plotted at $x = 0$ nm and $y = 110$ nm for the vertical and horizontal line plot, respectively.

Figure 2.5 shows the modal field distribution for a TM mode with similar waveguide geometry as for the TE mode shown in Fig. 2.4. In this case, the confinement factor is $\Gamma_{TM} = 0.42$, meaning that the majority of the mode's electric field propagates outside the waveguide. Integrating the electric field in these regions reveals that 36% is in the substrate while 32% is in the cladding. Since the cladding's refractive index is smaller than the substrate, an asymmetric modal distribution exists, as seen in the line profile shown in Fig. 2.5.

Confinement factor

An important measure of how the light is guided in the waveguide (and how much is extending into the cladding) is determined by the confinement factor, which is the fraction, Γ, of the total power residing in the core [95–97]:

$$\Gamma = \frac{\frac{1}{2}\iint_{core} Re(\mathbf{E}\times\mathbf{H}^*)\cdot\hat{\mathbf{z}}\cdot dxdy}{\frac{1}{2}\iint_{total} Re(\mathbf{E}\times\mathbf{H}^*)\cdot\hat{\mathbf{z}}\cdot dxdy} = \frac{\frac{1}{2}n_{core}c_0\epsilon_0\iint_{core}|E|^2\cdot dxdy}{\frac{1}{2}\iint_{total} Re(\mathbf{E}\times\mathbf{H}^*)\cdot\hat{\mathbf{z}}\cdot dxdy} \tag{2.2}$$

The confinement factor is implicitly a function of the mode number. The fundamental mode (or lowest mode number) has the highest confinement and Γ can be close to 1. For higher order modes, the confinement is reduced until the cut-off is reached, meaning the waveguide no longer supports the mode. The confinement factor depends on the index contrast between the waveguide core and cladding. For biosensing applications, $1-\Gamma$ is the fraction of power *outside* the waveguide in the substrate and cladding where can be exploited for biosensing applications.

The confinement factor is a key aspect in designing biosensors optimized for specific applications since it is a measure of the electric field overlap with the biomolecules of interest. While increasing the electric field overlap with the biomolecules improves sensitivity, it also increases absorptive losses to the aqueous media, decreasing the sensor's detection limit. Therefore, we investigate various structures that have different confinement factors and compare their performance for biosensing applications.

TE polarization fraction

Because of the lateral and vertical mode confinement in waveguides with a rectangular cross section, the polarization of the existing modes is not purely transverse magnetic (TM) or transverse electric (TE). It is useful to understand the measure of TE polarization fraction for a given mode profile when designing biosensors since the polarization of light needs to be matched with the waveguide and resonator. Therefore, the measure of TE polarization fraction is defined as:

$$\xi = \frac{\iint |E_x|^2 \cdot dxdy}{\iint |E_x|^2 + |E_y|^2 \cdot dxdy} \tag{2.3}$$

For pure TE modes, the TE polarization fraction is $\xi = 1$, whereas for pure TM modes, the TM polarization fraction is $\xi = 0$. Modes which are predominantly TE-polarized ($0.5 < \xi < 1$) are referred to as quasi-TE modes and similarly the term quasi-TM mode is used for modes with TM polarization fraction smaller than 0.5. However, throughout the remainder of this document, quasi-TE and quasi-TM modes will be referred to as TE and TM modes, respectively.

Effective refractive index

The refractive index, n, of a homogeneous medium defines the increase in the phase change per unit length (wavenumber) caused by the medium. Assuming the optical permeability is the same as free space ($\mu_r = 1$), refractive index, $n(f, \epsilon_r)$, can be defined as:

$$\textit{refractive index (RI)} \approx \sqrt{\epsilon_r(f)} \tag{2.4}$$

where ϵ_r is the material's relative permittivity and f is the frequency of light. For frequencies of light investigated as part of this research, silicon waveguides on a SOI substrate with a high index contrast with aqueous cladding have the following refractive indices: $n_{core} = n_{Si} = 3.45$, $n_{clad} = n_{H_2O} = 1.33$, and $n_{sub} = n_{SiO_2} = 1.4$ (see Fig. 2.3). The refractive index of proteins of hydrated, adsorbed proteins, n_{ad} has been reported to be between 1.45 and 1.5 [98–101] (see Sec. 2.5). The refractive index is a property of the material itself but does not express the refractive index experienced by a mode traveling through a waveguide.

The *effective refractive index* has the same meaning as the refractive index but for light propagation in a waveguide. Generally, every mode has a different effective refractive index. It is not just a material property but includes the refractive index contributions from all the materials experienced by the optical *mode* (n_{Si}, n_{H_2O}, and n_{SiO_2}) in addition to the waveguide geometry itself. The effective index can also be defined as the ratio of phase

velocity in vacuum, c, to the phase velocity in the waveguide, $v_{p,m}$:

$$n_{eff,p,m} = \frac{c}{v_{z,p,m}} = \frac{k_{z,p,m}}{k_0} = \frac{\beta_{p,m}}{k_0} \tag{2.5}$$

where $\beta_{p,m}$ is the mode's propagation constant ($k_{z,p,m} \equiv \beta_{p,m}$) and k is the wavenumber. The subscript p is the polarization (either TE or TM) and m is the m^{th} mode of the polarization. k_0 is the wavenumber in vacuum defined as: $k_0 = \frac{\omega}{c} = \frac{2\pi f}{c} = \frac{2\pi}{\lambda_0}$, where λ_0 is the wavelength in vacuum and f is the frequency in all media.

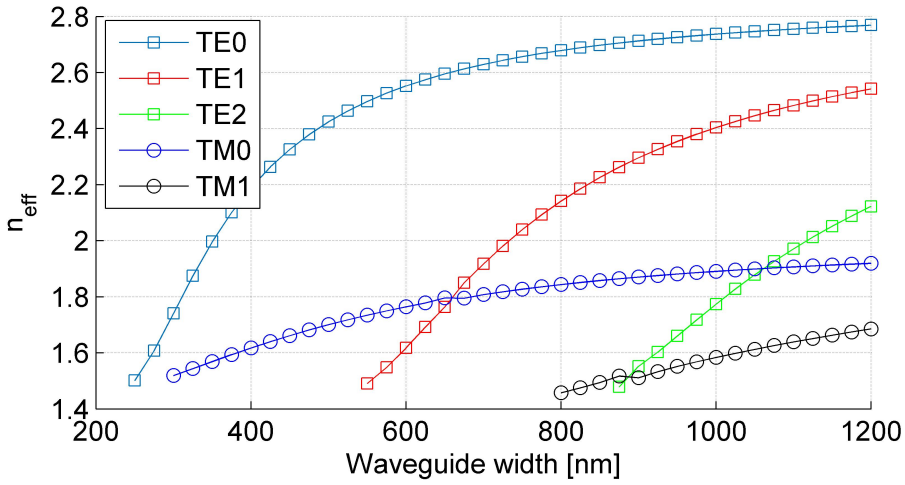

Figure 2.6: n_{eff} vs waveguide width (for thickness of 220 nm) for different modes

While an analytical solution to Maxwell's equations exist for a slab waveguide (confinement in one direction), numerical methods have to be applied to calculate electric field distributions in a rectangular, silicon waveguide [95, 97]. In this dissertation, MODE Solutions from Lumerical Solutions, Inc. is used exclusively. Figure 2.6 shows the effective refractive index as function of waveguide width for a waveguide height of 220 nm and wavelength $\lambda = 1.55$ μm for five supported modes (three TE and two TM modes). Below a width of 250 nm no mode is supported. For the range of waveguide widths $250 < w < 560$ nm the waveguide is said to be single mode, as it only supports one TE mode and one TM mode. At

$w = 660$ nm the second order TE mode (TE1) takes the same effective refractive index as the fundamental TM mode. For a waveguide width $w < 660$ nm the effective refractive index of the TM mode, $n_{eff,TM0}$, is larger than the effective index of second TE mode, $n_{eff,TE1}$ but smaller than the fundamental TE mode, $n_{eff,TE0}$.

In the context of biosensing the effective refractive index is the property affected by the adsorption of biomolecules on the waveguide's surface (which have a different refractive index than the solution). The most commonly used sensing configuration, a resonant structure, further translates the change in effective index into a change in resonant wavelength.

Dispersion

The effective refractive index of a propagating mode is not only dependent on geometry (as seen in Fig. 2.6 but also on frequency. *Dispersion* describes the mode's effective refractive index frequency dependence ($n_{eff}(f)$). This means that the phase velocity (and group velocity) is changing with frequency. The dispersion is typically visualized by plotting the wavenumber vs frequency (or wavelength) or alternatively the effective index vs frequency (or wavelength).

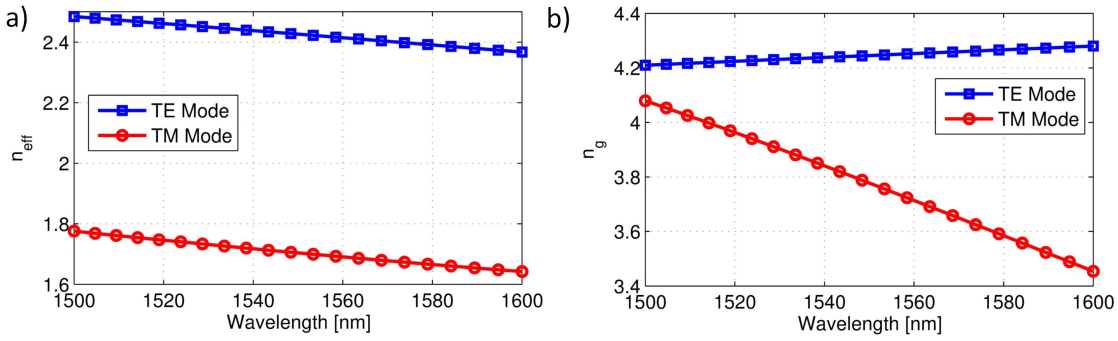

Figure 2.7: Dispersion of a waveguide with width of 500 nm and height of 220 nm: (a) effective index as function of wavelength and (b) group index as function of wavelength. The 2D model consists of a silicon waveguide on a buried oxide substrate surrounded by aqueous cladding on three sides.

Figure 2.7a shows the effective refractive index as a function of wavelength for both the TE and TM modes in a 500 nm wide by 220 nm thick waveguide. Note that the wavelength dependency of the effective refractive index shown in Fig. 2.7a is approximately linear over the wavelength range of interest, simplifying simulation models. For a waveguide mode ($n_{eff}(\lambda)$) the dispersion has two contributing factors: 1) the material dispersion; and 2) waveguide dispersion of the mode, a wavelength dependency caused by the lateral and horizontal field confinement.

Material dispersion *Material dispersion* includes the frequency dependence of the refractive index of a given material. A waveguide is comprised of high index and low index materials, e.g. $n_{Si}(f)$ as core material, $n_{SiO_2}(f)$ and $n_{H_2O}(f)$ as cladding materials. The individual material dispersion will affect the overall dispersion.

Waveguide dispersion It is helpful to introduce the term *waveguide dispersion* in contrast to *material dispersion*. Waveguide dispersion describes the mode's frequency dependence ($n_{eff}(f)$) caused by the 2D confinement.

For resonant biosensors, dispersion needs to be considered as it affects the sensitivity (see Eq. 2.15 and 2.16). A change in effective index caused by a cladding index change or adsorbed biomolecules, red shifts the resonant wavelength. Because of dispersion, the effective index is also different at that new wavelength. This is described in section 6.1.

Group index and group velocity Because of dispersion, the group index impacts sensitivity (Eq. 2.16) and not the effective refractive index (see section 6.1). The group index is defined by:

$$n_g(f) = n_{eff}(f) - \lambda_0 \frac{\partial n_{eff}}{\partial \lambda} \tag{2.6}$$

The group index, n_g, and the corresponding group velocity, $v_g = \frac{c}{n_g}$, is the measure of the speed at which the pulse envelope is traveling in a dispersive medium. Like the effective refrative index, the group index is dependent on wavelength as shown in Fig. 2.7b.

Evanescent field

The sensor's response scales with the modal overlap of the electric field vector with refractive index perturbation [102–104]. Section 2.2.1 describes how the electric field intensity decays away from the waveguide surface by plotting the electric field at a cross section of the waveguide. Therefore a waveguide sensor has a limited reach into the cladding. For a waveguide slab (mode confinement in y direction only) the electric field decay near the surface can be expressed as:

$$E(y) = E_0 e^{-y\frac{2\pi}{\lambda}\sqrt{n_{eff}^2 - n_{clad}^2}} \tag{2.7}$$

where E_0 is the electric field at the surface. For a waveguide (mode confinement in x and y) the equation approximately describes the evanescent field decay at the center of the waveguide, i.e. $E(x = w/2, y)$ and $E(x, y = \frac{h}{2})$ [105]. The characteristic decay length or penetration depth is defined as the distance after which the field is $E(y) = E_0/e$. The penetration depth is also sometimes referred to as 1/e length:

$$d_{1/e} = \frac{\lambda}{2\pi} \frac{1}{\sqrt{n_{eff}^2 - n_{clad}^2}} \tag{2.8}$$

Since the evanescent field decays exponentially, one can expect a higher surface sensitivity close to the waveguide. For an increasing thickness of adlayer the sensitivity will decrease and the next adlayer will eventually not change the propagation properties of the optical mode inside the waveguide anymore (see Fig. 2.8).

The characteristic length is used to indicate the reach of sensor into the analyte. For a quasi-TE mode with $n_{eff} = 2.43$ and $n_{clad} = n_{H_2O} = 1.333$ at $\lambda = 1550$ nm the characteristic length is $d_{TE} = 121$ nm while a quasi-TM mode with $n_{eff} = 1.8$ yields $d_{TM} = 203$ nm. An index perturbation beyond these distances will not cause a change in refractive index of the waveguide.

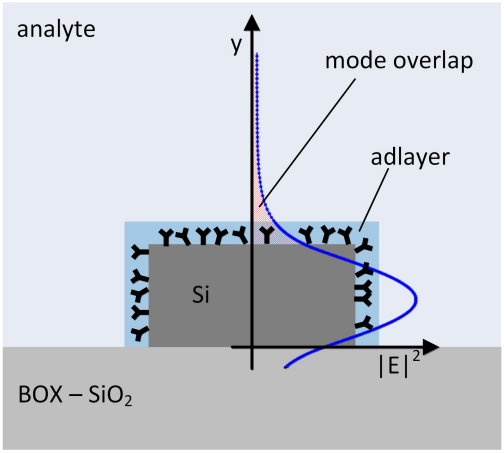

Figure 2.8: The sensitivity is proportional to the modal overlap with the analyte (hashed area)

Susceptability or waveguide sensitivity

For biosensing applications, it is of interest to understand the rate at which the effective refractive index changes (Δn_{eff}) as a function the cladding's refractive index (Δn_{clad}) or as a function of adlayer thickness (Δd_{ad}). Other factors can influence the effective refractive index as well (e.g. temperature and dispersion). When accounting for dispersion and temperature, a first order approximation for the change of effective refractive index (Δn_{eff}) is:

$$\Delta n_{eff} = \left(\frac{\partial n_{eff}}{\partial n_{clad}}\right)\Delta n_{clad} + \left(\frac{\partial n_{eff}}{\partial d_{ad}}\right)\Delta d_{ad} + \left(\frac{\partial n_{eff}}{\partial \lambda}\right)\Delta\lambda + \left(\frac{\partial n_{eff}}{\partial T}\right)\Delta T + \ldots \qquad (2.9)$$

The term $\frac{\partial n_{eff}}{\partial n_{clad}}$ is referred to as *waveguide susceptibility* or *waveguide sensitivity*. Similarly, the second term $\frac{\partial n_{eff}}{\partial d_{ad}}$ can be defined as the *adlayer susceptibility*. The third term $\frac{\partial n_{eff}}{\partial \lambda}$ is a consequence of dispersion and the fourth term $\frac{\partial n_{eff}}{\partial T}$ describes the *temperate susceptibility*. Assuming that temperature is constant, the last term can be ignored for now. In order to apply 2.9 and calculate all the susceptibility terms, the electric field distribution must be known. Since numerical methods are necessary, Lumerical Solutions Eigenmode solver MODE was employed.

Figure 2.9a and Fig. 2.9b show the waveguide susceptibility for a TE mode and TM mode respectively for different waveguide geometries. It can be seen that waveguides 220 nm thick is optimal for TM mode biosensors while 90 nm thick waveguides do better for their TE counterparts for waveguides 400 nm and larger.

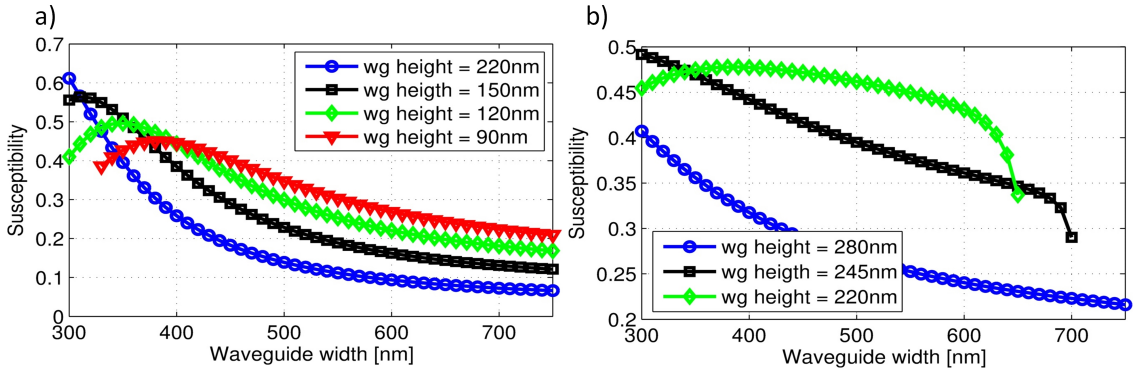

Figure 2.9: Waveguide susceptibility for the (a) the fundamental TE mode: Line plots for fixed waveguide heights of $h = 220$ nm, $h = 150$ nm, $h = 120$ nm, and $h = 90$ nm; and (b) the fundamental TM mode: Line plots for fixed waveguide heights of $h = 280$ nm, $h = 245$ nm, and $h = 220$ nm

To increase the bulk sensitivity, the mode overlap where the refractive index changes must be maximized. A weaker confined mode will therefore always have a higher bulk sensitivity since the mode is delocalized and more modal field is propagating outside the waveguide. However, for most biosensing applications, the refractive index only changes at the surface within a few tens of nanometers and a localized electromagnetic field near the surface is desirable [20]. It is helpful to distinguish between bulk and surface sensitivity (see Sec. 2.2.2). The dependence of both sensitivities on waveguide geometry is also discussed Sec. 2.2.2.

Loss mechanisms

Another important property of a mode is the loss, or power attenuation, as the mode travels down the waveguide. Loss is typically expressed in $\left[\frac{dB}{m}\right]$ but can also be converted to an absorption coefficient $\left[\frac{1}{m}\right]$ by:

$$\alpha_{[1/m]} = 10 \cdot \ln(10)\alpha_{[dB/m]} = \frac{\alpha_{[dB/m]}}{10\log_{10}(e)} = \frac{\alpha_{[dB/m]}}{4.34} \tag{2.10}$$

Loss is calculated by using the imaginary part of effective index:

$$\alpha_{\left[\frac{dB}{m}\right]} = 10\log_{10}\left(\frac{P(z=1)}{P(z=0)}\right) = 10\log_{10}\left(\frac{e^{-2n_i\frac{2\pi}{\lambda_0}}}{1}\right) = \frac{10n_i 4\pi}{\lambda_0 \ln 10} \tag{2.11}$$

where n_i is the imaginary part of the effective index of the mode. Losses in a waveguide can be attributed to different sources including scattering, absorption, radiation, and mode mismatch from bending waveguides. We will see later that loss is a significant factor in the sensor's intrinsic performance (as described by Equ. 2.20 and 6.3) but also in the system's overall signal path performance and detection limit.

Scattering loss For most fabrication processes, losses due to sidewall roughness and scattering dominate [106, 107]. The sidewall roughness depends directly on the fabrication processes and consequently, considerable effort has been invested into strategies that smooth the sidewalls [108, 109]. The roughness of the top of the waveguide is much smaller due to polishing processes [106–108]. Sidewall roughness increases for higher index contrasts like air versus those with aqueous or SiO_2 cladding [91]. A TE mode, 500 nm x 220 nm waveguide fabricated using deep UV lithography exhibits a loss of ≈2-3 dB/cm resulting from sidewall roughness [110] while the TM mode exhibits a loss of ≈0.5-1 dB/cm. Scattering loss can be reduced by minimizing the modal overlap with the sidewall, i.e. by increasing the waveguide width or by using rib waveguides.

Absorption loss Loss originating from material absorption is usually negligible for passive structures as both silicon and silicon oxide are nearly lossless at NIR wavelengths. However,

this is not the case for doped silicon [103] or when the oxide cladding is replaced by an aqueous solutions as the case in sensing applications. In fact, as described in Sec. 2.7.5, the water absorption is the dominant loss mechanism.

Radiation loss A mode confined in a silicon waveguide can couple to radiative modes into the cladding and substrate. For an SOI waveguide, the substrate leakage can be largely controlled by the thickness of the buried oxide layer. For a typical SOI wafer, the oxide layer is 2-3 µm thick which results in negligible substrate leakage losses for TE modes and 0.001 dB/cm for TM modes [107].

Bend loss The high index contrast between silicon, the oxide substrate, and aqueous cladding allows for sharp bends in a waveguide. The loss per bend originates from the radiation loss and the mode mismatch at the interface from a straight to bent waveguide. Because the mode is pushed towards the waveguide wall, scattering losses due to sidewall roughness might also increase slightly. Typical loss values for 90^o bend are around 0.01 dB/90^o for a TE mode and a bend radius of around 3 µm [52, 106]. For the work described in this dissertation, waveguide routing (connection from sensor to I/O location) bends with radius 5 µm for TE mode and 10 µm for TM mode have been chosen as the loss for such bends is sufficiently small minimizing its overall impact [52].

2.2.2 Biosensor performance metrics

There has been a fragmented effort to define a set of performance metrics for refractive index sensors [103, 111, 112]. The lack of universally accepted, comparative standards complicates performance comparisons among different types of silicon photonic biosensors. However, there are objective metrics that can be used such as: sensitivity, quality factor (Q), and detection limit. This section describes how the fundamental properties of light described in the previous sections extend to resonant cavities (biosensors) and impact their performance.

Resonator sensitivity

Section 2.2.1 introduced the concept of susceptibility which describes how a change in the cladding or an adsorbed adlayer can alter the propagation properties of the optical mode in a waveguide. A resonant structure can be used to translate the effective index change into a resonance wavelength shift ($\Delta\lambda_{res}$). Sensitivity can then be generalized as:

$$S = \frac{\Delta\lambda_{res}}{\Delta n} \tag{2.12}$$

where λ_{res} is the sensor's resonant wavelength [nm], and, n, is the refractive index [RIU] of the analyte. In case of a waveguide the refractive index, n, will be the refractive index of the cladding, n_{clad}. This generalized definition is important because it relates a change in the effective index (caused by molecular adsorption) to something that can be measured with a tunable laser and power meter (wavelength).

Two specific types of sensitivities are important in biosensing applications: (1) bulk sensitivity, which accounts for refractive index changes of the waveguide's entire cladding (the bulk) and (2) surface sensitivity, which describes resonant wavelength shifts for refractive index changes near the waveguide's surface (e.g.: protein adlayer). When not specifically called out, most discussions on sensitivity refer to the bulk sensitivity. This section briefly describes both types as well as how they are simulated numerically.

Bulk sensitivity For the definition of the bulk sensitivity, one can rewrite equation 2.12 to:

$$S_{bulk} = \frac{\Delta\lambda_{res}}{\Delta n_{clad}} \tag{2.13}$$

where Δn_{clad} is the cladding's refractive index change. RI sensitivity for a resonator is defined as the change in resonance wavelength ($\Delta\lambda_{res}$) per change in refractive index unit (Δn_{clad}) with units of [nm/RIU] [113–115].

For any resonator, a change in n_{eff} will affect the resonant wavelength λ_{res} and in turn

n_{eff} itself (non-zero slope of $\frac{\partial n_{eff}}{\partial \lambda}$). $\Delta\lambda_{res}$ is given by:

$$\Delta\lambda_{res} = \frac{\Delta n_{eff} L}{m}, m = 1, 2, 3, ... \tag{2.14}$$

where m is the longitudinal mode order of the resonant mode and L the round trip length. When accounting for dispersion, i.e. $n_{eff} = n_{eff}(\lambda)$, $\Delta\lambda_{res}$ becomes (using Eq. 2.14 and Eq. 2.9):

$$\Delta\lambda_{res} = \frac{L}{m}\left(\frac{\partial n_{eff}}{\partial n_{clad}}\right)_{\lambda_{res}, n^0_{eff}} \Delta n_{clad} + \frac{L}{m}\left(\frac{\partial n_{eff}}{\partial \lambda}\right)_{\lambda_{res}, n^0_{eff}} \Delta\lambda \tag{2.15}$$

where n^0_{eff} is the initial effective index at λ_{res}. Using Eq. 2.6 and rearranging this becomes

$$\Delta\lambda_{res} = \frac{\lambda_{res}}{n_g}\left(\frac{\partial n_{eff}}{\partial n_{clad}}\right)_{\lambda_{res}, n^0_{clad}} \Delta n_{clad} \tag{2.16}$$

For infinite slab waveguides, the bulk sensitivity can be analyzed analytically [114–116]. However, the lateral confinement of rectangular waveguides requires numerical solutions to find the mode field distribution, susceptibility, and group index (as described in Sec. 2.2.1). Using the computed waveguide susceptibility (see Fig. 2.9) and Equ. 2.16, the bulk sensitivity can then be determined.

Figure 2.10 shows the bulk sensitivity as function of waveguide geometry for the fundamental TE (Fig. 2.10a)and TM (Fig. 2.10b) modes. Based on these results, the bulk sensitivity for TE and TM is $\approx$ 60 nm/RIU and $\approx$ 200 nm/RIU, respectively, for a 500 nm x 220 nm waveguide. These plots also indicate that the bulk sensitivity can be improved by decreasing the waveguide's width and height.

Surface Sensitivity A sensor's resonant wavelength response ($\Delta\lambda_{res}$) to homogenous adlayer on its surface can be calculated using:

$$\Delta\lambda_{res} = \frac{L}{m}\left(\frac{\partial n_{eff}}{\partial d_{ad}}\right)\Delta d_{ad} + \frac{L}{m}\left(\frac{\partial n_{eff}}{\partial \lambda_{res}}\right)\Delta\lambda_{res} = \frac{\lambda_{res}}{n_g}\left(\frac{\partial n_{eff}}{\partial d_{ad}}\right)_{\lambda_0, d^0} \Delta d_{ad} \tag{2.17}$$

where d is the molecular layer thickness, assuming a homogeneous adlayer. Figure 2.11 shows the simulated surface sensitivity as function of layer thickness. The waveguide dimensions are 500 nm x 220 nm and the adlayer is assumed to have a constant refractive index of 1.48.

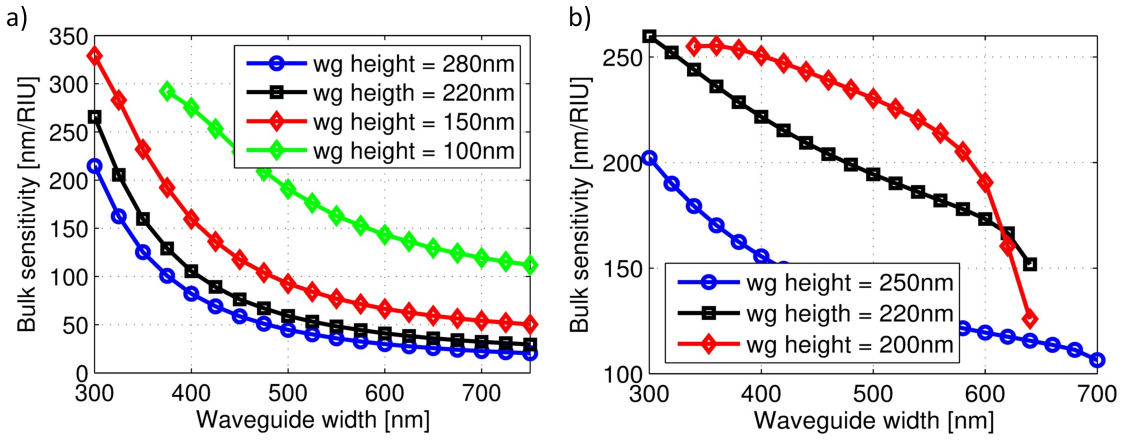

Figure 2.10: Bulk sensitivity for the fundamental TE and TM modes (1550 nm): (a) Line plots for fixed waveguide heights of $h = 280$ nm, $h = 220$ nm, $h = 150$ nm, and $h = 100$ nm for TE modes (b) Line plots for fixed waveguide heights of $h = 250$ nm, $h = 220$ nm, and $h = 200$ nm for TM modes.

By using the adsorbed mass rather than layer thickness Eq. 2.17 becomes:

$$\Delta\lambda_{res} = \frac{\lambda_{res}}{n_g A \rho} \frac{\partial n_{eff}}{\partial d} \Delta M \tag{2.18}$$

where M is the adsorbed mass ($M = \rho A d$), ρ is the molecular density, and A is the sensing area. For example, using a protein density of $1.33\,\mathrm{g/cm^3}$ [98, 99], an RI sensitivity ($\frac{\partial n_{eff}}{\partial d}$) of $0.2\ \mu\mathrm{m}^{-1}$, a sensing area (A) of $10\ \mu\mathrm{m}^2$, a group index (n_g) of 4.2, and a minimal detectable wavelength shift ($\Delta\lambda_{res,min}$) of 5 pm, a mass of 1.3 fg can be detected using Eq. 2.17. This example shows that sensing performance is not only described by sensitivity but also the minimal detectable wavelength shift of the system ($\Delta\lambda_{res,min}$). The detection limit is defined in Sec. 2.2.2.

Figure 2.12 shows the surface sensitivity of the fundamental TE mode for various waveguide dimensions at the wavelength of 1550 nm. The propagation property, n_{eff}, are computed for a strip waveguide in an aqueous solution with a 10 nm-thick protein adlayer (n=1.48) on the waveguide's surface.

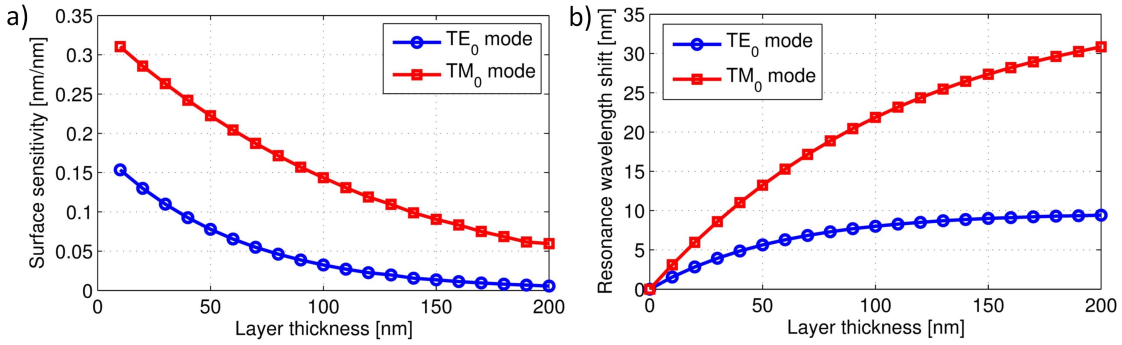

Figure 2.11: Surface sensitivity with a growing thickness of the adlayer (for a waveguide with dimensions 500 nm x 220 nm). (a) The surface sensitivity is plotted as function of layer thickness for TE modes; (b) The sensor output signal ($\Delta\lambda_{res}$) as function of the layer thickness for TM modes.

Temperature sensitivity The refractive index of a material is also dependent on temperature. For silicon the thermo-optic effect, $TOC = \frac{dn}{dT}$, is quite large with a coefficient of $1.8 \cdot 10^{-4}$ K^{-1} [117–119]. The temperature dependence originates from changes in the distribution functions of carriers and phonons, and temperature dependence of the band gap. The effect has been used in applications like thermal switching [120, 121] or to thermally tune modulators [122]. For biosensor, this sensitivity on temperature can impact detection limit. Therefore some effort has been put into the design of athermal devices [123–128] For silicon oxide, SiO_2, the thermo-optic effect is an order of magnitude smaller of about $\frac{dn}{dT} \approx 2.8 \cdot 10^{-5}$ K^{-1} [52]. Most biological applications are carried out in water, which has a negative thermo-optic coefficient of about $\frac{dn}{dT} \approx -9.9 \cdot 10^{-5}$ K^{-1} [129, 130]. The thermo optic coefficient for a waveguide mode with effective index n_{eff} will depend on the confinement factor of the mode as defined in Eq. 2.2. A TE mode is expected to have a higher temperature dependence than a TM mode as more of the electric field distribution overlaps with the silicon core. Similar to the bulk sensitivity as defined in Eq. 6.1 one can also define a temperature sensitivity for a resonator.

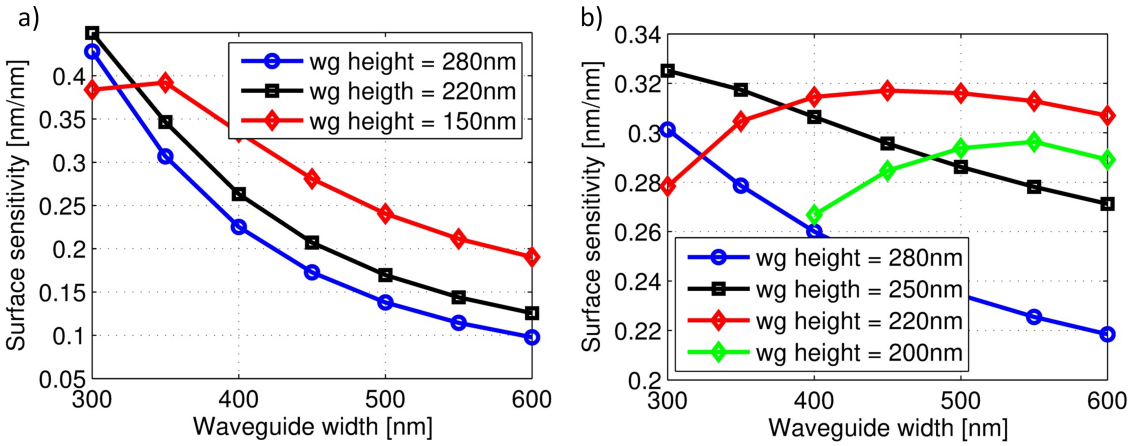

Figure 2.12: Waveguide surface sensitivity for the fundamental TE and TM mode (1550 nm): (a) Line plots for fixed waveguide heights of $h = 280$ nm, $h = 220$ nm, $h = 150$ nm for TE modes; (b) Line plots for fixed waveguide heights of $h = 280$ nm, $h = 250$ nm, $h = 220$ nm, and $h = 200$ nm for TM modes.

$$\frac{\Delta\lambda_{res}}{\Delta T} = \frac{\lambda_{res}}{n_g}\left(\frac{\partial n_{eff}}{\partial T}\right)_{\lambda_{res},T_0} \tag{2.19}$$

Chapter 4 will report measured temperature sensitivities for TE and TM resonators of $\approx$ 70 pm/K and $\approx$ 30 pm/K respectively.

Quality factor

The quality factor (Q) is a measure of photon lifetime in the resonator and represents the number of oscillations before the photon's energy has decayed to 37% (1/e). Q is a dimensionless number that incorporates the sensor's total loss in terms of the material's index of refraction [103] and is approximated experimentally by dividing the resonant peak's wavelength (λ_{res}) by its full width at half its maximum (FWHM). Higher quality factors reduce the spectral noise of the sensor [112]. Algebraically, the quality factor is:

$$Q = \omega_{res} \frac{\mathcal{E}}{\partial \mathcal{E}/\partial t} = \frac{2\pi \cdot n_g \cdot 4.34}{\lambda_{res} \cdot \alpha_{[dB/m]}} \approx \frac{\lambda_{res}}{\Delta\lambda_{3dB}} \tag{2.20}$$

where α is the losses in the resonator, $\omega_{res} = 2\pi f_{res}$ is the resonance frequency, $\mathcal{E}$ is the energy stored in the resonators and $\Delta\lambda_{3dB}$ is the 3 dB bandwidth of the resonance peak. Specific loss mechanisms are described in Sec. 2.2.1.

Intrinsic detection limit

As shown in Eq. 2.17 and Eq. 2.18, the smallest measurable (refractive index) change is limited by the minimal detectable wavelength shift of the system ($\Delta\lambda_{res,min}$). The system's detection limit ($sLoD$) depends on external instruments (laser, power meters, etc.) which makes it challenging to objectively compare sensor performance. Therefore, we introduced the intrinsic limit of detection ($iLoD$) [103] which depends on intrinsic characteristics of the resonator itself (see Eq. 6.3). This definition assumes that the minimum detectable wavelength shift is equal to one line width of the resonator $\Delta\lambda_{res,min} = \Delta\lambda_{3dB}$ as described in Sec. 2.2.2. The intrinsic limit of detection is defined as:

$$iLoD = \frac{\lambda_{res}}{Q \cdot S} \tag{2.21}$$

The iLoD [RIU] can be understood as the minimum index change required to shift the resonance wavelength by one line width ($\Delta\lambda_{3dB}$). If the loss of a round trip in the resonator is dominated by water absorption, then the intrinsic limit of detection has reached the fundamental limit and cannot be further improved by design of the resonators but only by choosing a wavelength where absorptive losses to water are reduced.

2.3 Porous membranes

One of the objectives of this research project involves the integration of porous membranes and silicon photonic biosensors. The ability to replace pumps, gaskets, and flow cells without impacting performance demonstrates a significant system simplification and integration

towards a portable diagnostic for point-of-care settings. Therefore, this section provides a brief background on porous membranes to provide a foundation for the work described in Chap. 5.

Lateral flow tests using nitrocellulose membranes were first described in the 1960s. The first application utilizing lateral flow strips included detecting human chorionic gonadotropin (hCG)(or pregnancy) and was commercialized in 1988 by Unipath [131]. Today, tests exist to detect infectious disease, illicit drugs, ovulation, and other important biomarkers [132–134]. Most nitrocellulose test strips are modeled after existing immunoassay formats but use immunochromatographic chemistries to visually report the result. A mix of capture and competitive assay formats exist but most share the formation of a complex between the target analyte, reporter particle, and capture agents immobilized to the membrane [135].

Nitrocellulose membranes have many unique characteristics requiring careful consideration when integrating them into a diagnostic system. While equations exist that describe flow in porous membranes, optimizing design parameters (pore size, reagent concentrations, etc.) for a particular application often needs to be determined empirically [135]. This section briefly highlights properties and characteristics of porous membranes relevant to the research herein.

2.3.1 Chemical composition and binding mechanism

The base material of nitrocellulose membranes comes from one of the most abundant resources on earth, cellulose. To facilitate hydrophilicity and the binding of proteins, native cellulose fibers are nitrated through an esterification process involving a nitrating acid to conjugate $-NO_2$ groups to the $-OH$ groups. Even though nitrocellulose membranes are overall neutral in charge, the primary binding mechanism between the membrane and proteins involves electrostatic interactions. The strong dipole moments of the nitrate esters in the membrane interact with dipole moments in a protein's peptide bonds and facilitate immobilization (through electrostatic interactions). This allows loading of the membrane with capture agents for an assay.

2.3.2 Capillary flow

Capillary flow describes how fluid moves through porous media without an external pressure gradient provided by a pump. The pressure that creates capillary flow originates at the fluid-front where a three phase interface exists among the membrane, the liquid, and air. A saturated membrane (behind the fluid front) creates a pressure differential at the fluid-air interface. The nitrocellulose membrane is polar resulting in a small contact angle for the liquid. This hydrophilic interface in addition to the pressure gradient across the liquid-air boundary helps push the liquid front forward. The fluid front will readily interact with the hydrophilic surface ahead resulting in forward flow.

Since the capillary pressure cannot be estimated easily using contact angle, porosity, and pore size radius for nitrocellulose membranes [136], it is often evaluated experimentally and paper manufacturers report the flow time of the fluid front wetting a dry membrane to a certain length (4 cm). The Millipore HF135 membrane[135] used for the experiments described herein report a capillary flow time of $(sec/4cm)$ is 135 ± 34. The estimated values are within the tolerances required for the work proposed herein. Empirical values provided by the Yager Lab (based on their experimental data) for permeability and capillary pressure were used as well.

2.3.3 Fluid flow

The flow rate in a fully wetted, porous membrane network can be approximated using Darcy's Law:

$$Q = \frac{\kappa wh}{\mu L}\Delta P \tag{2.22}$$

where Q is the volumetric flow rate, κ is the permeability of the paper, wh is the cross-sectional area in width and height, μ is the dynamic viscosity, and ΔP is the pressure drop occurring over the wetted length, L, in the paper network. This equation shows how volumetric flow rate in paper devices can be controlled by varying the fluid path length, L,

as has been demonstrated by Lutz, *et al.* [137, 138]. By defining the fluidic resistance as

$$R = \frac{\mu L}{\kappa w h} \tag{2.23}$$

one can compare a fluidic network to an electrical circuit. Ohm's law ($\Delta V = RI$) with I the electric current, R the electrical resistance, and ΔV the voltage becomes $\Delta P = RQ$ for flow rate (Q), with R the fluidic resistance as defined in Equ. 2.23.

2.3.4 Flow regimes

Flow rates in membranes with pore sizes on the order of 1-10 µm's have Reynolds numbers, Re, on the order of 10^{-3}. The Reynolds number is given as the ratio of inertial forces to viscous forces:

$$Re = \frac{inertial forces}{viscous forces} = \frac{\rho v L_{char}}{\mu} \tag{2.24}$$

where ρ is the fluid density $[\frac{kg}{m^3}]$, v is the mean velocity of the fluid $[\frac{m}{s}]$, L_{char} is the characteristic traveled length $[m]$, and μ is the dynamic viscosity $[Pa \cdot s]$. It is important to note that L_{char} in Equ. 2.24 is the characteristic length (perpendicular to the L in Equ. 2.22 and 2.23). For $Re < 2300$ laminar flow occurs whereas turbulent flow occurs for larger Reynolds numbers $Re > 2300$.

While the Reynolds number indicates the flow regime, the Peclet number, Pe is a characteristic number for mass transport. It is defined as the ratio of advective transport to diffusion transport:

$$Pe = \frac{advective\ transport\ rate}{diffusive\ transport\ rate} = \frac{v L_{char}}{D} \tag{2.25}$$

where D the mass diffusion coefficient. For $Pe << 1$ the mass transport is dominated by diffusion and a depletion can propagate upstream [139]. In porous networks the Peclet number is usually larger ($Pe > 100$) [140].

2.4 Bioconjugate chemistry

The term 'bioconjugation' refers to the joining of two biomolecules by biological or chemical means. Immobilizing biomolecules specific to a target analyte on a silicon's surface via chemical synthesis is fundamental to the operation of silicon photonic biosensors. Biomolecules include proteins, glycans, nucleic acids, or small molecules. The binding of an antibody to an antigen is an example of bioconjugation, or the immobilization of a capture molecule on the silicon photonic sensor is another. While various surface modification strategies of silicon-based substrates have been demonstrated [30, 40, 141–143] and reported in many review papers [87, 144–148], the sections below summarize the key points related to this research.

Selecting the proper immobilization technique is essential in ensuring optimal molecular orientation, surface density, and uniformity on the sensor's surface. Ideally, surface functionalization should employ chemistries that do not damage the silicon surface or receptor biomolecules, require few reaction steps, have low optical absorption, produce thin homogeneous layers, result in good coverage and reproducibility, and provide robust attachment for capture molecules close to the sensor's surface. Biomolecules should have high specificity and avidity to their respective targets.

The primary methods used to functionalize a silicon substrate include: (1) physical adsorption, (2) bioaffinity, and (3) covalent attachment [149]. Figure 2.13 shows a schematic representation of these methods and each is briefly discussed below.

2.4.1 Physical adsorption

The simplest approach to functionalize a silicon photonic biosensor is to immobilize proteins via physisorption. Physisorption, the irreversible binding of proteins to a surface, is a well-known phenomenon in biomaterials science [150, 151] and is sufficient for preliminary validation purposes. Voros *et al.* reported on protein adsorption, its density, and the refractive index change of protein adlayers [99]. He notes that despite the large number of studies, we only have a rudimentary understanding of the adsorption process at the molecular level.

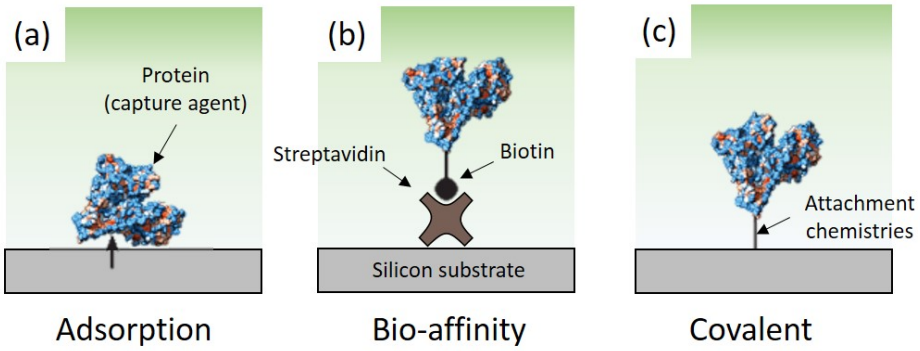

Figure 2.13: Schematic representation of functionalization strategies for silicon photonic biosensors. (a) Direct adsorption to the native silicon oxide substrate via physisorption. Binding occurs through intermolecular forces (charged species) (b) Bio-affinity interactions provide robust immobilization of capture molecules (biotinylated antibody in this example) to Streptavidin physisorbed to the substrate. (c) Covalent attachment via chemistries and functional groups.

He suggests that the adsorption process involves three phases:

1. Protein transport to the surface

2. Surface binding via hydrophobic and electrostatic interactions

3. Relaxation on the surface via conformational changes

The phases listed above depend on the water molecules, solvated ions, and other small molecules in the surrounding of the proteins and in proximity to the surface. These small molecules affect the protein's adsorption properties by mediating the electrostatic and hydrophobic interactions but also by destabilizing the secondary and tertiary structure [152–154].

Protein A adsorption

Originally derived from the bacterium *Staphylococcus aureus*, protein A is a 42 kDa globular protein with a diameter of approximately 3 nm [155, 156], a RI of 1.48 [99], and a high affinity for the Fc domain of human and mouse antibodies (IgG), facilitating their orientation towards the fluidic channel to maximize capture [157, 158]. Coen *et al.* observed that the first protein A adlayer often denatured resulting in a 1 nm thick, biologically inactive film but the second layer of protein A, forming on top of the first layer, provided active receptor sites to bind the Fc domain of IgG [159].

As described in Chapter 4, the biosensors developed during this research project were subjected to a sandwich assay (Sec. 4.2.1) to assess their performance for biosensing applications. We adsorb Protein A to the native oxide surface to immobilize antibodies which functionalize the sensor. We also assume a physisorbed layer of protein A (n=1.48) between 1-3 nm thick to determine sensor coverage when analyzing experimental results.

Streptavidin adsorption

Streptavidin is a 52.8 kDa protein purified from the bacterium *Streptomyces avidinii* and is approximately 5 nm in diameter [160, 161]. The tetrameric structure provides four binding sites for biotin. The biotin-streptavidin complex has the highest reported non-covalent bond, with an unbinding force of up to 250 pN [149]. While most commonly used for purification, it serves two purposes for my research. Firstly, it is used as the model target antigen used in sandwich assays during sensor characterization (Sec. 4.2.1). Its size is representative of most clinically relevant targets, like the PSA antigen, which is 34 kDa. Secondly, it is used to create a bio-affinity layer on the native oxide substrate to functionalize the sensor for the blood and serologic phenotyping assays described in Chapters 5 and 6.

Limitations

While efficient and simple, physisorption has a number of drawbacks. Immobilization is not as stable or robust as bio-affinity or covalent attachment. Desorption can occur under flow during assays altering the total bound mass and sensor signal. Physisorption also results in random orientations, providing a fraction of the total available binding sites. If immobilization density is too high, active sites could be sterically blocked, preventing binding. The randomness of adsorption makes it difficult to reliably reproduce surface functionalization. Relaxation and conformational changes at the surface often damage the protein or reduce its bio-activity [159]. Incubation times are long (typically 3 hours or more) and surface regeneration is challenging. Despite these deficiencies, physisorption provides a facile functionalization approach for silicon photonic biosensors and is used extensively in accomplishing the research described herein.

2.4.2 Bioaffinity

Bioaffinity interactions differ from physisorption because reactions yield stronger, highly specific, and oriented protein immobilization [162, 163]. Bioaffinity complexes are non-covalent ligand-receptor pairing and can often be reversed using heat, a change in pH, or chemical treatments [164]. Most often, bioaffinity reactions are used in conjunction with either physisorption or covalent attachment techniques.

Biotin-streptavidin systems

The bio assays described in Chapters 5 and 6 rely on bioaffinity reactions for serology and erythrocyte phenotyping. Biotinylated antibodies are conjugated to streptavidin-coated sensors.

Protein A-antibody systems

The bio assays described in Sec. 4.2.1 rely on bioaffinity reactions for the immobilization of the antibody (anti-streptavidin) to an adsorbed Protein A adlayer, the binding of its conjugate antigen (streptavidin), and then a final amplification step involving biotin-streptavidin conjugation.

Carbohydrate systems

Sugar molecules, like α-D-Mannose, β-D-Mannose, GDAP, provide primary conjugation sites on glycoproteins. For example, the disaccharide and trisaccharide epitopes on erythrocyte membranes ultimately determine someone's blood type (discussed in Sec. 2.6.1).

2.4.3 Covalent attachments

Covalent attachment is arguably the most popular functionalization strategy for silicon photonic biosensors due to the robust immobilization of the capture biomolecule and ability to regenerate the sensor [87, 141, 145, 146]. The sensor's native oxide surface is activated using a molecule like APTES that creates covalent linkages to the substrate and reacts with amino acid residues on proteins, forming an irreversible bond between the protein and surface. Functional groups facilitate such reactions and linkages.

Functional groups

Functional groups are collections of atoms that confer specific properties to molecules. They are present on nucleic acids, proteins, carbohydrates, and lipids and facilitate bioconjugation. Functional groups are usually categorized as hydrophobic or hydrophilic depending on their charge and polarity. Methane is an example of a non-polar, hydrophobic functional group whereas the carboxyl group found in amino acids is polar and hydrophilic. The most widely used functional groups for bioconjugate chemistry are listed in Table 2.1. While the C- and N-terminals of peptide chains can be used for bioconjugation, the popular side groups that

Table 2.1: **Common functional groups in proteins used for bioconjugation**

Group	Amino Acid	Surface
$-NH_2$	Lys	carboxylic acid, active ester (NHS), epoxy
$-SH$	Cys	maleimide, pyridyil disulfide, vinyl sulfone
$-COOH$	Asp, Glu	amine
$-OH$	Ser, Thr	epoxy

appear on a folded protein and can be used for conjugation reactions as well are listed in Table 2.1.

Silane chemistries

Organofunctional alkoxysilane chemistries facilitate self-assembled layers on the native silicon substrate and provide covalent linkages, through leaving groups, to various capture molecules (proteins, nucleic acids, etc.) [165]. A popular aminosilane, APTES (3-aminopropyl-triethoxysilane), can bind to hydroxil groups present on the native oxide silicon substrate with a linkage to a functional group at its other end. The reaction at the silicon surface involves condensation between the siloxanes of the organosilane and hydroxyl moieties present on the native oxide surface. Siloxane monolayers form by the chemisorption process of self-assembling molecules, such as trichloro-, trimethoxy-, or triethoxysilanes, onto the silicon substrate [165]. Water content, solvent use, age of the reagents, deposition time, temperature, and atmospheric moisture must be addressed to limit instability of silane layers and maximize ligand conjugation. The reaction is usually slow, requiring hours of incubation.

While a variety of commercially available organosilanes exist [166], $-NH_2$, $-SH$, $-COOH$, and epoxy functional groups are mainly employed. This may be due to the well established bioconjugation methods and the short alkyl chains they can provide. Immobilizing the capture agent as close to the silicon surface as possible maximizes the evanescent field overlap

and surface sensitivity of the overall sensor. If the APTES linkage is too short to properly immobilize large proteins (such as antibodies and enzymes) in high capacity owing to steric hindrances hydrophilic polymers such as dextran (DEX) [167], chitosan [168], and PEG [169] provide longer spacers for improved sensitivity.

Amine-glutaraldehyde-amine chemistry

Amines ($-NH_2$) are popular covalent binding sites since lysine residues are accessible on the exterior of most proteins. Aldehydes react with amines to form a Schiff base which can be further reduced to form a stable secondary amine bond. Glutaraldehyde is a *bis*-aldehyde compound with two reactive ends. It can be used to crosslink two amines, conjugating two proteins or forming a covalent bond between a protein and surface-immobilized polymer.

EDC/NHS chemistry

EDC-NHS chemistries are commonly used to in a two-step cross-linking procedure to conjugate a carboxylic acid and primary amine. N-hydroxysuccinimide ester (NHS), one of the most commonly used covalent linkers, reacts with amines resulting in stable amide bonds [166]. More often, a sulfo-NHS ester is used since it is water soluble.

EDC (1-ethyl-3-(3-dimethylamonipropyl) carbodiimide)) is a popular carbodiimide [166]. EDC is soluble in water and can react with proteins directly in aqueous buffer, unlike NHS which is dissolved in an organic solvent (e.g., DMSO). EDC reacts with carboxylic acid to form either an amide bond with a primary amine or an unstable intermediate, o-Acylisourea. Sulfo-NHS esters can react with o-Acylisourea to finish the reaction, forming a stable conjugate [166].

2.4.4 Surface regeneration

The most widely used oxidants in surface regeneration include oxygen plasma [30, 170, 171] and piranha solution [20, 172]. Both approaches were used to regenerate the silicon surfaces

in this research. Oxygen plasma ashing was performed at 125 W for 5 minutes at the Washington Nanofabrication Facility. Chips were also subjected to Piranha, prepared as 1:1 (30% H_2O_2:98% H_2SO_4), for 15 minutes while actively sonicated to reduce the formation of air bubbles on the surface. Both approaches help remove organic material from the surface and produce hydroxyl groups on the native silicon surface. While other groups have reported the number of regeneration cycles to range from three to five [87], we found that sensors could be regenerated dozens of times with minimal performance impact using these methods.

2.4.5 Fouling and non-specific interactions

To enable silicon photonic devices to detect certain biomolecules in clinically-relevant samples (e.g. plasma, cerebrospinal fluid) the silicon chip must possess both specificity towards target biomolecules within those complex matrices and the ability to prevent a nonspecific binding of biological interferants. When exposed to complex media, the surface of the sensing chip can be fouled by proteins. For example, high abundance species such as serum albumin, fibrinogen, fibronectin, and circulating immunoglobulins found at concentrations that dwarf most target analytes by several orders of magnitude. This biological noise can substantially degrade the chips sensitivity and impacts the systems detection limit. Protein fouling results from hydrophobic interactions that decrease a protein's surface energy. High hydrophobicity can be associated with a large free surface energy. Thus, strategies that minimize fouling focus on improving the hydrophilicity of sensor's surface.

Advanced interfacial science and polymer chemistry are providing novel solutions to this challenge. For instance, layers of electrostatically neutral zwitterionic polymers have been shown to produce ultra-low fouling surface capable of preventing fouling by nonspecific proteins in clinical samples [173, 174]. Our group has demonstrated that these zwitterionic polymers can be implemented on these silicon photonic chips to yield biosensing devices capable of performing with ELISA-like sensitivity in real-time in undiluted human samples (blood plasma) [40].

2.5 Refractive index of protein adlayers

Each biomolecule interacting with the surface of the sensor causes a local change in refractive index, which in turn alters the propagation properties of the guided light. The biomolecular layer can be modeled as uniform layer with thickness d_{ad} and refractive index n_{ad} [99, 175]. The refractive index of said layer, and even the thickness, is a matter of ongoing research, but general statements can be made. The refractive index n_{ad} is between the refractive index of the dry molecules and the refractive index of the solution, n_{bulk}, which, in most cases, is an aqueous solution or PBS [99]. The refractive index of such solutions is around 1.33. The refractive index for hydrated, adsorbed proteins, n_{ad} is between 1.35 and 1.6 in literature. For most proteins, it is between 1.45 and 1.5 [98–101]

In the context of biosensors, the main purpose is to measure the mass M of protein deposited per unit area $\left[\frac{g}{cm^2}\right]$]. A simple model, proposed by De Feijter *et al.* and validated for small molecules [176, 177], is:

$$M = d_{ad}\frac{n_{ad} - n_{bulk}}{\frac{\partial n}{\partial c}}, \tag{2.26}$$

where d_{ad} is the thickness of the adsorbed layer, n_{ad} the refractive index of the adsorbed layer, n_{bulk} the refractive index of the solution, and $\frac{\partial n}{\partial c}$ is the refractive index increment of the protein in solution and is about $0.18\,{}^{\mathrm{cm}^3}/_{\mathrm{g}}$ and more or less constant for most proteins [101, 178, 179]. This means that the bound mass can be calculated if the thickness and the refractive index of the depositied film is known.

The refractive index of adsorbed protein films, n_{ad} is typically 1.48 [98, 99]. However, also of interest is how d_{ad} and n_{ad} evolve as the monolayer builds up. The molecular layer can be modeled as an adlayer with fixed height and varying refractive index. This variation is assumed to be linear starting from the bulk solution index to a saturation index of a densely packed monolayer [98, 99]. Hook *et al.* showed that for submonolayer, the refractive index within the layer d_{ad} can be expressed by [98, 180]:

$$n_{ad} = n_{bulk} + c_{ad}\frac{\partial n}{\partial c}, \tag{2.27}$$

where c_{ad} is the mean concentration of the adsorbed species within the layer with thickness d_{ad}. Voros *et al.* further used the following equation to express the refractive index of the adsorbed layer as function of densities:

$$n_{ad} = n_{bulk} + \frac{\rho_{ad} - \rho_{bulk}}{1 - \frac{\rho_{ad}}{\rho_{protein}}} \frac{\partial n}{\partial c}, \tag{2.28}$$

where ρ_{ad}, ρ_{bulk}, and $\rho_{protein}$ are the densities of the adlayer, the bulk solution and the dry protein respectively. Alternatively, one can assume a constant refractive index of the layer, n_{ad}, but a changing effective thickness $d_{ad}(t)$, where t denotes the deposition time. This approach has been used in [181–184]. Both of the suggested approaches are approximations and their validity depends on the biomolecule and the experimental conditions. Therefore, it is necessary to perform a calibration with known concentrations for each biomolecule in order to be able to do a quantitative analysis.

2.6 Blood typing

Blood is the primary diagnostic window into the body's chemistry [185]. Whole blood contains plasma (≈55%) and cells (≈45%), which include leukocytes, platelets, and erythrocytes [186]. Leukocytes, or white blood cells, help form the immune system and protect the body against infectious disease and foreign matter. Platelets, or thrombocytes, are small disk-shaped cell fragments that help with clot formation to stop bleeding. Finally, erythrocytes, or red blood cells (RBCs), are biconcave discs cell that transport oxygen to and carbon dioxide from tissues throughout the body. Red blood cells exhibit inherited carbohydrate moieties on membranous glycolipids that determine their blood group.

In addition to the cells, whole blood is made up of plasma [185]. Plasma consists of serum and fibrinogen, a clotting factor. About 90% of serum is water, 8% proteins, 1% salts, with a combined remaining of lipids, sugars, hormones, enzymes, nutrients, and gases. Of the proteins, the three primary types exist: albumin (60%), which helps maintain osmotic pressure, immunoglobulins (35%), which are part of the immune system, and fibrinogen

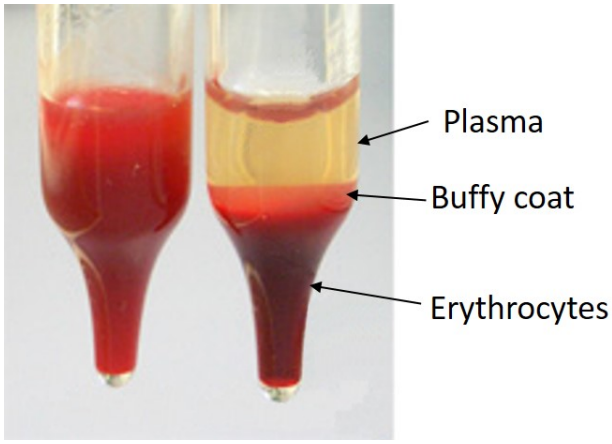

Figure 2.14: Photo of homogeneous whole blood (left) and separated constituents (left) after centrifugation. The Buffy coat contains leukocytes and platelets and is typically $< 1\%$.

(4%). The experiments performed as part of this research project involved the detection of immunoglobulins in serum as a way to determine blood type in a reverse fashion.

Figure 2.16 shows a picture of homogeneous whole blood (left) and centrifuged blood to separate its constituents. The plasma and cells can be separated by centrifugation resulting in three distinct layers. Plasma constituents and erythrocytes are primarily used to demonstrate the biosensing performance of sensors developed as part of this research project. Specifically, direct and indirect typing is performed to show the clinical utility and potential of the silicon photonic biosensor systems to perform blood typing on a single chip, potentially revolutionizing diagnostic work flows in transfusion medicine.

2.6.1 Transfusion medicine

Transfusion medicine involves delivering red blood cells and blood constituents to patients with blood loss or disorders. The first successful blood transfusion, performed in 1666 [187], involved transfusing blood between two canines [188]. Within a year, a French doctor performed the first human transfusion on a teenage boy in Paris [189] using lamb's blood. The controversial death of a subsequent transfusion patient a year later banned the practice for

over a century [189]. Today, approximately 9 million transfusions are performed worldwide annually [190]. In 2013, more than 14 million units of whole blood were collected for transfusions [70] and every unit underwent screening to determine the blood group type (A, B, AB, O, and Rh) and to detect for certain blood-borne infectious pathogens.

2.6.2 Blood groups

A set of experiments performed by Dr. Karl Landsteiner, a Viennese pathologist, and five of his colleagues in 1901 discovered the existence of blood types, forever changing transfusion medicine [191]. He noticed that when he and his colleagues serum was individually mixed with suspended RBCs, agglutination was observed in some mixtures but not others. In an agglutination reaction, antigens on the RBCs bind to antibodies, creating a cell-antibody complex. Several antigen-antibody interactions build up to a lattice-structure and form a visible clump that settles out of the solution. Landsteiner *et. al* showed that the six sera (he and his five colleagues) represented one of three blood groups: A, B, and O. Groups A and B denote the presence of A and B antigens on RBCs, respectively. Group O denotes the absence of both A and B antigens (originating from the German word *ohne*, meaning *without*). Although variations in A antigen expression was discovered in the early twentieth century [192], they are not central to this research project but may help explain differences observed in typing experiments.

In addition to the ABO blood group, the Rhesus (Rh) blood group system plays a significant role in transfusion medicine. While it consists of over 50 antigens, the D antigen is most significant. Therefore, a conventional blood screen will be *Rh positive* or *Rh negative* depending on the presence of the D antigen.

RBC phenotypes

Antigens define the ABO blood group, which is determined by the presence or absence of specific carbohydrate moieties on membrane-bound glycoproteins ($\approx 90\%$) and glycolipids ($\approx 10\%$) [191]. These Mendelian characteristics are inherited in a codominant, autosomal

fashion. Figure 2.15 shows a schematic representation of the carbohydrate structures that define the A, B, and H oligosaccharides.

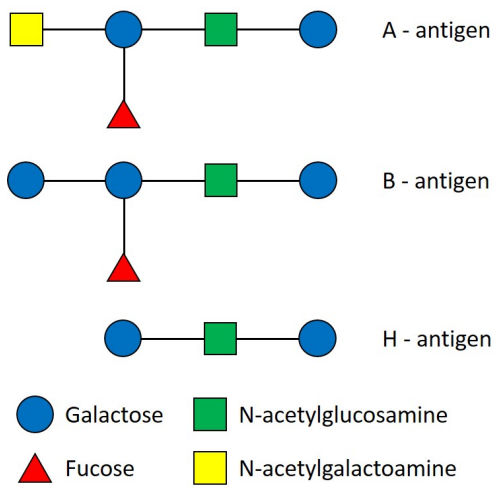

Figure 2.15: Schematic representation of the chemical moieties that determine the A, B, and H blood group di- and trisaccharide determinants.

Simple genetic screening is unable to correctly predict a RBC's phenotype (antigen status) [191]. While each antigen is derived from a similar precursor glycan (type-2 and type-4 on RBCs), genes encode transferases that form the determinants for either of the A or B group antigens. The A allele of the ABO locus encodes the α1-3 GalNAc-transferase, producing a terminal GalNAc on the A group trisaccharide determinant. In the same way, the B allele of the ABO locus encodes the α1-3 galactosyltransferase, producing a terminal galactose on the A group trisaccharide determinant. A modification by an α1-3 fucosyltransferase yields the H determinant [191, 193, 194]. These antigens are expressed on a variety of cells (e.g.: endothelial, gastrointestinal, respiratory, and skin) and can be secreted in biological fluids (e.g.: saliva, seminal fluid) [191, 193]. The significance of this enzymatic determination is that aberrant intracellular trafficking of ABO transferase may result in weak subgroup phenotypes [195].

Serum alloantibodies

A significant consideration for transfusion medicine involves the 'naturally occurring' antibodies against antigens *absent* from the host's erythrocyte membrane [194]. While the origin and production of these alloantibodies is not fully elucidated, their existence is largely attributed to similar terminal carbohydrate structures on intestinal bacteria. The presence or absence of antibodies cannot be determined via the hosts genotype, therefore bioaffinity reactions are necessary for detection.

2.6.3 Phenotyping blood

Blood typing is the process of determining which antigens and antibodies are present or absent from red blood cells (RBCs) and plasma, respectively. Figure 2.16 shows a schematic panel representing an ABO panel with the antigens and serum antibodies. While greatly simplified for illustration, each RBC has approximately 2 million ABO antigens on its surface [196]. Although their functional purpose remains largely unknown [197], identifying these antigenic carbohydrates and alloantibodies is paramount to transfusion medicine. Hemolytic responses due to improperly matched blood between recipients and donors account for approximately 25% of fatalities associated with transfusion errors [72]. Therefore, it is important to establish blood type compatibility between donor and recipient.

Figure 2.16 schematically represents a person's phenotype for the ABO blood types. Antigens presenting on the RBC membrane determine which serum antibodies exist. For A type individuals, their RBCs have A-antigens while their serum contains antibodies against B-antigens. The converse is true for B type individuals. Their RBCs have B-antigens while their serum contains antibodies against A-antigens. AB type persons present both A and B antigens on their RBCs and lack serum antibodies against A or B antigens. Finally, O type individuals present the H antigen (not A or B) and have antibodies against both the A and B-antigens in their serum.

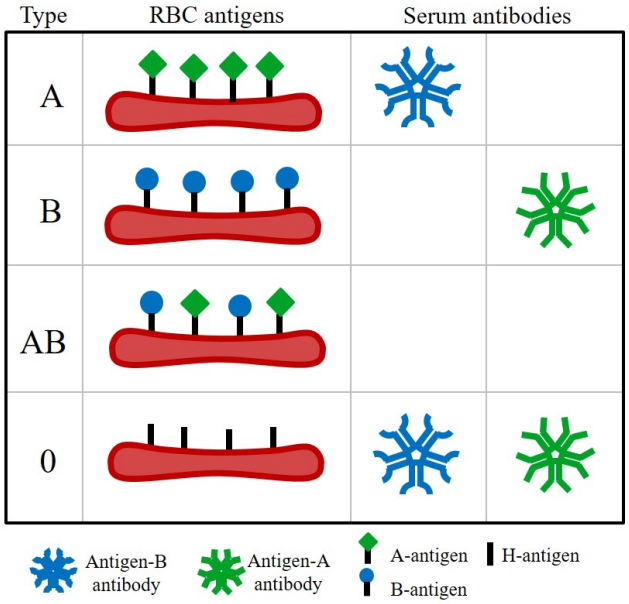

Figure 2.16: This table schematically represents the different trisaccharide determinants on RBCs and naturally occurring alloantibodies that determine the hosts blood type. For example, an A type has A-antigens on the RBC and serum antibodies against the B-antigen. The converse is true for B group individuals. AB individuals present both antigens and have no serum antibodies, and the O group presents on the H antigen and has both A-antigen and B-antigen antibodies in the serum.

2.6.4 Conventional blood typing

While many approaches to type blood exist, tube-based agglutination assays remain the gold-standard due to their efficiency and simplicity [71]. Agglutination assays can be either direct or indirect but both rely on a trained operator and a semi-quantitative analysis determined by the technician.

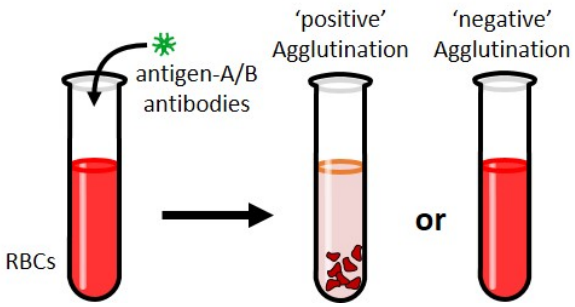

Figure 2.17: Schematic representation showing direct typing, or 'forward typing', using A/B-antigen antibodies and RBCs suspended in buffer. Antibodies are mixed with two reaction tubes (only one is shown here). Agglutination indicates the presence of A or B-antigens on the host RBC determining the blood group.

Direct typing

For direct typing assays, monoclonal anti-A/B IgM antibodies are introduced into suspended RBCs, as shown in Fig. 2.17. The sample is mixed, incubated, and then centrifuged to precipitate any agglutinated RBCs. The degree to which RBCs clump together is qualitatively assessed. The intensity of agglutination is rated on a scale of +1 (low) to +4 (high), indicating the presence of the antigen. A '0' indicates that no agglutination occurred and the antigen is absent from the RBC.

Indirect typing

Samples can be 'reverse typed' by detecting the presence of 'naturally occuring' anti-A/B antibodies in plasma. For indirect typing, commercial pre-typed A or B reference RBCs are added to diluted plasma. The sample is mixed, incubated, and centrifuged by a technician. Agglutination indicates the presence of the alloantibody, also referred to as an isohemagglutinin [198]. In the same way as for direct typing, the amount of agglutination is semi-qualitatively rated on a scale of +1 (low) to +4 (high), indicating the presence of the

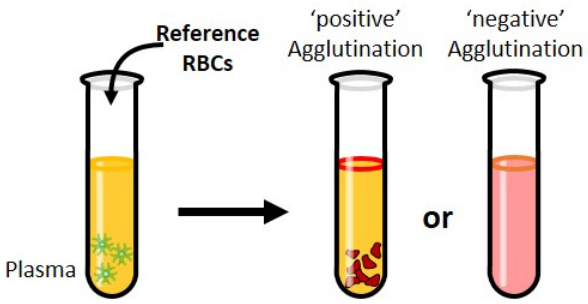

Figure 2.18: Schematic representation showing indirect typing, or 'reverse typing', using reference RBCs and plasma. Reference RBCs with A, B, AB, and O antigens mixed with four reaction tubes (only one is shown here). Agglutination indicates the presence of alloantibodies against the reference RBC antigens determining the blood group.

isohemagglutinin. A '0' indicates that no agglutination occurred and the isohemagglutinin is absent.

2.6.5 Pathogen screening

While 68 potential disease threats have been identified to transfusion safety [199], donated blood is currently only screened for bacteria, Hepatitis B and C virus (HBV and HBC, respectively), Human Immunodeficiency virus Types 1 and 2 (HIV), Human T-Lymphotropic virus types 1 and 2 (HTLV), *Treponema pallidum* (syphilis), and West Nile virus (WNV). While not required for all transfusions, testing for *Trypanosoma cruzi* (Chagas disease) and Cytomegalovrius (CMV) are often performed for special needs patients [186]. These tests involve different laboratory methods including nucleic acid amplification, isoagglutinin detection, and antibody screening [191, 199, 200]. Testing can take hours and typically occurs in clinical laboratories by specially-trained technicians that prepare samples, run the test, and then interpret the results. The detection of proteins (e.g.: antibodies) [43, 44], viruses [46], and bacteria [47], have been previously demonstrated on the silicon photonic biosensor platform.

2.6.6 Silicon photonic biosensor array concept for blood typing

For multiply transfused patients where alloantibody identification in the donor sample against other blood groups such as Lewis, Kell, Duffy, or Kidd is significant to limit hemolytic reactions, testing panels are greatly expanded incurring more reagent consumption and technician time (often hours) [201]. Additionally, mistakes can occur in the reading of the resulting matrix impacting diagnosis and treatment. A chip-based solution capable of screening against a myriad of antigens and antibodies in a single test could improve work flows and reduce costly errors. Additionally, blood donation screening could be improved testing each sample for its antigen status, isohemagglutinin presence, and pathogen contamination on a single substrate.

Figure 2.19 shows a concept a silicon photonic biosensor platform capable of simultaneous direct and indirect typing. Matrixed sensors functionalized to assess entire blood samples (primary type, secondary type, and pathogens) could greatly improve testing efficiency. The research aims outlined in this dissertation aim to accomplish steps toward this goal.

2.7 Design considerations

Figure 2.20 depicts key aspects that must be considered for optical biosensor design. Ideally, the sensor should mimic the target molecule's native environment. The sections below briefly highlight both system-level and sensor-level choices that will impact overall performance. Some are explored as part of this research project and referenced appropriately, such as various optical resonator topologies, waveguide dimensions, wavelength regimes, and porous membrane networks.

2.7.1 Capture agents

Bio-recognition molecules, or capture ligands, should be specific with high affinity and avidity towards its binding conjugate. While monoclonal antibodies are expensive their biological specificity make them the capture agent of choice for most protein or small molecule diag-

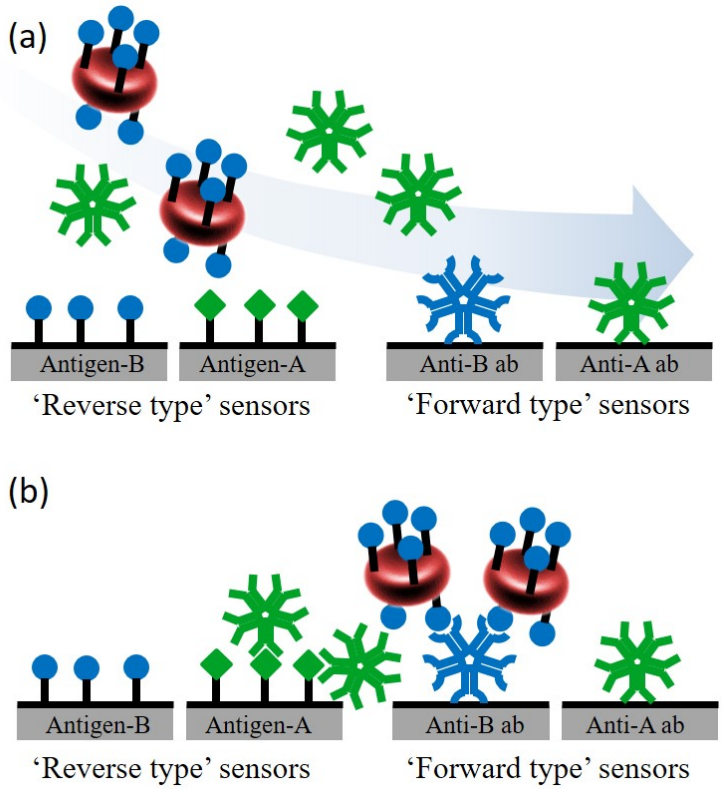

Figure 2.19: Schematic representation of a silicon photonic biosensor array concept for blood typing. (a) Sensors functionalized for direct and indirect blood typing subjected to a patients sample. (b) Bound RBCs and isohemagglutinins after the rinse step indicating B-type blood.

nostic assays in use today.

2.7.2 Surface chemistries

The strategy used to functionalize the surface is key since the orientation and probe density of the receptor impact biosensor performance, especially for target molecules at low concentrations. Surface chemistries that immobilize these capture ligands should also resist non-specific binding interactions from off-target molecules increase 'biological noise' in the system. This noise, or fouling, limits the overall sensitivity or detection limit. Silane

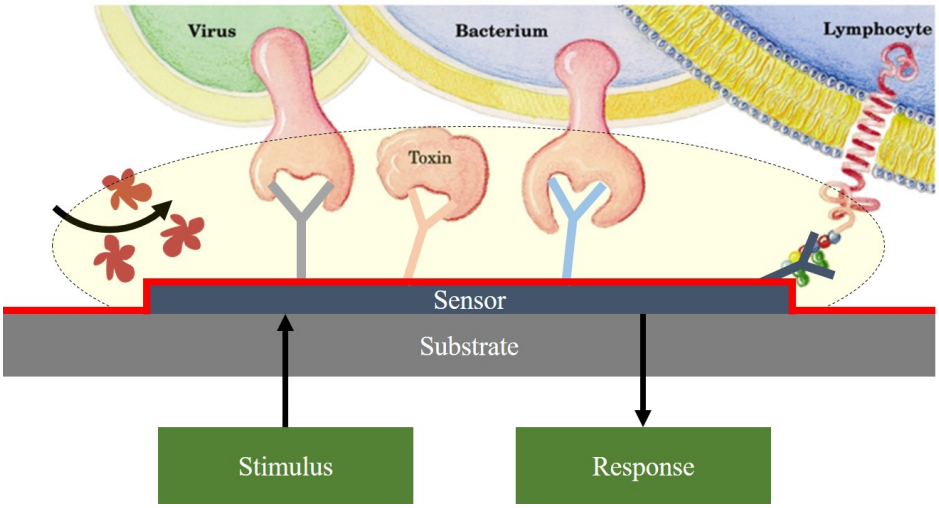

Figure 2.20: Schematic representation of key aspects of an optical biosensor. The sensor should mimic the target analyte's scale and native environment while allowing facile stimulus and binding response monitoring. Surface chemistries should facilitate robust immobilization of bio recognition molecules that have high affinity and avidity to the target analyte while resisting adsorption from unwanted molecules (fouling).

chemistries can facilitate the covalent attachment of capture molecules (e.g.: proteins) to native oxide surfaces (e.g.: silicon photonic biosensors) through end-group functionality as described in Sec. 2.4.3. They not only offer robust attachment but the ability to regenerate the sensor's surface multiple times during assay development.

2.7.3 Instrumentation, noise, and detection limits

The system should have an efficient way to stimulate the sensor and read its response to detect and quantify binding events. Most often, a signal baseline is established before introducing the sample so that the overall response to the target analyte can be determined. The system's limit of detection, as introduced in Sec. 2.7.3, is defined as the minimum refractive index change ($\Delta n_{clad,min}$), or smallest mass change, necessary to cause a detectable change in the

output signal (above 3σ of the noise floor). The system's limit of detection (sLoD) is defined as the minimum refractive index change ($\delta n_{clad,min}$), or smallest mass change, necessary to cause a detectable change in the output signal (above 3 σ of the noise floor). The sLoD depends on the readout instrumentation and the experimental setup, including associated noise sources (spectral and amplitude noise of the light source), electrical readout circuitry noise, and thermal stability. Noise can be reduced digitally by employing statistical signal processing algorithms. Because all of these factors can impact the sLoD, a truly objective comparison of sensors characterized using different assays and experimental systems can be challenging.

2.7.4 Fabrication

The sensor should be compatible with affordable manufacturing processes and cost-effective functionalization protocols. This is important when prototyping sensors to evaluate design parameters. While foundries offer economies of scale at wafer-level production, fabrication often takes 6 months or more delaying projects. While ebeam lithography provides affordable, quick-turn fabrication in a week or less, manually processing chips results in inconsistent structure geometries, ultimately impacting circuit behavior and performance.

2.7.5 Operating wavelengths

Operating wavelengths impact the detection limit for biosensors. While most biosensors operate at 1550 nm wavelengths due to historical reasons (availability of equipment because of datacom and telecom applications at that wavelength), 1310 nm wavelength sensors are becoming more popular and have advantages for biosensing. For biosensors, with most of the analytes in aqueous solutions, the absorption loss is usually dominated by the water. Figure 2.21 shows the absorption loss in water and theoretical quality factors achievable in an aqueous environment over the wavelength range of interest for devices described herein. Assuming that the susceptibility is 1 and the quality factor is limited by water loss, then the fundamental intrinsic limit of detection is $2.4 \cdot 10^{-4}$ RIU at 1550 nm wavelengths [103]. The

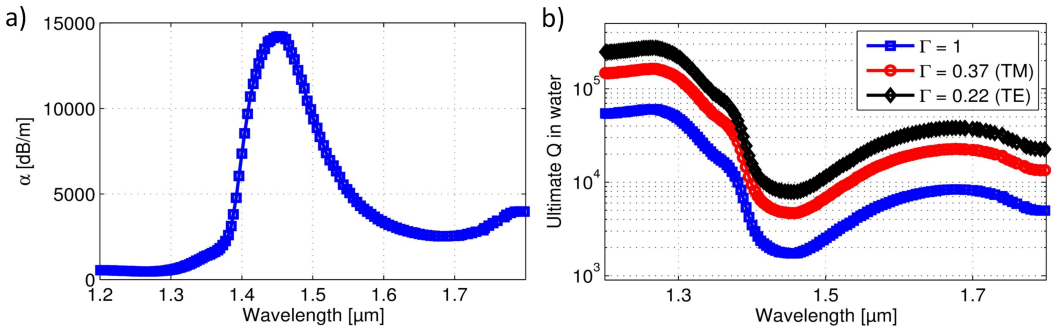

Figure 2.21: a) Absorption loss in water; and (b) ultimate Q calculations for resonators in water. $\Gamma = 0.37$ and $\Gamma = 0.22$ is the simulated confinement factor for TM and TE mode respectively for a waveguide with dimensions of 500 nm x 220nm.

fundamental intrinsic limit of detection is $3.14{\cdot}10^{-5}$ RIU at 1310 nm wavelengths, as described in Table 4.3. Therefore, the *iLoD* can be improved by an order of magnitude by switching to a shorter wavelength of 1310 nm as the water absorption is decreased (accompanied by slightly higher scattering losses) [103]. The *iLoD* is approaching the fundamental limit if $\alpha_i < 10$ m^{-1} as described in Sec. 4.6.3.

2.7.6 Sensor size

The sensor's scale, in relation to target molecule or cell's size, will determine the sensor's response to a single binding event, or overall sensitivity. For example, a RBC covering a TE mode disk resonator approximately its own dimension, will be impacted more than a 30 µm diameter ring where the RBC is covering just a portion of the entire optical path.

Waveguide dimensions will also impact performance. Smaller waveguides increase the mode's susceptability and overlap with the aqueous cladding. Devices operating at 1310 nm wavelengths require smaller waveguides to support single mode operation than their 1550 nm wavelength counterparts.

2.7.7 Polarization

As described in Sec. 2.2.1, TM modes offer increased susceptibility and electric field overlap with the aqueous cladding for the waveguides employed herein. Yet, absorptive losses are increased, impacting the detection limit. In addition, TM modes offer higher surface sensitivity over TE modes as described in Sec. 6.3.1.

2.7.8 Sensitivity

Chapter 4 discusses different strategies to improve sensitivity including optimizing the waveguide geometry, sensor topology (such as rings, slot waveguides, Bragg gratings, disk resonators, and sub-wavelength grating), polarization (TE and TM modes as discussed in the previous section). Based on group index results shown in Fig. 2.7 and Equ. 6.1, TE mode resonators have improved sensitivity at longer wavelengths while TM mode resonators offer improved sensitivity at shorter wavelengths.

2.7.9 Resonator topologies

Resonator topologies impact sensitivity, quality factor, and detection limit. It is known from Eq. 6.3 that both a high quality factor and a high sensitivity will improve the detection limit. In ring resonators the quality factor is primarily limited by water absorption losses but if not carefully designed bending loss, scattering loss from waveguide roughness, and mode mismatch loss can also become an issue. Especially bending loss can become an issue for small radii, like disk resonators, and TM polarized light. Bending losses can be eliminated by using resonant structures with only straight waveguide segments.

Barrios *et al.* and Claes *et al.* measure the detection limits on the order of $5 \cdot 10^{-6}$ RIU for slot waveguides [29, 35]. Bragg gratings offer similar sensitivities as ring resonators but with a much smaller footprint. Jugessur *et al.* fabricated vertical side-wall TE mode Bragg gratings integrated with a reversibly bonded PDMS fluidic network estimating a sensitivity of $5.5 \cdot 10^{-3}$ nm in a sensing volume of 2 μm^3 [202]. They designed slotted Bragg gratings as well

with a simulated sensitivity of 620 nm/RIU. However they did not report any experimental results confirming their theoretical values. Pbabhathan *et al.* designed and simulated similar vertical side wall TE mode gratings but introduced a period defect to create a resonance peak in the center of the photonic stop band [203]. Finally, Wang *et al.* fabricated a TE mode slot-waveguide Bragg grating for biosensing with a sensitivity of 340 nm/RIU and quality factor of $3 \cdot 10^4$ [204].

2.8 Summary

This chapter introduces the figures of merit for silicon photonics biosensors. They are: (1) Bulk sensitivity which is the change of resonance condition (wavelength shift) as function of uniform change of refractive index of the cladding; (2) Surface sensitivity which is the change of resonance condition (wavelength shift) as function of thickness of a molecular adlayer on the waveguide's surface; and (3) Limit of detection which is the smallest detectable refractive index or adlayer thickness change. Furthermore this chapter also discusses how intrinsic limits of detection can be improved. The remaining chapters discuss the tools and development methodologies used to develop a myriad of sensors and their biosensing performance in real biological samples.

Chapter 3

AUTOMATED PROBE STATION AND PDK FOR SILICON PHOTONIC BIOSENSORS

This chapter describes work completed in close collaboration with Jonas Flueckiger and Mr. Wenxuan Wu who helped develop, validate, and maintain the code base. Portions of this chapter were reprinted with permission and may be found in the following publications:

1. **S. Schmidt**, J. Flueckiger, W.X. Wu, M. Reis, P. Kulik, L. Chrostowski, D. Ratner, 'Automated Probe Station and PDK for Silicon Photonic Biosensors', *Manuscript in preparation*, 2016

2. **S. Schmidt**, J. Flueckiger, W. Wu, S.M. Grist, S. Talebi-Fard, V. Donzella, P. Khumwan, E.R. Thompson, Q. Wang, P. Kulik, X. Wang, A. Sherwali, J. Kirk, K.C. Cheung, L. Chrostowski, D. Ratner. 'Improving the performance of silicon photonic rings, disks, and Bragg gratings for use in label-free biosensing.' SPIE NanoScience Engineering VII. International Society for Optics and Photonics, 2014.

3. **S. Schmidt**, J. Flueckiger, W. Wu (2015). Silicon Photonic Test Bench [Computer software]. https://github.com/shonschmidt/SiPhoTestBench.

4. **S. Schmidt**, J. Flueckiger, W. Wu (2015). Silicon Photonic Test Bench for Biosensing [Computer software]. https://github.com/shonschmidt/SiPhoTestBenchBio.

5. **S. Schmidt**, J. Flueckiger, W. Wu (2015). Silicon Photonic Analysis Tool [Computer software]. https://github.com/shonschmidt/SiPhoAnalysisTool.

3.1 Introduction

Silicon nano-photonics, a technology that guides light in small silicon wires, has received considerable attention over the past decade. With a robust foundational knowledge of the technology fundamentals [97, 205–207], attention has shifted towards improving devices and integrating complex photonic integrated circuits (PICs) [208–210] (see Fig. 3.1). While high performance computing and data communication applications have catalyzed device development [53, 211, 212], silicon photonic also offer unique advantages for biosensing and show promise for lab-on-chip systems [12, 14, 41, 42].

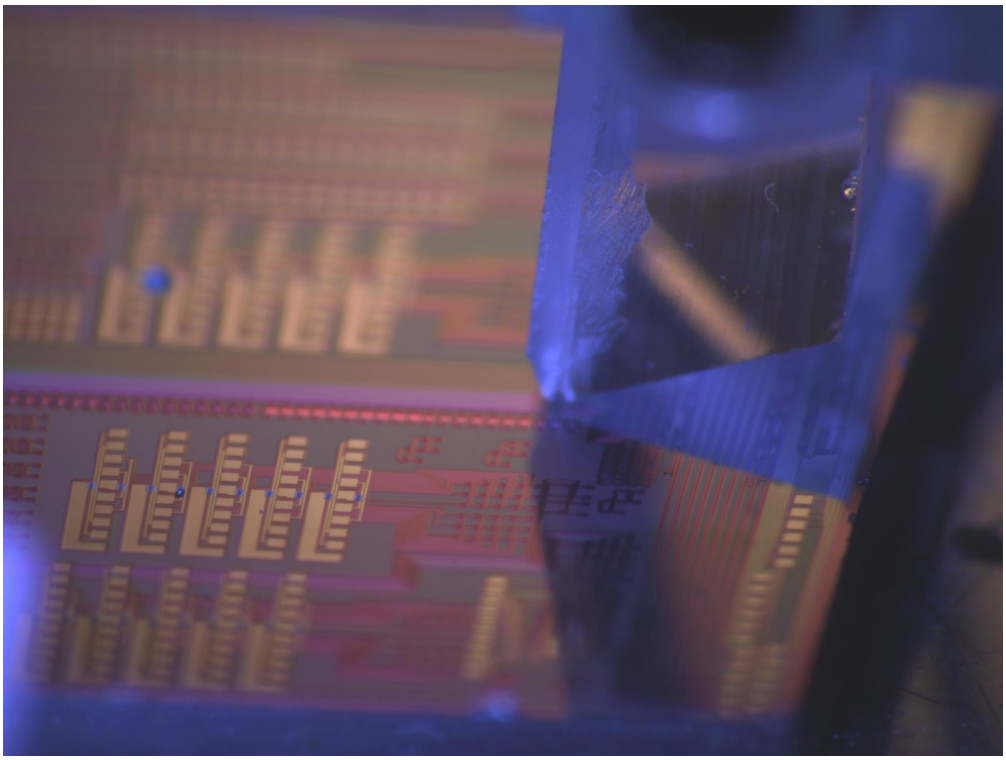

Figure 3.1: Fiber array aligned to devices on a silicon photonic integrated chip.

Silicon photonic biosensors utilize near-infrared light to detect molecular binding events on the silicon's surface. Confining the light in a silicon wire (waveguide) comparable in size to its own wavelength results in an intensity distribution within the waveguide. This

distribution is referred to as mode profile. The shape of these modes depend on the light's polarization and wavelength, and the waveguide's geometry. A portion of the electric field extends outside the waveguide as an evanescent field and is sensitive to refractive index changes on the waveguide's surface. Biomolecules have a higher refractive index compared to the aqueous media in which they reside. When molecules of interest bind to surface capture chemistries, they change the mode's propagation properties, namely the effective refractive index and loss, which can be quantified using a resonant sensor [91]. The resonator's wavelength shift can be correlated to the amount of added bound mass on the waveguide's surface. Different resonant configurations have been investigated as biosensors [21, 56, 91] for applications ranging from environmental monitoring [213] and basic science research [214] to threat detection [215] and medical diagnostics [26, 90]. While many have demonstrated impressive sensitivities, secondary amplification is often required to achieve clinically relevant levels [43].

Our recent research efforts have focused on improving the intrinsic performance of silicon photonic biosensors [20]. In doing so, we found that there exist barriers to developing and testing biosensors efficiently. Specifically, (1) the impact of basic components (e.g. grating couplers and splitters) to overall design risk and signal path performance, (2) the ability to adequately model an aqueous biological environment during sensor design, and (3) the time and effort required to assess many devices in a biological environment. Due to the complexity our samples (i.e. blood), we found it more efficient to evaluate the performance of the biosensors experimentally. Our initial setup consisted of manually aligned input and output fibers and a carefully positioned PDMS flow cell to deliver reagents, as shown in Fig. 3.2. A simple script performed wavelength sweeps and real-time monitoring of the optical response was not possible. For multi-hour assays, we would discover that the biological reagents were nonviable or an air bubble had destroyed adsorbed molecules only after post-processing the data. This approach proved to be time-consuming and inefficient, especially since hundreds of different devices needed to be assessed under these conditions.

We also learned the importance of minimizing the amount of novel design in the overall

signal path. All photonic integrated circuits (PICs) rely on a number of basic photonic building blocks, like grating couplers or waveguide splitters. The performance of every photonic component depends on the fabrication process and often requires multiple iterations to fully optimize. These general purpose components can be reused and shared more broadly for other applications through process design kits (PDKs).

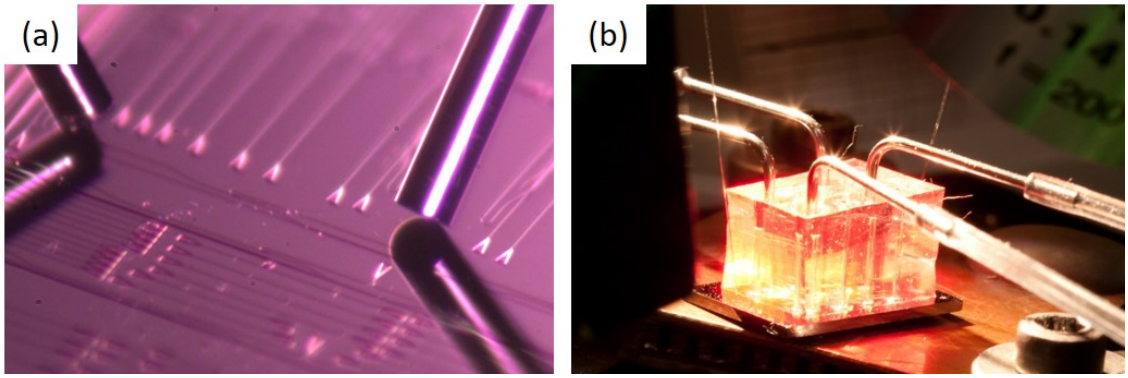

Figure 3.2: (a) Two single fibers aligned to input and output grating couplers on a silicon photonic chip. (b) Four-port PDMS gasket with two channels used to sequence reagents for biological assays. The two signal fibers coupling on and off the chip are faintly visible on the left and right edges of the gasket.

Therefore, we created a design methodology (PDK) and test platform to improve the efficiency of silicon photonic biosensor development. The system includes software to interface with the various test equipment, to provide automatic algorithms to find first light, and to conduct multi step biological assays. The platform is currently in use at more than a dozen sites across different countries and has helped generate scores of publications. The probe station software can be accessed on GitHub [48]. In addition, an on-line silicon photonic design course uses the automated probe station to assess students' designs [50]. The test setup also helped characterize a PDK with IO cells for ebeam prototyping which is provided through the SiEPIC program [216].

3.1.1 Development process

Fig. 3.3 shows the methodology we use for silicon photonic biosensor development. This iterative cycle begins with design and simulation to determine device dimensions for the layout. The most accurate tool to model light interactions with complex nanostructures is a three-dimensional (3D) finite-difference time-domain (FDTD) solver. However, the small mesh sizes required for accurate results in large simulation domains makes 3D FDTD simulations (shown in the upper right of Fig. 3.3) computationally expensive. We have found that for most biosensor designs, it is often sufficient to compute the optical mode in a 2D waveguide cross section since the mode shape does not change significantly as it propagates along the waveguide [217]. Design for test (DFT) should be considered during this phase as well, especially when the chip contains optical, electrical, and fluidic interconnects [52]. Therefore, the ebeam PDK contains a process test cell and framework that facilitates timely and efficient setup for testing as well as process characterization.

Most silicon photonic biosensors are fabricated in 220 nm thick silicon on top of 2-3 µm buried oxide (SOI wafer). Ebeam lithography provides an affordable, fast turn-around foundry-compatible fabrication process that produces consistent, robust, low-loss silicon photonic components [218] (an example chip is shown in the lower right hand corner of Fig. 3.3). Optimized designs can be scaled up using a foundry's deep, ultra-violet (DUV) lithography when many replicates are needed for assay development. Multi-project-wafers, organized by CMC Microsystems or MOSIS, provide access to foundry processes offered by ePIXfab/IMEC, CEA-LETI, or Astar/IME by sharing the reticle (cost) across its participants [219–223].

The final step in the process involves characterization. We first test devices for fabrication yield under dry conditions to determine which ones should be characterized in an aqueous environment. A gasket and flow cell facilitate the delivery of reagents to the sensors where key performance parameters like loss, Q, extinction ratio (ER), sensitivity, and spectral response are assessed. Results are then analyzed and design parameters optimized (if need

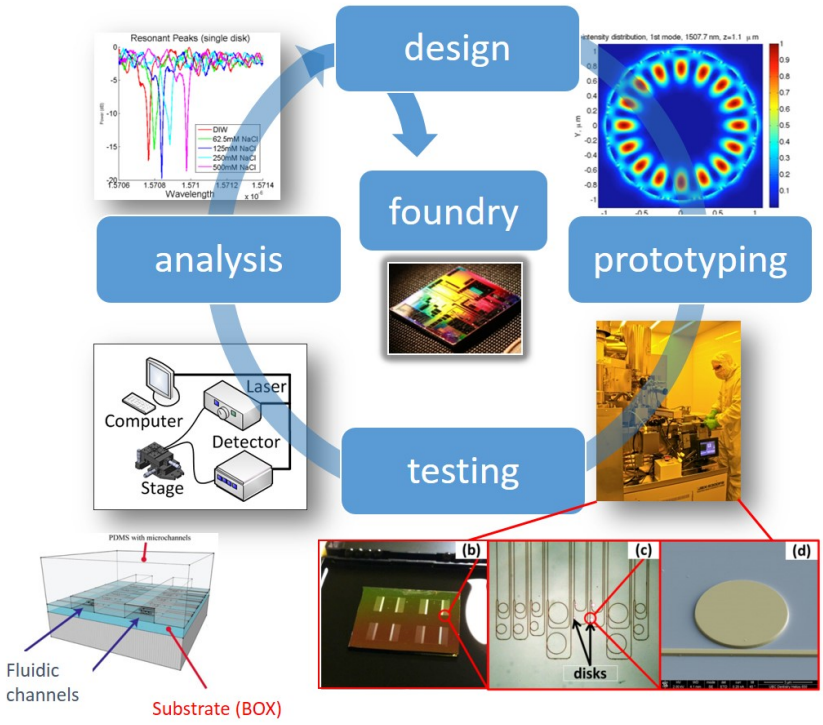

Figure 3.3: Rapid and affordable development process for creating application-specific and foundry-compatible, silicon photonic biosensors for label-free sensing. (a) Optical mode profile simulated using Lumericals MODE solutions. (b) Fabrication and SEM using the UWs JEOL ebeam. (c) Optical setup schematic for dry and wet testing. (d) Optical transmission spectrum for various NaCl concentrations using MATLAB. (e) Optimized sensor designs scaled-up in foundry processes through and MPW broker.

be) before fabricating devices again.

We have found that designs can be efficiently developed using the process shown in Fig. 3.3 and scaled up using the foundry when optimized. The remaining sections present key aspects of the automated test platform and how it leverages basic building blocks in the PDK. We also discuss the hardware components, open-source software, and provide examples of how devices and entire signal paths can be characterized using these tools.

3.2 Methods and materials

3.2.1 PDK and chip framework

There are a number of basic building blocks every designer will use to complete an optical circuit. For example, vertical gratings [224] to couple light on and off the chip or waveguide splitters to fanout a single input to many devices. Typically, such components are collected in a shared library and along with their process information (eg: layer definitions) collectively make up a PDK [217]. PDKs can reduce design time and risk. Characterized components can be leveraged into optical circuits and placed into a GDS framework to realize whole chips quickly, as shown in Fig. 3.4. A GDS is an industry-standard CAD format that defines geometries and layers for chip fabrication.

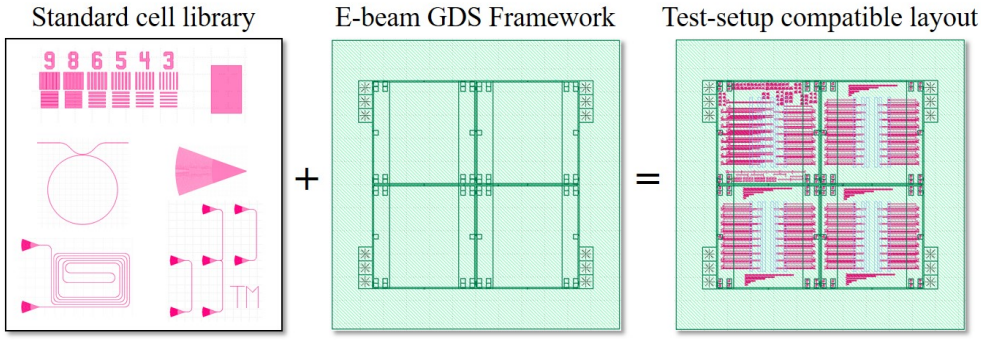

Figure 3.4: PDK concept and chip framework that expedites development and lowers design risk. The chip framework specifies features to assess fabrication steps (in the saw lane) and specifies alignment structures that facilitate the automated testing of all devices on the chip.

Our PDK contains a GDS framework with additional layout components to monitor the quality of the fabrication process. Such test structures are designed to understand basic optical properties of components and to get a statistical measure on yield. Examples include the propagation loss in a waveguide or the effective or group index of an optical path. Furthermore, the GDS framework defines four quadrants that can be diced into die. Within

each die, alignment structures exist at specific locations to facilitate efficient registration and setup with the probe station.

3.2.2 Generating a device list

All of the devices defined in the GDS have coordinate pairs that define their locations relative to each other. The probe station software translates these GDS coordinates into stage positions to move from one device to another during automated testing. The PDK provides a script that automatically generates a text file with all the devices and their coordinates. The script can be run from KLayout or Mentor Graphics Calibre. The input grating coupler of each device to test should get a text label starting with 'opt_in' to be recognized by the script. The coordinate of the text label will be written to the coordinate file and used to align the input fiber array to the grating coupler during automated testing. A text file with devices of interest can be created by hand but must have the following format:

```
opt_in_<mode>_<wvl>_<type>_<deviceID>_<comment>
```

where <*mode*> is the polarization ('TE' or 'TM'), <*wvl*> is the operating wavelength, <*type*> is the class of the device (e.g. RingResonator, or YieldRing), <*deviceID*> is a unique device name, and <*comment*> is an optional field for comments (e.g. resonator radius or gap).

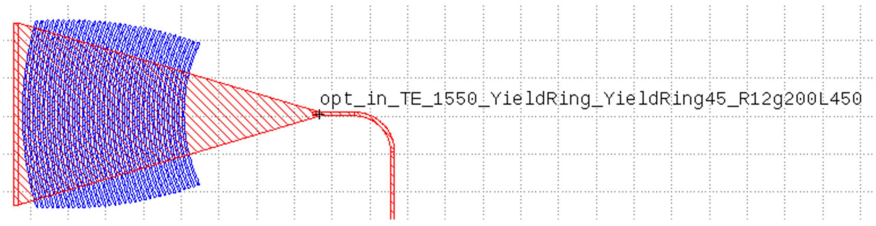

Figure 3.5: Each input grating coupler has a unique text label. This label is used to generate a device list for automated measurement.

Figure 3.5 shows a GDS example of a label for a ring resonator for TE polarized light and a wavelength of 1550 nm belonging to the class *YieldRing*. The exact same device is in the GDS more than 500 times and so the class *YieldRing* can be used to select only a sub-group of devices or to run post processing scripts on a subset of measurements, e.g. to extract manufacturing variability [225]. From the comment field we know that the ring has a radius of 12 μm, a gap of 200 nm, and a coupling length of 4.5 μm.

3.2.3 Hardware assemblies

The probe station hardware includes a custom chip stage, fiber array stage, fluidic stage, and flow cell, as shown in Fig. 3.6.

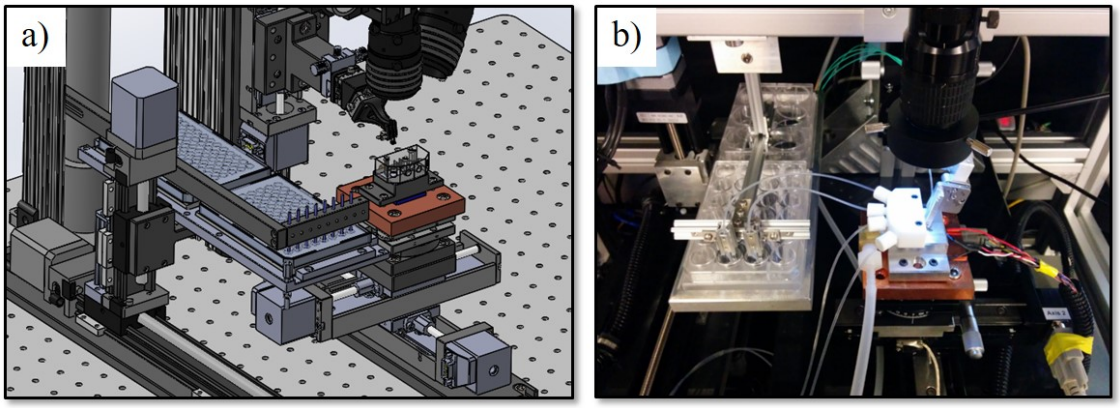

Figure 3.6: Silicon photonic probe station hardware overview. (a) CAD rendering showing the fluidic stage, chip, and fiber stage assemblies. (b) Photograph of the probe station used for biosensing, including flow cell and reagent sequencing trays.

Chip stage assembly

Figure 3.7 shows the chip stage which consists of two motorized, VT-50 linear stages with active feedback (Micronix, Irvine, CA). They control X and Y movements relative to the fiber array.

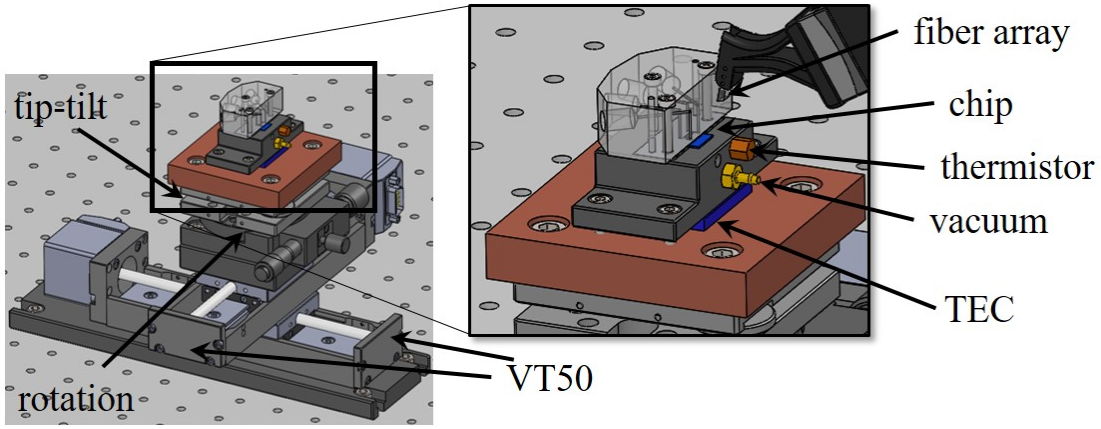

Figure 3.7: Motorized XY chip stage assembly with rotation, tip-tilt, and Peltier element to thermally tune the chip during measurements. The enlarged inset shows a mounted Teflon flow cell for biosensing with a small portion of the chip (in blue) exposed for coupling light on and off chip using a fiber array.

The chip stage is thermally tuned using a 30 x 30 mm Peltier element (Laird Technologies, Earth City, MO) mounted between a large piece of copper that acts as a heat sink and the chip mount block. A thermistor (Omega Engineering, Stamford, CT), potted into the chip block, is wired to the temperature controller. The copper sink mounts on a tip-tilt stage (AIS-50BUU, OptoSigma, Santa Ana, CA) and rotation stage (KSP-406M, OptoSigma, Santa Ana, CA). Custom adapter plates connect these parts to the linear stages.

Fiber array stage assembly

A fiber array (PLC Connections, Columbus, OH) mounts on a 3D printed holder positioned at a nominal insertion angle of 20^o. The holder connects to a goniometer (GOH-25A50, OptoSigma, Santa Ana, CA) to allows fine adjustments to the insertion angle (see Fig. 3.8). A second goniometer (GOH-25A50, OptoSigma, Santa Ana, CA) provides yaw alignment of the fiber array to the chip stage. Finally, a rotation stage (KSP-256, OptoSigma, Santa

Ana, CA) provides adjustments about the arm's axes (roll). The arm assembly connects to a linear stage (VT-50, Micronix, Irvine, CA) to provide Z-axes motions that raise and lower the fiber array to the chip.

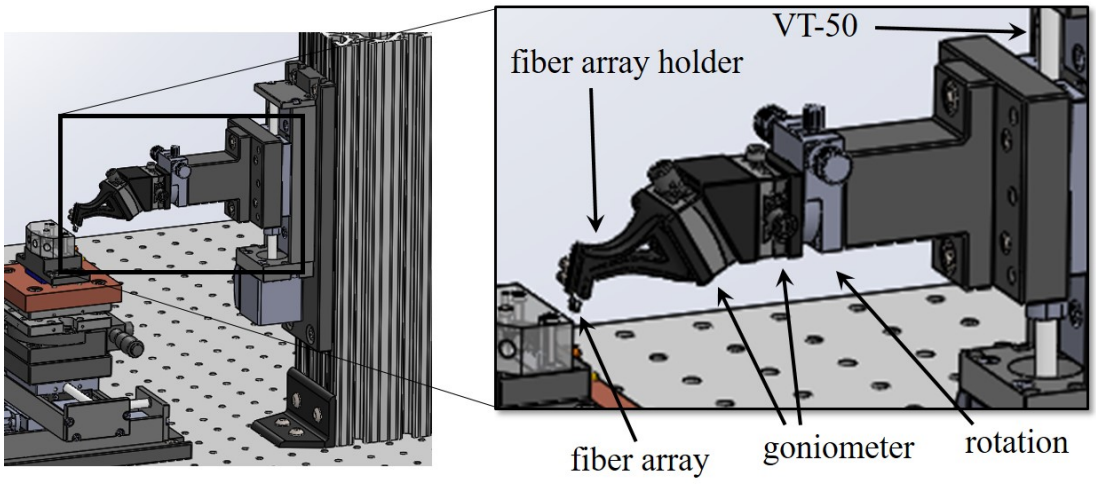

Figure 3.8: Motorized Z stage and fiber array arm supporting manual alignment on three axes (yaw, pitch, and roll). The enlarged inset shows the fiber array holder and alignment stages. The design ensures that points of rotation happen at the tip of the fiber array.

Flow cell and channel gaskets

The chip block contains a 400 µm deep cavity to facilitate mechanical alignment of the fluidic channels on chip to the gasket and flow cell. The chip block has tapered pins (McMaster-Carr, Santa Fe Springs, CA) to align the flow cell and threaded holes which secure it tightly over the gasket (Fig. 3.9). The small, exposed portion of the chip allows fiber array access to the on-chip grating couplers. Fluidic gaskets are made from 250 or 500 µm-thick silicone sheets (Grace BioLabs, Bend, OR). They define two 250 µm-wide by 6000 µm long channels on a 750 µm center which are fabricated using a 10 µm laser (Universal Laser Systems Inc., Scottsdale, AZ). The gasket has openings which mate to ports on the flow cell and define

fluidic channels over the on-chip sensors.

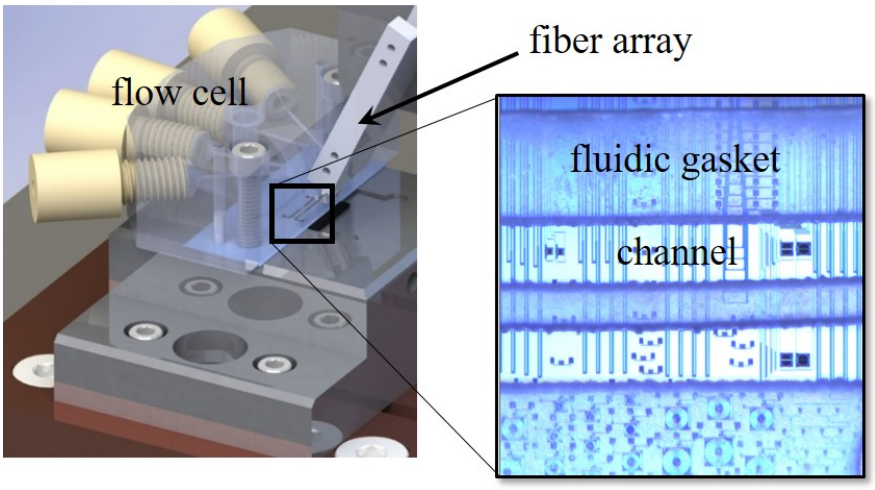

Figure 3.9: Four port Teflon flow cell that mates to a two-channel silicone gasket to define fluid lanes over the sensors. A recessed cavity in the chip stage mechanically aligns chips to the silicone gasket. Pins pressed into the chip stage facilitate the proper alignment of the flow cell and gasket. The enlarged inset shows a photograph of biosensors exposed in the two fluid lanes. While the alignment features facilitate a timely setup, the chip must be designed to ensure the biosensors reside in the channels.

Reagent sequencing stage assembly

Two linear stages (XSlide, Velmex Inc, Bloomfield, NY) provide reagent sequencing during wet assays by moving two well plates in any combination of 96, 24, or 6 wells (Fig. 3.10). A user-defined recipe file specifies the well number sequence and dwell time within each well during assays. An arm with metal sleeves to guide the flexible Tygon tubing (Vici Valco Instruments Co. Inc., Houston, TX) into the well has sharpened tips that punch holes in cover film if installed on the reagent trays.

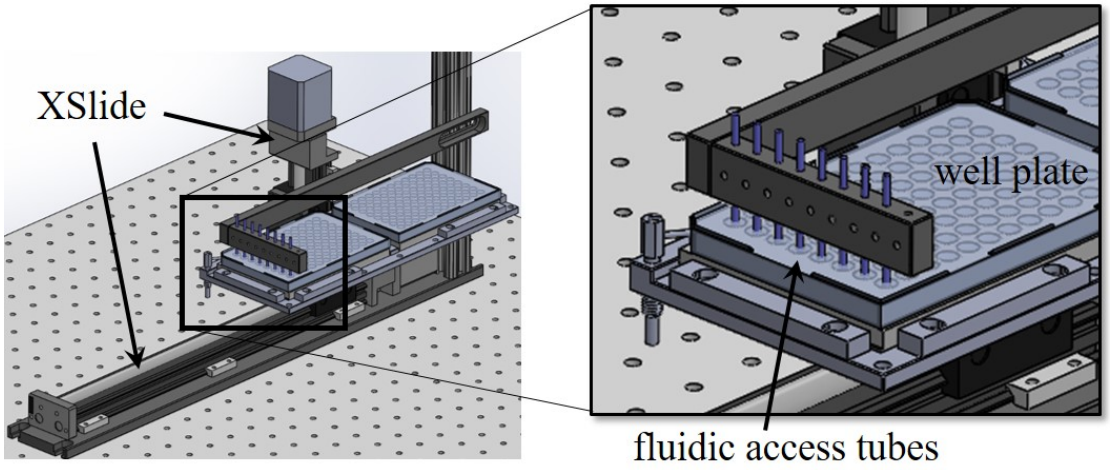

Figure 3.10: CAD renderings of the reagent sequencing stage comprised of two motorized X and Z axes. The stage supports two well trays (6, 24, or 96 plates). The enlarged inset shows the metal guide sleeves that ensure the tubing aligns with each well.

3.2.4 External instruments

The open-source software controls external, bench-top components to test devices. A laser mainframe, set of power meters, temperature controller, pump, and alignment cameras were selected for their performance, utility, and driver availability. Currently supported components include: Agilent 81682A, 81600B, and 81689A laser (within the 8164A mainframe), Santur TL-2000 laser module, ILX Lightwave LDM-4980 laser diode mount (and SRS LDC501), Agilent N7744A and 81635A power meters (the later within an 8164A or 8163A mainframe), a Newport 3040 TEC and Stanford Research Systems LDC501 to thermally tune the stage, and a Chemyx Nexus 3000 syringe pump. Three 3.2MP Lumenera USB cameras (Ottawa, Ontario) mount on Navitar's Zoom6000 high magnification modular zoom lens systems to facilitate alignment (fiber array and chip alignment). All of the components are connected via USB (either directly, through a GPIB-to-USB, or serial-to-USB dongle) to a generic PC with Windows 10 (Microsoft, Redmond, WA) and MATLAB R2013a

(Mathworks, Natik, MA).

3.2.5 Control and analysis software

The choice to use MATLAB for the control software was largely motivated by the need for maintainability and extensibility as a lab instrument. Most university engineering students get exposure to MATLAB sometime during their academic tenure and can therefore make any code modifications as necessary. The source is kept under revision control using GitHub (San Francisco, CA) and bugs were tracked using Jira (Atlassian; Sydney, Australia) during its development.

The software architecture follows the industry standard model-view-controller scheme to the extent possible. The 'models' define instrument interactions. The 'view' was designed using GUIDE and controls the user interaction experience. Figure 3.17 shows the GUI panel for testing devices. The 'controller' handles communication between the view and models and orchestrates automated testing. Since the first code version was implemented with stand-alone scripts, much of the controller code remains as scripts. This allows others familiar with MATLAB's scripting language to make changes in program sequences without having to understand much object-oriented design.

3.3 Results

3.3.1 Fiber array alignment

The on-chip grating couplers and the fiber array must be aligned to optimally couple light. Figure 3.11 shows the degrees of freedom available to the user for adjusting the fiber array. As stated previously, the fiber array is attached to two goniometers (α', γ'), a rotation stage (β'), and a linear stage (z'). The two translation axes (x',y') must align to the chip stage (x,y). Depending on how the fiber array is mounted, the incident fiber angle Θ and misalignment angles Ω and δ (see Fig. 3.12 for definition of δ) are a function of α', γ', β'. Every time a different fiber array is mounted the misalignment angles Ω and δ need to be

minimized. We accomplish this using two Navitar's Zoom6000 high magnification modular zoom lens systems.

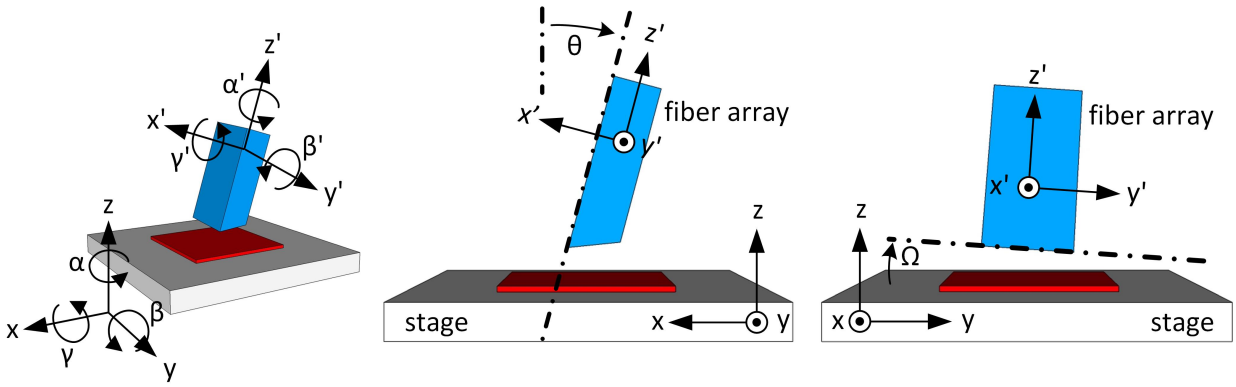

Figure 3.11: Degrees of Freedom of stage: tip and tilt (β, γ,), rotation (α), and translation (x and y, locked z); Degrees of Freedom fiber array: tip and tilt (α', γ'), rotation (β'), and translation (z', locked x',y').

For a fiber array with a large number of fibers, it is important that the fiber array plane (plane through fiber axis) is aligned with the grating couplers. Figure 3.12 shows schematically the effect of a misalignment. The fine align algorithm uses GC1 to optimize the return power (input on GC2). Because of a rotational misalignment δ the second output grating coupler (GC3) has a decreased power reading.

3.3.2 Chip alignment

The chip stage must be aligned to the fiber array across its entire dimensions. As stated previously, the chip block mounts on top of two motorized stages (x and y), a rotation stage (α), and a tip-tilt stage (β, γ). The rotation stage (γ) is used to align the x-axis of the chip to the fiber array such that the fiber array remains parallel to the chip across its entire length. Ideally the two linear stages align perpendicular to each other eliminating error in y-axis moves after proper x-axis alignment. However, an angle error exists since it is impossible

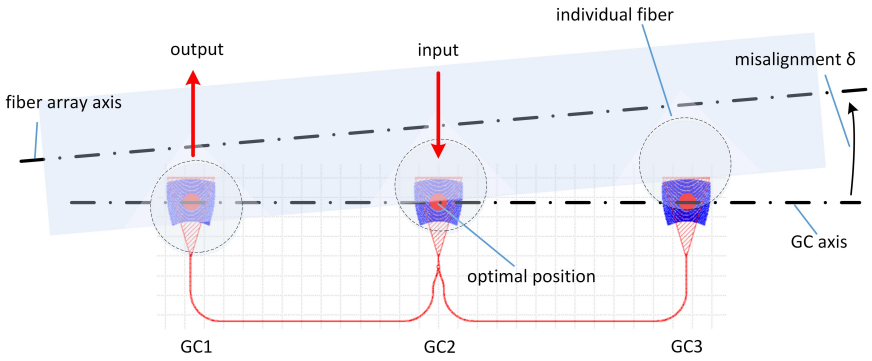

Figure 3.12: Unbalanced power reading due to misalignment (δ), the fine align function uses only one detector (i.e. GC1, user specified) and optimizes the output power as function of stage position leading to a misalignment of GC3.

to mount the stages perfectly. Setting up a coordinate system (described later) will account for and correct this error. The tip-tilt stage (α and β) helps maintain a similar distance between the fiber array and entire chip. We have found that the optimal distance from the fiber array tip to the chip is approximately 30 µm. If the angles (α, β) are misaligned by more than 8.5 degrees, the fiber array would collide with the chip when moved by 12 mm (across the chip).

An overhead USB camera connected to a monocular zoom lens helps rotationally align the chip to the fiber array. To correct any misalignment, the user marks a position on the chip with a sticky note and then traverses the chip to a complementary feature (shown in Fig. 3.13(a) and Fig. 3.13(b)). This process is repeated until the features align with the sticky note.

Next, the user lowers the fiber array until its reflection off the chips surface can be seen from the second alignment camera, or a few hundred microns above the chip (see Fig. 3.13c)). Once again, the user places a sticky note at the reflected edge and traverses the chip in both X and Y. If the chip and fiber array are out of plane (dz), the shadow will increase or lessen. The tip-tilt stage can be adjusted until the reflected edge is consistently coincident with

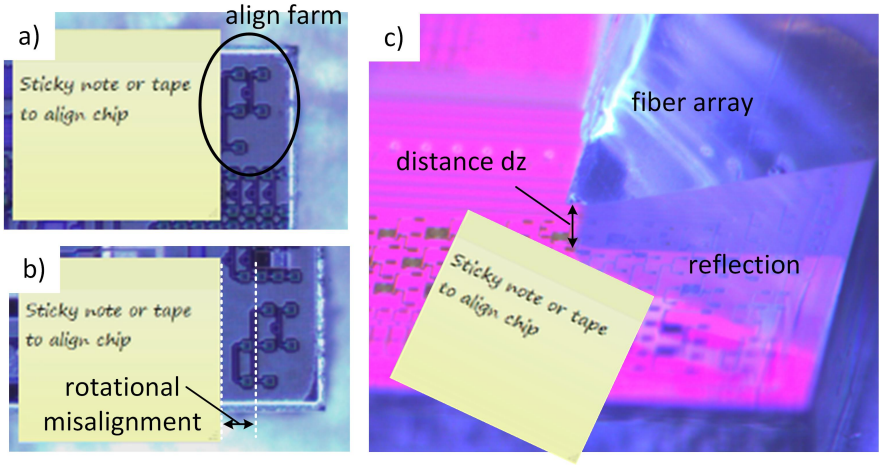

Figure 3.13: The chip must be rotationally aligned to the fiber array prior to setting up a coordinate system for automated testing. (a) Any feature can provide a reference to rotationally align the chip but it must have a complementary, in-line marking on the other side of the chip (in this case, the loop backed alignment grating couplers are used). The user moves to the other end of the chip and checks for rotational misalignment (b). This process is repeated until the misalignment is gone. (c) The tip-tilt stage is used to ensure a fully parallel plane between the chip and fiber array. The corner of the fiber array's reflection is marked and the user moves the chip to each corner, ensuring the marked gap is consistent at all locations.

the sticky note. Once the chip is in plane with the fiber array, it can be lowered to within 30-50 µm's of the surface to begin the registration process.

3.3.3 Mapping grating couplers

To find first light, the fiber array must be moved within the vicinity of the device and a 2D raster performed. The mapping involves stage moves along one axis, e.g. y-axis (line scan) while power values are recorded. The stage is incrementally moved along the other axis (x-axis) and then another line scan is performed. Once complete, a 2D 'heat map' is displayed

as shown in Fig. 3.14. The location of reflected light (grating coupler pairs) appears in red while the background (no reflected power) is blue. The user then clicks a red spot on the image to move the fiber array to that location. The next step involves a fine-alignment at that location to optimize the optical transmission.

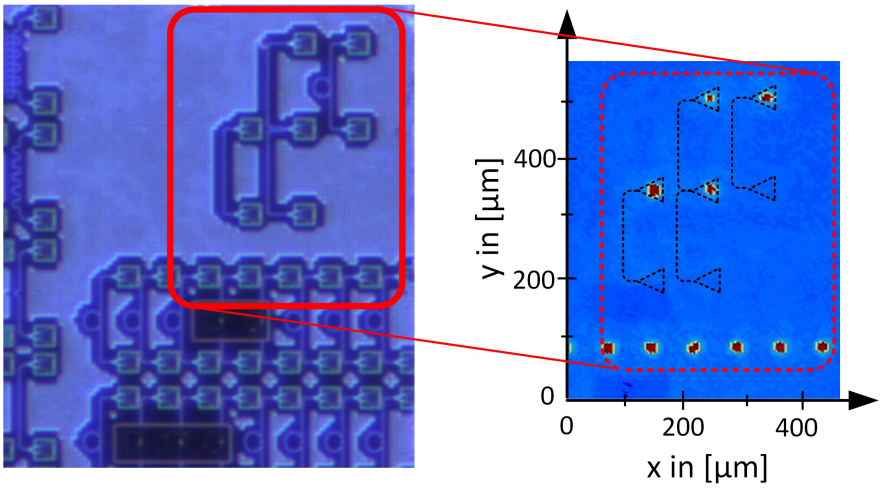

Figure 3.14: Mapping of grating coupler pairs: An area of typical 400 µm x 600 µm is scanned and a 'heat map' is generated. Red blobs indicate that there is power returned and hence that input and output grating couplers are aligned with the fiber array.

3.3.4 Fine align

The fine align algorithm performs small stage movements to align the on-chip gratings to the fiber array. The algorithm involves three phases. When started, the software queries the power meter and if the reading falls below a user specified threshold (i.e. -30 dBm), then the algorithm advances to a search-phase called phase i) in Fig. 3.15(b). The stage is moved in an outward-growing rectangular pattern comparing the queried power to the threshold. The size of the spiral and the step resolution can be specified in the fine align settings.

If the queried power never exceeds the threshold during phase i) within the specified

search window, the algorithm switches to an alternate detector and starts once again. If the queried power never exceeds the threshold using the alternate detector, the algorithm quits and alerts the user of the failed fine align. The primary and alternate power meter can be specified in the fine align settings.

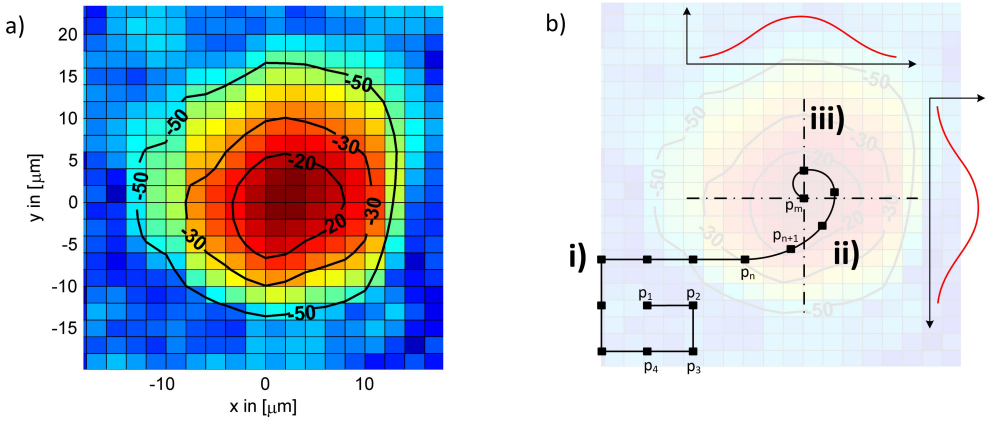

Figure 3.15: a) Power returned as function of position of fiber array relative to the grating coupler pair. The power returned is in the units of dBm. b) The full fine align method consists of three phases: i) spiral method; ii) gradient method; iii) crosshair method

When the queried power exceeds the threshold, the algorithm enters the 'hill climb' (phase ii) in Fig. 3.15(b)). This phase implements a *gradient method* which compares power values from the neighboring points to determine the direction of higher power readings (see Eq. 3.1).

$$\begin{bmatrix} \cdots & p_{n,m-1} & \cdots \\ p_{n-1,m} & p_{n,m} & p_{n+1,m} \\ \cdots & p_{n,m+1} & \cdots \end{bmatrix} \tag{3.1}$$

The software moves the stages along the gradient acquiring power readings and completes once it reaches the maximum in both X and Y, as defined by:

$$\begin{aligned} p_{n-1,m}, p_{n+1,m} &< p_{n,m} \\ p_{n,m-1}, p_{n,m+1} &< p_{n,m}. \end{aligned} \tag{3.2}$$

where $p_{n,m}$ is the power at position $x_{n,m}, y_{n,m}$. A point-by-point line scan with a 1 µm step is performed and the stage is moved to the position with the highest reading. This is done along the x-axis and the y-axis and at the end of the algorithm, the stage is moved to the X and Y position with the highest reading.

3.3.5 Coordinate system

In order to automatically measure many devices simultaneously, the software needs to translate GDS coordinates into motor positions. To accomplish this, the user must configure a coordinate system. This involves moving to three known devices, performing a fine align, and setting the stage position to the device's GDS coordinates. When the user selects the device from the list, the software populates the GDS coordinates in the coordinate system table. The user then 'sets' the stage position for that device. The software then populates the stage position for that device in the table. With three devices specified, the software automatically computes a transformation matrix between GDS coordinates and motor position and outputs the residual to console window.

This section describes how the software computes the transformation. Assuming an affine transformation between the GDS plane and the motor plane $f : \mathbb{R}^2 \to \mathbb{R}^2$, it assumes the form $\vec{x} \mapsto T\vec{x} + \vec{b}$, where T is a linear transformation including: scaling, rotation, and shearing, and $\vec{b}$ is the pure translation. Therefore, the mapping definition is:

$$\begin{bmatrix} x_{motor} \\ y_{motor} \end{bmatrix} = \underbrace{\begin{bmatrix} s_x \cos\alpha & -s_y \sin\alpha \\ s_x \sin\alpha & s_y \cos\alpha \end{bmatrix}}_{\textbf{scaling and rotation}} \underbrace{\begin{bmatrix} 1 & \sigma_1 \\ 0 & 1 \end{bmatrix}}_{\textbf{shear x}} \underbrace{\begin{bmatrix} 1 & 0 \\ \sigma_2 & 1 \end{bmatrix}}_{\textbf{shear y}} \begin{bmatrix} x_{gds} \\ y_{gds} \end{bmatrix} + \begin{bmatrix} b_1 \\ b_2 \end{bmatrix}, \tag{3.3}$$

where s_x and s_y are the scaling factors in x and y, respectively, α is the rotation angle between the two planes, and σ_1 and σ_2 are the shear factors in x and y, respectively. The scaling operation accounts for different units in the two spaces ([µm] to [mm]) and any optical

encoder errors in the linear stage while the rotation corrects the rotational misalignment of the two planes. The shearing transformation compensates for angle errors between the X and Y stages (x-axis and y-axis). We typically observe worst case angle errors of about 1 degree compensated by the transformation.

Since the motor position is affected by measurement errors, an exact solution for the transformation parameters cannot be found. Instead, the function $\min_p \|f(\vec{p_{gds}}, \vec{p_m})\|_2^2 = \min_p (f_1(\vec{p_{gds,1}}, \vec{p_{m,1}})^2 + \cdots + f_n(\vec{p_{gds,n}}, \vec{p_{m,n}})^2)$ is optimized using a least squares fit, where $p_m = [x_{motor}, y_{motor}]$ and $p_{gds} = [x_{gds}, y_{gds}]$ which are the motor position and GDS coordinates respectively. Then $f(\vec{p_{gds}}, \vec{p_m})$ becomes:

$$f(\vec{x}) = \begin{bmatrix} T_{11} & T_{12} & 0 & 0 & \cdots \\ T_{21} & T_{22} & 0 & 0 & \\ 0 & 0 & T_{11} & T_{12} & \\ 0 & 0 & T_{21} & T_{22} & \\ \vdots & & & & \ddots \end{bmatrix} \begin{bmatrix} x_{gds,1} \\ y_{gds,1} \\ x_{gds,2} \\ y_{gds,2} \\ \vdots \end{bmatrix} + \begin{bmatrix} b_1 \\ b_2 \\ b_1 \\ b_2 \\ \vdots \end{bmatrix} - \begin{bmatrix} x_{motor,1} \\ y_{motor,1} \\ x_{motor,2} \\ y_{motor,2} \\ \vdots \end{bmatrix}. \tag{3.4}$$

At least three ($n = 3$) motor position and coordinate pairs ($[x_{gds,n} y_{gds,n}] \mapsto [x_{motor,n} y_{motor,n}]$) are needed for a robust geometrical solution. While any device can be used to configure the coordinate system, it is often easiest to use the looped-back GC alignment structures provided in the GDS framework. Since they reside in the chip corners (Fig. 3.16), they are easy to find and provide distant, distinct coordinate pairs to minimize errors in the transformation.

3.3.6 Software application

The software application facilitates sequence to setup and characterize silicon photonic devices and orchestrates assays. The graphical user interface (GUI) has eight panels which are hidden or made visible based on controls required at that step in the process. Figure 3.17 shows the test panel but also highlights the partitions within the entire window.

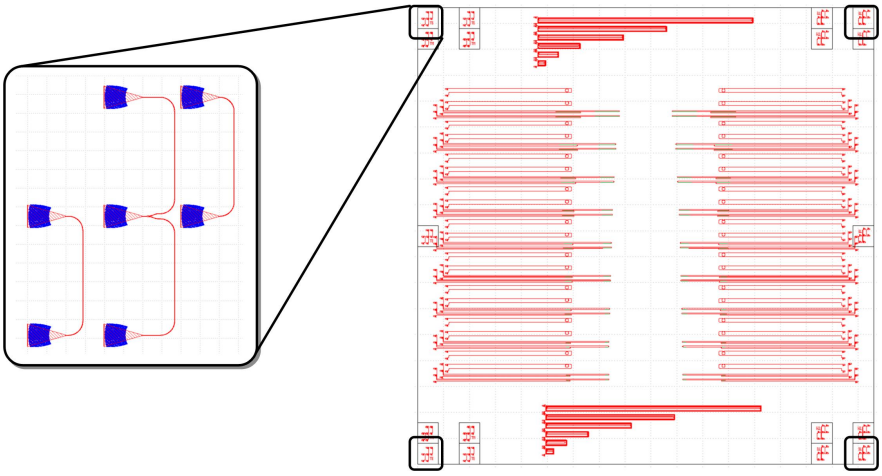

Figure 3.16: Alignment structures to facilitate the timely setup of a coordinate system are placed in corners of the photonic chip as shown in the GDS2 above.

3.3.7 Automated testing and assay orchestration

Using the coordinate system described above, the probe station automatically tests many devices in a single setting. Figure 3.18 shows the flow diagram how the software executes the automated measurements. A transformation matrix converts the GDS coordinates into motor positions. A fine align executes at each new device and then a wavelength sweep is performed. The software saves the results and proceeds to the next device. This process repeats until all the devices have been tested.

Automated testing initially screens devices for yield under dry conditions. The ones that work are then subjected to an aqueous environment and characterized. The software uses a 'recipe' file specified by the user to orchestrate the sequence. The user sets the reagent order, dwell time in each well, and pump flow rate in a text file we call a 'recipe' file. This simple text file specifies comma-separated parameters and must follow the format shown below:

```
%<well>,<time(min)>,<reagent>,<ri>,<velocity>,<temp>,<comment>
```

User configurable parameters include: the well number ($\# > 0$), the dwell time in the well ($\# > 0$), the reagent name, the reagent's refractive index (if known), the pump flow rate in

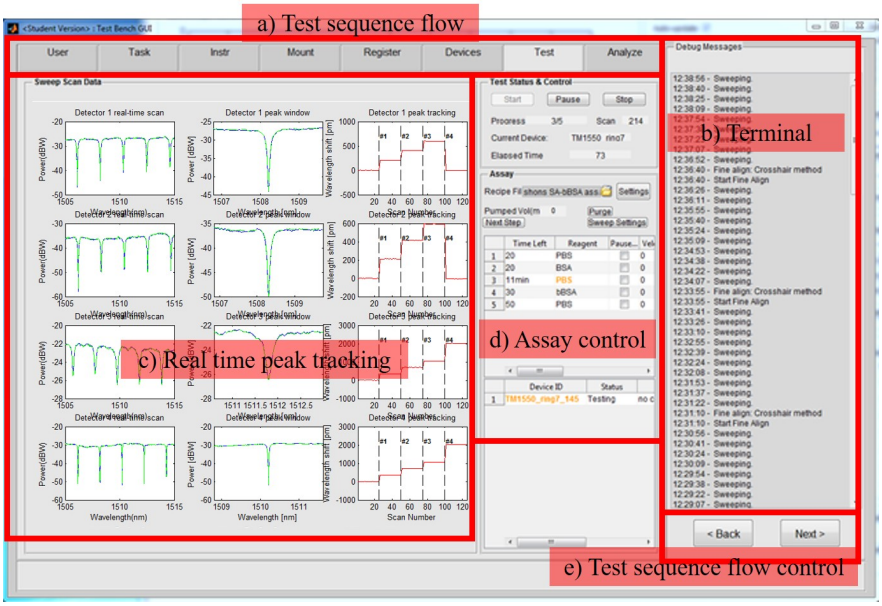

Figure 3.17: A screen clip of the application window with an active test panel is shown. a) Sequence tabs that highlight the active step in the overall setup and testing process. b) Window with informational messages provided to the user. c) Test panel showing the acquired spectra for four channels (left), the windowed peak that is tracked (center), and the resulting sensogram with wavelength shifts from the tracked peak (center) over the course of the assay. d) Assay control window highlighting the active recipe step and device under test. This panel also has the testing control and settings buttons. e) 'Previous' and 'Next' buttons that sequence the user through the various panels enumerated in a).

uL/min (> 0), the stage temperature in Celsius, and a comment string if desired (optional). An example recipe file is included the GitHub repository with the source code. A '0' specified for flow rate disables the pump. And the time can be translated into number of sweeps via a setting accessible from the test panel.

If multiple devices are selected for test, the user can specify to loop through all devices at each reagent step or sequence through all the reagents for each device. These features allow performance parameters of many devices to be experimentally assessed quickly and

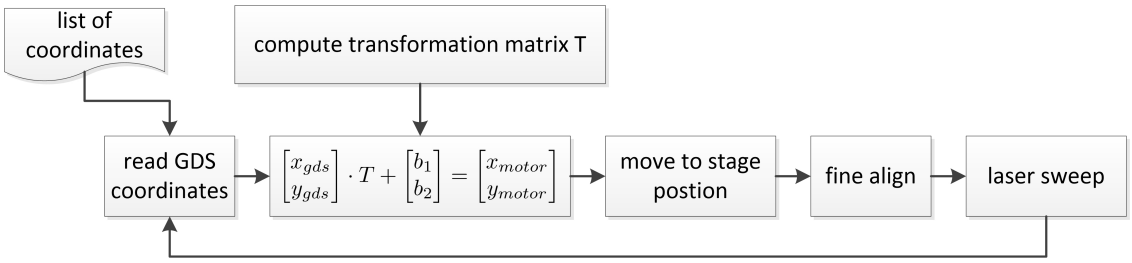

Figure 3.18: Flow diagram of automated measurement: from the device list the GDS coordinates are read and translated into a motor position by using the transformation matrix T. After fine align the measurement, i.e. wavelength sweep, is performed.

efficiently. Figure 6.7 shows an example of the bulk sensitivity being observed for two devices simultaneously. For this case, the software acquired 20 wavelength sweeps per sensor at each refractive index solution step. The data in Fig. 6.7 was acquired in less than 10 min (including the analysis time) plus 15 min of setup up time (including aligning of chip, setting up flow cell, finding first light, configuring the coordinate system, and launching the assay).

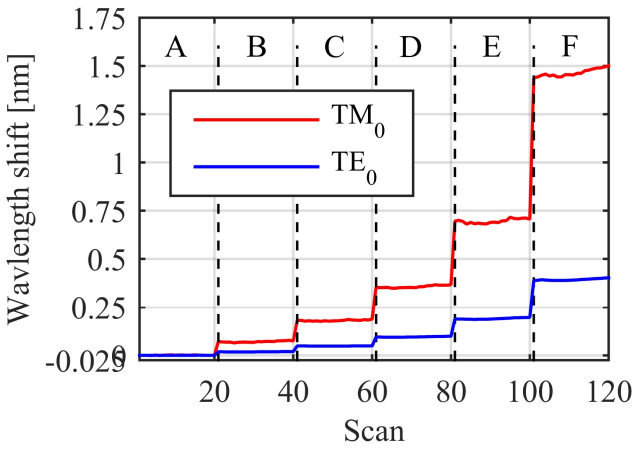

Figure 3.19: Example of how the bulk refractive index sensitivity of two different devices, such as a TE and TM mode ring, can be assessed simultaneously.

3.3.8 Analyzing data

A custom analysis tool compliments the probe station control software and provides more sophisticated processing of acquired datasets. While the user can select and track peaks during an assay, circumstances arise when the peak may be lost. If this happens, the only way to recover the sensogram is post-acquisition. For example, the accidental introduction of an air bubble may move resonant peak out of the tracking window or the slow (laser-dependent) scan rate may not be able to keep up with a quickly shifting peak. The analysis tool helps recover the tracked peak under these circumstances.

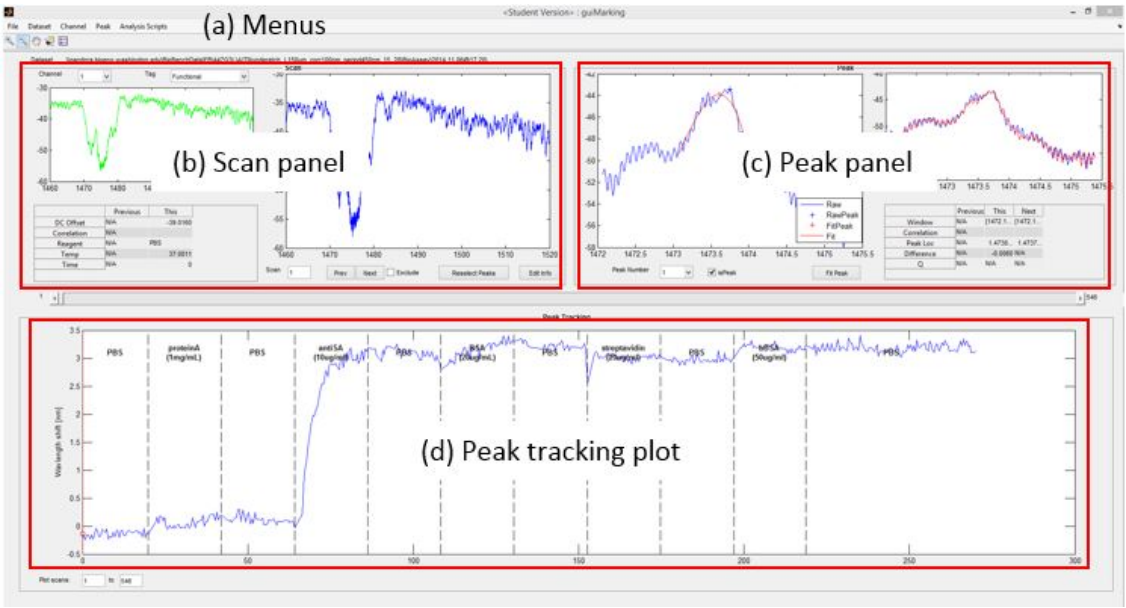

Figure 3.20: Analysis tool UI. (a) Menus that provide access to opening datasets, saving analysis parameters, and executing user-defined analysis scripts on the processed data. (b) The scan panel shows the entire wavelength range and the selected peak for a single sweep. (c) The peak panel highlights the windowed peak and overlays a fitted result. (d) The peak tracking plot shows the sensogram of the entire assay which includes the tracked peak for every sweep.

Figure 3.20 shows a screen clip of the analysis tool which imports an acquired dataset and facilitates post processing. The user can remove unwanted scans, select and track different peaks, curve fit peaks using a polynomial or Lorentz function, subtract reference channels, compare a functional sensors drift to the system temperature, correlate entire scans or the peak window with previous ones, measure y-offsets on the sensorgram, and export the analyzed data and figure, as shown in Fig. 6.7 and Fig. 6.12.

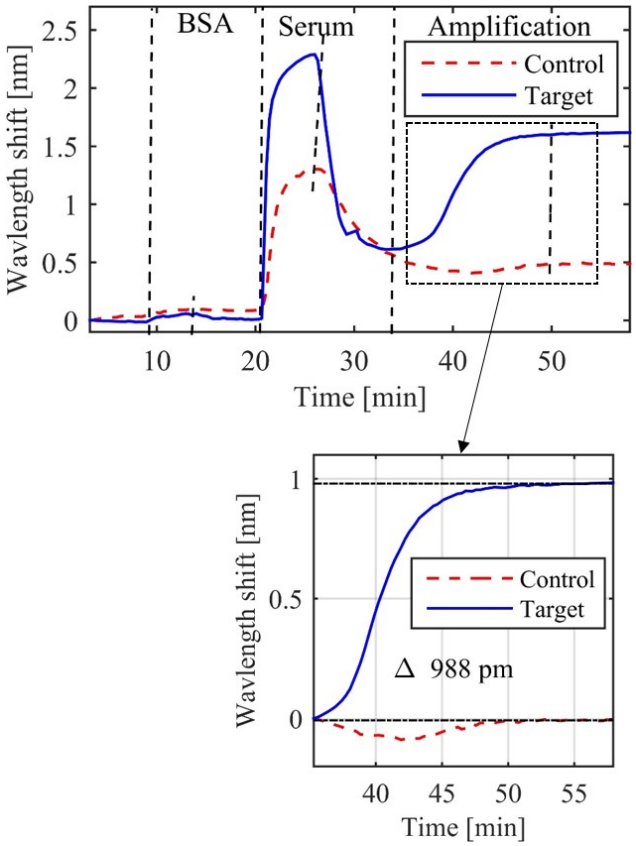

Figure 3.21: Example of biosensing assay data processed using the analysis tool. Multiple sensograms can be plotted within the same figure and normalized to compare regions (as done in the enlarged inset during secondary amplification).

After processing, the user can save all the parameters and excluded scans to an analysis file that can be reloaded when accessing the dataset in the future. Figure 6.12 shows an example

of a biological assay processed using the analysis tool. A portion of the amplification step has been renormalized and windowed in the inset below to highlight the offset between the two channels.

The tool also supports user-defined analysis scripts. Using the provided scripting template as a starting point, the user can gain access to the processed data in applications namespace. This allows the user to quickly develop custom routines to further analyze their data. Scripts can invoked from within the tool by simply adding them to the 'analysisScripts' directory in the tool and selecting them from the 'Analysis Scripts' menu shown in Fig. 3.20(a).

3.4 Platform Characterization

In addition to testing devices, recipe files can be developed to characterize the system itself, including the bench top instruments. As an example, we report on noise floor measurements as function of laser sweep speed and flow rate under aqueous conditions. We also describe how algorithm stability and robustness (e.g. fine align) were assessed using user-defined scripts.

3.4.1 Noise floor as function of sweep settings

While sensor design impacts detection limits, it also depends on other noise sources in the signal path (i.e. external instrumentation such as the laser and power meter). We wanted to understand how their settings might impact device characterization in regards to sweep speed and resolution.

Two (extreme) cases were investigated: (1) maximum resolution (0.1 pm) and long averaging at the slowest sweep speed (0.1 nm/s), and (2) moderate resolution (1 pm) and short averaging at the fastest sweep speed (40 nm/s). A custom high-Q TE/TM mode disk resonator sensor designed by our group [21] and a reference acetylene cell (Wavelength References, Corvallis, OR) were used to evaluate trade-offs among sweep speed and step size (resolution). In both cases, the stage was thermally tuned to 30 ^{o}C. Table 3.1 lists the power meter connections.

Table 3.1: Power meter connections

Channel 1	Disk resonator TM mode resonant peak
Channel 2	Disk resonator TE mode resonant peak
Channel 3	Capped (no input) to measure detector noise
Channel 4	Acetylene cell for wavelength reference

Measurements were performed under dry conditions without the gasket and flow cell. Sweeps were continuously acquired for 1 hour (around 120 scan lines). A resonant minima (or null) for a high Q peak, low Q peak, and acetylene absorption peak were tracked for every scan and their distribution determined. In both cases (fast and slow sweep speed) the acetylene reference cell showed an rms noise below the resolution. Table 3.2 lists the computed rms noise and Q for different resonance modes in the disk resonator. We observed a Q of 950k for the acetylene reference peak with an rms jitter of less than 1 pm. The wavelength sweep resolution for these measurements was set to 1 pm.

Table 3.2: Resonance peak jitter at sweep speed of 0.1 nm/s (0.1 pm resolution) and 40 nm/s (1 pm resolution)

speed	peak	Channel 1		Channel 2	
nm/s	#	rms [pm]	Q [k]	rms [pm]	Q [k]
40	1	1.5	125	1.8	154
	2	1.4	60	1.5	138
0.1	1	1.6	126	2.1	255
	2	1.5	6	2.2	215

Since the acetylene cell does not exhibit the same rms noise as the disk resonator, we assume that the variation originates in the chip's photonic signal path. Possible noise sources include the time-dependent alignment of I/O fibers and grating couplers or slight temperature fluctuations in the photonic chip due to bulk air flow around the test setup. It appears both

the slow and a fast sweep exhibit similar noise floors. This means that assays can use the higher sampling (number of sweeps per minute) without affecting the detection limit.

3.4.2 Noise floor as function of flow rates

Typical flow rates range from 1-100 µL/min for most bio-assays. To investigate the impact of flow velocities on rms noise, we performed repetitive sweeps and tracked resonant peaks while exposing sensors to different flow rates of ultra-pure, degassed water. We used the same disk resonator and tracked similar peaks as the noise floor assessment previously described. Spectral responses were acquired at a sweep speed of 40 nm/s and resolution of 1 pm. The stage was thermally tuned to 30 ^{o}C.

Figure 3.22 shows the observed rms noise for the various resonance peaks. Peak 1 has a quality factor of 18k and rms noise of 3 pm and appears to be slightly decreasing with increasing flow rate. Peak 2 with a quality factor of 50k has an rms noise of 1 pm but seems to be independent of flow rate. The reported rms values correspond to what was observed in air (see section 3.4.1). These results suggest that flow rates ranging from 1-100 µL/min do not significantly impact the system's noise floor.

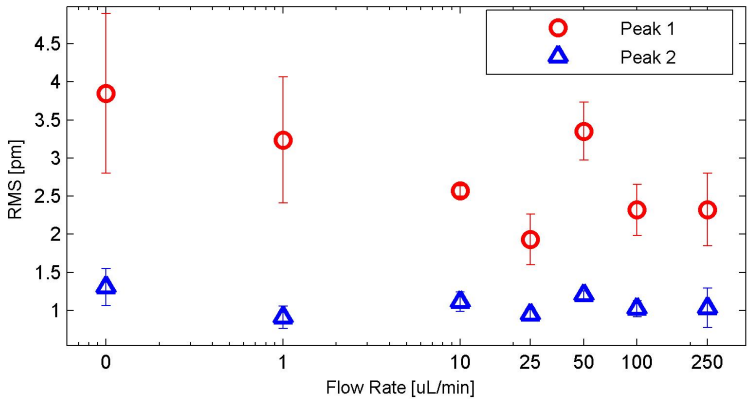

Figure 3.22: The wavelength variation is reported as function of flow rate. For peak 1 (Q = 18k) the rms is between 2 and 4 pm. For peak 2 (Q = 50k) the rms is around 1 pm

3.4.3 Stage stability and algorithm robustness

The second example of system characterization scripts focuses on the fine align algorithm. In particular we wanted to assess: (1) grating coupler insertion loss as function of position in relation to the stage and (2) repeatability of the algorithm to optimize the fiber array position over the on-chip grating couplers.

Insertion loss as function of stage position

The fine align robustness was assessed using a TE mode alignment farm (as described in section 3.3.3). The power meters were configured for a dynamic range of -10 dBm to -40 dBm to avoid saturation and connected as follows: channel 1 to a TE mode looped-back grating coupler port and channel 4 to the acetylene cell for wavelength reference. The remaining channels were capped and unused. The fiber array was centered on a grating coupler pair at a distance from the chip surface of about 10 µm. A volume of size 80 µm x 120 µm x 180 µm is scanned with a step size of 2 µm. At each point in space the power returned by the grating coupler pair is recorded (average of 3 readings). Tests were performed in a dry, climate controlled laboratory setting (normal conditions).

Figure 3.23 shows four slices of a scanned, 3D volume. The red areas indicate low insertion loss and blue means little or no power was returned. As the distance of the fiber array to the chip surface increases, the red area moves along the x-axis since the grating couplers used here were designed for an incident angle of 20^o. The axis through the points with lowest insertion loss for each slice has an angle of 20^o with respect to the x-axis. The horizontal shift (with increasing distance) is therefore expected and confirmed. The top view of the first slice indicates an acceptance area with a radius of about 20 µm. This means that for a fast mapping algorithm a step size of 5 µm will be sufficient.

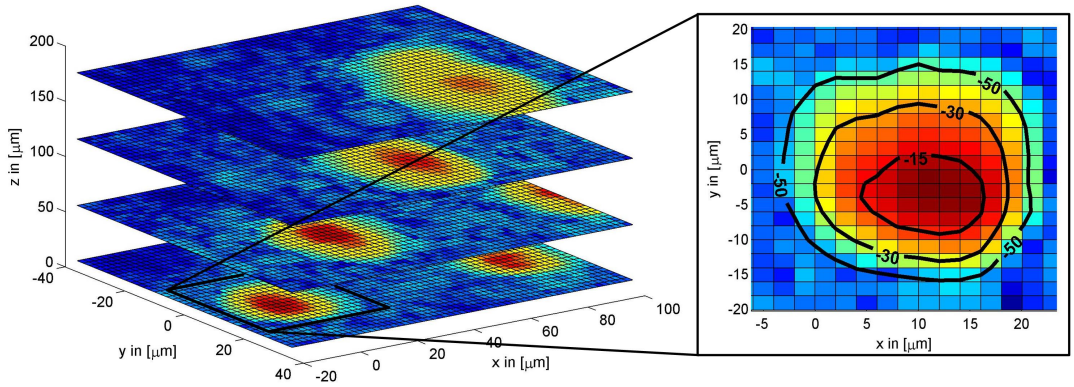

Figure 3.23: A volume of size 80 µm x 120 µm x 180 µm is scanned with a step size of 2 µm. At each point in space the power returned by the grating coupler pair is recorded (average of 3 readings). The acceptance angle of a grating coupler is about 20 µm in diameter.

Stability of fine align algorithm

The fine align repeatability was assessed by doing 600 consecutive sweeps (10 pm step at 40 nm/s) while performing a fine align between each sweep. The insertion loss of grating coupler pair was extracted for each scan.

Figure 3.24(a) shows a scatter plot of recorded motor positions. The histograms visualize the distribution along the x-axis ($\sigma = 2\ \mu m$) and y-axis ($\sigma = 2.4\ \mu m$) respectively. The maximum power of each transmission is recorded in Fig. 3.24(b). The outliers ($N = 25$ with IL > 24 dBm) correspond to a motor position outside the circle with radius of $r = 4\ \mu m$ and signify an unsuccessful fine align sequence. With removed outliers the standard deviation of the insertion loss is $\sigma_{adj} = 0.49$ dBm. There are cases when the algorithm partially fails. At this point, it is unclear why the algorithm fails for a small number of fine align tries. We hypothesize it is due to the PID settings in the controller itself and have engaged the manufacture to help resolve the issue.

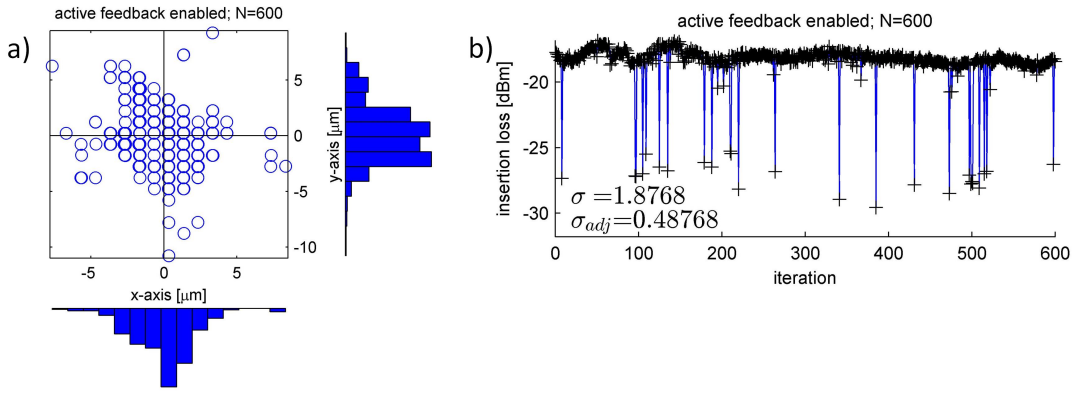

Figure 3.24: Fine align stability: a) recorded motor position after each fine align cycle. The histogram visualizes the distribution along x-axis ($\sigma = 2\ \mu m$) and y-axis ($\sigma = 2.4\ \mu m$); and b) recorded insertion loss of grating coupler pair.

3.5 Conclusion

To the best of our knowledge, we have created the first open-sourced tool kit for silicon photonic biosensor design and characterization. We described an ebeam-compatible PDK with core I/O components and a framework that facilitates alignment and registration using the automated probe station. The test setup software is freely provided on GitHub under the Gnu Lesser General Public License Version 3. The various hardware assemblies were explained and results shown for algorithm characterization and validation. Finally, we report on the performance impact of laser and flow rate settings for biosensing assays. We believe this platform helps lower the barrier to entry while accelerating the field of silicon photonic biosensors towards commercialization.

3.6 Acknowledgements

The authors would like to thank Andrew Millspaugh for his help in developing the initial code base. We are also thankful for mechanical design and fabrication provided by Qian Wang. We appreciate the efforts of Matt Doerfler and Victor Bass, two visiting summer

students, who helped validate GUI elements and instrument drivers. Furthermore we would like to thank Miguel Angel Guillen Torres for testing the software and feedback. We are also grateful to Dr. Nicholas Jaeger for the use of his laser in our probe station setup.

This work was supported by the University of Washington (UW) Royalty Research Fund, NSF CBET (Award no. 0930411), and the Washington Research Foundation. We gratefully acknowledge Lumerical Solutions, Inc. for providing the simulation software. Fabrication support was provided via the Natural Sciences and Engineering Research Council of Canada (NSERC) Silicon Electronic-Photonic Integrated Circuits (SiEPIC) Program. The PDK devices were fabricated at the University of Washington Washington Nanofabrication Facility, part of the National Science Foundations National Nanotechnology Infrastructure Network (NNIN).

Chapter 4

IMPROVING THE PERFORMANCE OF SILICON PHOTONIC RINGS, DISKS, AND BRAGG GRATINGS FOR USE IN LABEL-FREE BIOSENSING

This chapter describes work completed in close collaboration with Jonas Flueckiger who designed all the devices except the thin TE and TM mode ring resonators, which were designed by Dr. Sahba Talebi Fard, and the disk resonators, which were designed by Dr. Samantha Grist. Portions of this chapter were reprinted with permission and may be found in the following publications:

1. **S. Schmidt**, J. Flueckiger, W.X. Wu, A. Lingley, K. Bohringer, K.C. Cheung, L. Chrostowski, D.M. Ratner, 'Enhancing Silicon Photonic Bragg Grating Performance for Biosensing Applications', *Manuscript in preparation*, 2016.

2. S. Talebi Fard, **S. Schmidt**, W. Shi, W. Wu, N. Jaeger, E. Kwok, D. Ratner, L. Chrostowski, 'Optimized Sensitivity of Silicon-on-Insulator Strip Waveguide Resonator Sensor', *Submitted*, 2016.

3. **S. Schmidt**, J. Flueckiger, W. Wu, S.M. Grist, S. Talebi-Fard, V. Donzella, P. Khumwan, E.R. Thompson, Q. Wang, P. Kulik, X. Wang, A. Sherwali, J. Kirk, K.C. Cheung, L. Chrostowski, D. Ratner. 'Improving the performance of silicon photonic rings, disks, and Bragg gratings for use in label-free biosensing.' SPIE NanoScience Engineering VII. International Society for Optics and Photonics, 2014.

4. **S. Schmidt**, S. Grist, J. Flueckiger, V. Donzella, W. Shi, S. T. Fard, J. T. Kirk, D. Ratner, K. Cheung, and L. Chrostowski, "Silicon photonic micro-disk resonators for

label-free biosensing," Optics Express, 2013.

5. J. Flueckiger, **S. Schmidt**, V. Donzella, A. Sherwali, D.M. Ratner, L. Chrostowski, K.C. Cheung, 'Sub-wavelength grating for enhanced ring resonator biosensors', Optics Express, 2016.

6. J. Flueckiger, **S. Schmidt**, Z. Chen, X. Wang, A. Liu, L. Chrostowski, D.M. Ratner, K.C. Cheung, 'TM polarized Silicon Photonic Bragg Gratings for Biosensing', *Manuscript in preparation*, 2016.

7. S. Talebi Fard, V. Donzella, **S. Schmidt**, J. Flueckiger, S.M. Grist, P. Talebi Fard, Y. Wu, R. Bojko, E. Kwok, N.A.F. Jaeger, D.M Ratner, L. Chrostowski, 'Performance of ultra-thin SOI-based resonators for sensing applications', Opt. Express, vol. 22, no. 12: OSA, pp. 14166–14179, 06/2014.

8. X. Wang, J. Flueckiger, **S. Schmidt**, S. Grist, S. T. Fard, J. T. Kirk, M. Doerfler, K. Cheung, L. Chrostowski, "A silicon photonic biosensor using phase-shifted Bragg gratings in slot waveguide," Journal Biophotonics, vol. 6, issue 10, pp. 821–828, 04/2013.

4.1 Introduction

Silicon photonic sensors have achieved sensitivities close to clinical levels for label-free sensing in complex media (≈10 ng/mL)[26, 40, 43, 53, 54]. Although single molecule detection has been reported using toroids [226, 227] and anti-resonant reflecting optical waveguides [228], these sensors are not suitable for high-volume manufacturing due to their fabrication complexities. Yet today's commercially available silicon photonic biosensor systems often require label-based signal amplification for detection of extremely low concentrations [90]. Achieving sensitivities at pg/mL levels or lower for label-free, silicon photonic sensors suitable for high-volume fabrication would greatly expand their potential as a label-free diagnostic device.

As described in chapter 2.2.1 the figures of merit to describe a sensor performance include sensitivity, S, and the limit of detection. The sensitivity is determined by the overlap of the electric field with the analyte and can be improved by increasing that overlap. Genalyte, a commercially available silicon photonic biosensing platform, utilizes ring resonators designed for TE polarized light with a bulk sensitivity of 54 nm/RIU [30, 229].

In this chapter a variation of sensor designs are experimentally characterized and discussed in terms of the figure of merit introduced in Sec. 2.2.2. The devices discussed include TM ring resonators in Sec. 4.3.2, thin TE ring resonators in Sec. 4.3.2, disk resonators in Sec. 4.4, sub-wavelength grating based ring resonators in Sec. 4.3.4, on slab and suspended TE Bragg gratings in Sec. 4.5.2 and Sec. 4.5.5, on slab and suspended TM Bragg gratings in Sec. 4.5.4 and Sec. 4.5.5, and TE slot Bragg gratings in Sec. 4.5.3.

4.2 Methods and materials

Devices are fabricated on SOI wafer with a 220nm thick Si layer 2 or 3 µm buried oxide layer. For fabrication two strategies can be used. 1) Electron-Beam lithography as offered through many universities [230–232] or; 2) Deep-ultraviolet (DUV) lithography available at CMOS foundries [219–223].

Foundry fabrication

Foundry access was provided via multi-project-waver runs (MPW) organized by CMC Microsystems. Predominantly two foundries were used for fabrication: (1) IMEC through ePIXfab/Europractice (ISIPP25G platorm, 193 nm lithography); and (2) Astar/IME (248 nm lithography).

Ebeam fabrication

The Ebeam provides a low-cost, fast turn-around CMOS-foundry-compatible fabrication process that has been optimized [233–236] to produce consistent, robust, low-loss silicon

photonic components [236, 237]. Multi-etch layer designs were realized by repeating the resist, ebeam write, and etch process on the 220 nm SOI material.

CYTOP cladding

To improve durability, reuse, and reduce optical losses in the long routes between the vertical grating couplers and biosensors, chips are often cladded with CYTOP, a perfluoro-polymer with exceptional chemical resistance and useful optical properties (Over 95% light transmittance through DUV to NIR range and a RI of 1.34) [238]. Openings in the CYTOP cladding are then created around the photonic sensors [239]. Undiluted CYTOP was spun onto the chip at 3500 rpm and then baked at 60^oC for 30 minutes. After 30 minutes, the temperature was ramped up to 180^oC at 4^oC/min and held for 1 hr before ramping back down to 90^oC. AZ9260 was spun onto the CYTOP at approximately 7 µm thick, and then patterned to create the etch windows around sensors. An Oxford Plasmalab System 100 was used to etch the CYTOP using oxygen. Finally, the AZ9260 was removed with acetone and cleaned with isopropanol.

Suspending waveguides

Suspending silicon waveguides on SOI substrates to increase confinement and reduce absorptive losses through the substrate has been demonstrated for high performance and telecommunication applications [240–243]. Suspending TM mode biosensors could be advantages by exposing the energy typically guided in the substrate to the cladding, essentially doubling the device's sensitivity. Therefore, TM mode Bragg gratings were post-processed at the WNF to suspend them in a fluidic channel.

Chips on which to create the suspended sections were first cleaned in a piranha solution and then surface treated using hexamethyldisilazane to promote photoresist adhesion and to help avoid resist lift off during the buried oxide etch. Next, AZ1512, a standard broadband Novalak based photoresist, was spun onto the chip, baked, exposed, and developed to pattern regions for undercut. Buffered oxide etch (10:1) was used to etch through the 3 μm thick

buried oxide later. Without drying, chips were rinsed in water and then bathed in acetone to dissolve the photoresist.

Next, the chips were transferred (while still wet) to a beaker of isopropanol (to avoid stiction) for rinsing and then dried with a gentle stream of nitrogen. SEM images confirmed that the structures were released, as shown in Figure 4.28.

4.2.1 Device testing and performance characterization

Automated testing was used to characterize every silicon photonic biosensor using specific modes in the control software application which include: (1) dry test, (2) wet test (salt steps), and (3) bio assay. Since wet performance characterization and bio demonstrations are time consuming and involve the sequencing of various reagents, devices are first tested are screened with a dry test to ensure the waveguides yielded as expected from the fabrication process. Although each device is designed for an aqueous cladding, performing this initial test in air is enough to determine if it should be tested further. If so, the gasket and flow cell are mounted and devices are wet tested to assess performance parameters such as its quality factor and extinction ratio (ER). The best performing devices are then subjected to a series of refractive index solutions to determine their sensitivity and intrinsic limit of detection (iLoD) using the software's automated assay conductor with a salt-step recipe [20].

Characterizing sensitivity, quality factor, and iLoD

Refractive index solutions of 62.5 mM, 125 mM, 250 mM, 500 mM, and 1 M NaCL are diluted from a 2M stock of NaCl (Acros Organics, Thermo Fisher Scientific) using ultra-pure deionized water (Barnstead Nanopure, Thermo Scientific). Titrations are degassed under vacuum using and ultrasonic bath (VWR B2500A-MTH) and stored in 50 mL Falcon tubes until used.

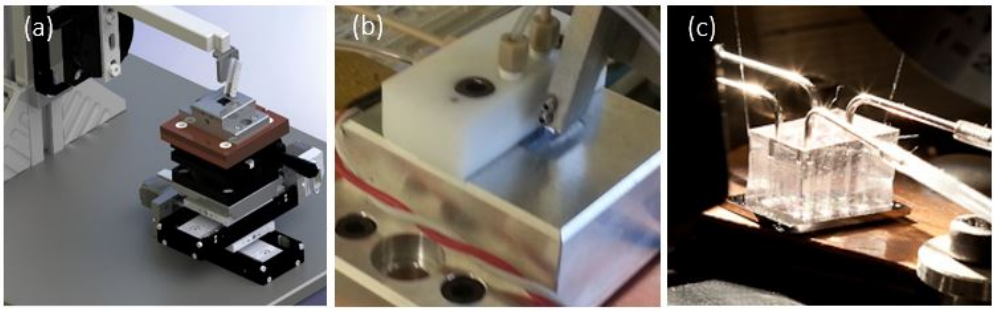

Figure 4.1: Devices can be characterized in a dry environment by thermally tuning the stage or in wet environment. (a) Rendering of the custom hardware platform. (b) Image of fiber array, Teflon flow cell, and device under test. (c) Custom PDMS flow cell reversibly bonded to a chip under test.

Assessing biosensing performance

A modified sandwich assay comprised of well-characterized biomolecules was implemented to verify each sensors capacity to probe biomolecular interactions with specific and non-specific targets (Figure 4.2) [244, 245]. All sensors were exposed to the same sequence of biological reagents, and flow rates between 10-15 L/min using the microfluidic device described above. The syringe pump was paused briefly after each phase of the assay in order to facilitate switching of solutions. Additionally, the microfluidic chamber was flushed with phosphate buffered saline (PBS) between each reagent step to remove any unbound molecules from the sensor surface. The optical stage was thermally tuned to 37^{o}C, which maintained constant sensor temperature throughout the assay while mimicking physiological conditions. Wavelength and power values were recorded every 5-10 seconds using the MATLAB software, and post-processing of data was performed in a separate script.

Prior to any functionalization with biological molecules, the sensors were rinsed with PBS solution (n = 1.35) for 20 minutes to establish a baseline for further signal measurements. The first biological reagent introduced to the system was Protein A, a 42 kDa globular protein with a diameter of 3 nm [155, 156] and a refractive index of 1.48 [99]. Originally isolated from

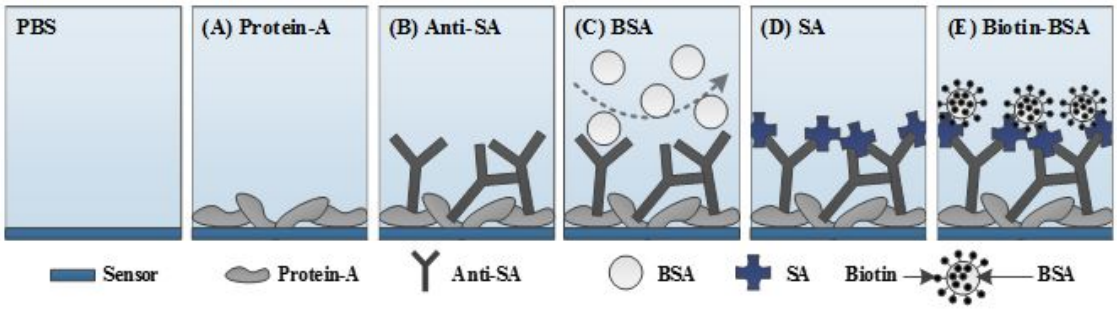

Figure 4.2: Modified sandwich bioassay. Reagent sequencing corresponding to regions [A-E] subjected to each sensor and shown in the results section. Region A = Protein A adsorption, B = anti-streptavidin (Anti-SA) functionalization, C = Bovine Serum Albumin (BSA) challenge and block, D = streptavidin (SA) target analyte binding, E = Biotin-BSA amplification step. Introduction of each reagent was followed by a PBS wash.

Staphylococcus aureus, Protein A demonstrates a high affinity for human and mouse IgG antibodies. We utilized physisorption techniques to irreversibly bind Protein A to the sensor surface as shown in Region A of Figure 4.2 [150, 151]. Functionalization was performed either passively (off-line before executing the assay) or in real-time as the first step of the assay after achieving a baseline signal with PBS. The initial deposit of Protein A has been shown to denature and form a biologically inactive layer, but the second layer forms on top of the first and presents a film of active receptor sites to bind the Fc domain of IgG [159]. Therefore, we assumed a 1-3 nm thick physisorbed layer of Protein A for assessment of experimental results (using MODE simulations). The high binding affinity of Protein A facilitated proper orientation of the capture antibodies in step two; antibodies are predominantly arranged on the surface with their antigen-binding domains directed toward the flow of conjugating solutions. It should be noted that while covalent methods of surface functionalization are preferred for robust, prolonged biological assays, physisorption was considered sufficient as a validation process for our system.

Following a flush with PBS solution, the IgG isotype antibody anti-streptavidin (anti-

SA) (Vector Labs, Burlingame, CA) was introduced to the channel at 10-125 g/mL. Anti-SA is a 150 kDa protein with a length of 15 nm, so resulting resonant peak shifts were larger in comparison to those of other biomolecules used in the modified sandwich assay. Immobilization to Protein A oriented the anti-SA Fab binding domains toward the center of the microfluidic channel (Figure 4.2, Region B). This prepared the channel for the third assay step, in which bovine serum albumin (BSA) (Sigma Aldrich, St. Louis, MO) was introduced to the channel at 20-100 g/mL and immobilized to the Fab binding domains of anti-SA (Figure 4.2, Region C). BSA acted as a negative control for non-specific binding, demonstrating the bio-specificity of the modified sandwich assay. Furthermore, the 66 kDa globular protein blocked parts of the sensor not functionalized with anti-SA to ensure that molecules in the subsequent solution steps would bind to the antibodys Fab regions and not to the sensor surface. Ideally, this assay step would not result in resonant wavelength shifts, but small positive shifts indicated small amounts of non-specific BSA adsorption.

The fourth biomolecule introduced to the sensor, streptavidin (Vector Labs, Burlingame, CA), is a 57 kDa antigen conjugate of anti-SA. This solution was presented to the anti-SA molecules on the sensor surface at 10 g/mL (Figure 4.2, Region D) and a significant shift in resonant wavelength was observed. Rinsing with PBS did not cause a decrease in signal, indicating irreversible binding and confirming the sensors ability to bind specific biological species. For the final assay step, biotinylated BSA (bBSA) (prepared per instructions; SoluLink, San Diego, CA) was introduced to the channel at 10-50 g/mL (Figure 4.2, Region E). The resulting wavelength shift demonstrated that captured SA retained its biotin-specific targeting function. Addition of a secondary antibody also provided signal amplification, further intensifying the sensors response and improving sensitivity to low concentrations of analyte.

4.3 Ring resonators

Ring resonators have attracted interest from both academia and industry, and have found widespread application as biological sensors [25], modulators, and filters [246, 247]. A ring

resonator for TE polarized light is the type of sensor utilized in Genalyte, the first commercially available silicon photonic biosensing platform [30, 229]. The ring resonators in the Genalyte system have bulk sensitivity of 54 nm/RIU. Their design will serve as a performance reference. A ring resonator consists of an optical waveguide looped back onto itself (the resonator) together with a straight waveguide (directional coupler) to couple light into the resonator. Section 2.2.1 describes how the propagation properties are affected by environmental changes, i.e. a change in optical properties of the cladding. Adsorbing molecules cause an effective refractive index change of the optical mode. The resonator translates the effective index change into a resonant wavelength shift which is a much easier quantifiable signal.

4.3.1 Theory of operation

The resonance condition (constructive interference) is met when the optical length of the resonator is equal a multiple of the wavelengths:

$$\lambda_{res} m = n_{eff}(\lambda) \cdot L_{roundtrip} \tag{4.1}$$

where λ_{res} is the sensor's resonant wavelength, L the roundtrip length, and m is the longitudinal mode order of the resonant mode ($m = 1, 2, 3...$). The effective refractive index is a function of wavelength, $n_{eff}(\lambda)$. A schematic representation of a ring resonator is depicted in Fig. 4.3 (b). Because there are two straight waveguides to couple light in and out of the resonators, this configuration is called a double bus ring.

Eq 4.1 assumes that the effective refractive index is the same in the coupling region and the bent waveguide segments. For the numerical model used for simulating the transmission spectrum, the extended resonance condition is used:

$$\delta(\lambda, T) = 2\pi \frac{L_{1,2} \cdot n_{eff,straight}(\lambda, T) + 2\pi R \cdot n_{eff,bend}(\lambda, T)}{\lambda} = 2\pi m \tag{4.2}$$

where $\delta(\lambda, T)$ is the phase shift after a round trip as a function of temperature T and wavelength λ, $n_{eff,straight}$ and $n_{eff,bend}$ the effective refractive index in the straight and the

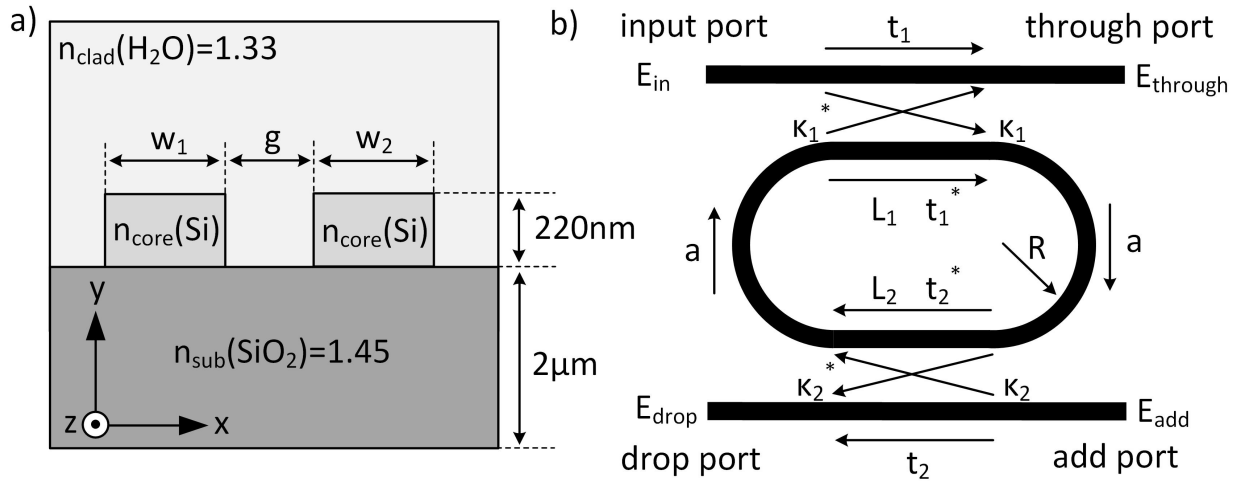

Figure 4.3: a) cross section of a directional coupler with design parameters w, the waveguide width and g, the waveguide gap. The thickness is giving by the choice of SOI wafer (t = 220 nm). b) Schematic of a ring resonator with coupling coefficient $\kappa_{1,2}$, transmission coefficient $t_{1,2}$, coupling length $L_{1,2}$, radius r, and power attenuation in the ring due to propagation loss, a. The subscript 1 and 2 refer to the coupling region.

bent region, respectively.

Spectral response

The analytical solution for a transmission spectrum for a double-bus ring resonator is given by [248]:

$$\frac{E_{through}}{E_{in}} = \frac{t_1 - t_2^* a e^{i\delta}}{1 - t_1^* t_2^* a e^{i\delta}} \tag{4.3}$$

where the subscripts on the values for field transmission refer to the through port coupler, t_1 and the add/drop port coupler t_2. Figure 4.4 shows the simulated and measured transmission spectrum.

Due to the integer-dependent resonance condition (m), multiple resonances are supported, where the spacing between these resonances, the free spectral range (FSR), depends on the

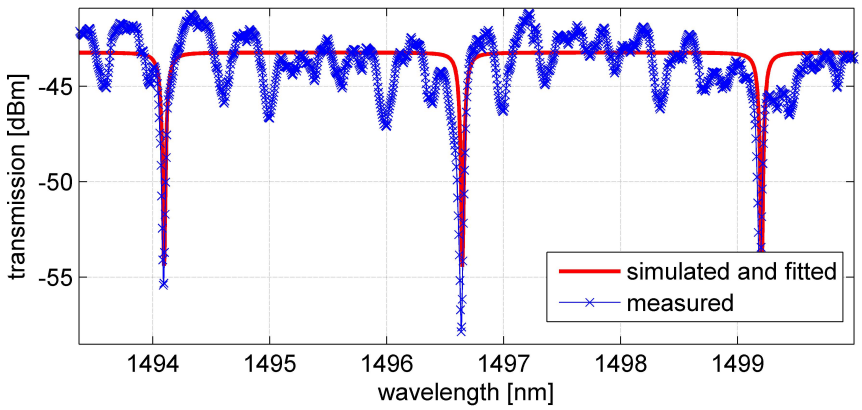

Figure 4.4: Transmission spectrum of a ring resonator (waveguide width $w = 500$ nm, waveguide thickness $t = 220$ nm, coupling gap $g = 200$ nm) resulting in a free spectral range of $FSR = 2.6$ nm.

optical length of the resonator and is given by [91]:

$$FSR = \frac{\lambda^2}{n_g L} \tag{4.4}$$

where n_g is the group index (as defined in Eq 2.6) and L is the round trip length.

When ring resonators achieve critical coupling between the resonant cavity and waveguide bus, a high extinction ratio results. Critical coupling describes the condition when the power loss in the ring is equal to the power coupled to the ring, and can be achieved by optimizing the coupling gap for point-coupled ring resonators [91] or coupling length, L_c, of a racetrack resonator [57]. The critical coupling condition for a ring resonator as depicted in Fig. 4.3 is reached when [91]:

$$|k_1|^2 = 1 - |at_2|^2 \tag{4.5}$$

The amplitude transmission a is related to the power attenuation coefficient α [1/cm] by $a^2 = e^{-\alpha L}$. The power attenuation coefficient α is sometimes also given in [dB/cm]. The two are related by:

$$\alpha_{[1/m]} = 100 \frac{\alpha_{[dB/cm]}}{10 \cdot \log_{10}(e^1)} \tag{4.6}$$

The coupling coefficient κ_1 (in Eq 4.5), is defined as the cross-coupling coefficient (the subscript refers to the individual coupling region in a double bus ring), and t_2 is defined as the transmission coefficient (or self-coupling coefficient). If there is no loss in the coupling region then $t^2 + \kappa^2 = 1$ and therefore the t^2 and κ^2 can be seen as the power splitting ratios. For accurate simulations of resonance width, the losses in the coupling region needs to be included in the roundtrip loss (or transmission) coefficient a. The critical coupling condition (Eq. 4.5) states that the power coupled into the ring is equal to the power loss inside the ring. If the attenuation is negligible ($a \approx 1$), critical coupling occurs for $\kappa_1 = \kappa_2$. It is easier to design a racetrack resonator (with a straight waveguide coupling region) as the coupled mode theory can be used, whereas point couplers require fully-vectorial 3D modeling.

Coupling region

Coupling from one straight waveguide to a second waveguide in proximity can be determined using coupled mode theory and supermode analysis (or eigenmode expansion analsyis) [97, 249, 250]. The two eigenmodes of the coupled parallel waveguides (symmetric and anti-symmetric supermodes) as shown in Figs. 4.5(a) and 4.5(b) have slightly different effective refractive indices. That difference in propagation constant causes the modes to interfere constructively and destructively in the waveguides. For long parallel waveguides the power oscillates from the main waveguide to the coupled waveguide and back. Assuming that all the power is in the main waveguide at $z = 0$ the fraction of power in the second waveguide is then given by:

$$|\kappa|^2 = \frac{P_2(z)}{P_0} = \sin^2(C \cdot z) = \sin^2\left(\frac{\pi \cdot z \Delta n}{\lambda_0}\right) \tag{4.7}$$

where P_0 is the power at $z = 0$ and C is the coupling coefficient (not to be confused with the field coupling coefficient κ). The cross over length, L_x, is defined as the distance after which all the power is transferred to the coupled waveguide. The crossover length is dependent on the wavelength λ and the distance between the waveguides, g, and is given by:

$$L_x(\lambda, g) = \frac{\lambda}{2 \cdot \Delta n(\lambda, g)} = \frac{\pi}{2 \cdot C} \tag{4.8}$$

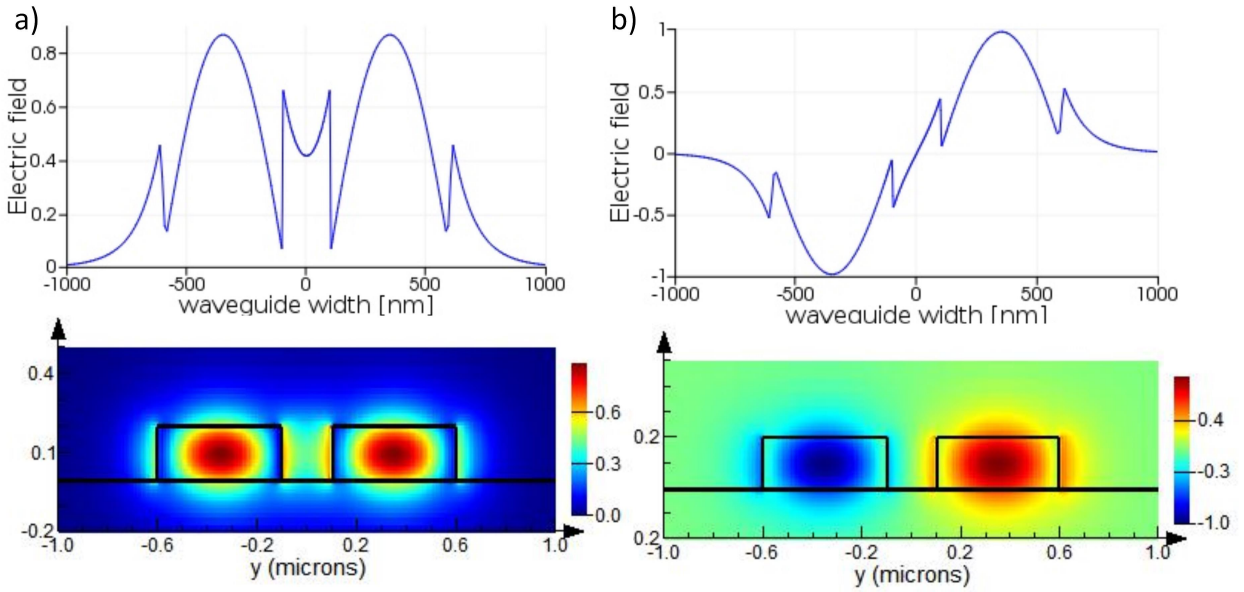

Figure 4.5: Mode profile of supermodes in directional coupler with geometry waveguide width $w = 500$ nm, waveguide thickness $t = 220$ nm, coupling gap $gap = 200$ nm. a) symmetric mode profile ($n_1 = 2.336$) and; b) anti-symmetric mode profile ($n_2 = 2.323$).

The mode profiles of the symmetric and anti-symmetric supermodes are shown in Fig. 4.5 for a coupling gap $g = 200$ nm, and waveguide dimensions of $w = 500$ nm and $h = 220$ nm. The effective index of the symmetric super-mode is $n_1 = 2.336$ and the for the anti-symmetric mode it is $n_2 = 2.324$ and the resulting index difference is $\Delta n = 0.012$. For a wavelength $\lambda = 1.55$ µm the crossover length is therefore $L_x = 62.8$ µm. In practice, the parallel waveguides in the coupling region are connected to waveguide bends which also contribute to the coupling between waveguides. In the extreme case of a point coupled ring with coupling length $L_c = 0$, light is still coupled from one waveguide to the other. To include the contribution of the bend region Eq. 4.7 is extended and can now be fitted to measurement data to extract the coupling length [52] and the extra effective coupler length z_{bend}. Using

Eq. 4.8 the field coupling coefficient is then given by:

$$|\kappa|^2 = \frac{P_2(z)}{P_0} = \sin^2\left(\frac{\pi}{2L_x} \cdot [z + z_{bend}]\right) \tag{4.9}$$

In a similar way the transmission can be understood as the power remaining in the original waveguide and can be written as:

$$|t|^2 = \frac{P_2(z)}{P_0} = \cos^2\left(\frac{\pi}{2L_x} \cdot [z + z_{bend}]\right) \tag{4.10}$$

This set of equation assumes a lossless coupler satisfying $\kappa^2 + t^2 = 1$.

MODE Solutions was used to compute the effective indices (super modes, straight and bend waveguides). The results from MODE and experimental propagation loss was imported into MATLAB to find κ from Eq. 4.7 so that $|\kappa_1|^2 = 1 - |at_2|^2$. The script employed analytic functions previously presented by our group [251] to determine these values. For a ring resonator with radius $R = 30$ µm the length of the coupling region should be $L_c = 8.57$ µm for a critically coupled double bus ring with $g_1 = 200$ nm and $g_2 = 300$ nm. Fig. 4.4 shows a simulated transmission spectrum compared to an actual measurement. The insertion loss of the grating coupler and propagation loss of the routing waveguides is adjusted manually to have similar baselines. The effective index required slight adjustment (to match the resonance condition) to compensate for fabrication variations or different temperature conditions.

In an effort to accurately simulate the waveguide geometry and account for any discrepancies between fabrication and design, Scanning Electron Microscope (SEM) images were taken of the design. In order to image the waveguide cross-section and estimate the sidewall slope of the waveguides, a Focused Ion Beam (FIB) was used to mill trenches over a straight waveguide as well as two coupler regions (one of 200 nm waveguide spacing and the other of 400 nm waveguide spacing). After FIB milling, the waveguides were imaged with a 52^o tilt to observe their cross-sections. The pixel lengths of the waveguides were then compared with the pixel length of the scale bar to determine the widths of the top and bottom of the waveguides; the coupler gaps were determined with a similar method. The average of five measurements was used as the waveguide dimensions for simulation. Only one measurement

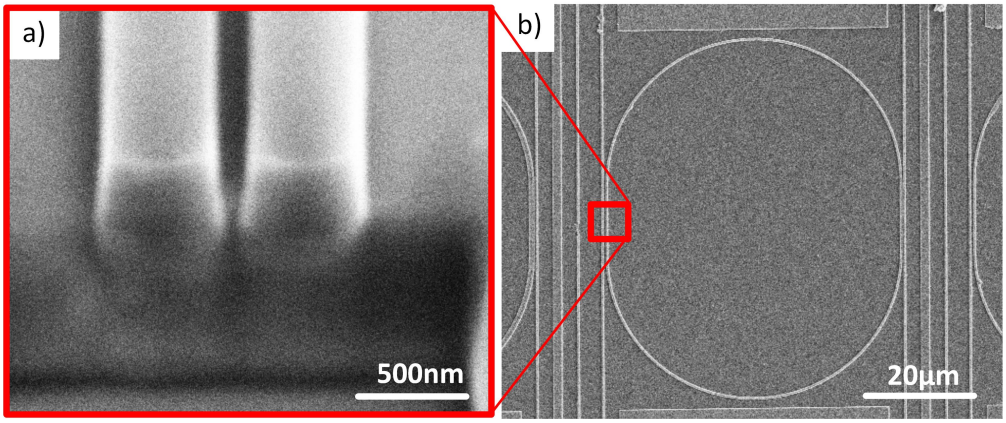

Figure 4.6: SEM image of a) cross-section of coupling region with $gap = 150$ nm and b) ring resonator with radius $R = 30$ µm.

was obtained for each of the coupler gaps. It was determined that the 220 nm (as verified by profilometry) silicon layer was approximately 470 (±17) nm wide at the top edge and 575 (±11) nm wide at the SiO_2 interface, indicating a sidewall angle of approximately 14^o ($\pm 2^o$). The coupler gaps at the SiO_2 interface were determined to be approximately 113 nm for the 200 nm coupler gap design and 327 nm for the 400 nm coupler gap design. The coupler geometries were imported into Lumericals MODE Solutions to simulate the mode profiles and coupling coefficients (see Fig. 4.5) .

4.3.2 TM mode ring resonators

TM mode ring resonators offer unique properties which are advantageous for biosensing applications. The sensitivity (both surface and bulk) is largely dependent on the overlap of the electric field with the analyte as described in Sec. 2.2.2. Waveguides guiding TM mode light offer three times the sensitivity over the TE mode at 1.55 µm in a 220 nm thick SOI waveguides [252] due to their larger evanescent field component traveling above the waveguide. In addition, TM modes experience less scattering loss because the mode's electric field is guided above the waveguide in the cladding and below in the substrate.

Therefore, scattering losses resulting from sidewall roughness due to fabrication is avoided (unlike TE modes).

Design

Figure 4.7a shows the electric field intensity of the fundamental TM mode traveling in a 220 nm x 500 nm waveguide. Figure 4.7(b) shows the simulated sensitivities of a TM

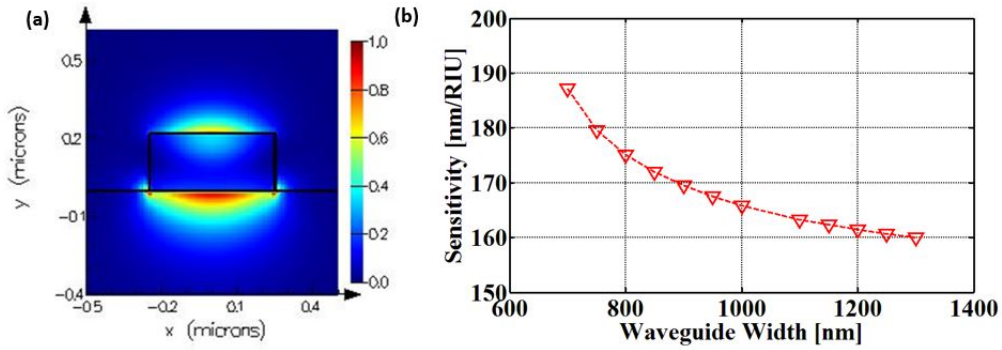

Figure 4.7: TM mode ring resonator simulation results. (a) Electric field intensity of a TM mode in a 220 nm x 500 nm silicon waveguide. (b) Simulated sensitivity versus waveguide width for TM modes

mode in a 220 nm thick silicon waveguide as the waveguide width varies. Mode profiles and effective refractive index was simulated in MODE Solutions. MODE was also used to calculate bending and mode-mismatch loss. Propagation losses were estimated based on our previous experimental results [52]. These values were used in an analytical MATLAB model to optimize the racetrack resonator coupling length to achieve critical coupling. The surface sensitivity is simulated with 10 nm thick adlayer with a refractive index of $n_{ad} = 1.48$. The devices were fabricated and characterized as described in Section 4.2.

Results

TM mode ring resonators with waveguide thicknesses of 150 nm and 220 nm were fabricated using 193 nm deep-UV lithography and dry etching at IMEC through ePIXfab multi-project wafer service. Figure 4.8(a) shows the microscope image of the fabricated, 40 µm radius TM racetrack ring resonators (along with other TE mode rings and disk resonators). The sensors were characterized using methods described in Sec. 4.2.1. The resulting spectra when subjected to the refractive index solutions or characterization are shown in Fig. 4.8(b). Plotting these resonant wavelength shifts against the measured refractive index of the solution set is the sensitivity shown in Fig. 4.8(c).

The sensitivity of the 220 nm thick waveguide ring was measured to be 147 nm/RIU with a quality factor of 9,200 and $iLoD$ of $7.09 \cdot 10^{-4}$ RIU (Fig. 4.8(c). The sensitivity of the 150 nm thick waveguide ring was measured to be 238 nm/RIU with a quality factor of 1,914 and $iLoD$ of $3.28 \cdot 10^{-3}$ RIU. The thinner, 150 nm waveguide, confines less of the TM mode and results in a greater evanescent field in the cladding and higher sensitivity. The 150 nm thick waveguide ring's quality factor could be increased as simulations show that the ring may be over coupled. As expected, TM modes (in general) provide higher sensitivities than their TE mode ring counterparts (54 nm/RIU). Furthermore, the simulated surface sensitivity for a protein adlayer with $n_{ad} = 1.48$ was 312 pm/nm for the 220 nm thick waveguide and 243 pm/nm for the 150 nm thick waveguide.

A bio assay (as described in Section 4.2.1) was performed to assess the TM mode ring resonator's biosensing performance. The results are shown in Fig. 4.8(d). Protein A was passively adsorbed to the chip off-line creating a thin film on which to immobilize the capture antibody, antiSA. The unintended introduction of an air bubble mid-way through the antiSA rinse cycle (Region B) is indicated by the red-dashed vertical line although it does not impact the viability of the biological species. The slight negative shift in resonant wavelength after the BSA block and challenge (Region C) suggests that a small portion of the antibody adlayer lifts off but the original sensor coverage (Region B) was robust. The binding of SA (Region

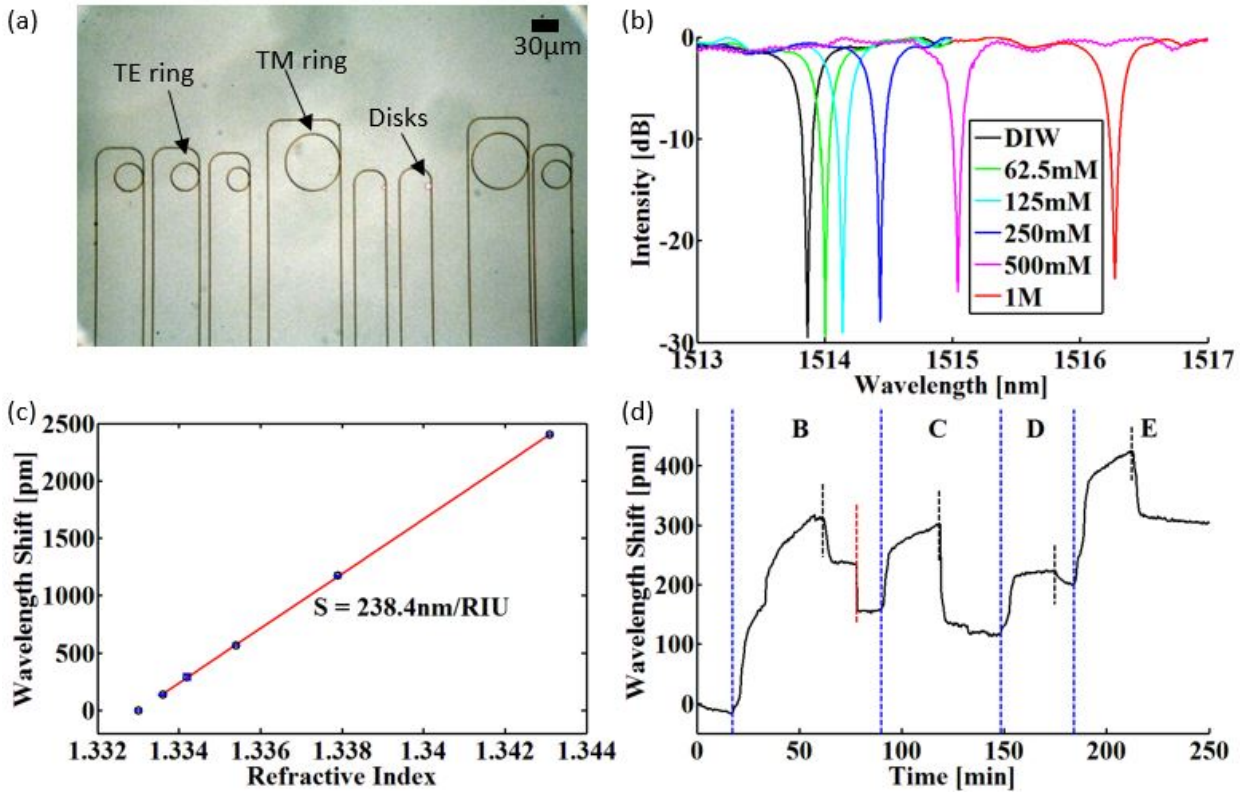

Figure 4.8: Experimental results for the TM mode ring resonator. (a) Microscope image of the TE and TM mode ring resonator set. (b) Transmission spectra showing the resonant peak shifts when subjected to a NaCl RI solution set. (c) Sensitivity response measured for the RI solution set of (b) resulting in a sensitivity of 238 nm/RIU. (d) Biosensing demonstration using a model biological system; Regions B, C, D, and E are described in Section 4.2.1; air-bubble during the rinse cycle between regions B and C (indicated by the red-dashed, vertical line).

D) and subsequent amplification using bBSA (Region E) result in permanent resonant shifts as expected.

4.3.3 Thin TE mode ring resonator

Using thinner waveguides leads to lower confinement of the propagating TE mode and results in deeper penetration of the evanescent field into the cladding, offering enhanced sensitivity and more field overlap with biomolecules on the waveguide's surface. Based on these advantages, we fabricated and experimentally assessed TE mode ring resonators with varying thicknesses available through MPW foundries (90, 150, 220 nm) for biosensing applications [57].

Design

Figure 4.9(a)-(c) illustrates the mode profile of the propagating TE mode in waveguides for a range of silicon thicknesses, namely 90, 150, and 220 nm. The evanescent field in the cladding medium decays exponentially as a function of distance from the silicon core. The point where the evanescent electrical field decays to 1/e of its initial value is called the penetration depth (d_e) as defined in chapter 2.2.1 in Eq. 2.8. Various effective refractive indices for various waveguide thicknesses and widths were calculated using Lumerical MODE solutions. These values were used to calculate the penetration depths of the electric field which are plotted in Fig. 4.9(f). The sensitivities of these resonators were calculated based on Eq. 6.1, and Lumerical MODE solutions was used to calculate $\delta n_{eff}/\delta n_{clad}$ for each case of waveguide thicknesses and widths. The resulting sensitivities are plotted in Fig. 4.9(d). Figure 4.9(e) shows simulated results for temperature sensitivity for the various waveguide dimensions. MODE was also used to simulate surface sensitivities for each of the waveguide thicknesses with the assumption that the refractive index of the adlayer is $n_{ad} = 1.48$.

To validate these calculations, we designed, fabricated, and compared racetracks with waveguide thicknesses of 90 nm, 150 nm, as well as the standard 220 nm. The devices were fabricated using 248 nm deep-UV lithography and dry etching at IME through a multi-project wafer run organized by CMC-SiEPIC, and characterized as described in Sec. 4.2.

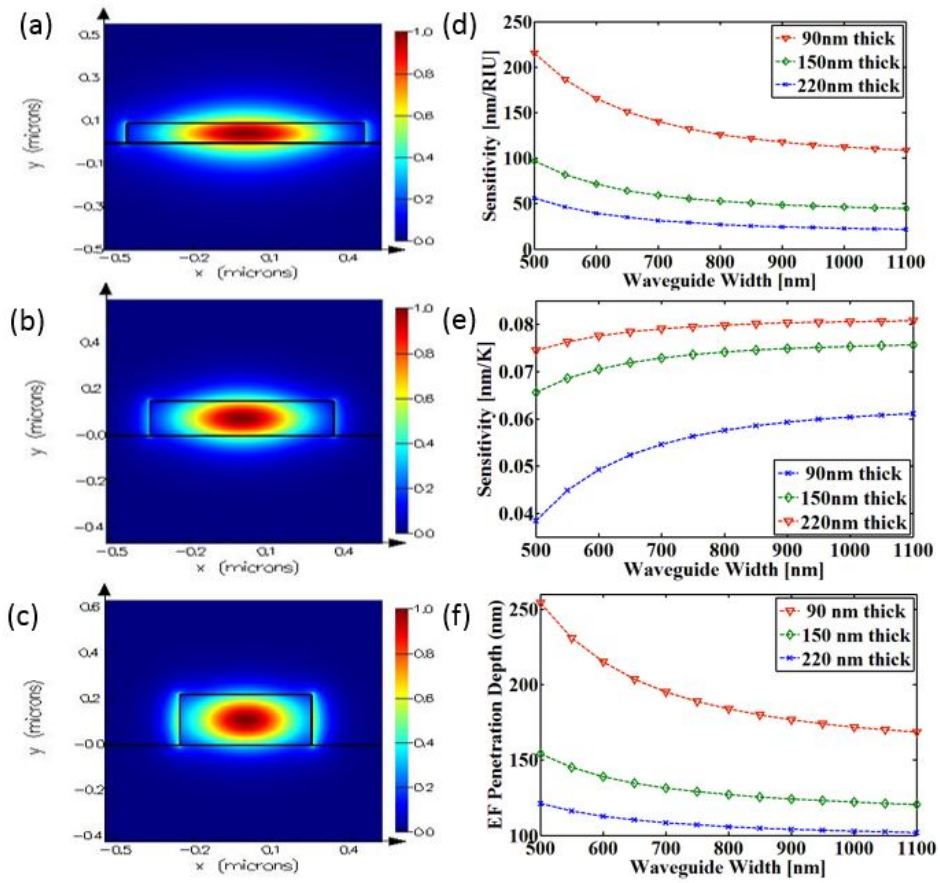

Figure 4.9: TE mode, thin ring resonator simulation results. (a) Electric field intensity of a TE mode for 90 nm thick silicon core (b) Electric field intensity of a TE mode for 150 nm thick silicon core (c) Electric field intensity of a TE mode for 220 nm thick silicon core (d) Sensitivity of TE waveguides for three different waveguide thickness, 90 nm, 150 nm, and 220 nm, (e) Temperature sensitivity for three different waveguide cross sections; (f) Simulated 1/e electric field penetration depth of the evanescent field into the solution for various waveguide core thicknesses and widths.

Characterization

Unlike the other sensors, the thin TE rings were subjected to different concentrations of D-Glucose (D16-500, Fisher Chemicals, Fisher Scientific, Inc.). The titrations range from

0 M to 110 mM. The refractive index of such solutions is estimated using $n_{glucose}(\lambda) = n_{H_2O} + 1.515 \cdot 10^{-6} c_{glucose}$ [253]. Sensors were exposed to the solutions at a flow rate between 5-15 µL/min to measure quality factors (Q), the bulk RI sensitivity (S), and the detection limit (iLoD).

Results

Figure 4.10(a) shows the SEM image of our ultra-thin racetrack resonator (fabricated using ebeam). The slope of the dashed and red lines in Fig. 4.10(b)-(d) show the sensor's response when subjected to different refractive index solutions. Sensors with a waveguide thickness of 220 nm, 150 nm, and 90 nm results in sensitivities of 38 nm/RIU (ebeam), 83 nm/RIU (foundry), and 153 nm/RIU (foundry), respectively. The 90 nm thick waveguide's quality factor in water was measured at 9,200 yielding an $iLoD$ of $1.11 \cdot 10^{-3}$ RIU, while the 150 nm thick waveguide sensor had a quality factor of 14,000 and $iLoD$ of $1.33 \cdot 10^{-3}$ RIU, and the 220 nm thick waveguide had a quality factor of 15,000 and $iLoD$ of $2.72 \cdot 10^{-3}$ RIU. Furthermore, the simulated surface sensitivity for a protein adlayer with $n_{ad} = 1.48$ was 160 pm/nm, 212 pm/nm, and 289 pm/nm for a waveguide with width $w = 500$ nm and with thicknesses of 220 nm, 150 nm, and 90 nm, respectively. These results show that the most commonly used waveguide thickness of 220 nm for datacom applications is not optimized for sensing applications. In addition, a carefully design waveguide for biosensing would also involve finding the optimal width.

4.3.4 Subwavelength grating ring resonators

In this section, we report on the biosensing performance of a sub-wavelength grating (SWG) ring resonator, resulting in a 2X sensitivity improvement over the best TM ring / slot rings. The SWG waveguide consists of small strip waveguide segments (periodic arrangement of silicon blocks) rather than a continuous strip waveguide. But because of the small period, Λ, relative to the wavelength of the propagating light ($\Lambda < \frac{\lambda}{2 \cdot n_{eff}}$), the SWG waveguide behaves as if it is continuous. The propagation properties of the light depends on the period and the

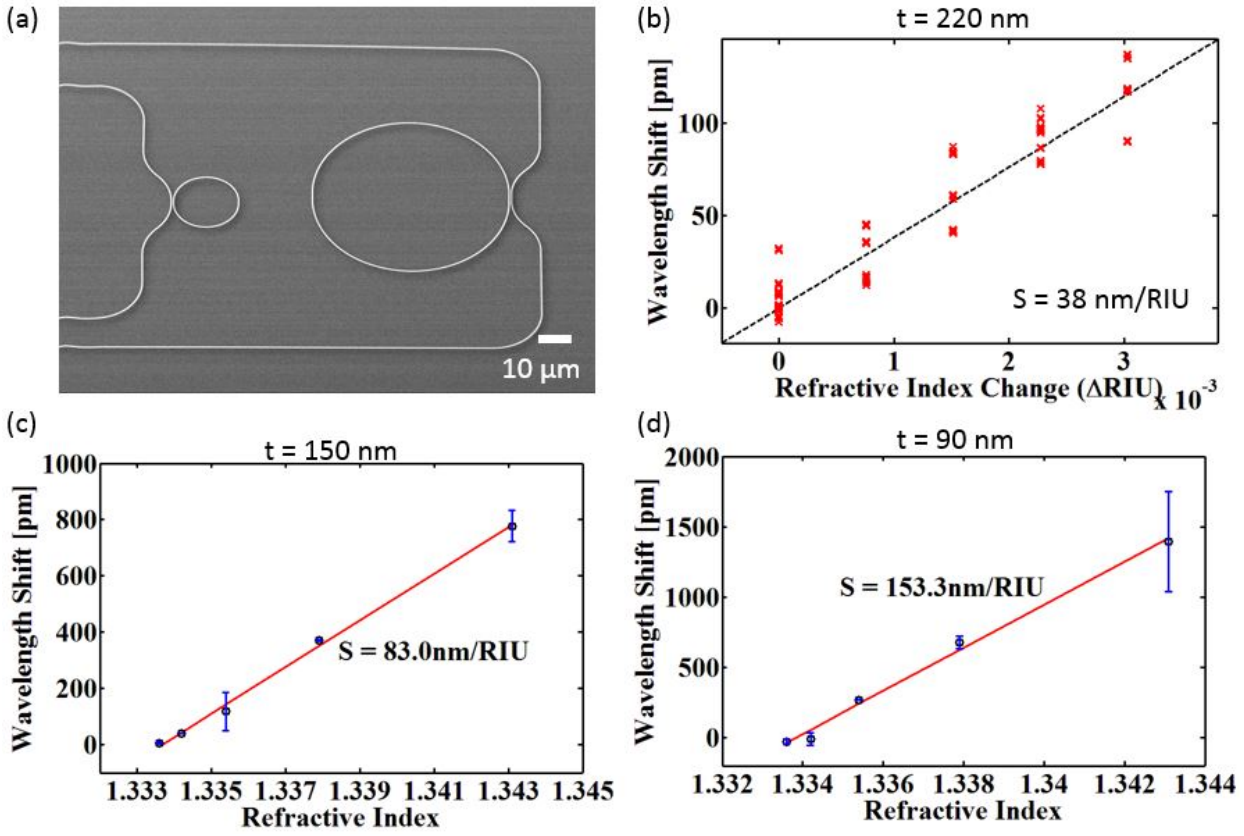

Figure 4.10: Experimental results for the thin waveguide TE mode ring resonators. (a) SEM image of 90 nm thick (10 µm radius) and 220 nm thick silicon (30 µm radius) TE mode ring resonators fabricated using ebeam lithography [57].(b) Measured sensitivity (38 nm/RIU) of a 220 nm thick TE sensor (ebeam chip) [57] (c) Measured sensitivity (83 nm/RIU) of a 150 nm thin waveguide TE sensor (foundry chip). (d) Measured sensitivity (153 nm/RIU) of a 90 nm ultra-thin waveguide TE sensor (foundry chip).

duty cycle of the grating. Sub-wavelength grating waveguides allow the designer to engineer the effective index of the guiding structure to minimize loss, enhance guiding capabilities, and more importantly improve the field overlap with biomolecules on the waveguide's surface. Sub-wavelength gratings in SOI waveguides have recently been proposed by the National Research Council of Canada (NRC) [254–256].

Design

A SWG ring resonator sub-circuit consists of strip-to-SWG converter [257], straight-to-bent SWG waveguide directional coupler, looped-back bent SWG waveguide to create the resonant structure. The coupling coefficients for the directional coupler were estimated from 3D FDTD simulations. 3D FDTD simulations were also used to simulate the propagation properties of the SWG waveguides. We make use of the periodicity, by simulating only one unit cell with Bloch boundary conditions. This approach is borrowed from band structure calculations of photonic crystals [258, 259] and we have used this method previously to determine coupling coefficients in SOI Bragg gratings [260]. SWG rings with radius of 20 µm and 30 µm, duty

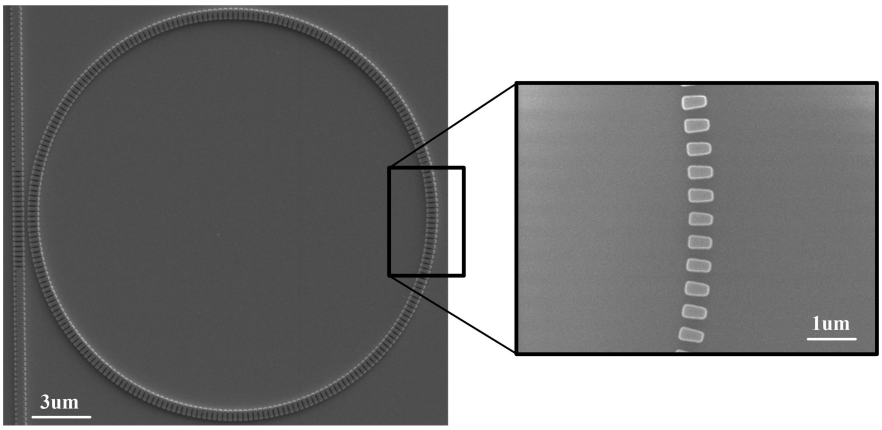

Figure 4.11: SEM image of SWG ring resonator fabricated by Ebeam lithography. Waveguide geometry: $w = 500\ nm$, grating period $\Lambda = 250\ nm$, waveguide thickness $t = 220\ nm$, and duty cycle $\eta = 0.7$.

cycles $\eta = [0.5, 0.6, 0.7]$, and coupling gaps $g = [200, 250, 300, 350, 400]$ nm were fabricated and characterized to determine the optimal design parameters for biosensing applications. SWG photonic circuits were realized on a 220 nm thick SOI wafer (SOITec, Grenoble, France) using a JEOL JBX-6300FS Direct Write E-Beam Lithography System at the University of Washington's Nanofabrication Facility (WNF). Figure 4.11 shows a SEM image of a SWG ring resonator with the following design parameters: waveguide width $w = 500$ nm, grating

period $\Lambda = 250$ nm, waveguide thickness $t = 220$ nm, and duty cycle $\eta = 0.7$. Devices were characterized as described in Sec. 4.2.

Results

Figure 4.12(a) shows the measured transmission spectrum of the SWG ring exposed to ultra-pure water and the refractive index solution standards. The chip stage is thermally tuned to 25 ^oC to limit thermal drift. For each concentration the optical spectrum was measured ten times to ensure repeatability and signal stability. The resulting stepped, resonant wavelength shifts are shown in Figure 4.12(b).

The group index, n_g, of the waveguide can be extracted from the free spectral range (FSR) of a ring resonator given by $n_g = \frac{\lambda^2}{FSR \cdot L}$ with L the ring resonator round trip length ($L = 2R\pi$). For the SWG ring resonator with radius $R = 30$ µm and duty cycle $\eta = 0.7$, the $FSR = 3.936$ nm and the corresponding group index $n_g = 3.27$. For a ring with the same radius but different duty cycle of $\eta = 0.6$, results in a $FSR = 4.54$ nm and group index of $n_g = 2.81$. The slope of the resonant wavelength shifts per refractive index standard is the bulk sensitivity of the sensor, as shown in Figure 4.12(c). The SWG ring with duty cycle $\eta = 0.6$ yields a bulk sensitivity of $S_b = 491$ nm/RIU. Compared to regular TE ring resonators [25, 40] SWG ring resonators show an eight-fold increase in sensitivity, and compared to TM [20] a two-fold increase.

The measured quality factor factor of $3.9 \cdot 10^3$ and sensitivity of $S_b = 405$ nm/RIU result in a intrinsic limit of detection as described by Chrostowski *et al.* [103] of $iLoD = \Delta n_{min} = \frac{\lambda}{QS_b} = 8.1 \cdot 10^{-4}$ RIU. The minimal detectable wavelength shift of our probe station used to characterize biosensors is $\Delta\lambda_{min} = 1$pm, which translates into a system detection limit $sLoD = 2.01 \cdot 10^{-6}$ RIU. The surface sensitivity is simulated to be 789 pm/nm.

A sandwich assay involving well characterized biomolecules with high binding affinities (as described in Section 4.2.1) was used to evaluate the biosensing performance of the SWG ring. The results are shown in Fig. 4.12(d). Protein A was passively adsorbed to the chip off-line creating a thin film on which to immobilize the capture antibody, antiSA (Region A). The

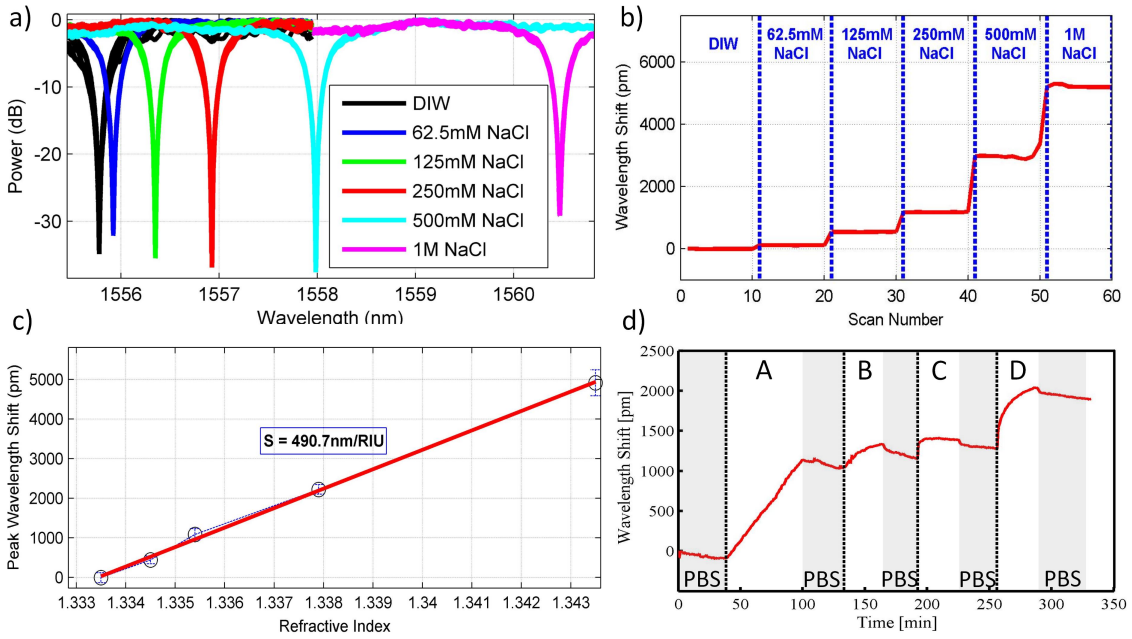

Figure 4.12: a) Transmission peak for a ring with $R = 30$ µm, $w = 500$ nm, $\Lambda = 250$ nm, $\eta = 70$ %, $t = 220$ nm, and gap $g = 400$ nm exposed to different solutions of NaCl; b) reported peak wavelength shift; c) Measured wavelength shifts vs refractive index. The slope indicates the bulk sensitivity; and d) Biosensing experimental results: Region A = anti-streptavidin (antiSA) (10 µg/mL), B = Bovine Serum Albumin (BAS) (20 µg/mL), C = streptavidin (SA) (20 µg/mL), and D = biotinylated-BSA (50 µg/mL). After each reagent the sensor is washed with PBS, indicated by the grey area mid-way through each region.

adsorption of this 160 kDa protein results in a 1.5 nm resonant wavelength shift. The linear increase suggests that the affinity reaction is transport limited rather than reaction limited. To show that subsequent molecular binding interactions are specific, BSA (20 µg/mL) was introduced to block any remaining exposed sensor area, as shown in Region B. The slight wavelength shift offset at the end of the Region B rinse step suggests adsorption of BSA as a result of incomplete coverage of the Protein A - antiSA complex [159]. The permanent resonant shift observed during the PBS rinse cycle (region C) suggests specific and irreversible

binding of SA to antiSA. This step also indicates that the antiSA bound to the Protein A retains its bioactivity and specificity. The final step (Region D) further demonstrates the biological specificity of the captured SA while amplifying overall wavelength shift.

These results show that we can achieve $\approx$ 10X enhanced sensitivity over their slab-based TE mode waveguide counterparts. This achievement expands their use in applications that require greater sensitivities and detection limits then what can be achieved today.

4.4 Micro-disk resonator biosensors

4.4.1 Theory of operation

Micro-disk resonators share a similar design theory and approach to strip waveguide ring resonators but utilize a circular plate (or disk) for the resonant cavity instead of a single-mode waveguide (Fig. 4.13(a)). The most significant difference from ring resonators is that the optical mode travels along the disk's perimeter and is in contact with only one side-wall. This fact can decrease sidewall scattering, thus improving the quality factor [261, 262] and detection limit [21]. Disks can also support multiple modes beyond the fundamental TE and TM modes of most common waveguide geometries. In addition, due to the asymmetric coupling from a straight waveguide into a disk all the modes are excited for a given coupling gap and can exist simultaneously. This allows for differential sensing in a single device (i.e., TE and TM modes). However, because bending losses are higher for TM modes, larger disk radii are required for high-Q TM resonance peaks (simulated TM mode bending loss are reported to be around 4 dB/cm [263]). The mode's evanescent field overlap with the cladding determines the sensitivity. It is evident from the mode profiles in Fig. 4.13(b) that the TM mode electric field extends further into the cladding over similar TE modes. The distance at which the electric field intensity ($|E|^2$) has decayed to $1/e$ with respect to intensity at the waveguide's surface was estimated to be 60 nm for TE modes and 110 nm for TM modes, demonstrating the significant sensing advantage of TM modes for molecular adlayers or large biomolecules [103].

Additionally, disks have usually a smaller footprint (radii of 1.5-5 µm) [21]. A benefit of small footprints is that the biosensors can get closer to the size scale of the biological molecules and cells they interrogate than other silicon photonic biosensors. This can lead to lower mass-limits of detection given that each bound biomolecule will have a higher effect on the field distribution [24].

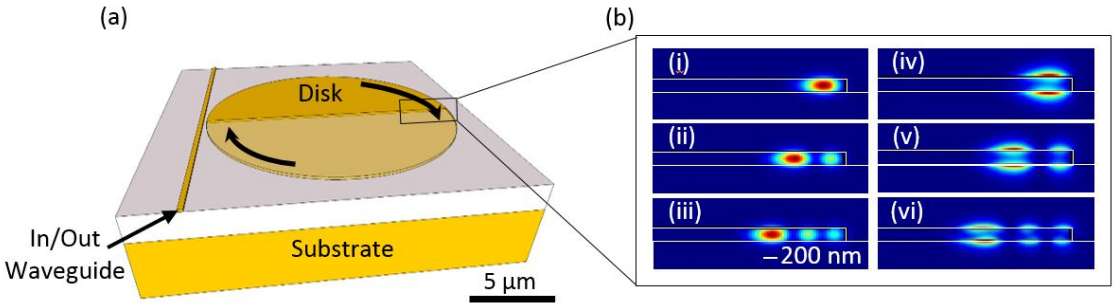

Figure 4.13: (a) 3D schematic of a disk biosensor on a SOI substrate. (b) Simulated mode profiles (electric field intensity) for a 10 µm disk. (i)-(iii) Show electric field profiles for the first three TE modes and (iv)-(vi) show the first three TM modes.

4.4.2 Design

We used a method previously demonstrated by our group [103] to calculate the expected Q's and coupling coefficients between the waveguide and resonator sensor. To determine optimal coupling, a 400 nm wide bus waveguide and a wide, bent waveguide to represent the disk (5 µm for 10 µm disks; 1.5 µm for 3 µm disks) was simulated using the FDTD method. Combining scattering loss values (10 dB/cm for the 3 µm disk and 1 dB/cm for the 10 µm disk which were obtained experimentally) and losses to water absorption, the optimal coupling distance was calculated to be 200 nm. Because TM modes are less confined within the waveguide than their TE counterparts, a larger radius (10 µm) was required, resulting in a disk that supported TE and TM modes simultaneously. Both 3 µm and 10 µm radius disk resonators were fabricated and characterized as described in Sec. 4.2.

4.4.3 Results

Both 3 µm and 10 µm radius disk resonators were realized on a CMOS-compatible 220 nm SOI substrate using ebeam lithography, characterized, and subjected to a model biological system to assess their biosensing capability using approaches described in Sec. 4.2.

The 3 µm radius disk supports TE modes only and results in a large FSR, which is advantageous for multiplexing many sensors on a single waveguide bus [264]. To evaluate multiplexing, we cascaded six disks on a single waveguide bus varying each disk's radius by 10 nm to avoid overlapping FSRs and ensure their resonant peaks occupy different locations within the spectra (as shown in Fig. 4.14(a)).

The fundamental TE mode (TE0) of the 3 µm disk had an observed quality factor of 33,000 and its resonant peak shifted when subjected to the refractive index solution standards (Fig. 4.14(b). We measured a sensitivity of 26 nm/RIU (Fig. 4.14(c) from which we calculated an $iLoD$ of $1.81 \cdot 10^{-3}$ RIU. The measured quality factor of the TE1 mode of the 3 µm disk was 22,000, with a sensitivity of 29 nm/RIU (Fig. 4.14(c) and $iLoD$ of $2.43{\cdot}10^{-3}$ RIU. The free-spectral range (FSR) range is 35-40 nm depending on the mode. Furthermore, the simulated surface sensitivity for a protein adlayer $n_{ad} = 1.48$ was 289 pm/nm and 75 pm/nm for the fundamental TM and TE mode respectively.

The sandwich assay described in Section 4.2.1 was used to assess the disk's biosensing performance and is shown in Fig. 4.14(d) for the TE1 mode. Simulations suggest that a 1 nm adlayer with a coverage of 51.9% of the sensor's surface would cause a shift of 30 pm (as we experimentally observed in Fig. 4.14(d). A 3 nm adlayer would only need to cover 17.1% of the surface to cause a similar wavelength shift (thicknesses of protein layers are difficult to measure). Assuming a monolayer of each protein, the relative resonance wavelength shifts for each bimolecular adlayer corresponds well to the expected shift based on their molecular weights [160, 161].

Experimental results for the 10 µm disks are shown in Fig. 4.15. The 10 µm disks fundamental TM yielded a sensitivity of 142 nm/RIU (Fig. 4.15(a)), quality factor of 16,000,

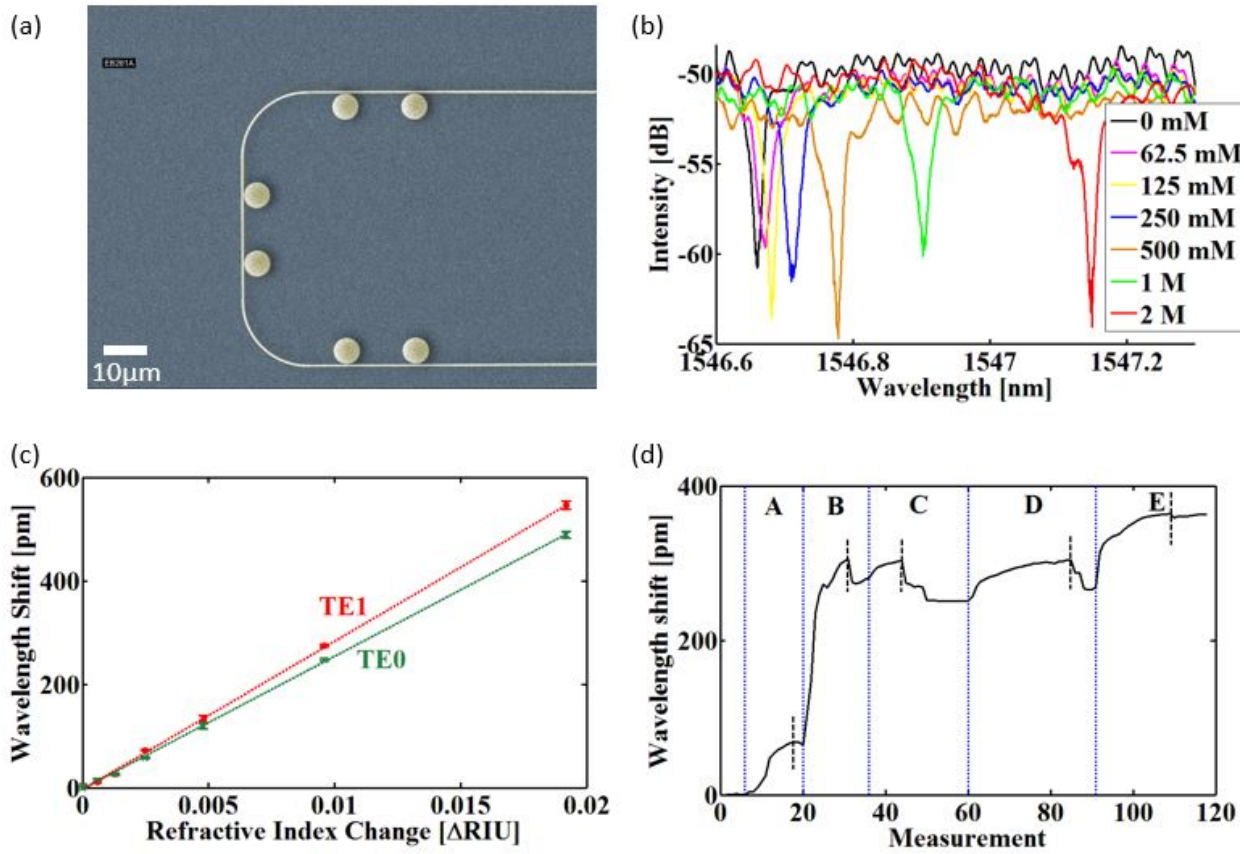

Figure 4.14: Experimental results for the 3 µm disk resonator. (a) False color SEM image of six, cascaded resonators on a single waveguide bus. (b) Transmission spectra showing the resonant peak shifts when subjected to a NaCl solution set. (c) Sensitivity response measured for the first two, supported TE modes (26 nm/RIU and 29 nm/RIU respectively). (d) Biosensing demonstration using a model biological system as described in Section 4.2.1.

and $iLoD$ of $6.82 \cdot 10^{-4}$ RIU. The TM mode had a FSR of 9.66 nm. The fundamental TE mode in the 10 µm disk yielded a sensitivity of 21 nm/RIU (Fig. 4.15(a), quality factor of 131,000, and $iLoD$ of $5.63 \cdot 10^{-4}$ RIU. Furthermore, the simulated surface sensitivity for a protein adlayer with $n_{ad} = 1.48$ was 289 pm/nm, and 75 pm/nm for the fundamental TM and TE mode, respectively. The biosensing capability of the 10 µm disk is shown in Fig.

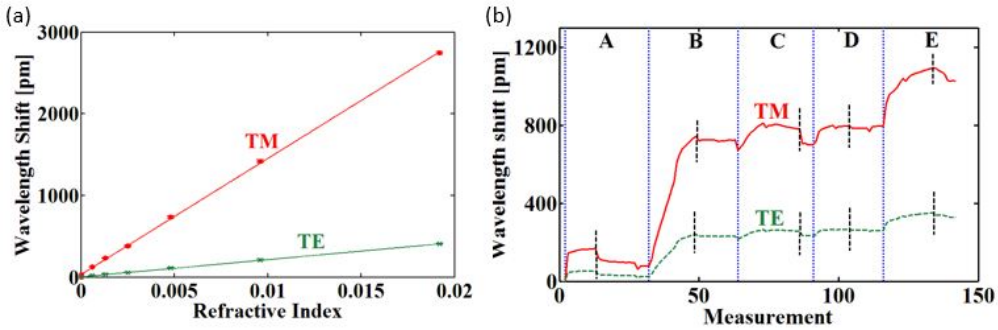

Figure 4.15: Experimental results for our 10 µm radius disk resonator. (b) Sensitivity response measured for the RI solution set of the first TM and TE modes (142 nm/RIU and 21 nm/RIU respectively). (d) Both mode responses to a biosensing demonstration using a model biological system as described in Section 4.2.1.

4.15(b). Simulations indicate that a 1 nm adlayer with 41.4% coverage of the sensor's surface would result in the (observed) wavelength shift of 98.5 pm for the TM mode in Region A. Similarly an adlayer of 3 nm thickness and coverage of 13.7% would have the same effect. Our simulated and experimental results are within the surface coverage ranges observed by Coen *et al.* for Protein A adsorption to a silicon dioxide surface. [159]

The TE mode quality factor in the 10 µm disk is much improved over that in the 3 µm disk due to the larger radii which provides reduced sidewall scattering and bending losses. Also, the larger evanescent field overlap with the cladding of the TM mode (Figs. 4.13(iv-vi)) should permit the detection of larger biomolecules (over their TE mode counterparts (Figs. 4.13(i-iii)). This differential detection capability may provide additional sensing information on the target molecule's size, distinguishing whole cell and protein-binding to the sensor surface. However, the multi-mode nature (TE and TM modes of multiple orders) of the 10 µm disks makes tracking resonant peaks difficult. Suppressing unwanted modes would improve the ease-of-use in tracking resonant peak shifts.

4.5 Bragg gratings

An important measure of performance is the detection limit which is defined as the minimum detectable RI change (see Sec. 2.2.2). Genalyte reports a detection limit of 1 ng/mL, or 10^{-5} RIU, while Barrios *et al.* and Claes *et al.* measure the detection limits on the order of $5 \cdot 10^{-6}$ RIU for slot waveguides. It is known from equation 6.3 that both a high quality factor and a high sensitivity will improve the detection limit. In ring resonators the quality factor is primarily limited by the bending loss, scattering loss from waveguide roughness, and mode mismatch loss. Bending losses can be eliminated by using resonant structures with only straight waveguide segments. Therefore Bragg gratings have been investigated for use in biosensing applications as well [202–204, 265]. They offer similar sensitivities as ring resonators but with a much smaller footprint. Jugessur *et al.* fabricated vertical side-wall TE mode Bragg gratings integrated with a reversibly bonded PDMS fluidic network estimating a sensitivity of $5.5 \cdot 10^{-3}$ nm in a sensing volume of 2 μm^3 [202]. They designed slotted Bragg gratings as well with a simulated sensitivity of 620 nm/RIU. However they did not report any experimental results confirming their theoretical values. Pbabhathan *et al.* designed and simulated similar vertical side wall TE mode gratings but introduced a period defect to create a resonance peak in the center of photonic stop band [203]. This section describes our effort to improve the sensing performance of Bragg gratings by investigating Bragg gratings for TE and TM polarized light on regular strip and slot waveguides and suspended waveguides.

4.5.1 Theory of operation

To avoid complicated fabrication steps, the desired index modulation is most commonly achieved using sidewall corrugations [266]. The design parameters of Bragg gratings are depicted in Fig. 4.16. The corrugation depth, d (the waveguide with variation, or Δw), and period (length of a single unit, Λ) modulate the effective refractive index.

This index modulation in a waveguide gives rise to a stop band in the transmission spectrum, similar to photonic crystals. The center wavelength of the stop band, λ_B is

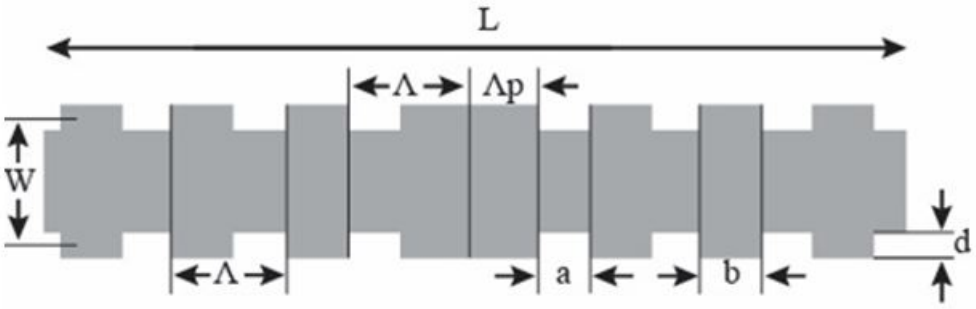

Figure 4.16: Design parameters for Bragg gratings: Λ is the period, a and b the individual segment lengths, Λp the phase shift ($p = 0.5$), w the average waveguide width, and L the grating length.

determined by the period of the index modulation, Λ according to the Bragg condition:

$$2\Lambda n_{eff} \;=\; m\lambda_B. \tag{4.11}$$

Here, the period is held constant but in a more general approach, the period (and corrugation width) could also vary as function of position in the grating to optimize the spectral response and dispersion of the grating [267, 268]. The duty cycle of the grating is 50% (a=b) and n_{eff} is the effective index of the waveguide with average width w. Fig. 4.17(a) and 4.17(c) show the effective index of a waveguide (width height 220 nm) for the TE and TM mode respectively. The phase shift, Λp with $p = 0.5$, forms a first-order Fabry-Perot cavity [97], resulting in a high-Q peak centered in the stop band. To limit the number of peaks inside the stop band to one, the phase shift length is equal to a grating period [269]. This peak resulting from the two Bragg-reflectors with length $L/2$ facilitates more robust peak tracking during biosensing experiments. The grating strength is given by [270]:

$$\kappa = \pi n_g \frac{\Delta\lambda}{\lambda_B^2} \tag{4.12}$$

where n_g is the group index and $\Delta\lambda$ is the bandwidth of the stop band. κ can be understood as the magnitude of the coupling between the forward and backward propagating mode [260] or

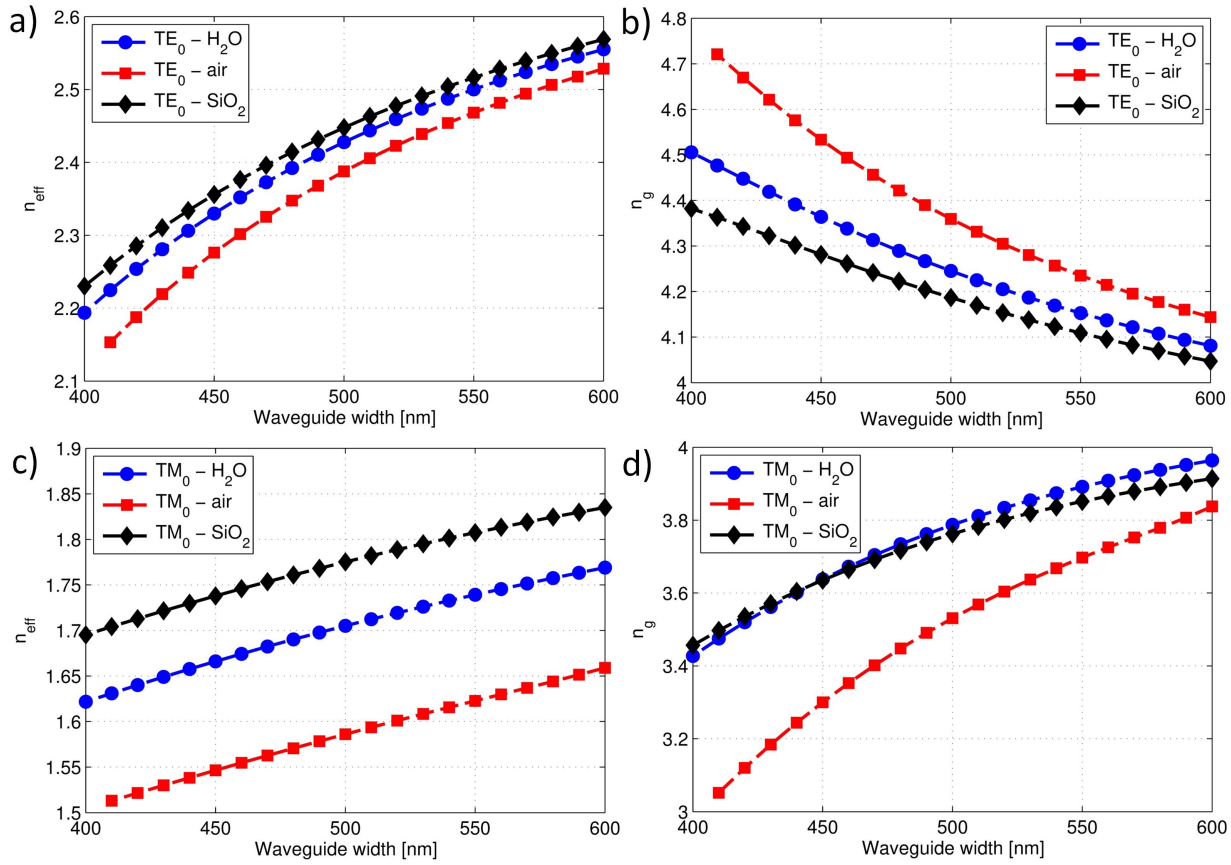

Figure 4.17: Propagation properties as function of waveguide width (and height of 220 nm) for air, H_2O, and SiO_2 cladding: a) Effective index for TE polarized light; b) group index for TE polarized light; c) Effective index for TM polarized light; and d) group index for TM polarized light.

as the field attenuation constant for the forward propagating mode. The coupling coefficient is used to calculate the reflectivity of the grating which is given by $R_{peak} = tanh^2(\kappa L)$ for the lossless case. The reflectivity is an important design parameter to optimize the quality factor of a resonance peak of a uniform grating with a phase shift at the center. Equation 4.12 is used to calculate the coupling coefficient from a measured stop band width in a transmission spectrum. The bandwidth, $\Delta\lambda$ is determined by the index modulation which in turn is

controlled by the corrugation depth. However because of lithography effects, especially when fabricated through DUV-lithography rather than ebeam, it is very challenging to simulate accurately the relationship between corrugation and coupling coefficient. Our group has characterized both TE and TM gratings for a number of fabrication processes [52, 260, 267, 269, 271]. Figure 4.17(b) and 4.17(d) show the group index of a waveguide (width height 220 nm) for the TE and TM mode respectively. Introducing a phase shift of half the grating

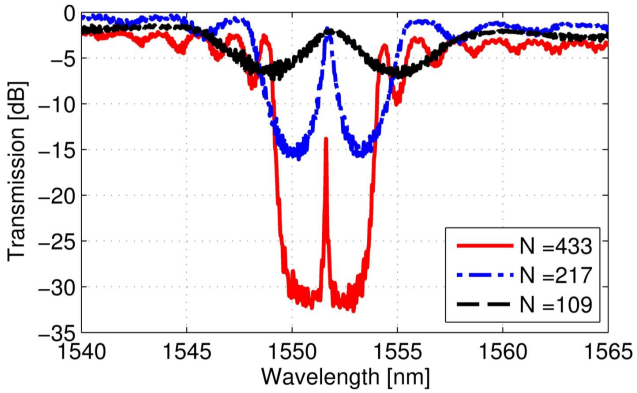

Figure 4.18: Measured transmission spectra for TM uniform gratings with phase shift for different number of periods ($L = N \cdot \Lambda$) on either side of the cavity, $N = [433, 217, 109]$]. The period $\Lambda = 416$ nm and the corrugation $\Delta w = 140$ nm are held constant. All gratings are fabricated through 193 nm lithography and have an average waveguide width $w = 500$ nm and are measured with air cladding.

period (Λp, see Fig. 4.16) in the middle of the grating leads to the appearance of a resonance peak at the center of the stop band. The grating on either side of the phase shift can be viewed as distributed mirrors creating a Fabry-Perot cavity. The quality factor (sharpness) of the resonance is determined by the grating strength and the cavity loss. It is approximated experimentally by dividing the resonant peak's wavelength (λ_{res}) by its full width at half its maximum (FWHM). The loss attributed to the mirror is determined by the reflectivity and dependent on the coupling coefficient κ and the length of the grating L (also sometimes given as the number of grating periods N, with $L = N \cdot \Lambda$). Figure 4.18 shows the transmission

spectrum for a uniform grating with period $\Lambda = 416$ nm, corrugation $\Delta w = 140$ nm and different grating length expressed as the number of periods. The quality factor varies from $Q \approx 500$ for the shortest grating ($N = 109$), $Q = 3.9k$ for $N = 217$, to $Q = 32.3k$ for $N = 433$.

4.5.2 Uniform strip-waveguide Bragg grating with phase shift for TE polarized light

Design

Strip waveguide Bragg gratings, similar to those shown in Fig. 4.19(a), were designed similar to Prabhathan et al. [203] and Jugessur *et al.* [202] (for TE mode) consisting of a straight waveguide, with an average width of 500 nm, with periodic side wall corrugations of 40 nm, and with a grating period (Λ) of 440 nm and duty cycle of 50% ($a = b$), resulting in 20 nm stop band [202, 203]. The TE mode field intensity distribution is shown in Fig. 4.19(b).

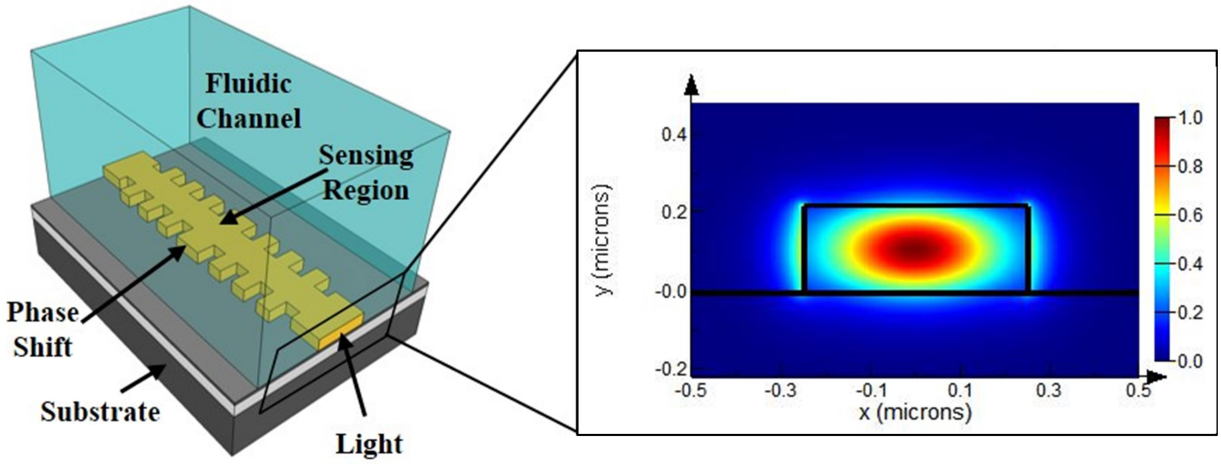

Figure 4.19: Strip waveguide Bragg grating biosensor. (a) 3D schematic rendering of a Bragg grating in a fluidic channel. (b) Electric field intensity distribution of a TE mode at the input of a Bragg grating waveguide.

The half period phase shift ($\Lambda p = 220nm$) at the center of the grating introduces a high

quality factor resonant peak (with water cladding at around 1.517 µm). With 100 pairs of gratings on each side of the phase shift the total footprint of the sensor is about 90 μm^2. The devices were fabricated and characterized as described in Section 4.2.

Results

Bragg gratings were fabricated on a 220 nm SOI wafer with a 2 µm buried oxide layer using 193 nm deep-UV lithography and dry etching at IMEC through the ePIXfab multi-project wafer service. Figure 4.20a shows an SEM image of the fabricated Bragg gratings. The sidewall corrugations depth of 40 nm modulates the effective refractive index leading to a stop band in the transmission spectrum. The grating period is 440 nm with a 50% duty cycle and the phase shift in the center is 220 nm (660 nm in total as shown in Fig. 4.20(a). Proximity effects during the lithography process are responsible for the resulting waved sidewall [272]. Using lithography simulation tools [273] this smoothing effect can be predicted [273].

Sensor characterization and a biosensing demonstration were performed as described by the methods in Section 4.2. Wavelength shifts of the resonance peak when subjected to the refractive index solutions are shown in Fig. 4.20(c) and resulted in a sensitivity of 59 nm/RIU (Fig. 4.20(b)). The resonance peak has a quality factor of 28,000 resulting in an $iLoD$ of $9.38 \cdot 10^4$ RIU. The surface sensitivity was simulated to be 160 pm/nm. Our model biological system assay, shown in Fig. 4.20(d), demonstrates its ability to sense and interrogate biomolecular interactions. Although the introduction of BSA in Region C shows a small permanent shift resulting from adsorption to exposed regions of the sensor, the subsequent binding steps involving SA (Region D) and bBSA (Region E) correlate well to expected results.

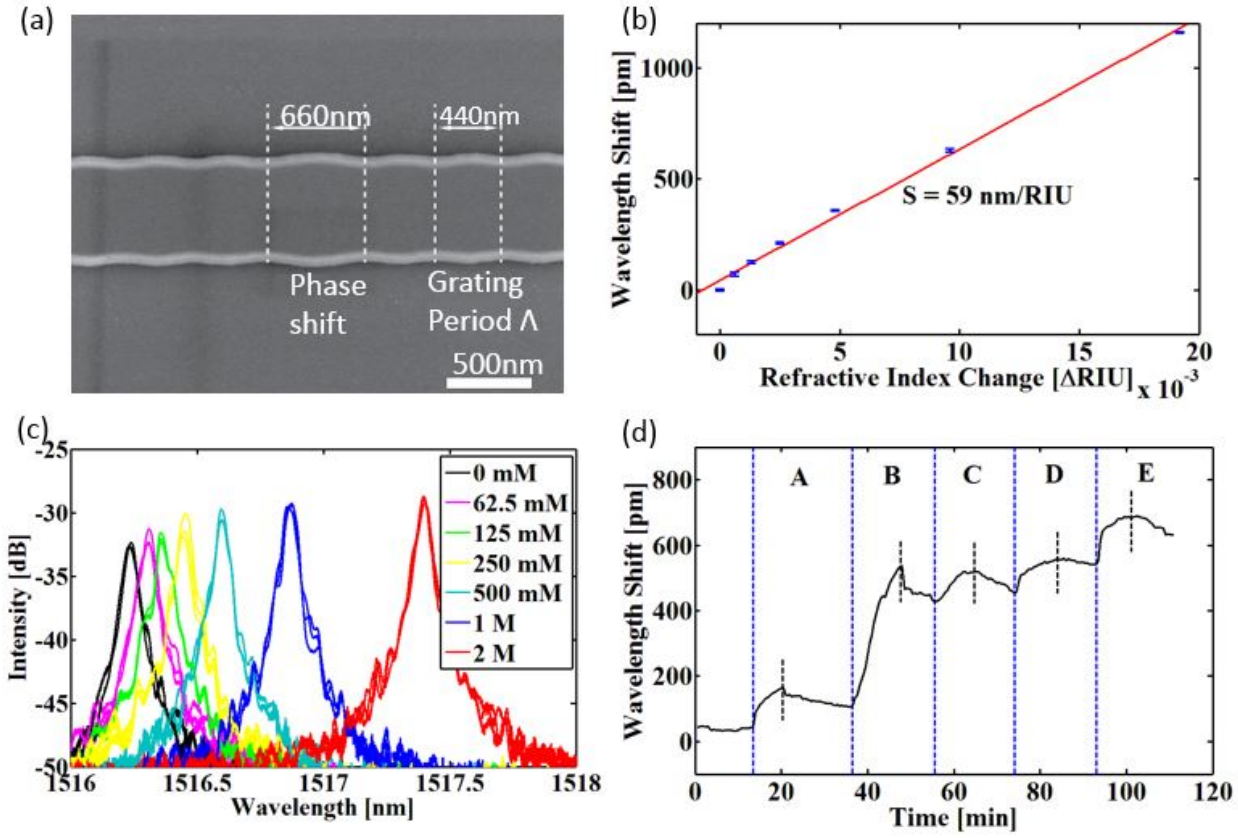

Figure 4.20: Experimental results for our TE mode strip-waveguide Bragg grating biosensor. (a) SEM image of the Bragg grating with the phase shift. (b) Transmission spectra showing the high-Q resonant peak shifts when subjected to a NaCl RI solution set. (c) Sensitivity response measured for the RI solution set. (d) Biosensing demonstration using a model biological system as described in Section 4.2.1.

4.5.3 Uniform slot-waveguide Bragg gratings with phase shift for TE polarized light

Design

Although the slot-waveguide Bragg design principles and theory are similar to their strip counterparts, the slot-waveguide configuration offers some unique advantages that have been investigated to enhance sensitivity for silicon photonic biosensors [29, 263, 274, 275]. In

slot-waveguide devices, the electric field intensity is concentrated between the waveguides (Fig. 4.21(a)), increasing the field and analyte overlap and resulting in 5-6X sensitivity improvement over their strip-waveguide counterparts [25, 29, 35]. Unlike rings, Bragg gratings do not suffer from bending losses that limit the performance of slot-ring resonators. The Bragg condition, susceptibility, and quality factor of slot-based sensors can be determined in a similar fashion to strip waveguide Bragg gratings.

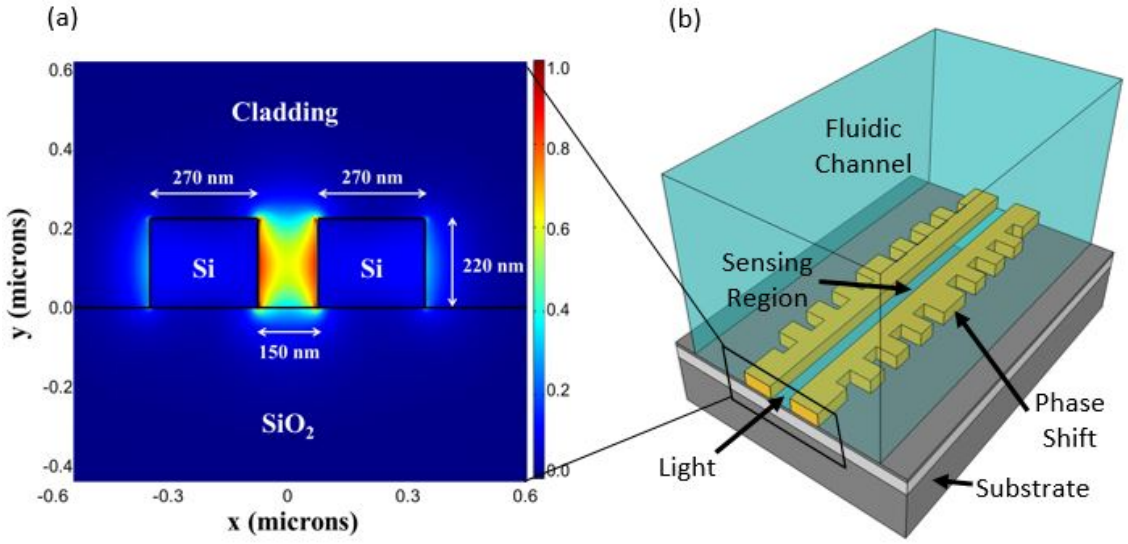

Figure 4.21: Simulation and design concept of a slot-waveguide Bragg grating biosensor. (a) Electric field intensity distribution of TE light showing the strong confinement of the TE mode in the slot between the waveguides. (b) A 3D schematic rendering of a slot-waveguide Bragg grating in a fluidic channel showing the phase shift and optimal sensing region.

We designed phase-shifted slot Bragg gratings similar to those shown in Fig. 4.21(b). Optimized design parameters resulting from simulations include 40 nm sidewall corrugations on the outside of the waveguide (270 nm average width), a slot gap of 150 nm, and a 600 nm long phase shift in the center which creates a high quality factor resonant peak within the stop band. The period on either side of the phase shift is 440 nm (150 periods on either side). The devices were fabricated and characterized as described in Section 4.2.

Results

Slot-waveguide Bragg grating sensors were fabricated on a CMOS-compatible SOI substrate with a 220 nm silicon layer on top of a 2 µm buried oxide layer at IMEC's ePIXfab foundry and is shown in Fig. 4.22(a). The 150 nm wide slot between two 270 nm wide, corrugated waveguides (arms), strongly guides the fundamental TE mode in the low-index cladding between the arms and results in high sensitivity and quality factor (Fig. 4.21(a)).

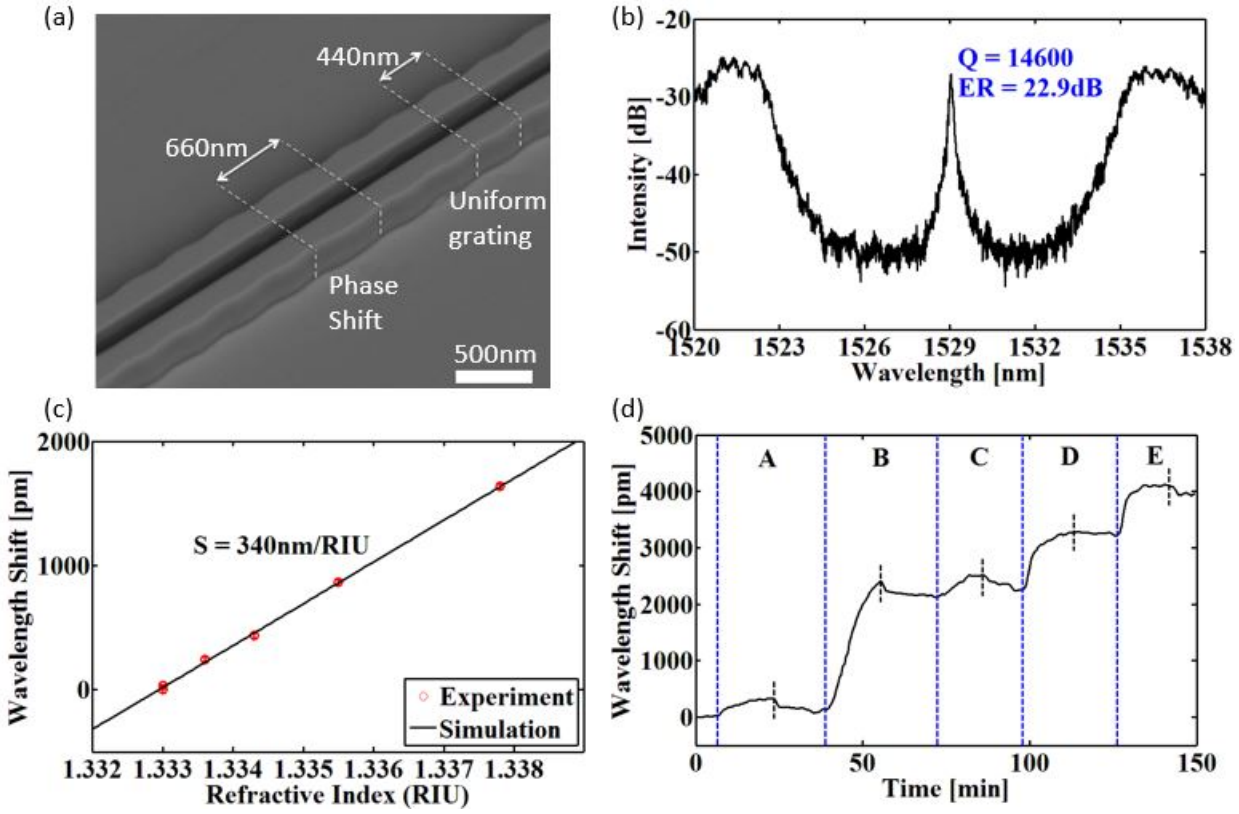

Figure 4.22: Experimental results for our TE mode slot-waveguide Bragg grating biosensor. (a) SEM image of the slot-waveguide Bragg grating with the phase shift. (b) Transmission spectrum showing the high-Q resonant peak within the stop band. (c) Sensitivity response measured after subjecting the sensor to a NaCl RI solution set. (d) Biosensing demonstration using a model biological system as described in Section 4.2.1.

The optimal corrugation depth for aqueous claddings is 40 nm (each arm width is 270±20 nm) with a grating period Λ of 440 nm and duty cycle of 50%, resulting in Bragg wavelength near 1.53 µm. A sharp resonance peak in the stop band was achieved by introducing a phase shift (Λp = 220 nm) in the middle of the gratings Fig. 4.21(b). With 150 pairs of gratings on each side of the phase shift; the sensor is about 132 µm long and results in a footprint of 132 µm^2.

Following the characterization procedure described in Section 4.2, NaCl RI solution standards were flowed over the sensor while tracking the peak location in the stop band. The observed shifts resulted in a sensitivity of 340 nm/RIU (Fig. 4.22(c) and quality factor of 15,000 (Fig. 4.22(b) the highest reported for slot-based biosensors to-date. Based on the quality factor and sensitivity, the $iLoD$ for this device is $3.04 \cdot 10^{-4}$ RIU, which is close to the theoretical limit of an ideal water-based resonator sensor operating at 1.55 µm wavelengths [103]. Furthermore, the surface sensitivity of the slot Bragg sensors was simulated to be 748 pm/nm. Finally, the sensor's biosensing capability is assessed using a modified sandwich assay which is shown Fig. 4.22(d). The BSA block and challenge in Region C results in a slight, permanent shift indicating that BSA adsorbed to exposed portions of the sensor. With a finite adsorption step for antiSA (Region B), it is reasonable to expect that portions of the sensor remain exposed at the start of the BSA challenge and subsequently adsorb BSA, especially when considering analyte transport challenges and limitations to the slot region between waveguides [29]. For the remaining steps, the relative resonance wavelength shifts for each captured biomolecule corresponded well to the expected shift based on their respective molecular weights [160, 161].

This sensor exhibits significantly higher Q's over slot-waveguide ring resonators since it does not suffer from bending losses or mode mismatch losses like rings. Using higher resolution lithography processes would further improve the performance of this sensor [203]. The IMEC foundry process required a larger than optimal slot dimension of 150 nm due to limitations of the fabrication process. Proximity effects during the lithography process result in wavy sidewalls [272] (observed in Fig. 4.22(a) and make it challenging when designing

Bragg gratings as lithography tools are required to predict the smoothing of the corrugations [273]. This is important as the corrugation determines the coupling strength of the grating and therefore the quality factor of the resonance peak. Finally, designing a similar sensor for 1.3 µm wavelengths, where loss to water absorption is reduced by an order of magnitude [276], should improve the $iLoD$.

4.5.4 Uniform strip-waveguide Bragg grating with phase shift for TM polarized light

Design

Strip waveguide Bragg gratings with sidewall corrugation were designed on a SOI substrate as described by Wang *et al.* [56, 266] and Chen *et al.* [267]. All designs were based on a SOI waveguide with width $w = 500$ nm and height $h = 220$ nm. MODE Solutions from Lumerical Solutions, Inc. was used to simulate the effective index of the waveguide and Bragg condition given in Eq. 4.11 was used to determine the required period, Λ, to center the stop band around $\lambda_B = 1550$ nm. As proposed by Wang *et al.* [260], a 3D finite-difference time-domain (FDTD) simulation on a single unite cell using Bloch boundary conditions in the direction of propagation, is employed to determine the coupling strength for a given corrugation width. Using this approach, an infinitely long grating can be studied without considering the whole structure and effects of design parameters (corrugation, period, thickness) on bandwidth ($\Delta\lambda$) and center of stop band (λ_B) can be verified. The devices were characterized as described in Section 4.2.

Results

To better understand fabrication limitation the gratings were fabricated using two methods: (1) Ebeam lithography and (2) a foundry service as part of a multi-project wafer organized by CMC Microsystems (Ontario, Canada). Since silicon photonic foundry processes cannot yet achieve the lithography resolution offered by direct-write systems using an electron beam [234, 236], topologies with higher resolution and accuracy could be evaluated using Ebeam

lithography instead. Foundry fabrication was done at IMEC, Belgium, via ePIXfab on a

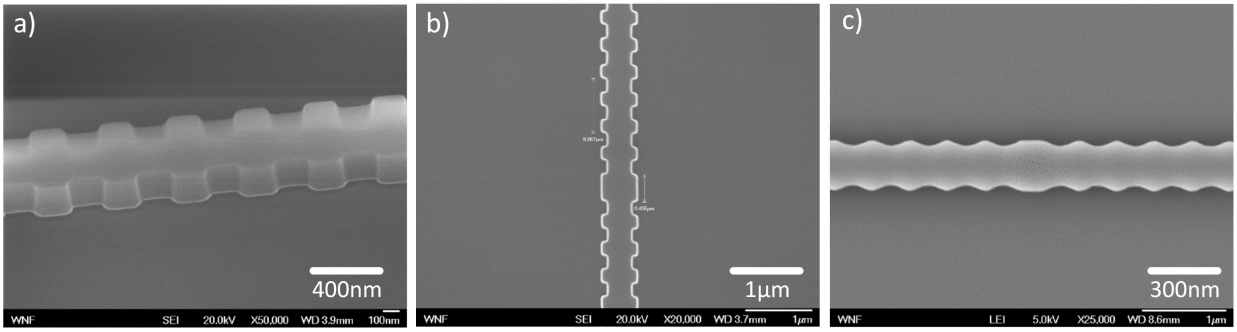

Figure 4.23: SEM images of fabricated Bragg gratings (a) Uniform grating portion of a TM Bragg grating biosensor fabricated using Ebeam lithography. (b) Top-view of a Bragg grating similar to (a) and showing the phase shift region which creates the resonant peak within the stop band. (c) Image of a foundry-fabricated TM mode, uniform Bragg grating with phase shift for biosensing.

SOI wafer with a 200 nm thick Si top layer and a 2µm buried oxide layer using 193-nm lithography [277]. Ebeam fabrication was done at the WNF in Seattle, WA. Chips were then cladded with the perfluoro-polymer CYTOP purchased from Asahi Glass (Tokyo, Japan) [238, 239]. The cladded chips were further patterned to etch openings around the gratings to ensure complete exposure of the sensing region to their aqueous environment.

The evanescent field was characterized similar to what was described previously [24]. Briefly, the chip was cleaned using a Piranha solution (3:1 H2SO4:H2O2 (30%) for 30 minutes and rinsed with ultra-pure water prior to functionalization. Next, a solution of positively charged polyethylene imine (PEI, 5 mg/mL) was flowed over the sensor for 5 minutes to initiate the adhesion of subsequent electrostatic polymer bilayers. Electrostatic polymer bilayers were then created by alternating solutions of negatively charged polystyrene sulfonate (PSS, 5 mg/mL) and positively charged polyally-lamine hydrochloride (PAH, 5 mg/mL) for 5 minutes at 20 uL/min. Each solution was followed by a Tris buffer (0.5 mM, 100 mM NaCl,

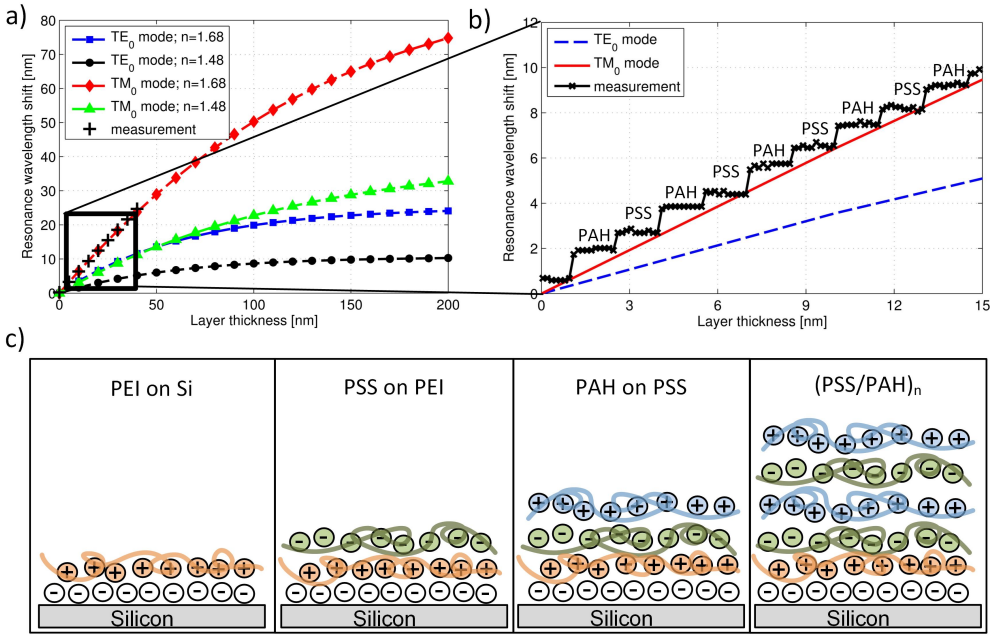

Figure 4.24: Surface sensitivity as function of thickness of adsorbed layer: a) Simulated sensitivities for both TE and TM modes (waveguide width $w = 500$ nm and height $h = 220$ nm) plotted versus layer thickness with refractive index of $n = 1.68$ and $n = 1.48$. The cladding index is assumed to be $n = 1.33$ for water; b) Comparison of experimental surface sensitivity of the TM mode to simulation. Electrostatic polymer bi-layers were created by alternating solutions of negatively charged polystyrene sulfonate (PSS, 5 mg/mL) and positively charged polyally-lamine hydrochloride (PAH, 5 mg/mL). The bi-layer thickness (after one cycle of PSS/PAH) is about 3 nm with a refractive index of n=1.68 [24]; and c) Schematic of the electrostatic polymer bi-layers created by alternating solutions of negatively charged polystyrene sulfonate (PSS) and positively charged polyally-lamine hydrochloride (PAH).

pH 7.1) rinse for at least 3 minutes to avoid polymer precipitation and clogging of the fluidic tubing (see also Fig. 4.24(c)). To measure the thickness of the bi-layers a glass slide with no bi-layers, 10 bi-layers, and 20 bi-layers was manually prepared using the same electrostatic

polymers and the resulting thicknesses was measured using ellipsometry. The measured surface sensitivity for an adlayer with $n_{ad} = 1.68$ is 650 pm/nm validates the simulation methodology (simulated surface sensitivity is 648 pm/nm, see Figs. 4.24(a) and 4.24(b). The simulated surface sensitivity for an adlayer with $n_{ad} = 1.48$ is 312 pm/nm.

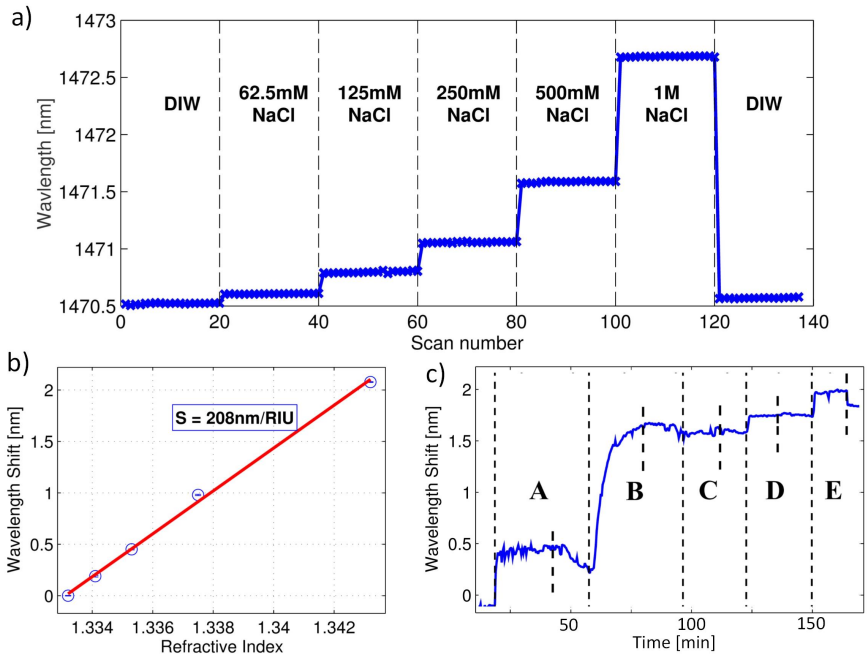

Figure 4.25: Example characterization data shown for on-substrate TM Bragg gratings with design parameters: period $\Lambda = 436$ nm, corrugation $\Delta w = 140$ nm, and number of periods on each side $N = 155$. a) Peak wavelength when subjected to refractive index standards. (b) Bragg grating sensitivity [nm/RIU] determined from (a); and c) Sensogram of the sandwich assay used to assess the Bragg grating's biosensing performance. Region A: Protein A physisorption to promote immunoglobulin capture; Region B: immobilization of anti-streptavidin. Region C: BSA to block any exposed regions on the sensor and ensure specificity of subsequent steps. Region D: Streptavidin (SA) as the model target biomolecule. Region E: Final amplification using Biotin-BSA.

The Bragg gratings bulk sensitivity was experimentally assessed using refractive index

standards as described above. Figure 4.25(a) shows the resonant wavelength shift of a phase-shifted Bragg grating as different refractive index standards were introduced. Points at each step were averaged and plotted against the solution's measured refractive index to determine a bulk sensitivity of 208 nm/RIU as shown in Fig. 4.25(b). The measured quality factor of the sensor used in the experimental work is 1.93k and the bulk sensitivity is S_b = 215 nm/RIU which results in a intrinsic limit of detection of $iLoD = 3.73 \cdot 10^{-3}$ RIU. Taking the experimental noise floor of 1 pm the system limit of detection is given by $sLoD = \frac{\delta\lambda_{min}}{S_b} = 4.65 \cdot 10^{-6}$ RIU.

The performance of the TM Bragg gratings were evaluated for biosensing applications using a modified sandwich assay [245] (also described in chapter 4.2.1). Figure 4.25(c) shows the sensor's response to a sequence of biological reagents. The assay started with PBS buffer for 20 minutes to establish a signal baseline. Next, Protein A (1 mg/mL) was physisorbed onto the sensor's surface for 30 minutes to immobilize the capture antibody (Region A). Assuming the sensor's surface sensitivity is 0.32 nm/nm (meaning, an adlayer with thickness of 1 nm shifts the resonant wavelength by 320 pm), the ≈ 300 pm shift after the Protein A suggests a 0.9 nm adlayer which is consistent with what has been reported previously [159]. Anti-streptavidin (10 µg/mL) was then introduced to functionalize the sensor (Region B). The observed shift of ≈ 1.1 nm is expected since the immunoglobulin is ≈3.3x larger than protein A (160 kDa / 48kDa = 3.3) and suggests robust immobilization and sensor coverage. Region C shows the result of challenging the sensor and adsorbed molecules with BSA (20 µg/mL). This step not only confirms the biological specificity of the molecules used in the assay but blocks any remaining exposed portions of the sensor to limit subsequent non-specific interactions. The absence of an offset (or resonance wavelength shift) after the rinse step of Region C suggests robust coverage of the sensor with antiSA (Region B). Region D shows the permanent and irreversible wavelength shift of ≈140 pm when adsorbing SA (20 µg/mL). A final amplification step biotynilated BSA (bBSA) is shown in Region E. The permanent wavelength shift suggests specific binding of the bBSA with the immobilized SA.

4.5.5 Suspended waveguide TE and TM mode Bragg gratings

For on-substrate Bragg grating sensors (the standard SOI geometry), a portion of the evanescent field is guided by the buried oxide (BOX). This is especially true for TM modes where more than half of electric field is in the buried oxide substrate (with air or water cladding above). Exposing all sides of the sensing region would allow more overlap of the evanescent field with the bulk solution, improving sensitivity. While under-etched waveguides have been demonstrated for high performance computing applications [240–243] and photonic crystal biosensors [278] they have yet to be investigated for strip and slot waveguide Bragg grating biosensors. Therefore, suspended waveguide TE and TM mode Bragg gratings for 1.55 µm wavelengths were developed and compared with their on-substrate counterparts.

Design

The electric field intensity distribution was calculated for on-substrate and suspended strip waveguides using Lumerical MODE for both, the fundamental TE and TM mode (see Fig. 4.26).

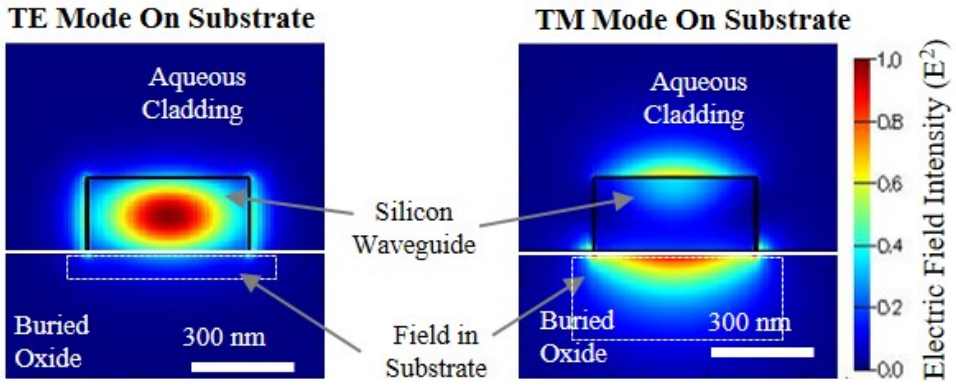

Figure 4.26: Simulated electric field density for 1.55 µm wavelength TE (left) and TM (right) modes in a 500 nm wide by 220 nm tall silicon waveguide.

The electric field overlap with the aqueous cladding was extracted from the mode profile simulation to determine the portion of the mode's field susceptible to refractive index changes in the cladding. Table 4.1 lists the evanescent field overlap and the expected sensitivity improvement gained in suspending the waveguides. The expected sensitivity improvements are calculated using Eq. 4.14 and the overlap integrals as defined in Eq. 2.2.

Table 4.1: Electric field intensity in cladding and predicted bulk sensitivity improvement

	Type	% EV in the Cladding	Predicted Sensitivity Improvement	Experimental Improvement
TE	on substrate	22		
	suspended	34	48%	50
TM	on substrate	37		
	suspended	82	134%	127

Mode profile simulations for suspended strip waveguide sensors suggest a 45% increase in electric field overlap with target analytes in the bulk solution for a TM mode sensor and a 12% increase for a TE mode sensor. For TE gratings, simulations predicted a 48% improvement in sensitivity and 50% was experimentally observed. Likewise, TM simulations predicted a 134% improvement in sensitivity and 127% was experimentally observed.

To evaluate the silicon waveguide stress and potential failure points under flow, suspended waveguide lengths ranging from 10 to 50 µm were modeled in SolidWorks and simulated using COMSOL under worst case flow conditions, i.e. flow perpendicular to the waveguide (a 30 µm waveguide was fabricated). Modeling results are shown in Fig. 4.27 and suggest that stress and deflection on the suspended waveguide are within its tensile strength limits (168 MPa [279]) at the flow rates of interest (10-100 µL/min) for up to a 50 µm long strip waveguides. The simulations predict a beam deflection of 4 nm for a 500 nm by 220 nm by 50 µm long under flow at 10 µL/min. The beam deflection calculations are based on the assumption of uniform loading on a beam fixed at both ends due to an average flow velocity $u_0 = Q/A$.

In Fig. 4.27 the maximum beam stress at the fixed end is plotted versus flow rate. The Reynolds number at $Q = 10$ µL/min is Re = 3.73.

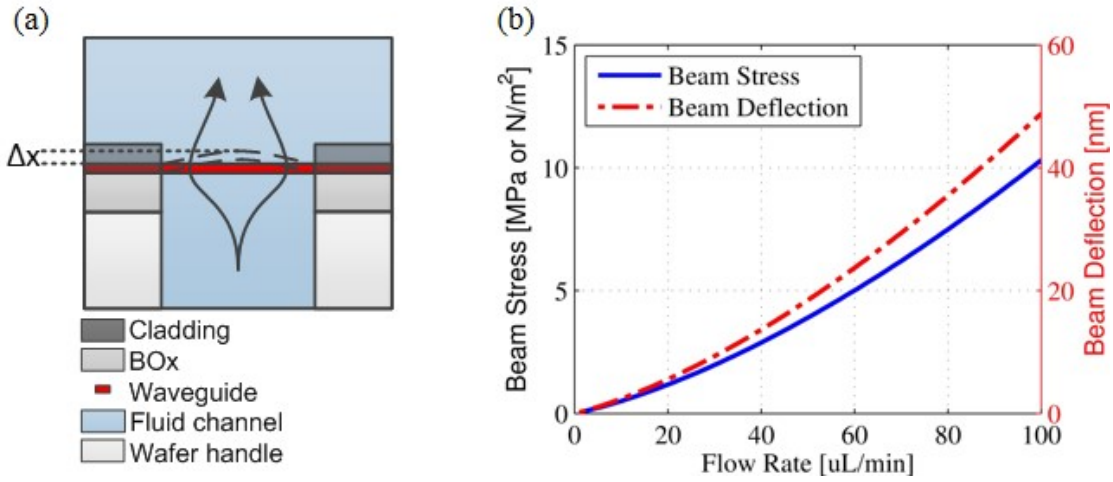

Figure 4.27: Suspended waveguide stress under flow analysis. (a) Schematic of worst-case simulation setup. Flow is perpendicular to the waveguide. (b) Simulation results showing a beam deflection of 4 nm for a flow rate of 10 µL/min and stress of 3.5 MPa.

Fabrication

Devices were fabricated on a 220 nm SOI wafer with a 3 µm BOX (SOITech) using a 100 keV JEOL JBX-6300FS Direct Write Ebeam Lithography System at the University of Washington's Nanofabrication Facility (WNF) [236]. After a solvent rinse and hot-plate dehydration bake, hydrogen silsesquioxane resist (HSQ, Dow-Corning XP-1541-006) was spin-coated at 4000 rpm, then hotplate baked at 80 ^{o}C for 4 minutes. Waveguide structures were written using the ebeam at 100 keV energy, 8 nA beam current, and 500 µm exposure field size. The machine grid used for shape placement was 1 nm while the beam stepping grid, the spacing between dwell points during the shape writing, was 6 nm. An exposure dose of 2800 µC/cm^2 was used. The resist was developed by immersion in 25% tetramethylammonium hydroxide for 4 minutes, followed by a deionized water rinse for 60 s, an isopropanol rinse for 10 s, and

then blown dry using nitrogen. The silicon was removed from unexposed areas using inductively coupled plasma etching in an Oxford Plasmalab System 100 with a chlorine gas flow of 20 sccm, pressure of 12 mT, ICP power of 800 W, bias power of 40 W, and a platen temperature of 20 ^{o}C, resulting in a bias voltage of 185 V. During etching, chips were mounted on a 100 mm silicon carrier wafer using perfluoropolyether vacuum oil.

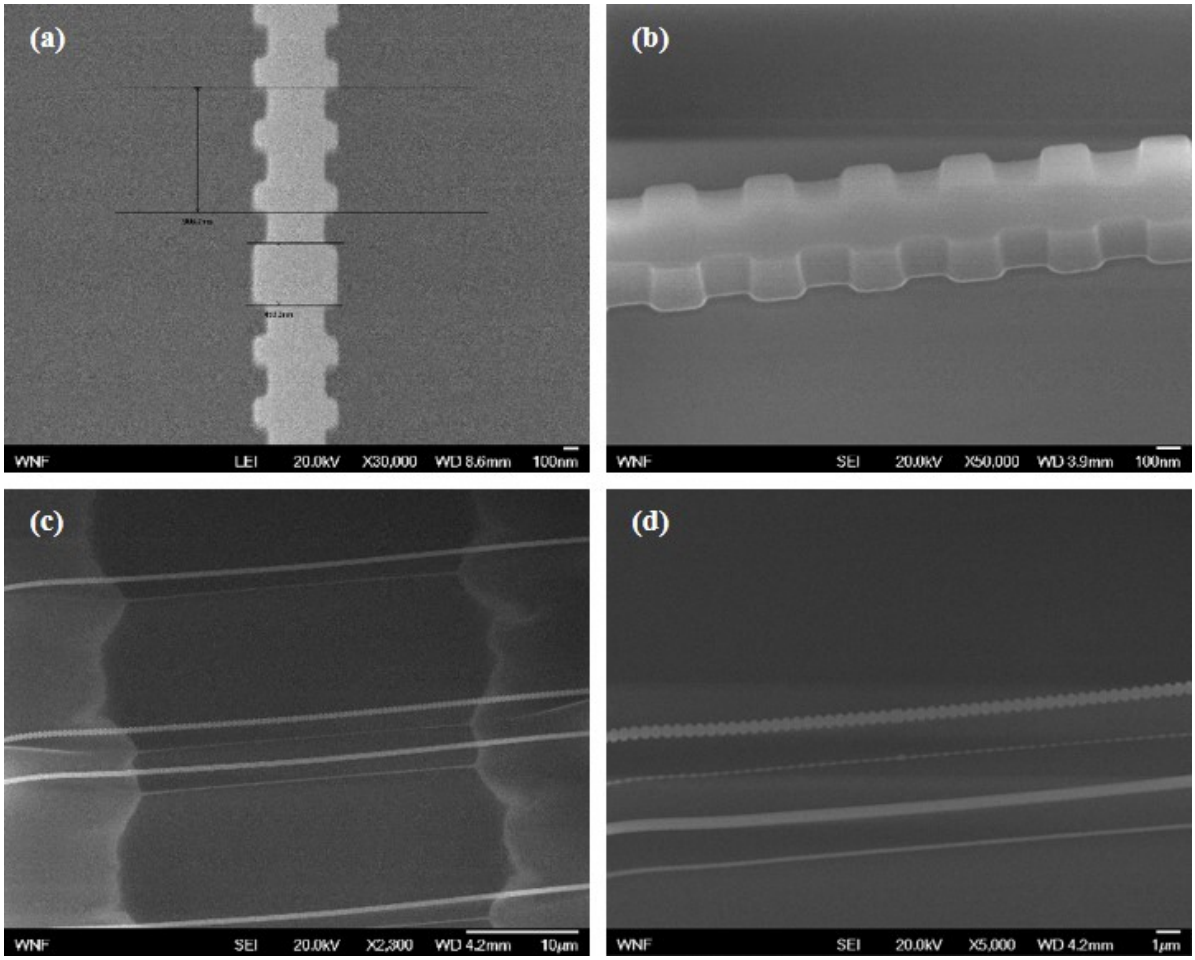

Figure 4.28: SEM image of a fabricated, suspended WG Bragg grating: a) Top view of grating with phase shift; b) Side view of grating on slab; c) Side view of undercut Bragg gratings waveguides; and d) zoomed in side view of undercut Bragg grating waveguide.

Chips with suspended waveguides were first cleaned with 1:3 piranha solution (H_2O_2:H_2SO_4)

followed by a hexamethyldisilazane surface treatment to promote photoresist adhesion and prevent lift off during the etch cycle. Next, AZ1512, a standard broadband Novalak based photoresist, was spun onto the chip, baked, exposed, and developed to pattern the undercut regions (waveguide suspensions). The undercut region was centered on the Bragg gratings with width of 30 µm. Buffered oxide (10:1) was used to etch through the 3 µm thick buried oxide layer to suspend the waveguide structures. Without drying, chips were rinsed with deionized water and then soaked in acetone to remove any remaining photoresist. While still wet, chips were then transferred to isopropanol bath to prevent stiction during the final dry step under a stream of nitrogen. SEM images confirmed that the structures were released as shown in Fig. 4.28.

Results

Devices were tested as described in chapter 4.2. Table 4.2 summarizes the measured perfor-

Table 4.2: Measured Bragg grating performance comparison

	Type	S [nm/RIU]	Q [1e3]	iLoD [RIU]
TE	on substrate	59	29	$3.8{\cdot}10^{-4}$
	suspended	89	10.1	$1.72{\cdot}10^{-3}$
TM	on substrate	215	1.9	$3.73{\cdot}10^{-3}$
	suspended	485	3.2	$9.99{\cdot}10^{-4}$

mance parameters of the four Bragg gratings compared in this manuscript. The on-substrate TE mode had the best quality factor and $iLoD$ but lowest sensitivity resulting from the high modal confinement within the waveguide core. Pre-fabrication simulations suggested a 1.48x sensitivity improvement when suspending the waveguide (87 nm/RIU). The measured sensitivity of 89 nm/RIU is within the measurement and fabrication tolerances and agrees well with the simulation. As more of the suspended waveguide's mode overlaps with the aqueous cladding, the quality factor decreases indicating an increase in absorption loss.

A sensitivity of 215 nm/RIU and quality factor of 1.9k was observed for the on-substrate TM Bragg grating. Pre-fabrication simulations suggested a 2.34x sensitivity improvement when suspending the waveguide (503 nm/RIU). The measured sensitivity was 485 nm/RIU (2.26x improvement) which is close to the predicted performance. The improved quality factor in the suspended TM Bragg grating over its on-substrate counterpart suggests that design parameters of the on-substrate grating should be optimized, namely the length of the grating to optimize the reflectivity of the distributed mirror on either side of the phase shift. Because of the higher index contrast when suspended in water the grating strength increases and the length has to be adjusted (shorter length) to have critical coupling.

A sandwich assay representing a model biological system was performed to assess the on-substrate and suspended waveguide Bragg gratings ability to detect molecular binding. Assay results for the two TM Bragg gratings are shown in Fig. 4.29. Measured sensitivity values suggest that the suspended waveguide sensor response to binding events is almost twice that of its on-substrate counterpart (Table 4.2).

Figure 4.29c is a cartoon representation of the reagent sequence and binding steps experimentally observed in Figs. 4.29(a) and 4.29(b). Both assays used similar reagents and concentrations but differed slightly in step durations. Both chips were thermally tuned to 37^{o}C and reagents were flowed over the sensors at 20 µL/min throughout the assay. The introduction of each reagent was followed by a 20 minute buffer rinse to remove any unbound species in the channel as indicated by the short, black dashed lines in Fig. 4.29.

After establishing a signal baseline in 1x PBS buffer (pH = 3.7), Region A shows the resonant wavelength response to the physisorption of protein-A (1 mg/mL) onto the sensor's native oxide surface. Physisorption is the irreversible binding of proteins to a surface and is a well-known phenomenon [150, 151]. Protein A has been observed to preferentially bind the Fc domain of antibodies [157, 158] and was used to bind and orient the capture antibody's Fab regions towards the channel for improved analyte binding. The large resonant wavelength shift in Region B confirms robust immobilization of the capture antibody, anti-streptavidin (antiSA, 10 µg/mL). A wavelength shift of 3 nm is observed for the suspended waveguide

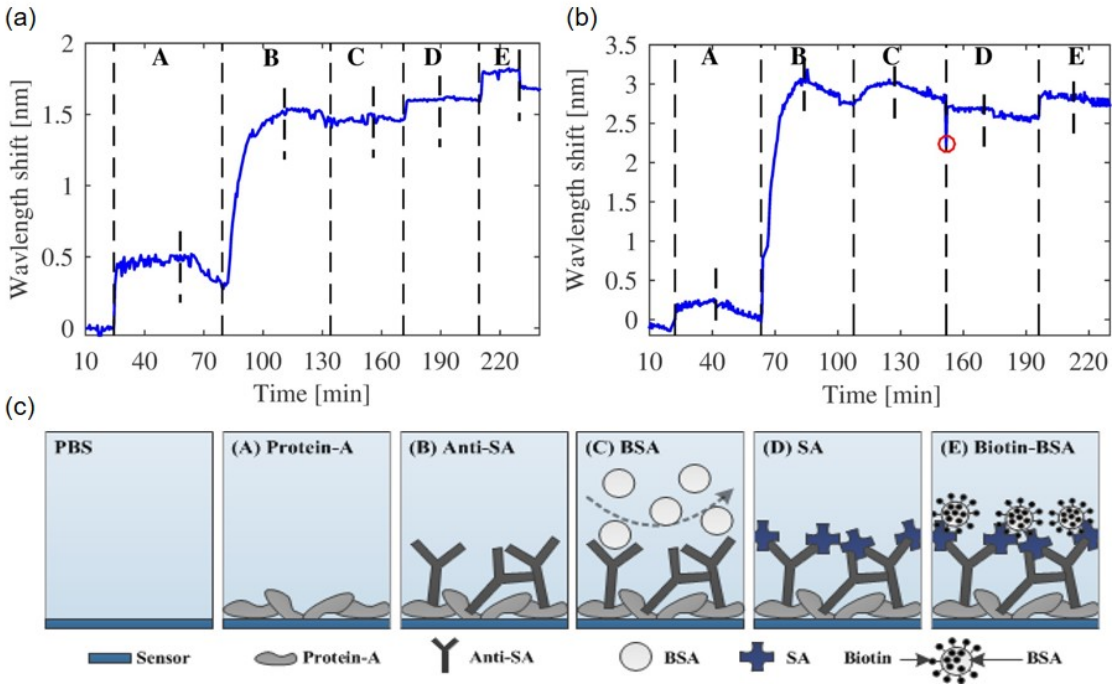

Figure 4.29: (a) On-substrate waveguide TM Bragg grating biosensing demonstration. (b) Suspended waveguide TM Bragg grating biosensing demonstration. (c) Reagent sequencing corresponding to regions [A-E]. Region A = Protein-A (1 mg/mL), B = anti-streptavidin (SA) (125 ug/mL), C = Bovine Serum Albumin (BSA) (2 mg/mL), D = streptavidin (SA) (1.8 µM), E = Biotin-BSA (2.5 mg/mL). Introduction of reagent in each region was followed by a PBS-wash.

(Fig. 4.29(b) and 1.25 nm for its on-substrate counterpart (Fig. 4.29(a), resulting in a 2.4x increase which is close to the simulated value of 2.34x and an experimentally observed sensitivity increase of 2.25x.

Region C shows the introduction of BSA (20 µg/mL) to block any remaining exposed surfaces on the sensor. This is necessary to prevent fouling and to validate that subsequent binding interactions are specific. Both sensors (Figs. 4.29(a) and 4.29(b) eventually return to Region C's initial resonant wavelength suggesting the sensor is sufficiently covered with the

antibody. Next, the sensor was subjected to streptavidin (SA, 10 µg/mL) as a model, target analyte (Region D). The permanent shift suggests a specific and irreversible binding interaction as expected. As a final amplification step, biotinylated BSA (bBSA) was introduced (Region E) resulting in another permanent resonant wavelength shift. The unfortunate introduction of an air bubble for one scan, as shown by the red circle in Fig. 4.29(b) Region C, results in the loss of some bimolecular mass from the sensor's surface. While this results in an offset, subsequent binding of the SA and irreversible shift of biotinylated BSA suggest the surface chemistry remains robust and specific.

Post-experiment simulations were performed to verify that the amount of observed bound species is within expectations. Since captured protein layers may not necessarily result in complete monolayers, the following assumptions were made: (1) proteins have refractive index of 1.48 [99], (2) protein A is 42 kDa and forms 1-3nm thick adlayers [156, 159], (3) the IgG antibody has a mass of 160 kDa, and (4) the total film thickness of the bound species is 15-30 nm thick [160, 161]. The experimentally measured resonance shift is in good agreement with simulations. The simulated surface sensitivities for and adlayer with $n_{ad} = 1.48$ are 640 pm/nm, 312 pm/nm, 210 pm/nm, and 160 pm/nm for suspended TM, on-substrate TM, suspended TE, and on-substrate TE Bragg gratings, respectively.

4.5.6 TM mode Bragg gratings at 1310 nm

As described in Sec. 4.6.3, the intrinsic limit of detection ($iLoD$) is improved by increasing the sensitivity or the quality factor (Q) of the resonator [103]. Unfortunately, an increase in sensitivity (mode overlap) impacts the quality factor as absorption losses due to the aqueous cladding dominate. Conversely, improving the quality factor by increasing modal confinement within the waveguide to avoid scattering and absorptive loss decreases sensitivity (see Sec. 4.6.3). If water absorption is the dominant loss, the sensor's intrinsic limit of detection cannot be further improved. However, the loss of water is dependent on the wavelength as described in Sec. 2.7.5. Water absorption has been observed to be approximately ten times lower around 1.3 µm wavelengths compared to 1.5 µm wavelengths [276, 280] (see also

Sec. 2.7.5). Assuming a similar waveguide susceptibility for a sensor designed for 1.3 µm wavelengths, the reduction in water absorption should offer an intrinsic limit of detection limit increase by an order of magnitude, up to the theoretical limit of $2.4{\cdot}10^{-5}$ RIU for 1.3 µm wavelengths.

Design

Figure 4.30 shows the loss simulation results for common waveguide widths which support single TE and TM modes for silicon thicknesses of 150 nm and 220 nm (for both wavelengths, 1.31 µm and 1.55 µm). The simulation setup consisted of a rectangular silicon waveguide on substrate with water cladding on three sides to mimic the biosensing environment. The range of typical waveguide widths are chosen for guiding single modes in 220 nm and 150 nm thick waveguides. Waveguide widths ranging from 250-450 nm were simulated for 1.31 µm wavelengths and widths ranging from 400-600 nm for 1.55 µm wavelengths.

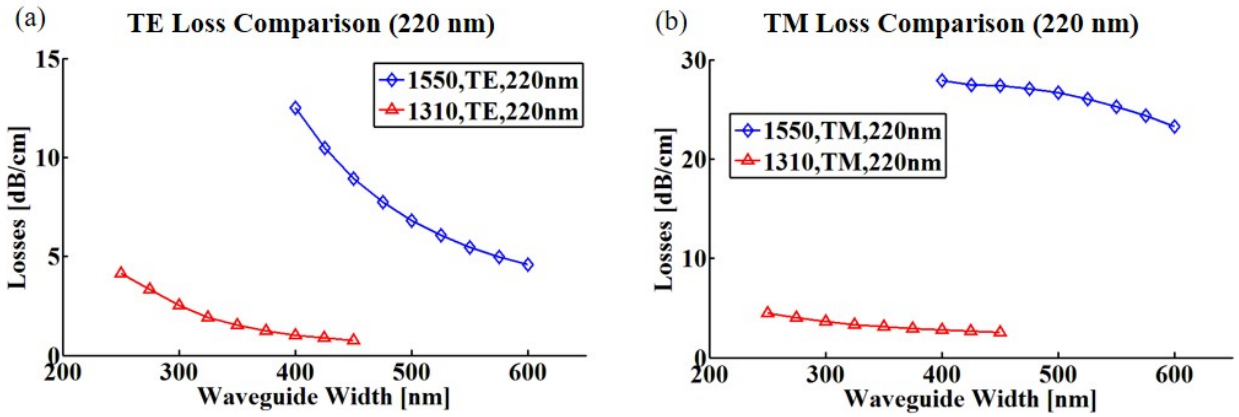

Figure 4.30: Simulation results to compare loss between 1.31 µm and 1.55 µm wavelengths across a range of waveguide widths 220 nm thick waveguide. Note, values were omitted for modes that were not guided by the waveguide dimensions being simulated. (a) Loss comparison for TE modes guided in a 220 nm thick waveguide with aqueous cladding. (b) Loss comparison for TM modes guided in a 220 nm thick waveguide with aqueous cladding.

The simulation results in Fig. 4.30 show an approximate order of magnitude decrease in loss (on average) for 1.3 µm wavelengths over their 1.5 µm counterparts. Note that TM modes are not supported in 150 nm thick waveguides at 1.55 µm wavelengths for waveguide widths less than 600 nm (and have been omitted).

For a 220 nm thick waveguide, the predicted sensitivity (based on our simulations) for 350 nm wide waveguide supporting a TE mode is about 90 nm/RIU. Likewise, a TM mode should result in a sensitivity of approximately 120 nm/RIU. Furthermore the surface sensitivity for and adlayer with $n_{ad} = 1.48$ is calculated to be 251 pm/nm for TM and 181 pm/nm for TE Bragg gratings, respectively.

Results

The devices designed for 1310 nm were fabricated using ebeam lithography on a 220 nm SOI substrate with 3 µm oxide layer at the WNF in Seattle, WA, and characterized as described in Section 4.2. Design parameters for the TM Bragg include a grating period of 330 nm

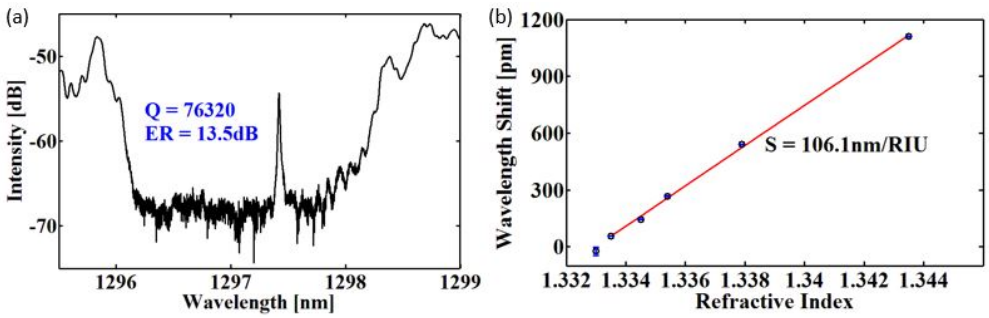

Figure 4.31: Experimental results for TM mode Bragg gratings designed for 1.3 µm wavelengths. a) Transmission spectrum of Bragg grating with resonant peak in stop band b) plot of resonance peak wavelength shift as function of refractive index change. The sensitivity is determined by the slope of the linear fit and is 106.1 nm/RIU.

(duty cycle of 50%) and a corrugation of 60 nm. The center of the grating has a phase shift to create a sharp, resonant peak in the stop band, as is shown in Fig. 4.31(a). The

resonant peak has a high quality factor of 76,320 with an extinction ratio of 13.5 dB. To assess sensitivity to refractive index changes in the cladding, the Bragg grating was subjected to a set of NaCl titrations. The resulting wavelength shifts were plotted for each solution and fit to determine a sensitivity of 106 nm/RIU as is shown in Fig. 4.31(b). The quality factor and sensitivity results in a intrinsic limit of detection of $iLoD = 1.62 \cdot 10^{-4}$ RIU, less than the 1.55 µm wavelength limit of $2.40 \cdot 10^{-4}$ RIU [103].

4.6 Sensor comparison

This section summarizes the performance of the investigated sensors and discusses advantages, disadvantages, and ramifications for use in biosensing. First, the sensor performance results are summarized in table 4.3. Next, mechanisms that determine detection limits and fundamental boundaries for 1.55 µm and 1.31 µwavelength sensors in an aqueous environment are discussed. The performance metrics used to compare biosensor performance include: the quality factor Q; bulk and surface sensitivity (S_{bulk} and S_{surf}), the resonator's susceptibility to refractive index perturbations; and the intrinsic and system limit of detection ($iLoD$ and $sLoD$), which determines the smallest unit of change the sensor can distinguish. The experimental results are summarized in table 4.3 in order of the measured bulk sensitivity. The sensors can be categorized into two groups according to the improved performance parameter; namely, 1) sensitivity improvements and 2) quality factor improvements.

Sensors that improve sensitivity: There exist many strategies to improve sensitivity by increasing modal overlap with the cladding, namely employing TM modes, using thinner waveguides (90 nm and 150 nm), and using sub-wavelength waveguide (SWG) configurations. This section describes experimental results for the (1) TE mode thin-waveguide ring resonators, (2) TM mode ring resonators, (3) TE mode SWG ring resonators, and (4) slot-waveguide TE mode Bragg gratings. It is also important to note here, that it is useful to distinguish between bulk sensitivity and surface sensitivity.

Sensors that improve the quality factor: This section briefly highlights experimental results towards improved quality factors for (1) 3 µm and 10 µm radius disk resonators, (2) TE mode strip- and slot-waveguide Bragg gratings, and (3) TE and TM ring resonators and TM Bragg gratings designed for 1.3 µm wavelengths.

4.6.1 Sensors that improve sensitivity

A sensor's sensitivity is determined by the overlap of the electric field and the analyte. This is true for the bulk and the surface sensitivity.

Bulk sensitivity

Because the bulk sensitivity is relatively easy to measure experimentally most published sensor designs use the bulk sensitivity as main performance indicator. Of all the sensors investigated, the SWG TE mode ring, slot-waveguide TE mode Bragg grating, and suspended TM mode Bragg gratings offered the highest sensitivities. SWG rings achieve this by guiding the mode through the cladding between the periodic sub-wavelength gratings (Fig. 4.11). The slot-waveguide Bragg gratings achieve this by guiding the majority of the mode's electric field in the cladding between the silicon waveguide arms (Fig. 4.21(a)). Suspended TM polarized sensors achieve this by exposing both sides of the waveguide to the analyte. While both SWG rings and slot-waveguide Bragg gratings demonstrate the highest sensitivity of all sensors investigated, their use in biosensing applications may be limited. Claes *et al.* suggested in an attempt to explain their under-performing slot ring resonators, that mass transport into the nano-scale slot might be limited by the size of the slot and steric hindrances [29]. They also observed wetting issues of the slot. A potential solution to improve molecule transport might be to employ larger slots between waveguides, although care must be taken to not degrade the quality factor (and ultimately detection limit). These transport issues might not be quite as severe for SWGs as the slot is not along the direction propagation but perpendicular to it and therefore much shorter.

Table 4.3: Performance metrics of investigated biosensors. Where SWG = sub-wavelength grating, Wvl = wavelength [µm], and Q, S_{bulk}, S_s, and $iLoD$ are the comparative performance metrics as described above.

Section	**Sensor Type**	**Mode**	**Wvl [µm]**	**Q [k]**	**S_{bulk} [nm/RIU]**	**S_{surf} [pm/nm]**	**iLoD [RIU]**	**sLoD [RIU]**
4.3.4	SWG ring	TE	1.55	3.9	490	789	$8.1 \cdot 10^{-4}$	$2.04 \cdot 10^{-6}$
4.5.5	suspended Bragg grating	TM	1.55	3.2	485	640	$9.98 \cdot 10^{-4}$	$2.06 \cdot 10^{-6}$
4.5.3	Slot Bragg grating	TE	1.55	15	340	748	$3.04 \cdot 10^{-4}$	$2.95 \cdot 10^{-6}$
4.3.2	Ring (h = 150 nm, w = 750 nm)	TM	1.55	1.9	238	243	$3.28 \cdot 10^{-3}$	$3.04 \cdot 10^{-6}$
4.3.4	strip Bragg grating	TM	1.55	1.9	215	312	$3.73 \cdot 10^{-4}$	$4.65 \cdot 10^{-6}$
4.3.2	Ring (h = 90 nm, w = 500 nm)	TE	1.55	9.2	153	298	$1.10 \cdot 10^{-3}$	$6.54 \cdot 10^{-6}$
4.3.2	Ring (h = 220 nm, w = 500 nm)	TM	1.55	9.2	147	312	$7.09 \cdot 10^{-4}$	$4.2 \cdot 10^{-6}$
4.4	10 µm Disk	TM0	1.55	16	142	289	$6.82 \cdot 10^{-4}$	$7.05 \cdot 10^{-6}$
4.3.2	Ring (h = 220 nm, w = 350 nm)	TM	1.31	33.5	113	251	$3.47 \cdot 10^{-4}$	$8.85 \cdot 10^{-6}$
4.5.2	Strip Bragg grating	TM	1.31	76	106	251	$1.62 \cdot 10^{-4}$	$9.5 \cdot 10^{-6}$
4.5.5	suspended Bragg grating	TE	1.55	10.1	89	210	$1.72 \cdot 10^{-3}$	$1.12 \cdot 10^{-5}$
4.3.2	Ring (h = 220 nm, w = 350 nm)	TE	1.31	9.8	91	181	$1.49 \cdot 10^{-3}$	$1.1 \cdot 10^{-5}$
4.3.2	Ring (h = 150 nm, w = 500 nm)	TE	1.55	14	83	212	$1.33 \cdot 10^{-3}$	$1.2 \cdot 10^{-5}$
4.5.2	Strip Bragg grating	TE	1.55	28	59	160	$9.38 \cdot 10^{-4}$	$1.7 \cdot 10^{-5}$
4.3.2	Ring (h = 220 nm, w = 500 nm)	TE	1.55	15	38	160	$0.72 \cdot 10^{-3}$	$2.63 \cdot 10^{-5}$
4.4	3 µm Disk	TE0	1.55	33	26	76	$1.81 \cdot 10^{-3}$	$3.85 \cdot 10^{-5}$
4.4	3 µm Disk	TE1	1.55	22	29	84	$2.43 \cdot 10^{-3}$	$3.45 \cdot 10^{-5}$
4.4	10 µm Disk	TE0	1.55	131	21	75	$5.63 \cdot 10^{-4}$	$4.76 \cdot 10^{-5}$
	Theoretical intrinsic detection limit in aqueous solutions at 1.55 µm wavelengths						$2.40 \cdot 10^{-4}$	
	Theoretical intrinsic detection limit in aqueous solutions at 1.31 µm wavelengths						$3.14 \cdot 10^{-5}$	

In general TM modes offer higher sensitivities over their TE mode counterparts since the majority of the TM mode electric field is in the cladding rather than the silicon waveguide. This was demonstrated by the TM mode ring resonators, disks, and 1.31 µm Bragg gratings. Yet, the sensitivity could be further improved by harnessing portions of the mode traveling in the oxide and exposing them to the cladding material. For TM mode Bragg gratings, this has been achieved by suspending the Bragg grating within a fluidic channel, doubling the sensitivity. For disk resonators, more of the TM mode could be exposed to the cladding by slightly under-etching its edges. Finally, the waveguide geometry can be optimized to increase the modal overlap with the cladding. This can be seen by the increased sensitivity of the 150 nm thick waveguide TM mode ring over its 220 nm thick waveguide counterpart (243 nm/RIU vs 147 nm/RIU respectively) and the TE mode rings designed for 90 nm, 150 nm, and 220 nm thick waveguides which offer sensitivities of 153 nm/RIU, 83 nm/RIU, and 38 nm/RIU respectively.

Of the sensors investigated, ones with the least sensitivity include the 3 µm and 10 µm disk and 220 nm thick TE mode ring (Sec. 4.4 and Sec. 4.3.2). For the TE mode ring, its standard waveguide dimensions guide more of the mode within the silicon core limiting its susceptibility to cladding changes. Therefore, reducing the waveguide dimensions, as was demonstrated in the 90 nm and 150 nm thin-waveguide rings, would offer higher sensitivities (153 nm/RIU and 83 nm/RIU respectively, see Sec. 4.3.2). For the disk resonators, slightly under etching around its edges would also expose more of the mode to the cladding, ultimately improving sensitivity.

Surface sensitivity

Even though the bulk sensitivity is relatively straight forward to verify experimentally, it is important to notice that for most bioanalytical applications, one is interested in how much of the target molecules are captured on the surface of the sensors. Most biological assays will stack up to an adlayer thickness on the order of 10 nm [19, 281]. It is therefore helpful to introduce the surface sensitivity as performance indicator. The surface sensitivity describes

the change in the resonance wavelength as function of adlayer thickness. Since the evanescent field decays exponentially and the sensitivity is proportional to the overlap of the analyte with the electric field, the surface sensitivity depends on the layer thickness. The surface sensitivity decreases with increasing layer thickness as depicted in Figs. 2.11(a) and 2.11(b). Each biomolecule interacting with the surface of the sensor causes a local change in refractive index, which in turn alters the propagation properties of the guided light. The biomolecular layer can be modeled as uniform layer with thickness d_{ad} and refractive index n_{ad} [99, 175]. The refractive index of said layer, and even the thickness, is a matter of ongoing research, but general statements can be made. The refractive index n_{ad} is between the refractive index of the dry molecules and the refractive index of the solution, n_{bulk}, which in most cases, is an aqueous solution or PBS [99]. The refractive index of such solutions is around $n_{bulk} = 1.33$. The refractive index for hydrated, adsorbed proteins, n_{ad}, is between 1.45 and 1.5 but typically the refractive index is assumed to be $n_{ad} = 1.48$ [98–101]. However, also of interest is how d_{ad} and n_{ad} impact the effective refractive index experienced by the mode as the monolayer builds up. The molecular layer can be modeled as an adlayer with fixed height and varying refractive index. This variation is assumed to be linear starting from the bulk solution index to a saturation index of a densely packed monolayers [98, 99]. Alternatively, one can assume a constant refractive index of the layer, n_{ad}, but a changing effective thickness $d_{ad}(t)$, where t denotes the deposition time. This approach has been used in [181–184]. Both of the suggested approaches are approximations and their validity depends on the biomolecule and the experimental conditions. Furthermore, upon adsorption of a protein onto a surface the bioactivity and specificity can also be altered affecting the subsequent adlayer density. Therefore it is necessary to run calibration experiments with known layer thicknesses for each biomolecule in order to be able to do a quantitative analysis. However, measuring the thickness of an adorbed protein layer can be challenging in itself. In Sec. 4.5.4 the surface sensitivity is measured by using alternating electrostatic polymer bi-layers with a reported thickness of about 3 nm per bi-layer [24]. This method was suggested and validated by Luchansky *et al.* on silicon photonic biosensors [24]. Even though the refractive index of

the bi-layer is $n = 1.68$ (compared to $n = 1.48$ for most proteins), the model assay is used to validate the simulation methodology. Table 4.3 reports the simulated surface sensitivities for each of the sensors investigated as part of this research effort. The reported sensitivities are simulated for the first 1 nm adlayer and are used to predict the expected shifts during the model biological assay. The adsorption of the Protein A layer in particular agrees very well with what is expected from literature (assumption of spherical shape and diameter of ≈ 5 nm) [21, 159]. Of the sensors investigated, the SWG ring resonator shows the highest surface sensitivity of 789 pm/nm. This means that each adlayer of 1 nm thickness will shift the resonance peak by 789 pm. A similar value is also reported by Wangüemert-Pérez *et al.* [282]. A similar high surface sensitivity of 748 pm/nm is reported for the slot waveguide Bragg grating. The surface sensitivity for an on-slab TM Bragg grating is about half of what is reported for the suspended TM Bragg grating (312 pm/nm compared to 640 pm/nm). This makes sense as the surface area is approximately twice for the suspended waveguide as compared to the on-slab counterpart. Even though the bulk sensitivity for the 150 nm thick TM ring resonator is higher than for a 220 nm thick waveguide, the surface sensitivity does not follow that trend. This can be explained by looking at the TM mode profile. The waveguide geometry of $h = 150$ nm and $w = 760$ nm is very close to the cut off region (barely supports a TM mode). Because of the higher refractive index of the substrate ($n_{SiO_2} = 1.45$) compared to the cladding ($n_{H_2O} = 1.33$) the mode overlaps more and more with the substrate as the waveguide gets thinner and hence the surface sensitivity is also decreasing.

4.6.2 Sensors that improve the quality factor

The quality factor is a measure of the photon life time in the resonator (see Sec. 2.2.2). The higher the quality factor is, the longer the photon circulates inside the resonator and is allowed to interact with the analyte [226]. Luchansky *et al.* defines an effective path length over which the electric field can interact with the analyte [281] which is proportional to the quality factor ($L_{eff} = \frac{Q\lambda}{2\pi n_{eff}}$). Equation 2.20 describes how the quality factor can be estimated by the line width of the resonant peak (λ_{3dB}). The line width is often used as the

fundamental limit of the spectroscopic resolution [103, 281]. Under the assumption that the spectroscopic noise is the limiting factor for the smallest detectable wavelength change then it is desirable to increase the quality factor for a sensor configuration. The quality factor can be enhanced by optimizing the coupling conditions for critical coupling and minimizing the loss in the resonant cavity [203]. Naturally, Bragg gratings do not suffer from bending, coupling mode-mismatch loss, or sidewall scattering in the same way as circular resonators. Yet their grating strength (corrugation width and period) and sensor length can be optimized to achieve critical coupling and improved Q. Since a foundry's lithography capabilities often dictate feature size resolution, fabricating Bragg gratings using the ebeam process described in Sec. 4.2 should reduce the sidewall smoothing effects (Fig. 4.20a) and improve the grating strength (this might change as foundries switch to shorter wavelengths). While the disk resonator quality factors are the highest among the 1.55 µm wavelength sensors due to higher modal confinement within the waveguide (as compared with rings), quality factors of disk, rings, and Bragg gratings can be improved even more by optimizing the coupling into the resonator and employing post-etching techniques [283] to reduce scattering losses caused by sidewall roughness [277, 284]. In addition, larger radii will further reduce bending and sidewall scattering loss at the expense of the ability to multiplex many sensors on a single waveguide bus.

For a wavelength in the near infrared spectrum, e.g. at 1550 nm, the overall cavity loss is largely dominated by absorption loss in the aqueous cladding (see also Sec. 2.7.5). This is especially true for sensor configurations with large portions of the electric field propagation in the aqueous cladding. While such configuration are in general more sensitive their quality factor is smaller as more light propagates in the lossy cladding rather then the low-loss waveguide core.

4.6.3 Improving limits of detection

As stated in chapter 1.3, the limits of detection for silicon photonic biosensors needs improvement to achieve ELISA-like sensitivities for medical diagnostic applications. Even though

the detection limit may be limited by non-specific binding or thermal fluctuations rather than the line width of the resonator, it is useful to introduce the definition of the intrinsic limit of detection ($iLoD = \frac{\lambda}{S_{bulk}Q}$, see Sec. 2.2.2), that is the limit of detection imposed by the resonator itself. On-chip thermal referencing, improved surface chemistries, or molecular amplification strategies such as presented in [285] are actively investigated to improve detection limits.

One technique for improving the limit of detection of a waveguide-based resonator sensor is to increase its sensitivity (S). This can be done by increasing the interaction between the propagating optical mode and the cladding medium (i.e. the sample). When a larger portion of the optical field travels outside the silicon waveguide core, the mode's susceptibility increases, enhancing sensitivity and causing a resonance wavelength change. However, increased water absorption losses of weakly confined modes combined with greater susceptibility degrades the resonator's Q. Thus, trade-offs exist among sensitivity, Q, and $iLoD$.

The loss term in Equation 2.20 is the total loss combining scattering loss, bending loss, mode mismatch loss, substrate leakage, and loss due to absorption in the cladding. Except for the absorption loss in the cladding, the losses can be minimized by design choices.

Using perturbation theory, a change of the dielectric constant (ϵ) in the cladding results in a change in frequency (ω) (using Dirac bracket notation):

$$\Delta\omega = \frac{\omega}{2}\frac{\langle E|\Delta\epsilon|E\rangle_{clad}}{\langle E|\epsilon|E\rangle} \tag{4.13}$$

The subscript in the numerator denotes the integration over the spatial domain of the cladding (aqueous solution or analyte). For a small perturbation of the cladding, like a molecular binding event, $\Delta\epsilon_{clad} \cong 2 \cdot n_{clad} \cdot \Delta n_{clad}$ the sensitivity can then be written as [286]:

$$\frac{\Delta\lambda}{\Delta n_{clad}} = \Gamma\frac{\lambda}{n_{clad}} \tag{4.14}$$

where Γ is the fraction of optical intensity overlapping with the cladding (or liquid). Γ is given by:

$$\Gamma = \frac{\langle E|\epsilon|E\rangle_{clad}}{\langle E|\epsilon|E\rangle} \tag{4.15}$$

According to Eq. 4.14, sensitivity increases with Γ and the upper limit is $\frac{\lambda}{n_{clad}}$. Additionally, the loss due to absorption in the cladding (α_{clad}) also increases with Γ. Q_{clad}, the quality factor associated with the absorption loss of the cladding is given by:

$$Q_{clad} = \Gamma^{-1} \frac{2\pi n_{clad}}{\lambda_{res}\alpha_{clad,[1/m]}} \tag{4.16}$$

This means that as the modal overlap with the cladding increases the sensitivity, the line width of the resonator (the smallest resolvable spectral change) is also increased and the detection limit remains constant. This is only the case when the total loss is dominated by the absorption loss of the cladding ($Q_{tot} \approx Q_{clad}$). The overall quality factor is given by:

$$\frac{1}{Q_{tot}} = \frac{1}{Q_i} + \frac{1}{Q_{clad}} + \frac{1}{Q_{noise}} \tag{4.17}$$

where Q_i is the intrinsic quality factor associated to scattering loss, radiation loss, mode mismatch loss, coupling loss, material absorption loss, Q_{noise} is associated to noise in resonance peak location. To relate the standard deviation of a spectral variation (σ) to the FWHM, $\Delta\lambda$, the numerical approximation proposed by White et al. is used $\sigma \approx \frac{\Delta\lambda}{(4.5 \cdot SNR^{0.25})}$ [112]. Resonators with high Q_i would be preferred as the line width is then determined by the cladding absorption (or absorbing biomolecules). An increase in sensitivity by changing the modal overlap with the analyte does not affect the $iLoD$ as a similar increase in line width is observed due to more loss in the cladding. And hence the $iLoD$ for TE and TM mode sensors at 1550 nm have the same theoretical limit.

To improve the intrinsic limit of detection, the sensitivity and the quality factor (Q) can be improved. However, as pointed out, both the sensitivity and quality factor are dependent on the confinement factor Γ which is a measure of how much of the electric field distribution resides in the core. The dependence is opposite in sign. Figure 4.32 shows the detection limit as a function of the intrinsic loss α_i. Resonators with high Q_i would

be preferred as the line width is then determined by the cladding absorption (or absorbing biomolecules). If $\alpha_i < 100$ m^{-1} the detection limit is constant as the loss is dominated by cladding absorption (see Fig. 4.32). An increase in sensitivity by changing the modal overlap with the analyte does not affect the $iLoD$ as a similar increase in line width is observed due to more loss in the cladding. And hence the $iLoD$ for TE and TM mode sensors at 1550 nm have the same theoretical limit. The $iLoD$ can be improved by an order of magnitude by switching to shorter wavelength (dashed green line in Fig. 4.32) as the water absorption is decreased (accompanied by slightly higher scattering losses) [103]. The $iLoD$ is approaching the fundamental limit if $\alpha_i < 10$ m^{-1}. Practically this is challenging to achieve as propagation losses for straight waveguides are on the same order (3 dB/cm) for strip waveguide dominated by sidewall scattering [52, 277, 284]). Of the 1.31 µm sensors mentioned in the previous chapters, the ring resonators (with additional bending losses) did not yield improved iLoD's, however, the TM Bragg gratings offered an $iLoD$ improvement over the theoretical limit for 1.55 µm but not yet approaching that for 1.31 µm.

It is also important to identify and quantify sources of noise in order to estimate the system's overall detection limit. During sensing experiments, extrinsic factors such as temperature fluctuations or fluctuating alignment of the I/O fibers due to vibration, can generate noise and limit the absolute detection limit of the system. For low quality factor resonators the dominant noise source is typically amplitude noise while for high quality factor resonators temperature fluctuations become the dominant mechanism [112]. Depending on the measurement setup spectral resolution of either the laser or the spectrometer can also impact the detection limit. Furthermore improved signal quantization, calibration methods, and data averaging could help improve signal to noise ratios and further improve detection limits. Although rigorous noise analysis in SOI sensors for biosensing has not yet been presented in the literature and would need to be addressed in the future, we can study the detection limit in the presence of noise. Figure 4.32 shows the intrinsic detection limit with added noise (s = 1 pm, and SNR = 60 dB).

The detection limit of the sensors investigated are plotted in Fig. 4.33. From Table 4.3,

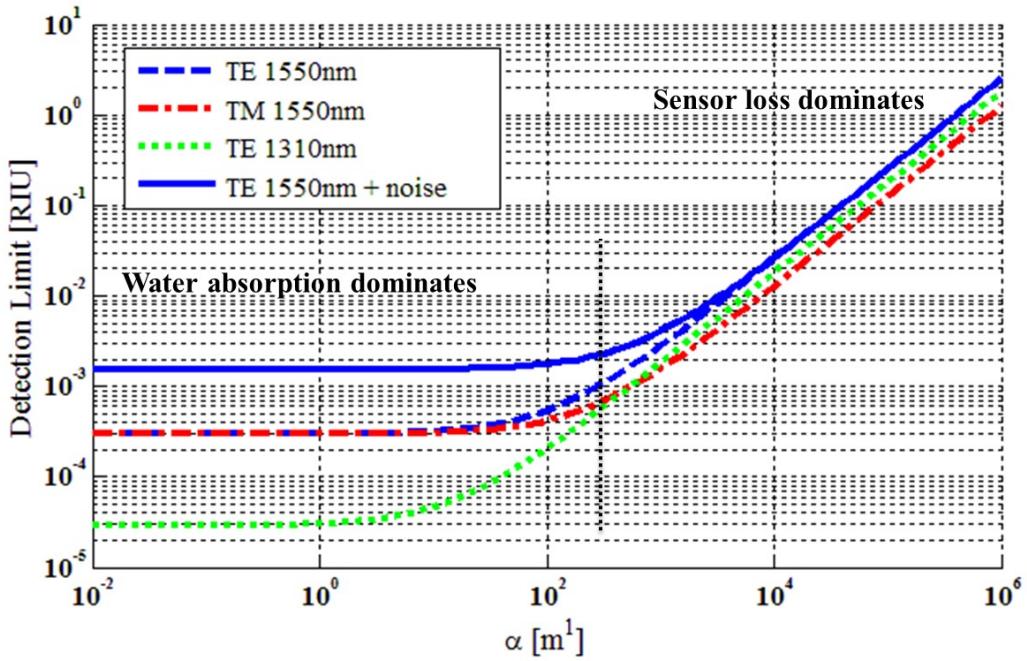

Figure 4.32: Detection limit as function of intrinsic loss (α_i) in waveguide-based resonators employing TE and TM modes at 1.55 µm and 1.31 µm wavelengths. For $\alpha_i < 100$ m^{-1} the quality factor is limited by the cladding absorption and the intrinsic limit is constant. The *iLoD* can be improved by an order of magnitude by switching to 1.31 µm.

the theoretical detection limit in aqueous media for 1.55 µm wavelengths is $2.40 \cdot 10^{-4}$ RIU. In Fig. 4.33 the theoretical limit of detection for a wavelength of $\lambda = 1550$ nm is represented by the solid blue line (and green dashed line for $\lambda = 1310$ nm). Of the 1.55 µm wavelength sensors investigated, the slot-waveguide Bragg grating had a *iLoD* of $3.04 \cdot 10^{-4}$ RIU [56], followed by the 90 nm thick waveguide TE mode ring at $3.47 \cdot 10^{-4}$ RIU, and finally the TM mode in the 10 µm disk at $6.82 \cdot 10^{-4}$ RIU. In general, these sensors had higher quality factors at 15,000, 24,700, and 16,000 respectively.

While the 1.55 µm wavelength sensors come close to the theoretical detection limit of $2.40 \cdot 10^{-4}$ RIU, one 1.31 µm wavelength sensor demonstrates a detection sensitivity beyond

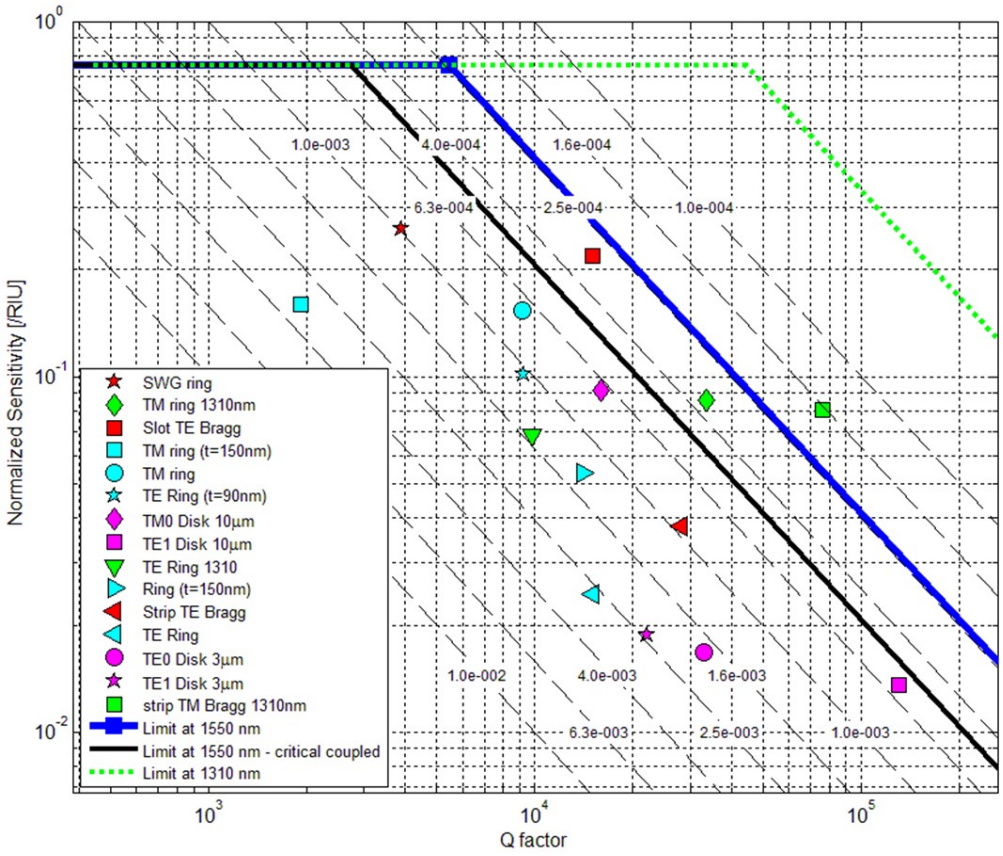

Figure 4.33: Comparison of the quality factor and S of the fabricated sensors. Blue and black lines are plotted to indicate the theoretical, water-limited, *iLoDs* for un-coupled (blue) and critically coupled resonators (black) at 1550 nm.

this limit. The TM mode Bragg grating had a quality factor of 76,000 yielding an *iLoD* of $1.62 \cdot 10^{-4}$ RIU. The TM ring had an *iLoD* of $3.47 \cdot 10^{-4}$ RIU and quality factor of 24,700. By employing strategies outlined above that would improve the quality factor and limit loss, this sensor could achieve greater sensitivities than the theoretical 1.55 µm wavelength limit.

Because of the successful improvement of sensitivities and quality factors, as presented in this work, most cases are not limited by optics anymore, but the non specific binding in relevant biological assays and thermal fluctuations [281].

Since most of the literature does not use the intrinsic limit of detection as figure of merit

but rather the system limit of detection, Table 4.3 also reports the system limit of detection for the measured devices. To calculate the $sLoD$ a smallest detectable change of 1 pm is assumed based on the experimental results from Sec. 3.4.2. In comparison, the commercially available platform Genalyte reports a wavelength resolution 0.1 pm [287]. Hence, with an improved readout noise of 0.1 pm, our best device (SWG) would offer a system limit of detection of $2 \cdot 10^{-7}$, which is 4X improvement over Genalyte's system [25].

4.7 Conclusion

The performance and biosensing capabilities of TE mode ring resonators with varying thickness of 90 nm, 150 nm, and 220 nm, TM mode ring resonators, sub-wavelength grating TE mode ring resonators, 3 µm and 10 µm TE and TM mode micro-disk resonators, and strip- and slot-waveguide Bragg gratings at 1.55 µm and 1.31 µm wavelengths was presented in this work. Table 4.4 summarizes performance trade-offs for the various design choices discussed in this chapter.

4.8 Acknowledgments

This work was supported by the NSERC CREATE Silicon Electronic Photonics Integrated Circuits (SiEPIC) training program, National Priorities Research Program grant from the Qatar National Research Fund, the University of Washington (UW) Royalty Research Fund, NSF CBET (Award nos. 0930411 and 1264174), and the Washington Research Foundation. The accomplishments described in this section would not have been possible without the generous support of Prof. Nicolas Jaeger at the University of British Columbia, who graciously provided a laser mainframe to the University of Washington. We also thank CMC Microsystems for fabrication access and design tool support as well as Mentor Graphics and Lumerical Solutions, Inc. for providing the layout and simulation software support (respectively). Part of this work was conducted at the University of Washington Nanotechnology Facility (WNF), a member of the NSF National Nanotechnology Infrastructure Network, and the Centre for High-Throughput Phenogenomics at the University of British Columbia

Table 4.4: Table comparing various sensor topologies and configurations

	Configuration	Advantages	Limitations	Section
Increased Sensitivity	Slot waveguides	Field confined to the slot region	High loss	4.5.3
	Sub-wavelength grating waveguides	Enhanced modal overlap with analyte	Compatibility with standard foundry processes	4.3.4
	Thin waveguides	Enhanced evanescent field	Compatibility with standard foundry processes	4.3.2
	TM modes	Enhanced evanescent field	High radiation loss	4.3.2
Increased quality factor	Disk resonators	Lower losses leading to higher quality factors	Difficulty controlling the coupled modes	4.4
	Phase-shifted Bragg gratings	High quality factor due to elimination of bending losses.	Compatibility with standard foundry processes	4.5.2
	Resonators at 1.31 μm	Reduced loss due to water absorption	Reduced evanescent field	4.5.6

(UBC). Finally, we thank the following persons for their contributions and support: Dr. Ali Ayazi for insightful discussions and mentorship, Professors Michael Hochberg and Tom Baehr-Jones the use of their optical test setup; Rick Bojko, Dr. Andrew Lingley, and Dr. Michael Kbheis at the WNF for fabrication and SEM imaging.

Chapter 5

SEROLOGIC PHENOTYPING USING SILICON PHOTONIC BIOSENSORS AND CAPILLARY DRIVEN NETWORKS

Portions of this chapter were reprinted with permission and may be found in the following publications:

1. **S. Schmidt**, J. Flueckiger, J. Buser, A. Wende, A. Bleem, L. Chrostowski, K.C. Cheung, D.M. Ratner, 'Serologic phenotyping using silicon photonic biosensors and capillary driven networks', *Manuscript in preparation*, 2016.

5.1 Introduction

Silicon photonic biosensors have received considerable attention for lab-on-chip applications recently [14]. These micron-sized sensors operate using near infrared light can be fabricated in volume using established CMOS foundry processes and show promise for highly multiplexed, chip-scale diagnostic devices able to detect a myriad of biological targets (see Fig. 5.1).

The high refractive index contrast between the cladding (silicon oxide or water) and waveguide core (silicon) allow the confinement of near infrared light in sub-micrometer waveguides [91]. A portion of the light's electric field exists outside the waveguide and decays exponentially away from the surface [91]. Figure 5.2(a) and Fig. 5.2(b) show the electric field distribution for the fundamental transverse electric (TE) and transverse magnetic (TM) mode in a waveguide. Biomolecules that bind on the waveguide's surface and overlap with the exponentially decaying electric field, as shown in Fig. 5.2(c) and 5.2(d), alter the propagation properties, including the effective index, n_{eff}, and loss. The amount of change is proportional to the overlap of the electric field with the analyte.

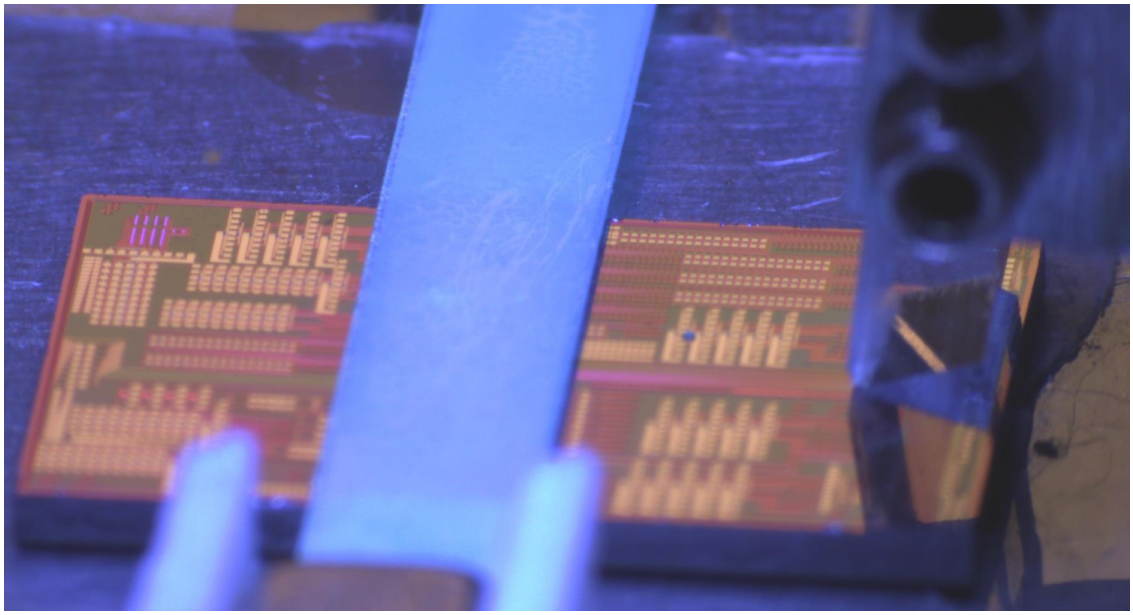

Figure 5.1: Silicon photonic biosensor chip with an integrated porous membrane. The membrane can sequence reagents across the sensors through capillary action eliminating the need for external pumps.

For a resonant structure typical of photonic biosensors, the change in effective index shifts the resonant wavelength accordingly (see Fig. 5.2(e)) as the resonance condition is given by $L \cdot n_{eff} = m\lambda$. L is the round trip length, for ring resonator $L = 2\pi R$, and λ the wavelength. During a biological assay the resonance peaks are tracked over time and compiled into a sensogram as shown in Fig. 5.2(f).

With sensors now offering clinically-relevant sensitivities, the focus is shifting towards entire lab-on-chip systems with integrated fluidics, lasers, detectors, and electronic readout. While a few groups have already demonstrated on-chip laser and detectors [42, 65, 66], most fluidic integration solutions require flow cells, tubing, valves, and external pumps to sequence reagents across the sensors [25, 67]. These components add cost and complexity to the overall system.

A growing body of literature is replete with examples of paper microfluidic networks

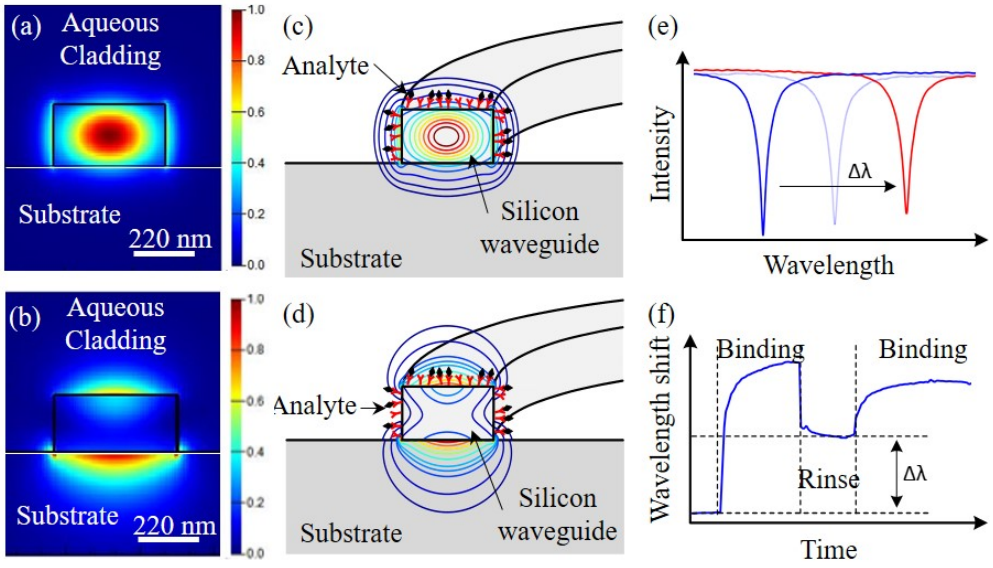

Figure 5.2: TE and TM biosensor principle of operation. Electric field intensity of a fundamental (a) TE and (b) TM mode profile in a in a 220 nm by 500 nm silicon waveguide on silicon oxide with aqueous cladding. (c) Electrical field overlap of the fundamental TE mode with the substrate and adsorbed biomolecules. (d) Electrical field overlap of the fundamental TM mode with the substrate and adsorbed biomolecules. (e) Example of the biosensor's resonant wavelength shift resulting from an effective refractive index change caused by adsorbing biomolecules. (f) Sensogram of tracked peaks over the course of an assay.

demonstrating complex fluidic operations on monolithic substrates [132, 137, 288]. Replacing the primary detection scheme (amplified immunochromatographic formats) of paper microfluidics with silicon photonic biosensors could allow sensitive quantification in small volumes, while maintaining the cost benefit of lacking pumps, tubing, and flow cells, as shown in Fig. 5.1. This simplified approach could expand access to integrated quantitative diagnostics that are less expensive than their traditional counterparts. In this manuscript, we investigate, characterize, and demonstrate the first to our knowledge paper-based fluidic networks integrated with silicon photonics, successfully detecting serology antibodies in

undiluted human plasma.

5.2 Methods and materials

5.2.1 Biosensor design and fabrication

Ring resonators were designed using methods described in Bogaerts *et al.* [91]. Mode fields in waveguide cross-sections were simulated using Lumerical's MODE Solutions [289] and custom MATLAB scripts helped determine optimal layout parameters [52]. TE mode ring design parameters include: radius $R = 40$ µm, waveguide width $w = 500$ nm, and coupling length $L_c = 7.24$ µm, and coupling gap $g = 200$ nm. TM mode ring design parameters include: radius $R = 40$ µm, waveguide width $w = 750$ nm, and coupling length $L_c = 3$ µm, and coupling gap $g = 200$ nm.

The sensors were fabricated using a 193 nm deep-UV lithography process offered through the ePIXfab [220] at IMEC in Belgium. Designs were realized in 220 nm thick silicon layer on 2 µm thick silicon oxide. To improve durability and reduce optical losses in the long waveguides, chips were cladded with CYTOP [238] with openings etched around the biosensors [239].

5.2.2 Biosensor characterization

A custom fiber-array based probe station was used to characterize the biosensors [20]. Figure 5.3(a) shows the chip stage and flow cell used to sequence reagents across the chip using a Teflon flow cell (Fig. 5.3(b)). A 500 µm thick silicone gasket defined 500 µm wide channels over the sensors (Fig. 5.3(c)). A syringe pump operating in withdraw mode sequenced reagents from 96-well plates. Acquired datasets were post-processed using a custom application [20].

Biosensor aqueous performance was assessed using previously described methods [20]. Briefly, bulk sensitivity was measured using refractive index standards made from sodium chloride (NaCl, Acros Organics, Thermo Fisher Scientific). The refractive index of titrations

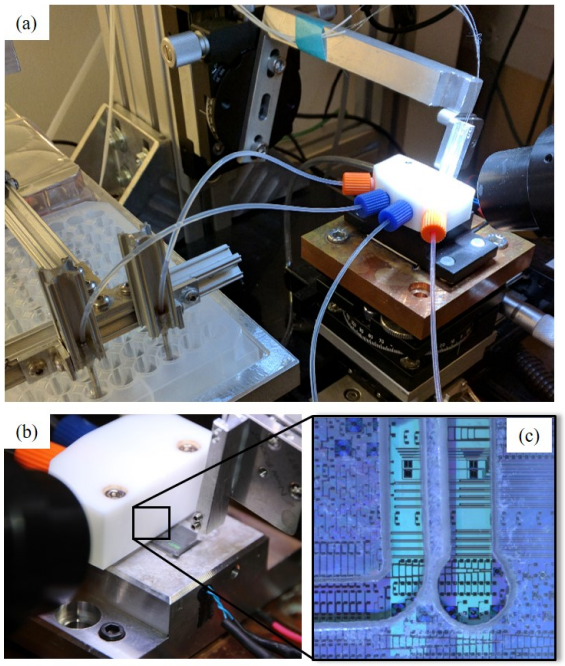

Figure 5.3: Test setup with conventional flow cell and pump. (a) Photograph of optical setup with the fluidic stage and well plates to sequence reagents across sensors using a PDMS flow cell mounted on the chip stage. (b) Four port PTFE flow cell that connects the inlet and outlet tubing to the silicone gasket in (c). (c) Laser cut silicone gasket that defines 500 µm wide channels on a 750 µm pitch over the sensors. The widened ports on the channel ends mate to openings in the PTFE flow cell shown in (b).

including 62.5 mM, 125 mM, 250 mM, 500 mM, and 1 M NaCl were measured using a Reichert AR200 digital refractometer (Depew, NY). Surface sensitivity was measured by alternating electro-statically charged polymers as previously demonstrated [24]. The negatively charged polystyrene sulfonate (PSS, 5mg/ml) and positively charged polyallylamine hydrochloride (PAH, 5mg/ml) bilayers are reported to be $\approx 3 \pm 0.2$ nm thick [24].

5.2.3 Porous network

The apparatus used to support the porous membrane network consists of five parts fabricated using VLS3.60 from Universal Laser Systems (Scottsdale, AZ). Figure 5.4 shows an exploded view of the various silicone membranes and acrylic base that comprises the test apparatus. A 3/16" thick, 18 mm wide, and 100 mm long acrylic base (McMaster-Carr 8560K211; Santa Fe Springs, CA) provides a rigid mount for two, 500 µm thick silicone sheets (Grace Biolabs; Bend, OR). This second layer provides an opening to recess the 750 µm thick chip while the third layer creates guides for the glass fiber and nitrocellulose strip. It also defines the void channel over the sensors. Finally, a 250 µm thick, translucent silicone sheet is the fourth layer and covers the porous membranes and channel to prevent evaporation. A 2 x 3mm window in the lid allows reagents to be delivered at the end of the glass fiber strip.

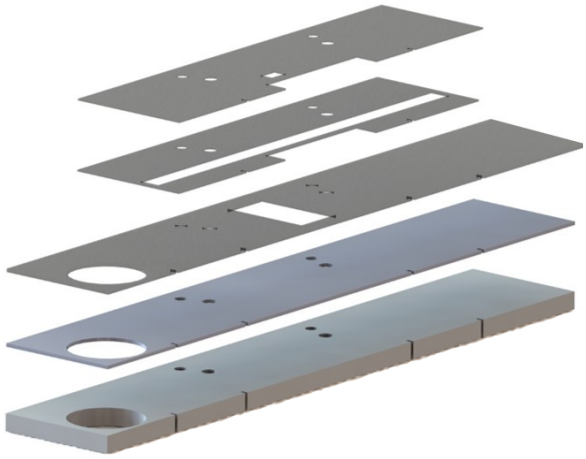

Figure 5.4: Exploded CAD model of porous membrane apparatus. The jig consists of an acrylic base with 3 additional silicone sheet layers that define the chip cavity and positions for the porous membrane components. A translucent lid covers the fluidic channel to prevent evaporation while allowing observation of the sensors during experiments.

Figure 5.5 shows the membrane network mounted on the optical test setup. Figure 5.5(a) shows a schematic of the fluid path including the source well, glass fiber, void channel on chip,

the nitrocellulose strip, and cellulose absorbent pad to help identify these components in the photograph shown in Fig. 5.5(b). A side-alignment camera facilitates fiber array alignment and provides a view of the sensors in the channel (Fig. 5.5(b)). An overhead-alignment camera provides a direct view of the sensors and channel, as shown in Figure 5.5(c). Both cameras provided real-time images during assays which was useful for visualizing flow with the colored solutions (see Fig. 5.8).

A 0.5 mL Eppendorf tube (Sigma Aldrich; St. Louis, MO) provides running buffer to the porous network through a glass fiber strip (Ahlstrom 8964; Helsinki, Finland) 2.5 mm wide and 50 mm long. Prior to installation, the glass fiber was blocked with 1 mg/mL BSA and then immersed in DryCoat Assay Stabilizer (Virusys Corporation; Taneytown, MD) and dried under ambient conditions. When installed, the glass fiber extends into the Eppendorf tube and overlaps the chip by 1-2 mm (Fig. 5.5(c)). After a 3-4 mm gap, a backed, nitrocellulose membrane (Millipore HF135; Billerica, MA) 2.5 mm wide and 32 mm long provides the flow rate control for the network. The nitrocellulose membrane overlaps the chip by 1-2 mm and connects to a cellulose absorbent pad (Millipore CF203; Billerica, MA). A paper clip ensured robust connection between the nitrocellulose and cellulose. The entire apparatus mounts over alignment pins similar to the conventional flow cell.

5.2.4 Typing reagents

Bovine serum albumin (BSA) and streptavidin were purchased from SigmaAldrich (St. Louis, MO, USA). Monoclonal A and B typing antibodies used to validate capture antigens were purchased from Immucor (Norcross, GA, USA). Biotinylated multivalent polyacrylamides containing blood group antigens A and B (PAA-A and PAA-B) were purchased from GlycoTech (Gaithersburg, MD, USA). Goat IgG (anti-human IgG/M/A) antibodies used for amplification were purchased from Thermo Fisher Scientific (Rockford, IL, USA).

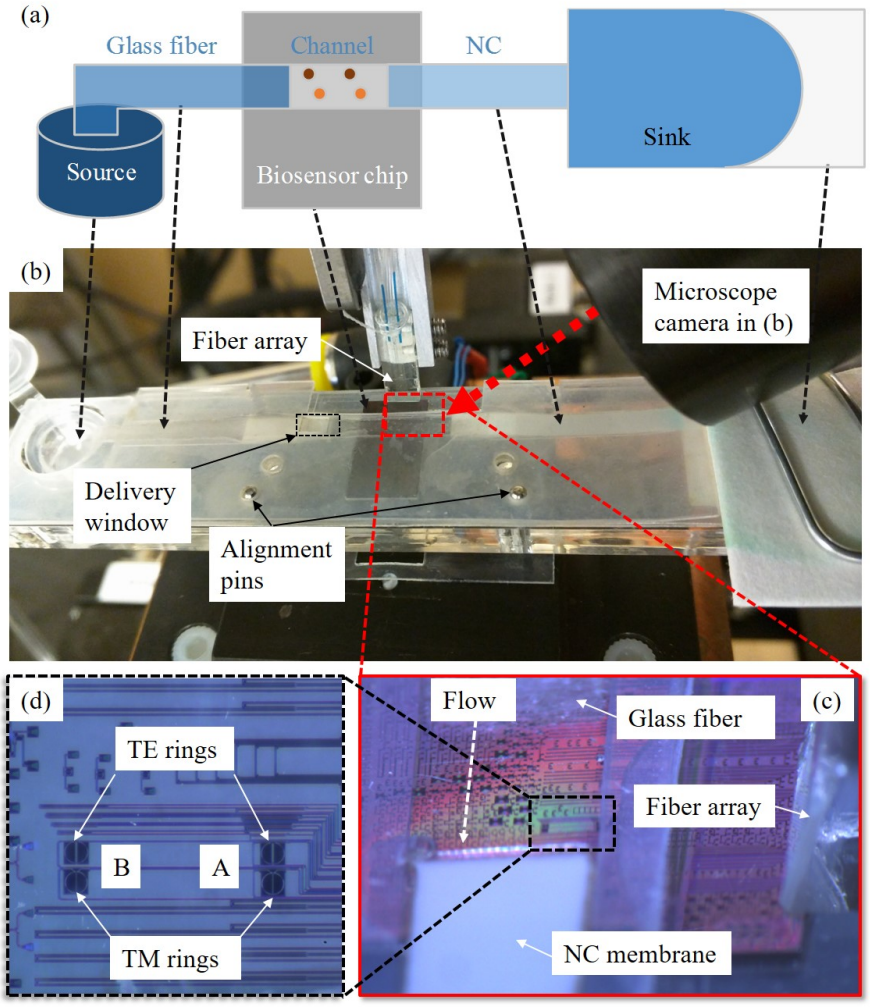

Figure 5.5: Porous membrane network setup. (a) Schematic representation of the porous membrane network including the source, glass fiber, void channel on chip, nitrocellulose strip to regulate flow rate, and cellulose absorbent pad that maintains flow. (b) Acrylic platform that hosts the silicone sheets and porous membranes. (c) Side-alignment microscope image (from (b)) showing the void channel with the biosensors and porous network. (d) Overhead microscope image seen through the silicone lid showing the B-antigen [B] and A-antigen [A] functionalized TE and TM mode rings.

5.2.5 Reagent validation

The biotinylated multivalent polyacrylamides blood group antigens A and B (PAA-A and PAA-B) were validated using IgM antibodies from ImmuCore. Figure 5.6 shows a validation assay using TE mode rings. The signal difference in the amplification step confirms the viability and specificity of the functionalized sensor.

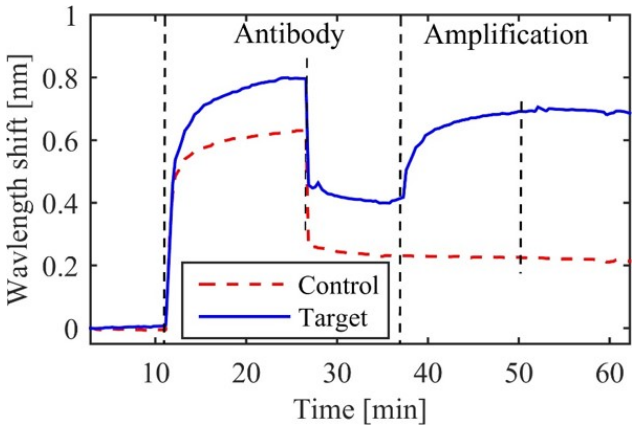

Figure 5.6: Validation assay of reagents used for indirect typing. An offset of 300 pm (after normalization) for the amplification step suggests the reagents are viable and work as expected.

5.2.6 Blood samples

Human blood samples were obtained from Bloodworks Northwest Research Institute (Seattle, WA, USA) in collaboration with Dr. Jill Johnsen. Samples had been typed and stored with ETDA to prevent coagulation at 4^{o}C. To obtain plasma samples, whole blood was centrifuged at 2000 G for 10 minutes at 4^{o}C. Following centrifugation, plasma and the buffy coat layer were removed from the cell pellet and stored separately. The samples used in the assays described below were undiluted human plasma from an A-type blood patient (006/12).

5.2.7 Biosensor functionalization

Chips were passively coated by full immersion in Eppendorf tubes with 400 µL of streptavidin (0.1 mg/mL) for at least three hours at room temperature, then rinsed with ultra-pure deionized water and blown dry. Laser-cut silicone gaskets were then reversibly bonded to the chips to create wells to spot PAA-A onto sensors in channel 1 and PAA-B onto the sensors in channel 2. Spotted chips were then placed in a humidity chamber for at least one hour and then rinsed and blown dry. Finally, the chips were blocked using 1 mg/mL BSA for at least 20 minutes. Blocked chips were rinsed briefly and then dipped in DryCoat and dried under ambient conditions. PAA-A and PAA-B antigenicity was assessed by subjecting sensors to ImmuCore's anti-A and B antibodies while monitoring the sensor response in real-time.

5.3 Results

5.3.1 Sensor characterization

Generally accepted performance metrics for refractive index sensors include sensitivity, quality factor (Q), and limit of detection [103, 111, 112]. Sensitivity quantifies the change in resonant wavelength (λ_{res}) to an environmental factor such as refractive index changes in the aqueous cladding (S_{bulk}) and addition of molecular adlayers onto the waveguide's surface ($S_{surface}$) [20]. Titrated NaCl solutions were sequenced across the fabricated sensors to assess S_{bulk} using the conventional flow cell and then the porous membrane network to assess any difference in performance. Figure 5.7(a) shows an early version of the porous membrane network setup used to characterize sensors. Figure 5.7(c) shows wavelength shifts corresponding to the NaCl refractive index solution standards. These results demonstrate the consistent flow and distinct reagent boundaries that can be achieved using porous membrane networks. Performance parameters like Q (Fig. 5.7(b)) and bulk sensitivity (Fig. 5.7(d)) can be assessed using the porous membrane with similar fidelity to the conventional flow cell. Briefly, bulk sensitivities of 41.2 ± 1.6 nm/RUI and 146.8 ± 2.5 nm/RUI were measured for the TE and TM mode rings, respectively. TE resonant peaks exhibited Q values of ≈22.5k while

their TM counterparts were ≈10.1k. Based on 2D waveguide mode simulations and evanescent field characterization via electrostatic polymers [24], surface sensitivities of 0.16 nm/nm and 0.31 nm/nm were observed for the region of interest (within 50 nm of the waveguide surface) for the TE and TM mode rings, respectively.

5.3.2 Porous network characterization

The flow rate in a fully wetted network can be approximated using Darcy's Law ($Q = \frac{\kappa wh}{\mu L}\Delta P$) where Q is the volumetric flow rate, κ is the permeability of the paper, wh is the cross-sectional area in width and height, μ is the dynamic viscosity, and ΔP is the pressure drop occurring over the length, L, in the paper network. Therefore, the volumetric flow rate in paper devices can be controlled by simply varying the fluid path length, L, as has already been demonstrated experimentally by Fu, Lutz, et. al. [137, 138]. The overall geometry of the glass fiber, nitrocellulose, and cellulose pads, along with material choices, determine the flow rate profile [138]. Nitrocellulose segments ranging in length from 30 mm to 60 mm were tested to determine the optimal flow rate for biological assays. While assays using the conventional flow cell/pump were performed at 20 µL/min, the porous network was designed to facilitate slower flow rates for increased binding time with the smaller sample volumes (20 µL serum samples vs. the 125 µL used for flow cell assays). Flow rate measurements were performed at the start and end of assays by injecting 10 uL of 2M NaCl solution with blue dye into the running buffer via the sample delivery window, as shown in Fig. 5.8(a). Recorded video images from the overhead and side-alignment cameras provided visual feedback on a sample's progression through the network while the sensor was monitored in real-time. Figure 5.8(b) shows sensor's response to the 10 µL sample of blue-dye 2M NaCl for a porous network with a 30 mm long NC strip. The upward and downward slope of the wavelength shift indicate slight lateral dispersion with the running buffer. The observed transit time of approximately 3 minutes (for 10 µL) results in a flow rate of ≈6.6 µL/min.

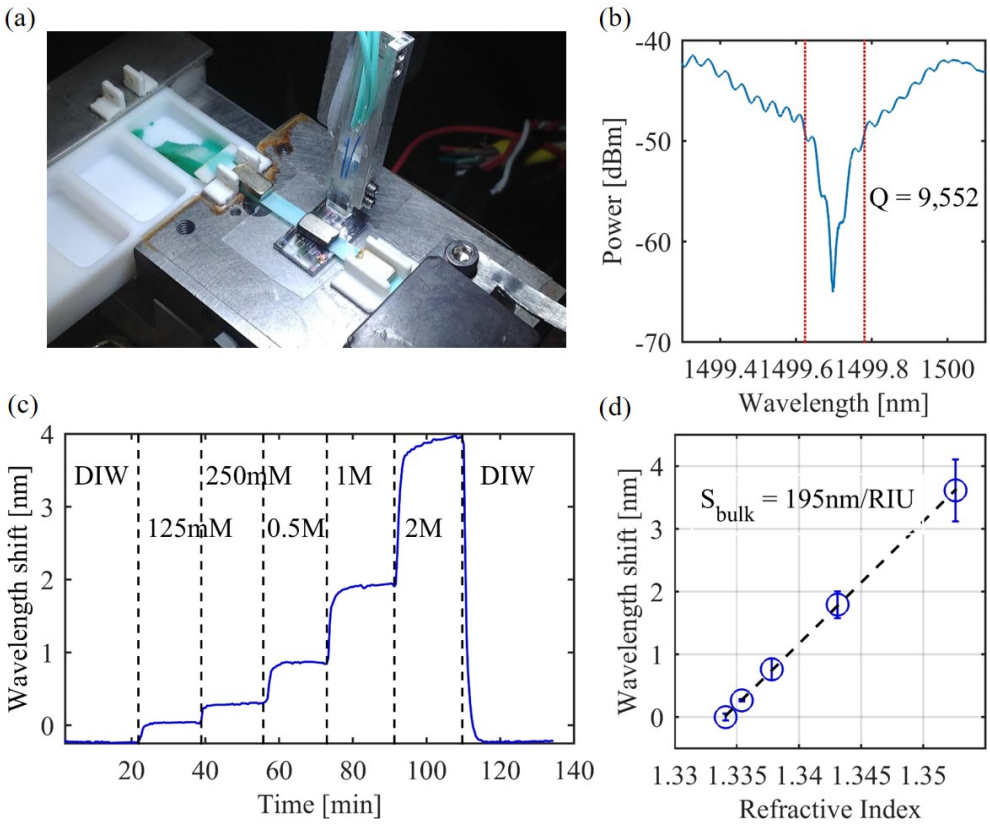

Figure 5.7: Characterizing sensors using the porous membrane network. (a) Experimental setup showing the Teflon source well with green-dye solutions to visual flow. The fluidic network is comprised of a single nitrocellulose membrane and cellulose pad for the sink. A magnet holds the membrane securely to the chip to avoid accidental movement during well changes. (b) Q measurement of a resonant peak for the device under test. (c) Resulting sensogram after subjecting the sensor to a refractive index solution set (125mM to 2M). (d) The calculated sensitivity based on the refractive of the NaCl solutions and the observed wavelength shift in (c).

5.3.3 Indirect typing

Indirect typing involves the detection of serum alloantibodies naturally developed against absent antigens from its erythrocytes [191]. Screening for these antibodies can be important

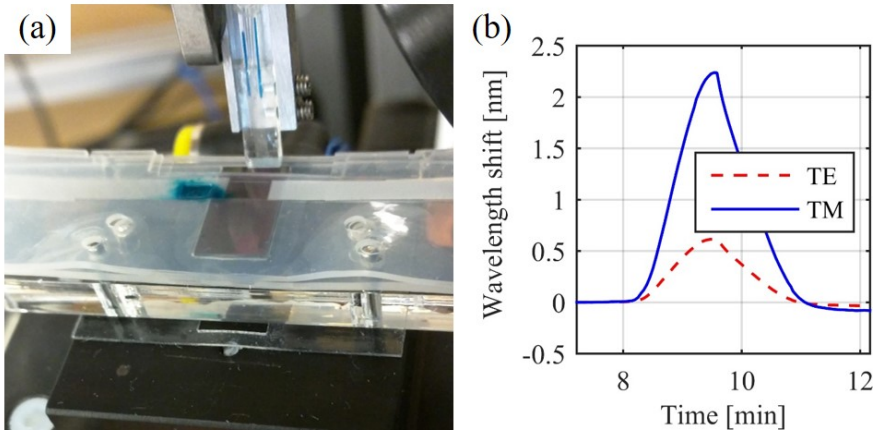

Figure 5.8: Porous network flow rate characterization. (a) Image showing 10 uL of a 2M NaCl solution with blue-dye delivered into the flow path through the lid's sample window. (b) TE (red-dash) and TM (blue) mode sensor response to the 2M NaCl solution introduced in (a). A transit time of approximately 3 minutes for 10 µL is observed.

for multiply transfused patients where adverse hemolytic responses may occur [191]. Therefore, we investigated the performance of silicon photonic TE and TM mode ring resonators for indirect typing since they show promise for a highly multiplexed lab-on-chip device [23]. While conventional gaskets, flow cells, and pumps were used to assess their performance, we also investigated the use of porous membrane networks in-lieu of external pumps, enhancing their portability and integrated system simplicity.

Figure 5.9(a)-Fig. 5.9(c) depict the offline steps used to functionalize the sensors for indirect typing. The reagents and protocols are discussed in section 5.2.7. The steps shown in Fig. 5.9(d), delivery of the undiluted human plasma sample, and Fig. 5.9(e), amplification via a secondary antibody, were performed during the assay and monitored in real-time.

To compare the biosensing performance between a conventional flow cell/pump system and the porous membrane network, a reverse blood-typing assay using human plasma was performed on both systems using similar biosensors (TM mode rings). Figure 5.10 shows the experimental results of reverse blood typing on both systems (the conventional flow cell

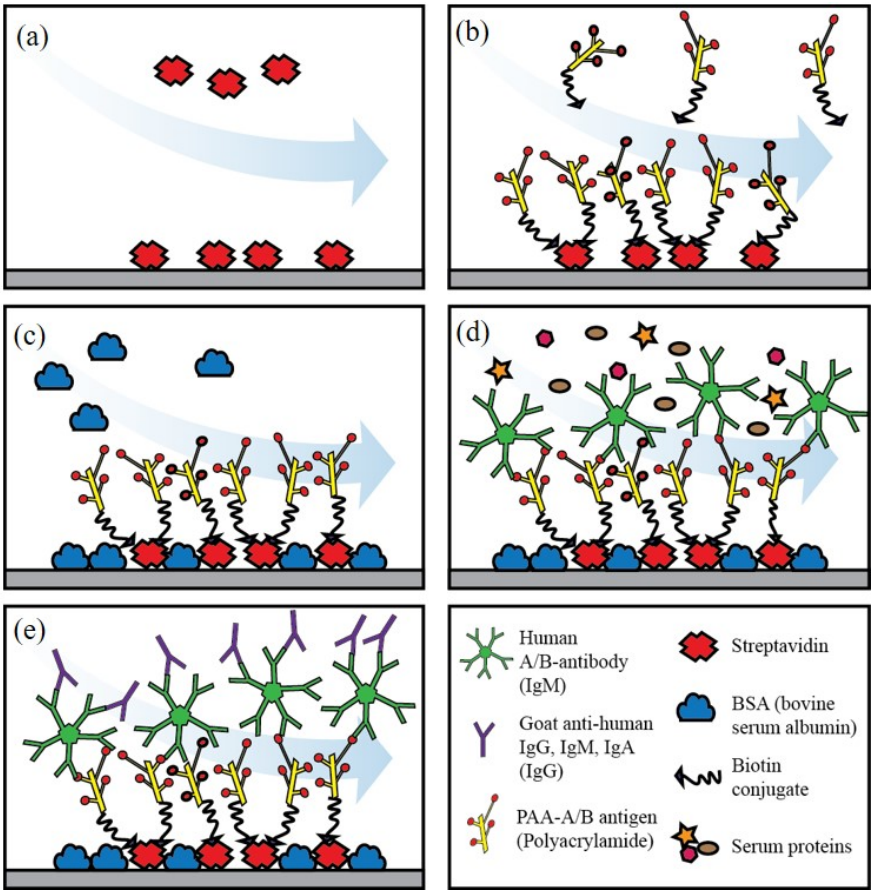

Figure 5.9: Schematic representing the steps involved with indirect typing assays. (a) Streptavidin is passively adsorbed to sensors. (b) Absorption of biotinylated multivalent polyacrylamides with A and B blood group antigens (PAA-A or PAA-B) to the streptavidin coated surface. (c) Blocking any remaining exposed surfaces on the sensor using BSA. (d) Introduction of undiluted human plasma samples and binding of antibodies to the surface-bound antigens. (e) Signal amplification using an anti-human IgG/IgM/IgA antibody. Steps (a)-(c) were conducted off-line while steps (d)-(e) were performed during the assay.

and porous membrane network). Figure 5.10(a) shows signal response using the conventional flow cell/pump while Fig. 5.10(b) shows the results using the porous membrane network.

The sample used was A-type serum. Therefore, binding to the sensors functionalized

with B-antigens is expected (blue line) while sensors functionalized with A-antigens provide a negative control (red-dash line). While steps were performed on a similar timescale for both systems, sample volumes and flow rates through the system differed. The plasma sample was flowed over the sensors for 5 minutes at 20 µL/min (100 µL in total) for the conventional flow cell and pump system. In contrast, a total of 20 µL of plasma was used in the porous membrane system. Its fluidic network was optimized to support flow rates of approximately 5 µL/min for biological assays. A lower flow rate was used for the porous membrane network to allow for smaller samples and the visualization of flow via an overhead microscope and camera. The other difference between the assays involved the secondary antibody. In the conventional flow cell system, 400 µL of secondary antibody at 0.1 mg/mL and 20 µL/min was used while 20 µL at 1 mg/mL and approximately 5 µL/min was used in the porous membrane system. A higher secondary antibody concentration was used in the porous membrane network to limit any depletion that might result from bound antibodies in the porous membrane up-stream of the sensors.

A signal baseline was first established in both systems by running buffer over the sensors. For the conventional flow cell system, sensors were blocked using BSA (1 mg/mL) inline to provide insight into the robustness of the sensor functionalization using PAA-A and PAA-B antigens. This step is clearly noted by the vertically dashed, black lines shown in Fig. 5.10(a). This steps was performed off-line (prior to the assay) for the porous membrane network. Sensors were subjected to undiluted human plasma. Sensors in both fluidic systems show a robust response to the patient's plasma, as evidenced by the large wavelength shift in during the 'Serum' step shown in Fig. 5.10(a) and Fig. 5.10(b). For the porous membrane network, two separate, 10 µL injections of plasma were delivered using a pipet into the sample window as indicated by 'A' in Fig. 5.10(b). The effects of the second injection can be seen by the sharp increase in resonant wavelength.

After introducing the plasma, the channel was rinsed using buffer to remove any unbound species. In the conventional system (Fig. 5.10(a)), buffer was re-introduced after 5 minutes as indicated by the short-dashed black line (within the 'Serum' step). While rinse step does

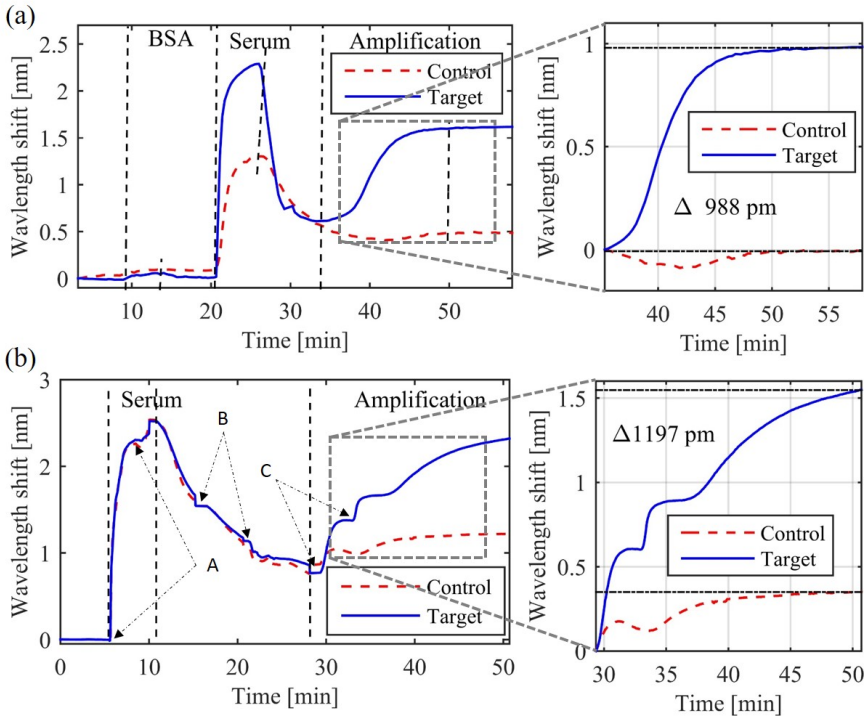

Figure 5.10: Indirect typing results for TM mode rings. (a) Sensogram of an indirect assay using a conventional flow cell/pump system with the amplification step normalized to the control (red-dash line) as shown in the enlarged inset. (b) Sensogram of an indirect assay using a porous membrane fluidic system with the amplification step normalized to the control (red-dash line) as shown in the enlarged inset.

remove species in the channel, the permanent wavelength offset in both the functional and control channel indicate bound species on both sensors. This 'fouling' is expected based on the complexity and content of the plasma matrix [185] and requires secondary amplification to validate the capture of B-antibodies. For the porous membrane network, the sample was introduced into a continuous stream of buffer. The running buffer dilutes the sample as it transits over the sensor and eventually washes any remaining species from the channel as shown between minutes 10 and 28 in Fig. 5.10(b) (after the 'Serum' step). The small plateaus in the spectra denoted by 'B' in Fig. 5.10(b) result from discontinuities in spec-

trum acquisition due to one minute long fiber array re-alignment. Re-alignment is required due to system vibrations and drift which reduce the signal amplitude from the sensor. Unfortunately, wavelength scans cannot be performed during realignment even though species continue to be rinsed from the channel.

The amplification step involved introducing a goat-derived, anti-human IgG/IgM/IgA to improve the signal response of bound human B-antibodies. The conventional flow cell/pump system clearly shows a differential response of 988 pm as seen in the enlarged inset for Fig. 5.5(a). The porous membrane network also showed robust differential response of 1,197 pm, as expected. Like the plasma sample delivery, the goat IgG was delivered in two, 10 µL injections as denoted by 'C' in Fig. 5.5(b). The conventional flow cell/pump system asymptotes nicely after 10 minutes of binding while the porous membrane shows a slower binding response. This is more than likely a result of the much slower flow rate (5 µL/min) designed for the porous membrane network versus the 20 µL/min used for the conventional system. Both control sensors exhibit a slight increase during amplification but the porous membrane network is more pronounced. This may be due to the higher concentration (1 mg/mL) of secondary antibody responding to fouling on the control sensor's surface compared to the conventional system (concentration (0.1 mg/mL). Regardless, the differential response between the functionalized sensor (PAA-B) and control (PAA-A) confirms the ability to perform indirect typing assays using a capillary-driven network with similar result as achieved using the conventional system.

Indirect typing results using TE mode rings are shown in Fig. 5.11. Since the sensor response was acquired simultaneously with the TM mode rings, the results for these sensors is similar to those described previously for the TM mode rings.

Assays were performed in triplicate on each fluidic system and patient sample. All resulted in a differential response after amplification. While the reverse type could be clearly distinguished after amplification on both the conventional flow cell/pump system and porous membrane network, the absolute values of the signal difference varied across patient samples. This could result from inconsistencies in spotting sensors by hand [290] as well as variations

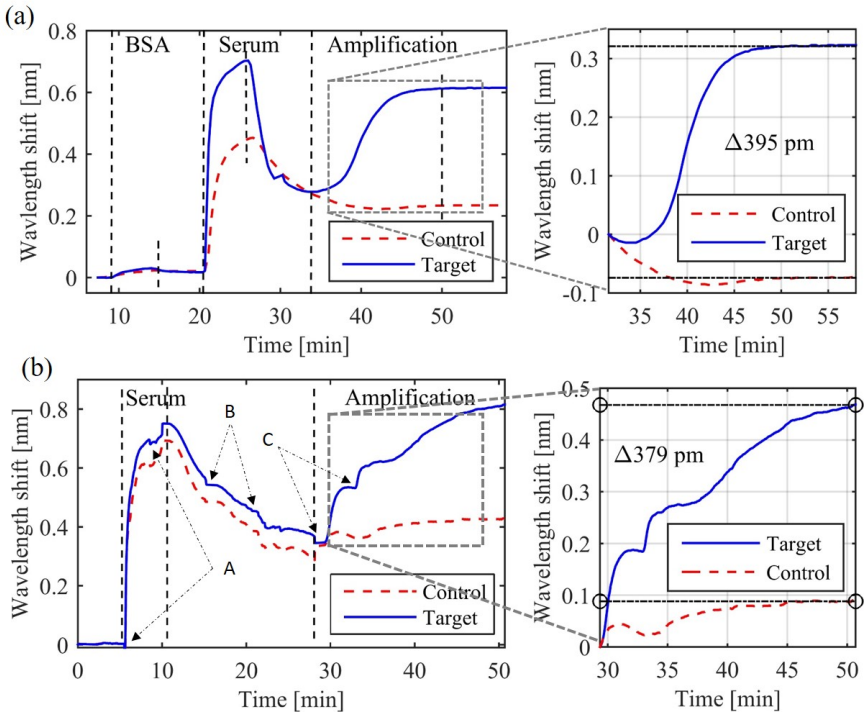

Figure 5.11: Indirect typing results for TE mode rings. (a) Sensogram of an indirect assay using a conventional flow cell/pump system with the amplification step normalized to the control (red-dash line) as shown in the enlarged inset. (b) Sensogram of an indirect assay using a porous membrane fluidic system with the amplification step normalized to the control (red-dash line) as shown in the enlarged inset.

in patient antibody titer and phenotypes [191, 197, 291].

Despite differences in the signal response, comparing wavelength shifts based on the simulated surface sensitivity offers useful insight into the average thickness of adsorbed biomass on the sensor [290]. The signal difference ratios between the TE and TM mode rings was 3.04 ± 1.59 and 3.66 ± 1.19 for the conventional flow cell/pump system and porous membrane network, respectively. A ratio of 3.04 suggests an average film thickness of 67 nm ± 50 nm for the conventional system and a ratio of 3.66 suggests an average film thickness of 89 nm ± 47 nm for the porous membrane system. The thicker adlayer observed

for the porous membrane system most likely results from the higher antibody concentration used for amplification. Considering the reported sizes for the molecules involved in these assays (eg: $\approx$ 40 nm diameter for IgM and $\approx$ 14 nm for IgG antibodies [99, 156, 292]), film thicknesses between 25 nm and 100 nm are expected. While the calculated ratios are based on simulations using an ideal model and do not account for sample or sensor functionalization variation, they correspond well to the expected results.

5.4 Discussion

Currently, the overall system cost of a silicon photonic biosensing platform is dominated by the laser (and detector) in comparison to the pumps, flow cell, and tubing. However there is growing evidence that chip-bonded lasers and integrated detectors will be affordable at the chip-scale in the near future [34, 42, 65, 66, 207, 293–295]. Therefore, these results demonstrate a meaningful step towards an integrated system without pumps for lab-on-chip applications. Porous membranes offer many additional capabilities that could further simplify and integrate the system. For example, they could be used to filter or separate blood constituents [296]. Membranes with larger pores could be employed to operate in samples with cells, such as typing erythrocyte antigens directly. Finally, complex 2D and 3D networks could facilitate the sequencing of the sample, rinse buffers, and any additional amplification chemistries to eliminate the need for user intervention [137, 297].

Sensor and functionalization improvements that enhance biosensing performance could also be made to improve the system. While the TM mode ring resonators offer 36% more surface area for sensing molecular interactions, their sensitivity could be further improved by optimizing their waveguide geometry to increase the sensing field at the waveguide's surface [252]. In addition, designing sensors for 1,310 nm wavelengths may reduce absorptive losses to the aqueous cladding by an order of magnitude [276], enhancing the sensor's detection limits [20]. Secondary amplification was required to detect the bound target due to fouling from the complex sample. Non-specific adsorption could be reduced by employing functionalization strategies that help resist fouling (as previously demonstrated by our group [40]) possibly

allowing label-free detection of the target.

5.5 Conclusion

The silicon photonic biosensor platform offers sensitive, multiplexed analysis of complex samples while porous membranes deliver fluids via capillary action, eliminating the need for pumps. To best of our knowledge, we are the first to demonstrate these technologies combined to create a simplified lab-on-chip system to detect serum antibodies in human samples. Indirect typing was performed using silicon photonic TE and TM mode ring resonators using a conventional gasket, flow cell, and pump-driven system as well as a porous membrane network. The results suggest that porous membrane networks can achieve similar results to their conventional flow cell/pump counterparts. With the advent of integrated lasers and on-chip detectors for highly multiplexed silicon photonic biosensor systems, porous membranes offer a welcome simplification to realize an integrated, lab-on-chip diagnostic device.

5.6 Acknowledgments

We gratefully acknowledge Dr. James T. Kirk and Dr. Jing Shang for developing the direct and indirect typing assay protocols, Dr. Jill Johnsen at BloodWorks Northwest for providing patient samples, Dr. Andrew Lingley and Duane Irish for cladding chips with CYTOP, Alissa Bleem and Qian Wang for prototyping early porous network apparatus concepts, and Dr. Nicholas Jaeger for the use of his laser in these experiments. JR Buser was supported by a grant from DARPA DSO/BTO–HR0011-11-2-0007, awarded to Paul Yager at the University of Washington. The authors acknowledge and thank Paul Yager and his research group at the University of Washington for use of the laser cutter and research guidance. This work was supported by the University of Washington (UW) Royalty Research Fund, NSF CBET (Award no. 0930411), and the Washington Research Foundation. Fabrication support was provided via the Natural Sciences and Engineering Research Council of Canada (NSERC) Silicon Electronic-Photonic Integrated Circuits (SiEPIC) Program.

Chapter 6

ERYTHROCYTE AND SEROLOGIC PHENOTYPING USING SILICON PHOTONIC RING RESONATORS

Portions of this chapter were reprinted with permission and may be found in the following publications:

1. **S. Schmidt**, J. Flueckiger, J. Buser, A. Wende, A. Bleem, L. Chrostowski, K.C. Cheung, D.M. Ratner, 'Serologic phenotyping using silicon photonic biosensors and capillary driven networks', *Manuscript in preparation*, 2016.

6.1 Introduction

Blood typing is the process of determining the presence or absence of certain antigens on the hosts red blood cell (RBC). These inherited traits manifest as polymorphic glycans on erythrocyte membranes and determine one's blood type as A, B, or O and D (Rh) [191]. Although their functional purpose remains largely unknown [197], identifying these antigenic carbohydrates is paramount to transfusion medicine as they give rise to naturally occurring alloantibodies against the antigens absent from the host's red blood cells [191]. Hemolytic responses due to improperly matched blood between recipients and donors account for approximately 25% of fatalities associated with transfusion errors [72]. Therefore, it is important to establish blood type compatibility between donor and recipient.

While many approaches to type blood exist, tube-based agglutination assays remain the gold-standard [71]. Agglutination assays can be either direct or indirect. For direct typing assays, IgM antibodies that target specific antigens are introduced into suspended RBCs from the blood sample. RBCs clumping together and then precipitating out of solution indicate the presence of the antigen. For indirect typing, special reference RBCs are added to diluted

plasma (absent of RBCs). Agglutination indicates the presence of the alloantibody. For both cases, a technician observes the result and rates the agglutination semi-quantitatively on a scale of +1 (weak) to +4 (strong).

In 2013, more than 14 million units of whole blood were collected in the U.S. for transfusions [70]. Every unit underwent screening to determine the blood group type (A, B, AB, O, and Rh) and to detect for certain blood-borne infectious pathogens. While 68 potential disease threats have been identified to transfusion safety [199], donated blood is currently screened for bacteria, Hepatitis B and C virus (HBV and HBC, respectively), Human Immunodeficiency virus Types 1 and 2 (HIV), Human T-Lymphotropic virus types 1 and 2 (HTLV), *Treponema pallidum* (syphilis), and West Nile virus (WNV). While not required for all transfusions, testing for *Trypanosoma cruzi* (Chagas disease) and Cytomegalovrius (CMV) are often performed for special needs patients [186]. These tests involve different laboratory methods including nucleic acid amplification, isoagglutinin detection, and antibody screening [191, 199, 200]. Testing can take hours and typically occurs in clinical laboratories by specially-trained technicians that prepare samples, run the test, and then interpret the results. A portable diagnostic capable of simultaneously typing blood and screening for pathogens could improve work flows and minimize the likelihood of transfusion errors.

Multiplexed platforms that utilize microarrays and SPR have been investigated for blood typing [71, 298–301] but have yet to be extended to the full panel of tests required. Bonanno *et. al* used a porous-silicon, label-free optical biosensor to detect rabbit IgG from whole rabbit blood with minimal sample preparation but no typing of human RBC antigens directly. Next-generation sequencing that can predict antigen phenotypes based on known blood group alleles has also been investigated [302, 303]. The drawback with this approach is that testing is cumbersome and blood group genes encode glycosyltransferases that in turn determine the oligosaccharide epitopes. Rare alleles lead to slight glycosyltransferase variations which ultimately impact antigen phenotypes [191, 291]. Paper-based diagnostic approaches have also been demonstrated for direct typing [304–306] but have yet to integrate pathogen screening, a critical step to ensuring the safety of the transfusion recipient. To this

end, we investigated the use of silicon photonic biosensors to phenotype RBCs and serum since they have already demonstrated multiplexed detection of antibodies, nucleic acids, and pathogens [20, 23, 40, 43, 46, 47].

Silicon photonics is a chip scale technology that guides near-infrared light in nano-scale silicon wires, or waveguides. While high performance computing and data communication applications have catalyzed their development [53, 211, 212], silicon photonic also shows promise for biosensing [12, 41] and for lab-on-chip systems [14, 42, 307]. These devices use an electric field to detect molecular binding events on the waveguide's surface. The electric field distribution within the waveguide, referred to as mode profile, depends on the light's polarization and wavelength, as well as the waveguide's geometry and material properties. For a single mode waveguide, a portion of the electric field mode profile resides outside the waveguide as an evanescent field.

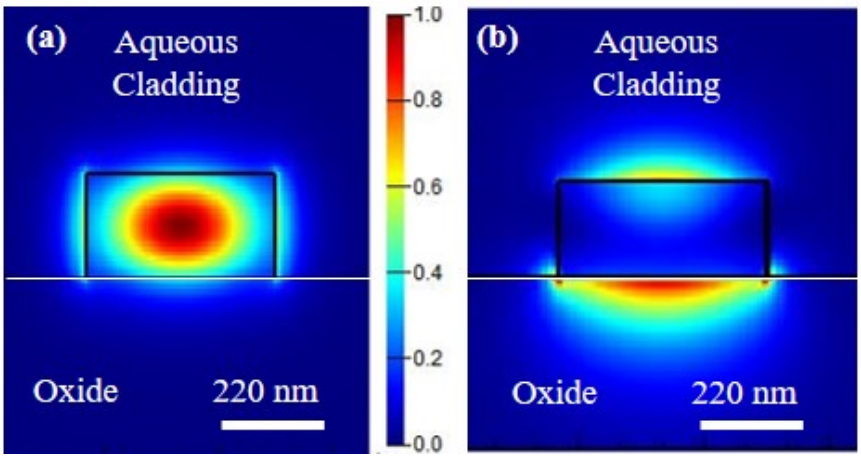

Figure 6.1: Modes in silicon photonic waveguide 2D cross-sections. (a) Fundamental TE mode profile in a 220 nm by 500 nm waveguide on buried oxide with aqueous cladding. (b) Fundamental TM mode profile in a 220 nm by 750 nm waveguide on buried oxide with aqueous cladding. The color bar represents the intensity distribution of the mode's electric field.

Figure 6.1(a) and (b) show the electric field distribution for the fundamental TE and TM mode in a silicon waveguide on a silicon oxide substrate and with aqueous cladding on remaining three sides. Since biomolecules have a higher refractive index compared to the aqueous media in which they reside [99], molecules that bind on the waveguide's surface, as shown in Fig. 6.2(a) and (b), alter the propagation properties of the mode, namely the effective index, n_{eff}, and loss. For a ring resonator, the resonance condition is met when the optical length of the resonator ($2\pi R \cdot n_{eff}$, with R being the radius of the ring) is a multiple of the wavelength [91]. A change in the effective index caused by a binding event will shift the resonant wavelength accordingly (see Fig. 6.2(c)). These wavelength changes can be quantified using a tunable laser and power meter and if continuously tracked, result in a sensogram similar to one shown in Fig. 6.2(d). The sensitivity of such sensors is largely dependent on the mode overlap with the analyte. From Fig. 6.1 it can be deduced that a TM mode is expected to be more sensitive compared to TE. However, due to the corresponding increase in absorption loss in the aqueous cladding for the TM mode, the intrinsic limit of detection remains constant for both modes [20].

While silicon photonic biosensors have been demonstrated for detection of proteins [43, 44], nucleic acids [45], viruses [46], and bacteria [47], their ability to perform direct or indirect blood typing has yet to be demonstrated. Therefore, the performance of silicon photonic biosensors for direct and indirect typing of human blood samples is investigated herein. In addition, the response of TE and TM mode ring resonators is compared to elucidate the adsorbed film thickness as described by Hoste et al. [229]. The remaining sections describe the design, fabrication, and characterization approach of both rings and the observed results from the direct and indirect blood typing assays.

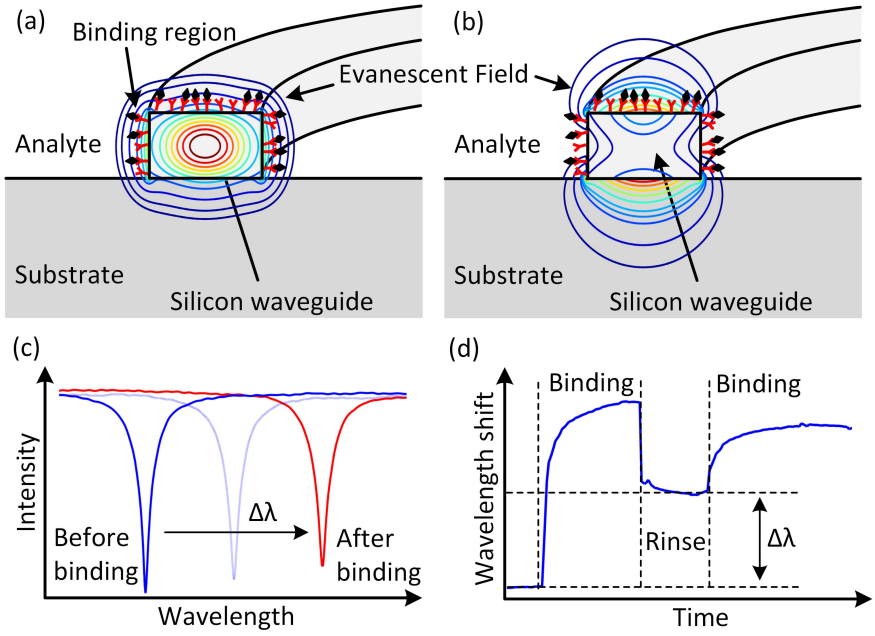

Figure 6.2: TE and TM biosensor principle of operation. Electric field intensity of a fundamental (a) TE and (b) TM mode profile in a silicon waveguide showing the evanescent field overlap with the substrate (silicon oxide) and adsorbed biomolecules in the aqueous cladding. (c) Example of the biosensors resonant wavelength shift resulting from an effective refractive index change caused by adsorbing biomolecules. (d) Sensogram of tracked peaks over the course of an assay. The permanent wavelength shifts indicate bound molecular adlayers to the waveguide's surface.

6.2 Methods and Materials

6.2.1 Design

Ring resonators were developed according to the methods described in Bogaerts *et al.* [91]. All designs assumed a 220 nm thick silicon waveguide on 2 µmof silicon oxide. Lumerical's MODE Solutions [289] were used to evaluate modal fields in 2D waveguides while custom MATLAB scripts were used to determine waveguide coupling gaps and lengths. Table 6.1

Table 6.1: **Ring resonator design parameters**

	TE ring	TM ring	units
Waveguide width	500	750	[nm]
Coupling length	7.24	3	[µm]
Optical path length	265.81	257.33	[µm]
Surface area	168.67	229.36	[µm^2]

summarizes design parameters and Figure 6.3 shows a screen clip of the GDS layout and photograph of fabricated devices.

6.2.2 Fabrication

The photonic biosensors were fabricated through a CMOS foundry compatible fabrication process (deep-UV lithography, 193nm) offered through ePIXfab [220] at IMEC in Belgium. The multi project wafer (MPW) was organized by CMC Microsystems. Waveguides were patterned onto 220 nm thick crystalline silicon on top of wafers with 2 µm of silicon-oxide.

To improve durability, reuse, and reduce optical losses in the long waveguides between the vertical grating I/O couplers and biosensors chips were cladded with CYTOP [238]. CYTOP is a perfluoro-polymer with exceptional chemical resistance and useful optical properties with over 95% light transmittance through deep ultra-violet (DUV) to nea-infrared (NIR) range and a refractive index of 1.34 [238]. Openings in the cladding were created to expose the biosensors to the aqueous environment [239].

6.2.3 Sensor characterization

Figure 6.3 shows a photograph of the silicon gasket used to create channels over the sensors. Bulk sensitivity was assessed in an aqueous environment using refractive index standards made from ultra-pure deionized water (Barnstead Nanopure, Thermo Scientific) and sodium

chloride (NaCl, Acros Organics, Thermo Fisher Scientific). Solutions of 62.5 mM, 125 mM, 250 mM, 500 mM, and 1 M NaCL were degassed under vacuum using an ultrasonic bath (VWR B2500A-MTH) and measured with a Reichert AR200 digital refractometer (Depew, NY).

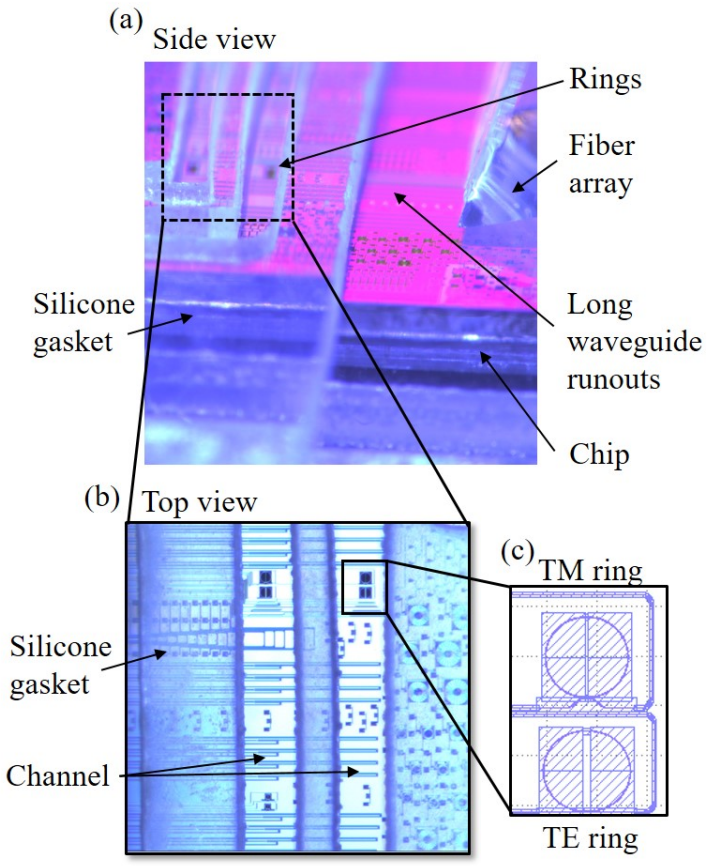

Figure 6.3: TE and TM mode rings in fluidic channels. (a) Side view showing the fiber array that was used to couple light on and off the chip, the long waveguide runouts, and the sensors in the silicone gasket channel. (b) Overhead photograph showing both sets of TE and TM mode rings in separate channels (functionalized as the target and control). (c) GDS screen clip showing the layout of the TE and TM mode rings.

Surface sensitivity was characterized via layer-by-layer adsorption of electro statically

charged polymers as demonstrated by Bailey *et al.* [24]. Briefly, sensors were cleaned with Piranha solution before exposure to polyethylene imine (PEI, 5 mg/mL), a positively charged polymer to provide a substrate anchor for subsequent bi-layers. Next, alternating solutions of negatively charged polystyrene sulfonate (PSS, 5mg/ml) and positively charged polyallylamine hydrochloride (PAH, 5mg/ml) were sequenced across the sensor to create bilayers reported to be $\approx 3 \pm 0.2$ nm thick [24]. The introduction of each electrostatic polymer was rinsed using Tris buffer (0.5mM, 100mM NaCl, pH 7.1) and water for to avoid precipitation and clogging.

Susceptibility to temperature variation was assessed by thermally tuning the chip in an aqueous environment and then performing multiple wavelength sweeps. Peaks were tracked and averaged in a similar way to the bulk sensitivity.

6.2.4 Modeling and experimental validation

Waveguide mode profiles were determined using MODE Solutions (Lumerical, Canada) to help validate the observed performance metrics and film thickness absorbed in biosensing assays. For TE sensors, the model consisted of a 220 nm by 500 nm waveguide on buried oxide with aqueous cladding on three sides. TM mode sensors were simulated under similar conditions except the waveguide dimensions were 220 nm by 750 nm. Bulk sensitivity for both waveguide geometries were simulated by performing frequency sweeps using measured refractive index values from the NaCl solutions. Surface sensitivity experiments using the electrostatic polymers were validated simulating adlayers with a refractive index of 1.68 in 10 nm increments up to 200 nm with a background cladding similar to water (n=1.333) [24]. Surface sensitivity predictions towards biofilms were determined by mimicking protein adlayers with a refractive index of 1.48 [98, 99] in 10 nm increments up to 200 nm with a background cladding similar to water (n=1.333). Modeling results were fitted with experimental data.

6.2.5 Blood typing reagents

Bovine serum albumin (BSA) and streptavidin were purchased from SigmaAldrich (St. Louis, MO, USA). DryCoat Assay Stabilizer was purchased from Virusys Corporation (Taneytown, MD, USA). For direct typing assays, biotinylated goat anti-mouse IgM antibodies were purchased from Fisher Thermo Scientific (Rockford, IL, USA). Murine IgM antigen-A and antigen-B antibodies were provided by Dr. Jill Johnsen of Bloodworks Northwest Research Institute (Seattle, WA, USA). A direct typing capture reagent mix (1:1 molar ratio) was prepared by incubating biotinylated goat anti-mouse IgM to either mouse antigen-A or B IgMs for one hour at 4^oC. Biotinylated anti-glycophorin A IgG antibody (positive control) was purchased from Miltenyi Biotec (San Diego, CA, USA). For indirect typing assays, monoclonal A and B typing antibodies were purchased from Immucor (Norcross, GA, USA). Biotinylated multivalent polyacrylamides containing blood group antigens A and B (PAA-A and PAA-B) were purchased from GlycoTech (Gaithersburg, MD, USA), as well as the same biotinylated polymers without either antigen (PAA). Goat IgG anti-mouse IgM and murine IgG anti-human IgG/M/A antibodies for secondary amplification were purchased from Thermo Fisher Scientific (Rockford, IL, USA).

Freshly drawn human blood samples stored in an appropriate anticoagulant at 4^oC were obtained in collaboration with Dr. Jill Johnsen of the Bloodworks Northwest Research Institute (Seattle, WA, USA). Whole blood samples were centrifuged at 2000 G for 10 minutes at 4^oC. Following centrifugation, plasma and the buffy coat layer were removed from the cell pellet and stored separately. Undiluted human plasma was analyzed directly while whole red blood cells were first diluted 1:10 in phosphate buffered saline (PBS) before use.

6.2.6 Reagent validation

Antigenicity of the RBCs was verified, as well as binding specificity of capture agents, prior to biosensing assays. Erythrocyte antigenicity was validated using a standard agglutination assay with commercially available monoclonal A and B typing IgM antibodies purchased from

Immucor (Norcross, GA). Capture reagent specificity was validated by direct comparison of sensor response to cells binding specifically to capture reagents with respect to sensor response to cells binding to anti-glycophorin A positive control. For indirect typing assays, the biotinylated multivalent polyacrylamides blood group antigens A and B (PAA-A and PAA-B) were validated using the commercially available IgM antibodies from ImmuCore. Figure 6.4 shows an example of a validation assay using TE mode rings. The large signal difference during the amplification step using anti-mouse IgM (Immucor; Peachtree Corners, GA) confirms the validity of capture chemistries.

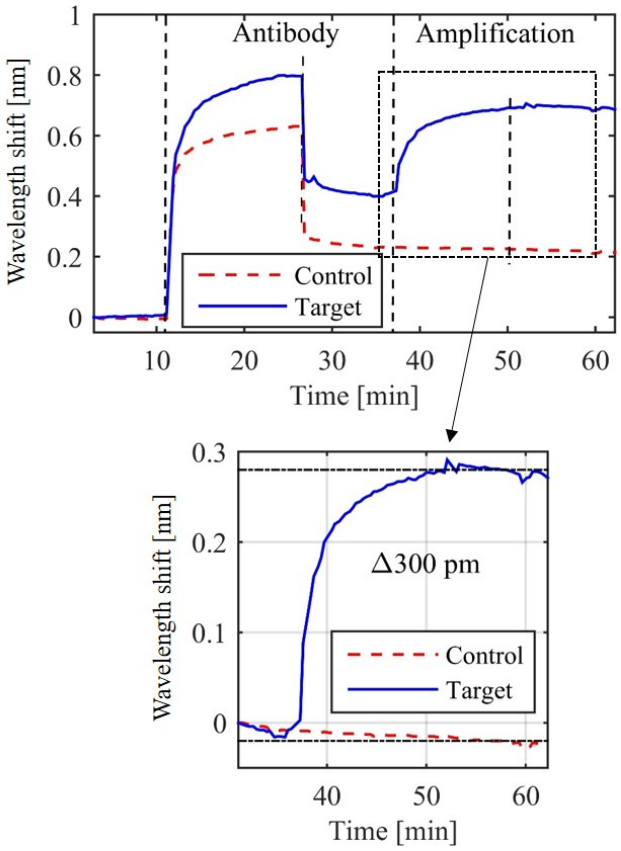

Figure 6.4: Example of assay to validate reagents for indirect typing. The magnified inset shows the amplification step normalized and resulting in a 300 pm offset.

6.2.7 Sensor functionalization

To functionalize chips for direct typing assays, streptavidin (0.1 mg/mL) was passively absorbed to the sensors' surface for at least three hours at room temperature. The chips were then rinsed with PBS and blown dry using house air. A laser-cut silicon gasket was placed on the chip to form two separate wells as shown in Figure 6.5.

Using a silicone spotting gasket, one channel was further functionalized with an antigen-A capture reagent mix, and the other channel with an antigen-B capture reagent mix. The chips were incubated in a humid environment for one hour at room temperature. Following incubation, chips were rinsed with PBS, and subsequently blocked with 1 mg/mL BSA in PBS for at least 20 minutes. The chips were rinsed again, dipped in DryCoat, and blown dry to be stored until use.

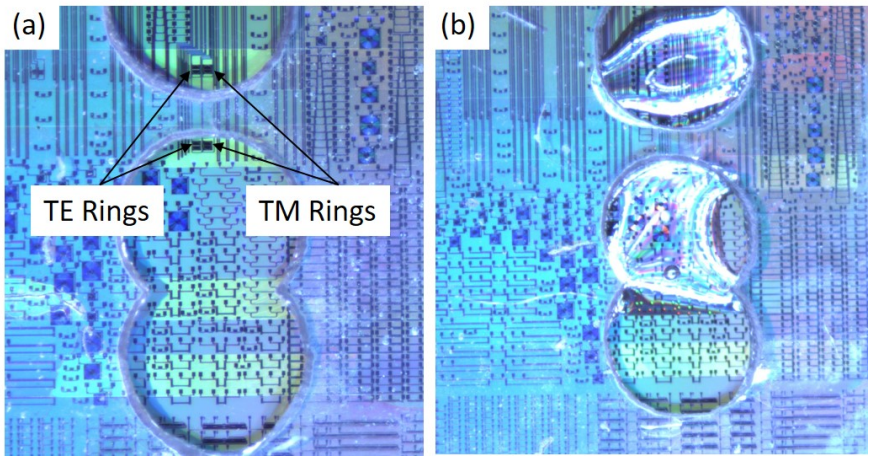

Figure 6.5: Offline functionalization. (a) Photograph of the 500 µm - thick silicone spotting gasket positioned over sets of TE and TM mode rings. (b) 25 nL - droplets of reagents (either PAA-A, PAA-B, or conjugated antibody complex for direct typing) to functionalize the streptavidin-coated sensors.

To functionalize chips for indirect typing assays, chips were passively coated with 0.1 mg/mL streptavidin in PBS for at least three hours at room temperature. Chips were then

rinsed with PBS and blown dry. A silicone spotting gasket was used to separate channels on the chips allowing for PAA-A to be spotted on one sensor and PAA-B on the other. Spotted chips sat in a humid environment for at least one hour before being rinsed off with PBS and blown dry. Finally, the chips were blocked in 1 mg/mL BSA solution in PBS for at least 20 minutes, rinsed, dipped in DryCoat, and blown dry for storage. PAA-A and PAA-B antigenicity was validated by comparing sensor responses of ImmuCore's antigen-A/B antibodies binding to PAA-A or PAA-B with respect to their binding to a PAA negative control.

6.2.8 Test platform

A custom fiber-array based probe station, built and previously described by our group [20], enabled the automated testing and characterization of devices. Figure 6.6 shows a picture of the main stage and two channel flow cell used for characterization and biosensing assays. A syringe pump, operating in withdraw mode, sequenced reagents from two well plates mounted on a motorized stage. In addition to orchestrating tests, our custom analysis software helped analyze acquired datasets. The analysis tool includes features such as: peak fitting, reference channel subtraction, and sensogram signal difference measurements.

6.3 Results and Discussion

This section details the experimental observations and discusses their significance. Before performing the blood typing assays, the TE and TM mode rings were characterized to quantify their native performance in aqueous environments. The rings were then functionalized for indirect and direct typing human blood. Assay replicates were performed on different samples to ensure operation across a wide range of human subjects.

6.3.1 Sensor characterization

While there has been a fragmented effort to define an agreed upon set of performance metrics for refractive index sensors, objective measures exist to help compare the performance

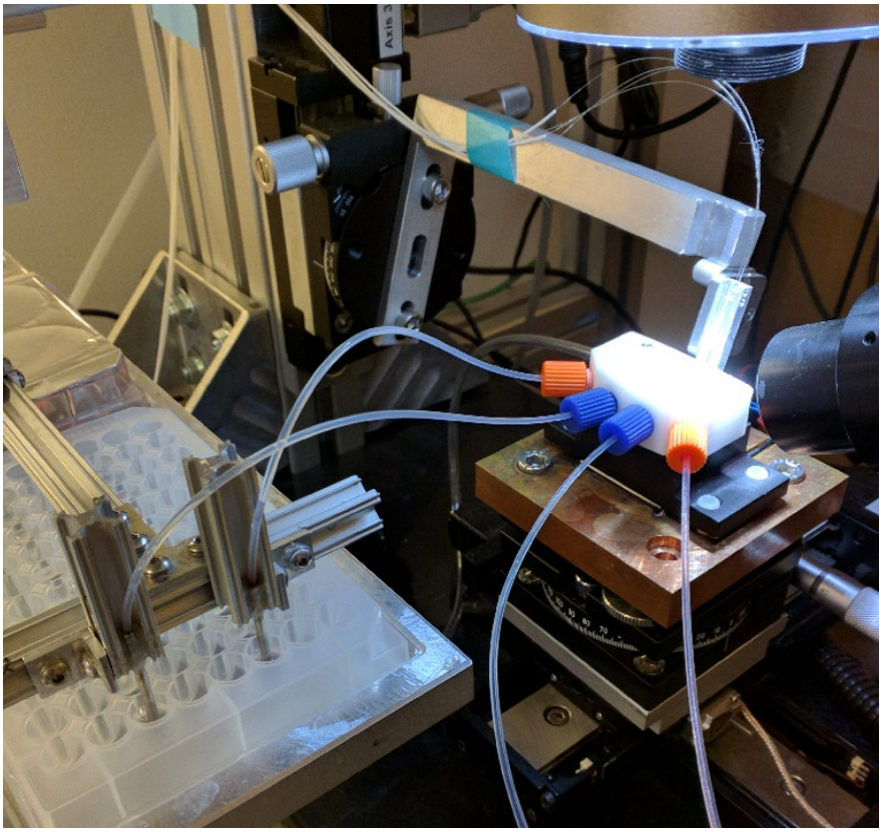

Figure 6.6: Test setup and custom analysis software. (a) Photograph of the automated probe station used to conduct biosensing assays. The thermally-tuned chip stage is seen with a mounted, four-port Teflon flow cell with tubing to sequence reagents from the well trays over the sensors. The fiber array used to couple light on and off the chip is positioned behind the flow cell. (b) An example screen clip of our custom analysis software used to process assay data post-acquisition. The two upper left figures show the scanned spectra while the upper right two figures show the tracked peak and fitting results. The bottom panel shows the acquired sensogram based on the resonant peak shift throughout the assay.

of different silicon photonic biosensors. These include sensitivity, Q, and limit of detection [103, 111, 112]. Sensitivity quantifies the change in resonant wavelength (λ_{res}) to an environmental factor such as refractive index changes in the aqueous cladding (S_{bulk}), addition

of molecular adlayers onto the waveguide's surface ($S_{surface}$), and system-wide temperature changes (S_{temp}) [20].

Bulk sensitivity

Bulk sensitivity describes how bulk refractive index changes around the waveguide impacts its resonant wavelength. It is highly dependent on the modal overlap with the cladding (via an evanescent field) and is one of the parameters that determines the sensor's intrinsic limit of detection (Eq. 6.3). Bulk sensitivity (S_{bulk}) is defined as:

$$S_{bulk} = \frac{\Delta\lambda_{res}}{\Delta n_{clad}} = \frac{\lambda_{res}}{n_g}\left(\frac{\partial n_{eff}}{\partial n_{clad}}\right)_{\lambda_{res},n^0_{clad}} \tag{6.1}$$

We performed MODE simulations [289] on a 500 nm by 220 nm waveguide to predict the bulk sensitivity of the fundamental TE mode. In the same way, a 750 nm by 220 nm waveguide was simulated to predict the bulk sensitivity of the fundamental TM mode. Simulated models suggest a bulk sensitivity of 44.7 nm/RIU for TE and 146.6 nm/RIU for TM in an aqueous environment at a central wavelength of 1505 nm.

We sequenced titrated NaCl solutions across the fabricated TE and TM mode ring resonators while monitoring its resonant wavelength to determined S_{bulk} experimentally. Figure 6.7 shows the observed resonant wavelength shifts to different concentrations of NaCl solutions for a TE and TM mode ring. The slope of the steps determines the bulk sensitivity. We observed sensitivities of 41.2 $\pm$ 1.6 nm/RUI for the TE mode rings and 146.8 $\pm$ 2.5 nm/RUI for the TM mode rings. Measurements were performed in triplicate and agree with the simulated model.

Surface sensitivity

Surface sensitivity ($S_{surface}$) is important for biosening applications involving the adsorption of biomolecular adlayers. It has been reported that protein adlayers exhibit a refractive index of 1.48 [98, 99] and often result in 1-3 nm adlayers when adsorbed to a native oxide

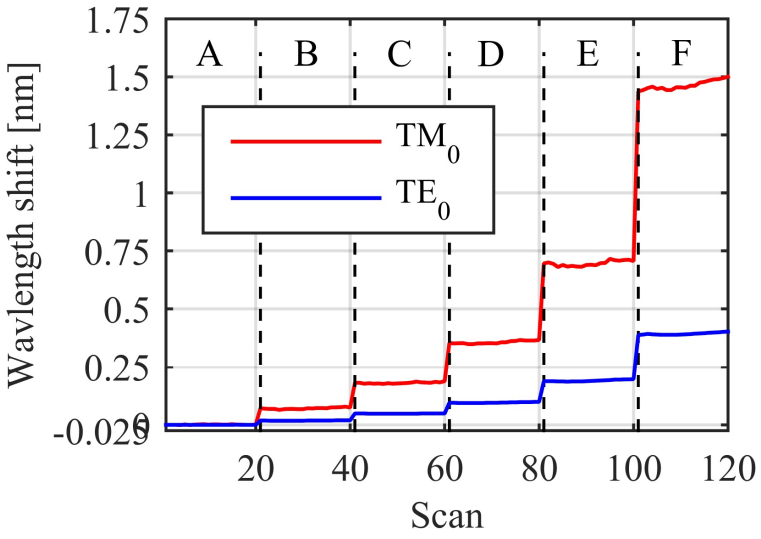

Figure 6.7: Sensogram of TE and TM mode ring resonator wavelength shifts when subjected to refractive index solutions. Their bulk sensitivity is determined by averaging the wavelengths at each step and fitting a line through the points.

surface [150, 151, 156, 159]. Therefore, a waveguide's resonant wavelength response ($\Delta\lambda_{res}$) to homogenous, protein adlayers can be calculated using:

$$\Delta\lambda_{res} = \frac{\lambda_{res}}{n_g}\left(\frac{\partial n_{eff}}{\partial d_{ad}}\right)_{d_{ad}^0}\Delta d_{ad} \tag{6.2}$$

where d_{ad} is molecular layer thickness, n_g is the group index, n_{eff} is the mode's effective index, and λ_{res} is the resonant wavelength. To better understand the ring's optical response to adsorbed molecular films during blood typing assays, we performed MODE simulations on a 500 nm wide TE and 750 nm wide TM mode waveguide operating at 1505 nm wavelengths to determine the surface sensitivity of the rings investigated herein. Simulations using refractive index adlayers (n=1.68) to mimic the alternating electrostatic polymer bi-layers correlated to the experimentally observed results providing confidence in the simulation model. Simulations were re-run with a refractive index representative of protein adlayers (n=1.48). Figure 6.8(a) shows the results of simulated adlayers up to 200 nm thick. While both TE and TM resonant wavelengths approach a horizontal asymptotes, TM waveguides offer improved

sensitivity to thicker protein adlayers due to their larger evanescent field [20]. Figure 6.8(b) shows shift in resonant wavelength [nm] per nanometer of protein adlayer. The ratio of these sensitivities is plotted on the y-axis and reveals that TM mode waveguides offer a 2x sensitivity improvement at the waveguide surface and 3x improvement for a 30 nm-thick protein adlayer. Based on the biomolecules involved in the blood typing assays discussed herein, we expect protein films ranging from 10 to 50 nm thick [160, 161, 292]. By comparing the experimentally observed wavelength shifts for the TE and TM ring resonators, this ratio can help elucidate the biofilm thickness assuming identical surface functionalization and analyte binding to the TE and TM mode sensors.

Temperature sensitivity

While thermally tuning the chip stage during measurements minimizes signal noise from thermal drift, a sensor's temperature sensitivity (S_{temp}) is an important system-design consideration and may impact its detection limit in thermally diverse environments. To assess temperature sensitivity, resonant wavelengths for TE and TM ring resonators were monitored while thermally tuning the chip between 15 and 40^{o}C. Measurements were performed in an aqueous environment on three TE and three TM mode rings across three different chips. We observed a thermal sensitivity of 39.8 $\pm$ 0.75 pm/K for the TM mode rings and 70 $\pm$ 0 pm/K for their TE counterparts. These results indicate that TM mode sensors exhibit more thermal variation immunity. This makes sense as silicon's thermal conductivity is 1.8x more than water and the majority of TE modes exist within the waveguide while the majority of the TM mode exists outside the waveguide (see Figure 6.1).

Quality factor and detection limit

The quality factor (Q) is a measure of how many round trips (in average) a photon makes in a resonator. It is a dimensionless number that incorporates the resonator's loss in terms of the material's index of refraction [103]. Q can be quantified experimentally by dividing the resonant peak's wavelength (λ_{res}) by its full width at half its maximum (FWHM) approxi-

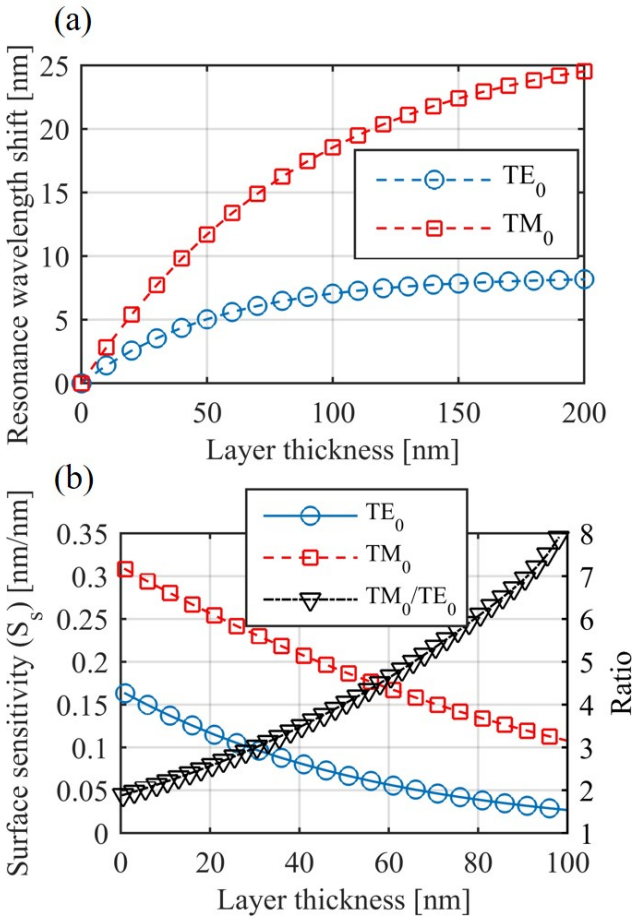

Figure 6.8: Surface sensitivity simulations. (a) Resonant wavelength shift for a 500 nm-wide waveguide supporting the fundamental TE mode and a 750 nm-wide waveguide supporting the fundamental TM mode up to a homogeneous protein adlayer 200 nm thick (n=1.48 with an aqueous background cladding of 1.33). (b) Resonant wavelength shift for similar waveguide dimensions and modes except normalized to wavelength shift per nanometer of adlayer up to a 100 nm thick protein film.

mates Q. Higher Q's reduce the sensor's spectral noise [112] and improve its instrinsic limit of detection ($iLoD$). The $iLoD$ can be understood as the minimum index change required to shift the resonance wavelength by one resonator line width ($\delta\lambda_{3dB}$) [20, 52]. Algebraically,

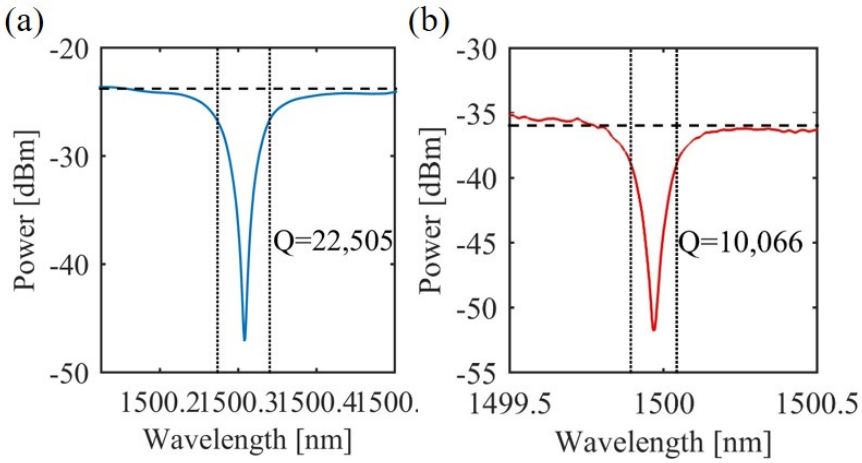

Figure 6.9: Measured resonant (a) TE and (b) TM peaks used to approximate resonator Q.

$iLoD$ is:

$$iLoD = \frac{\lambda_{res}}{Q \cdot S} \tag{6.3}$$

where λ_{res} is the sensor's resonant wavelength [nm], Q is the quality factor of the resonator, and S is the bulk sensitivity [nm/RIU]. Using the FWHM approximation, the fabricated TE rings exhibit a Q of $22.5 \cdot 10^3$ and $iLoD$ of $1.6 \cdot 10^{-3}$ [RIUs]. Likewise, the TM rings have a Q of $10.1 \cdot 10^3$ and $iLoD$ of $1.0 \cdot 10^{-3}$ [RIUs].

Table 6.2 summarizes the performance of the TE and TM mode rings used for blood typing. The increased bulk and surface sensitivity of the TM mode ring are expected as more of the mode overlaps the aqueous environment. The absorptive loss is also higher resulting in a lower Q. The temperature sensitivities correlate well to the simulated values. Based on these performance metrics, the TM mode rings are expected to provide enhanced sensitivity for the blood typing assays.

Table 6.2: **Summary of experimentally measured (Meas.) and simulated (Sim.) performance of the 1550 nm wavelength TE and TM mode ring resonator sensors used for blood typing**

	TE Meas. (Sim.)	TM Meas. (Sim.)	Units
S_{bulk}	41.2 (44.7)	146.75 (146.6)	[nm/RIU]
$S_{surface}$	(0.16)	(0.31)	[nm/nm]
S_{temp}	70 (67)	39.8 (38)	[pm/K]
Q	22.5k	10.1k	[]
$iLoD$	$1.6 \cdot 10^{-3}$	$1.0 \cdot 10^{-3}$	[RIU]

6.3.2 Indirect typing

Indirect typing involves the detection of serum alloantibodies (ab) which the body naturally raises against blood types that are not its own [191]. Screening for alloantibodies can be important in certain situations (e.g. multiply transfused patients) since the body can naturally raise antibodies to infectious pathogens with small phenotypic variations to the A and B antigens [191]. Figure 6.10 shows a schematic representing the steps involved to functionalize the sensor and perform indirect typing assays.

Methods to functionalize the sensors are described in section 6.2.7 and depicted in Fig. 6.10(a)-Fig. 6.10(c). For indirect typing assays, sensors were subjected to undiluted human plasma followed by a buffer rinse (Fig. 6.10(d)). A secondary antibody (anti-human IgG/IgM/IgA) to amplify the presence of the bound antigen-A or antigen-B antibodies was used to improve the signal-to-noise ratio (Fig. 6.10(e)). While replicate assays were performed, Figure 6.11 shows the acquired sensogram for an assay with type A plasma (targeting antigen-B ab) using a TE mode ring while Figure 6.12 shows the sensogram for its TM counterpart. The enlarged inset of the amplification step shows a difference of 395 pm and 988 pm between the control (antigen-A ab) and target (antigen-B ab) for the TE and TM rings, respectively. Sig-

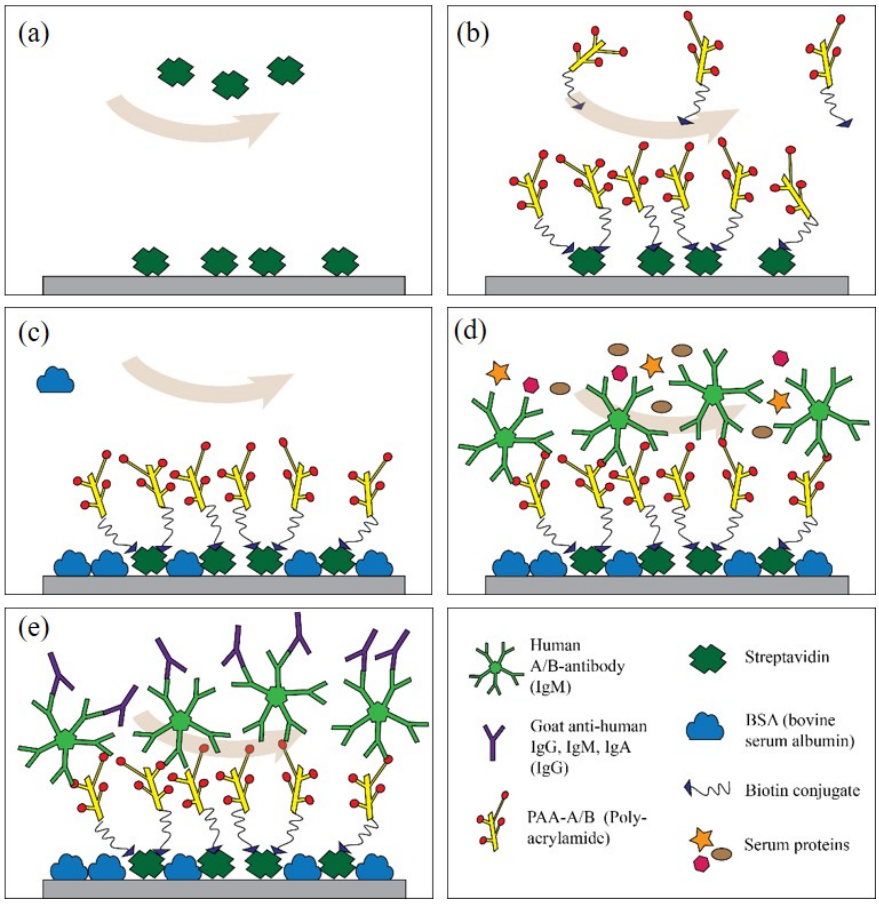

Figure 6.10: Schematic representing the steps involved with indirect typing assays. (a) streptavidin passively adsorbed to sensors. (b) Absorption of biotinylated multivalent polyacrylamides with A and B blood group antigens (PAA-A and PAA-B) to the streptavidin coated surface. (c) Blocking any remaining exposed surfaces on the sensor using BSA. (d) Introduction of undiluted human plasma samples and binding of IgM alloantibodies to surface-bound antigens. (e) Signal amplification using goat IgG anti-human IgG/M/A. Steps (a)-(c) were conducted off-line while steps (d)-(e) were performed during the assay.

nals were normalized at the start of the amplification step to accurately assess the resulting offset between the target and control channels.

Figure 6.11 shows the acquired sensogram for an assay with type B plasma (targeting

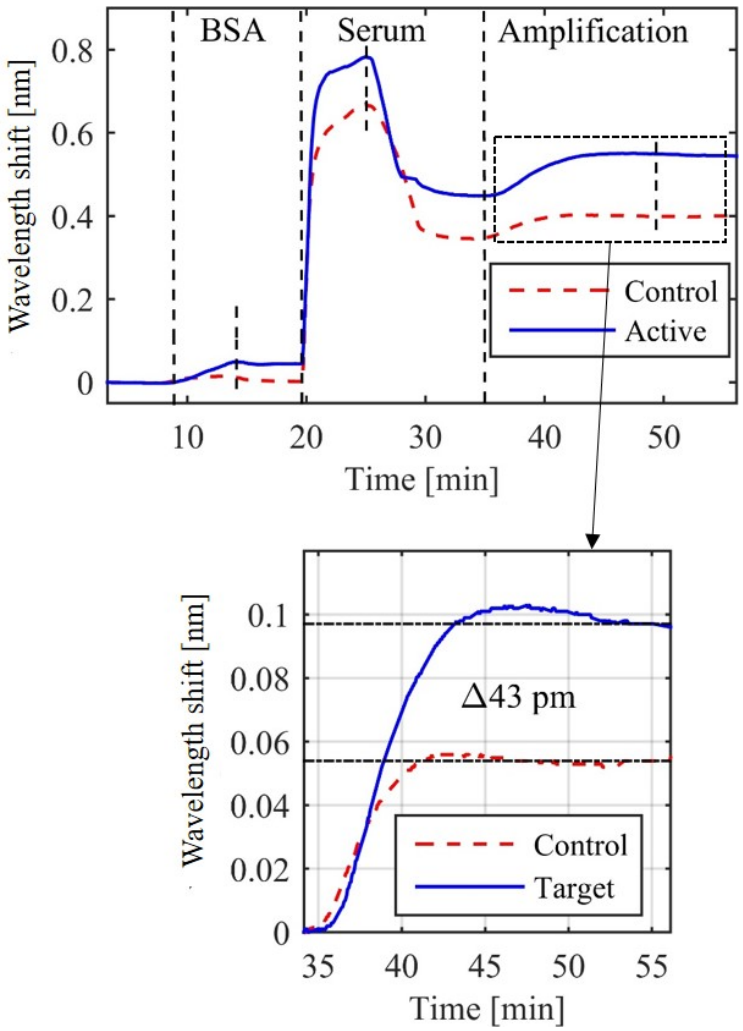

Figure 6.11: Indirect typing results for TE rings A-type plasma.

antigen-A ab) using a TE mode ring while Figure 6.12 shows the sensogram for its TM counterpart. The enlarged inset of the amplification step shows a difference of 43 pm and 161 pm between the control (antigen-B ab) and target (antigen-A ab) for the TE and TM rings respectively.

At least three replicates were performed for each indirect typing assay. All resulted in a differential signal after amplification. Table 6.3 summarizes the differences and ratios for A and B type plasma samples assessed using TE and TM mode rings.

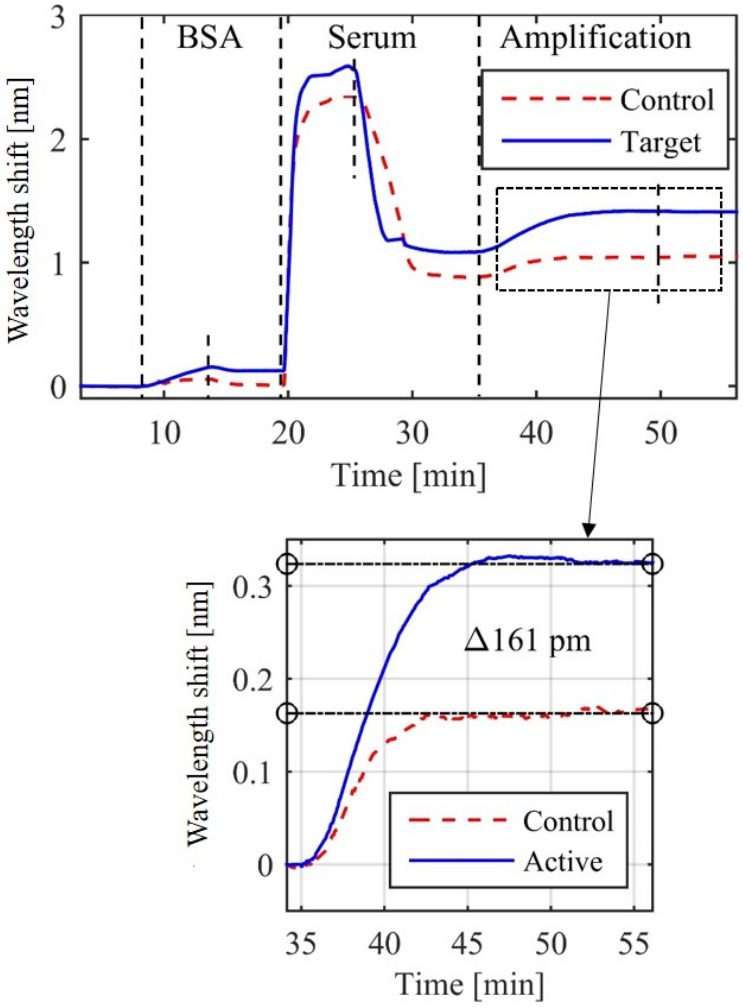

Figure 6.12: Indirect typing results for TM rings A-type plasma.

To assess the thickness of the biological film after amplification, the observed TM/TE ratios (from Table 6.3) were compared with the predicted adlayer thickness shown in Figure 6.8. For assays involving A-type plasma, an average ratio of 3.04 between observed TM and TE offsets suggests an adlayer thickness of 67 nm. In the same way, an average ratio of 3.04 observed for B-type plasma assays suggests a film thickness of 67 nm. Considering the reported sizes for the molecules involved in these assays (eg: $\approx$ 40 nm diameter for IgM and $\approx$ 14 nm for IgG antibodies [99, 156, 292]), these findings correspond well to expected

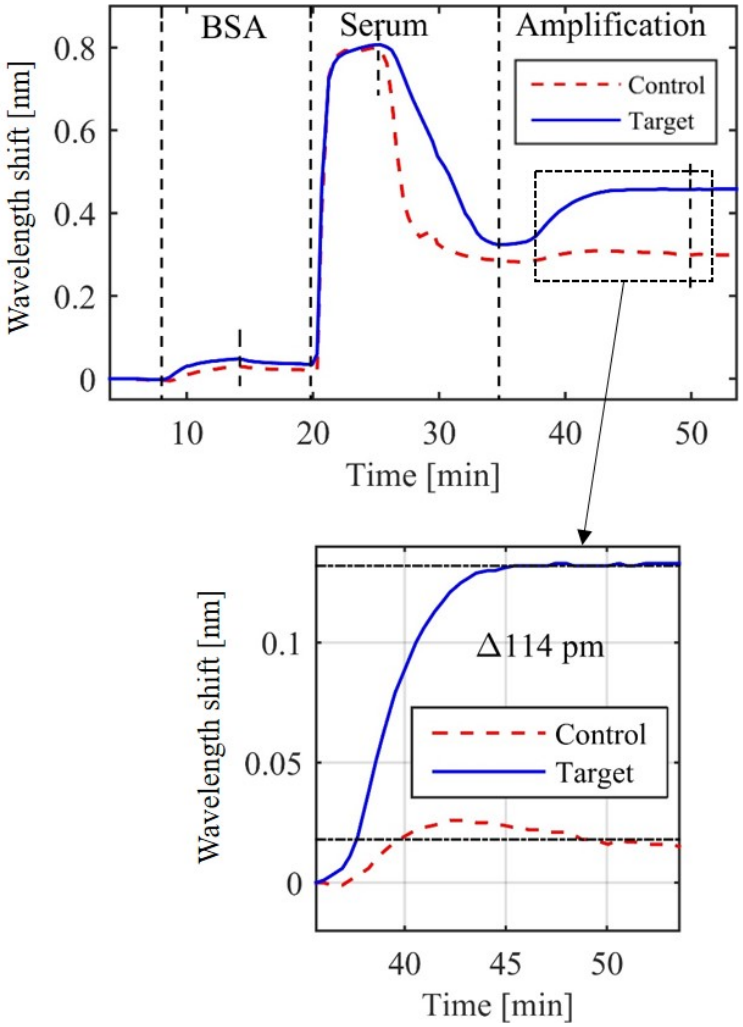

Figure 6.13: Indirect typing results for TE rings B-type plasma.

results.

The large standard deviation can be attributed to the variation in the sensor functionalization and titers across the human samples. While typings fall into one of four primary categories (ABO and D), previously reported research suggests that weak forms of A and B antigens exist resulting in sub-types within the A and B blood groups and antibody titers vary widely [191]. Since the TE and TM rings were functionalized with A and B antigens specific to a particular phenotype, slight variations in serum antibodies may impact the

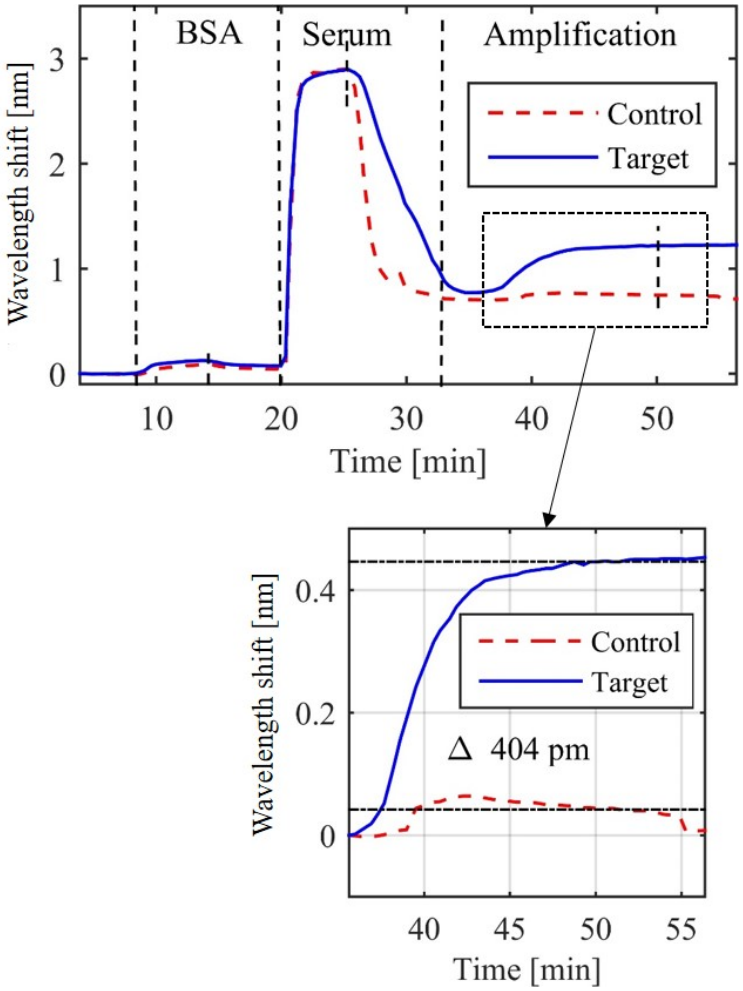

Figure 6.14: Indirect typing results for TM rings B-type plasma.

antigen-antibody binding across the human plasma samples. In addition, using the amplified offset ratio to determine adlayer thickness assumes identical functionalization and antibody capture on all four sensors which is highly unlikely with any biological system.

6.3.3 Direct typing

Direct typing involves the direct detection of carbohydrate-based A and B antigens decorating many membranous proteins on the erythrocyte. Agglutination assays remain the

Table 6.3: **Amplification results for indirect typing assays**

	TM difference	TE difference	Ratio (TM/TE)
A-plasma	187 ± 72 pm	67 ± 20 pm	3.04 ± 1.59
B-plasma	201 ± 144 pm	66 ± 32 pm	3.04 ± 0.59

gold-standard method for direct ABO typing today, but having a chip-based platform with the ability to do direct and indirect typing across many blood group systems could be advantageous to improving transfusion medicine work flows. To that end, we investigated the ability of TE and TM mode ring resonators for direct typing RBCs presenting either A or B antigens. Figure 6.15 shows a schematic with the steps involved to functionalize the sensor and conduct a direct typing assay.

Methods to functionalize the sensors are described in section 6.2.7 and depicted in Fig. 6.15(a)-Fig. 6.15(d). After achieving a signal baseline, washed RBCs (1:10 dilution) were introduced while the sensor's resonant wavelengths were monitored (Fig. 6.15(e)). Figure 6.16 shows results for the direct detection of A-type RBCs using TE rings (Figure 6.16(a)) and TM rings (Figure 6.16(b)). A differential signal of 177 pm for the TE rings and 344 pm for the TM rings is observed without the need for further amplification. The permanent signal shift in the control channel (antigen-B functionalized rings) suggests non-specific binding from remnant plasma constituents in the sample or blebbing from the erythrocytes themselves (i.e., the shedding of membranous antigens into the plasma or suspension buffer).

Figure 6.17 shows results for the direct detection of B-type RBCs using TE rings (Figure 6.17(a)) and TM rings (Figure 6.17b). A differential signal of 165 pm for the TE rings and 266 pm for the TM rings is observed without the need for further amplification.

At least three direct typing assays were performed on different human samples. All resulted in a differential signal and Table 6.4 summarizes the offsets and ratios for the TE and TM mode rings.

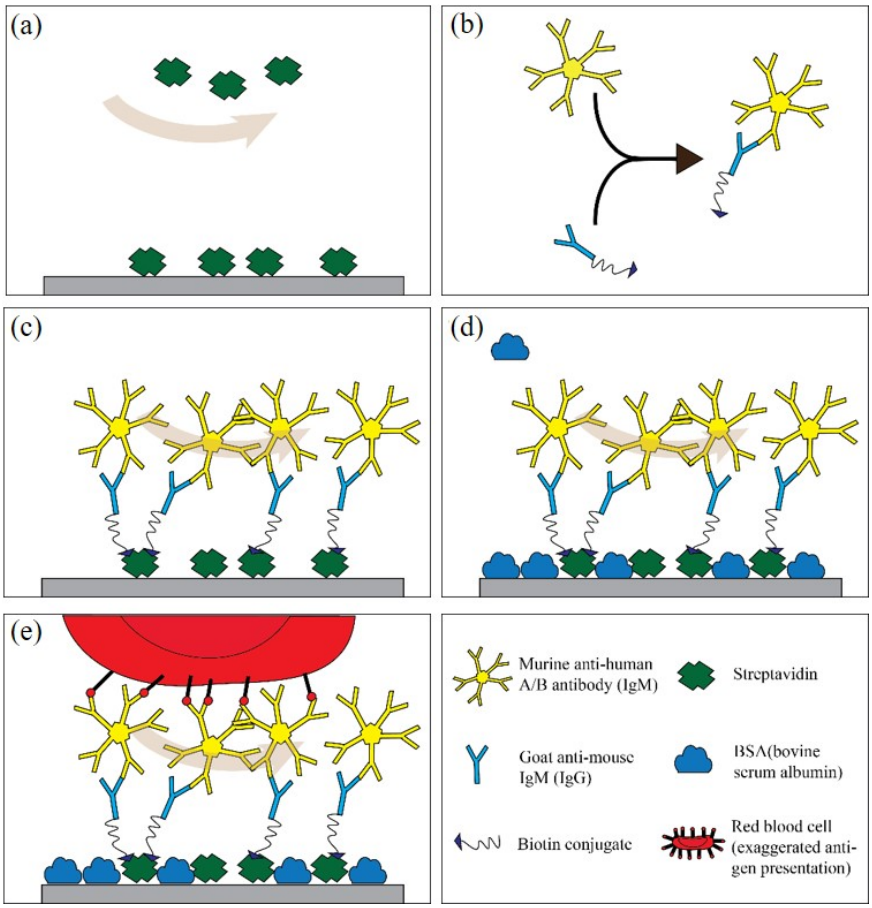

Figure 6.15: Schematic representing the steps involved with direct typing assays. (a) streptavidin passively adsorbed to sensors. (b) Conjugation of biotinylated (anti-human) IgG with human antigen-A or B group IgM. (c) Adsorption of biotinylated A and B group antigen antibody complexes to the streptavidin coated surface. (d) Blocking any remaining exposed surfaces on the sensor using BSA. (e) Introduction of human A or B type erythrocytes. Steps (a)-(d) were conducted off-line while step (e) was performed during the assay.

In a similar way to the indirect typing assays, the surface sensitivity TM/TE ratios shown in Figure 6.8 provide a qualitative assessment of biological film thickness observed during the direct typing assays. While this approach involves many assumptions like similar surface functionalization density and binding interaction from the sample which are impractical,

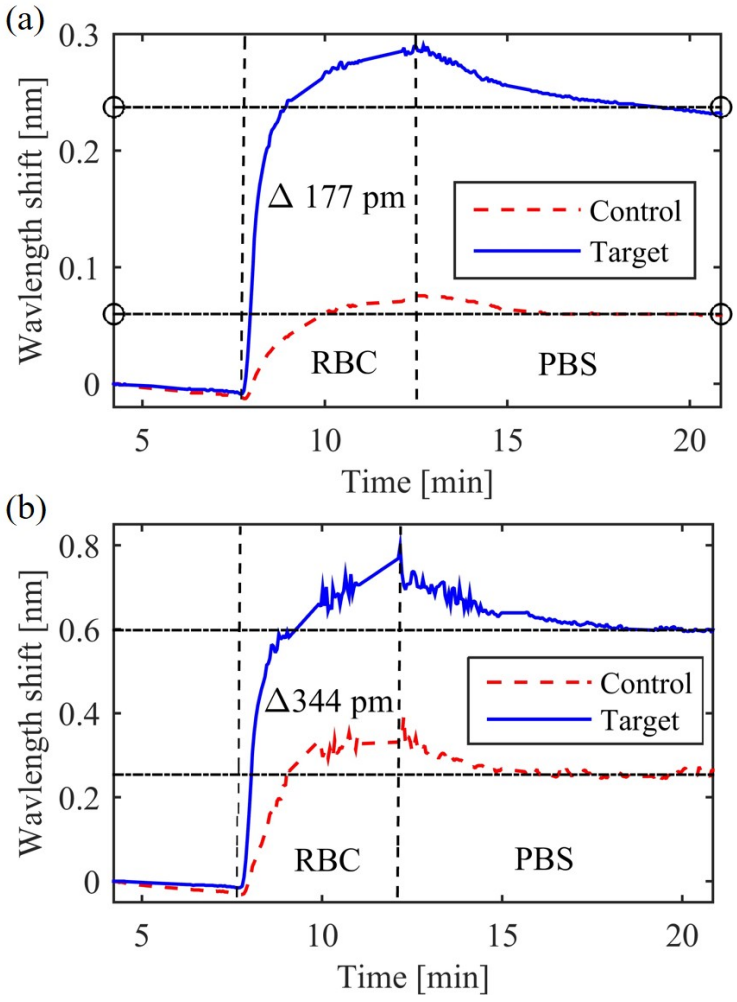

Figure 6.16: Direct A-type RBC detection. (a) TE rings. (b) TM rings

it offers some insight into the observed adlayer thickness across many assays. Since the sensors are functionalized by adsorbing streptavidin to a biotin-tagged IgG-IgM conjugated complex, we expect adlayers between 25-45 nm based on the species molecular sizes and possible deformation resulting from surface binding [156, 159–161]. Both sensors exhibit films within the expected range which provide additional confidence that the functionalized rings are a suitable platform to perform direct typing assays. The ratios, listed in Table 6.4) suggest a film thickness of 5 to 27 nm for A-type RBC assays and 32 to 48 nm for B-type

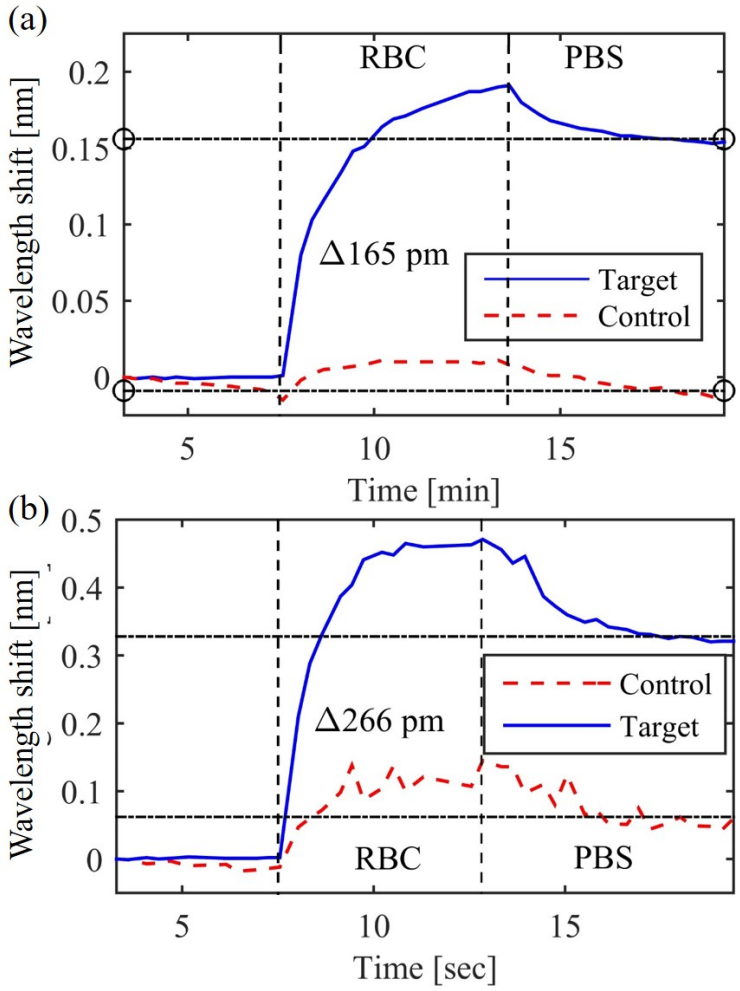

Figure 6.17: Direct B-type RBC detection. (a) TE rings. (b) TM rings

RBC assays. While a 5 nm-thick adlayer is less than expected, limited functionalization of the sensor's surface or asymmetric binding of antigens to the TE and TM ring might explain these observed results.

6.4 Conclusion

To the best of our knowledge, this work is the first demonstration of direct and indirect blood typing using silicon photonic biosensors. TE and TM mode ring resonators were designed,

Table 6.4: **Assay results for direct typing assays**

	TM offset	TE offset	Ratio (TM/TE)
A-type RBC	272 ± 113 pm	157 ± 85 pm	1.9 ± 0.4
B-type RBC	380 ± 141 pm	170 ± 70 pm	2.3 ± 0.3

fabricated, and characterized for use as biosensors. While the TE rings offer better limits of detection, they are more susceptible to thermal noise. Conversely, TM mode rings offer higher sensitivity resulting from a large evanescent field overlap with the aqueous cladding but suffer from absorption loss to the sample. Both rings were functionalized for indirect and direct typing assays and simultaneously monitored when introduced to human plasma and RBC samples. Even though sensogram results varied due to differences in the sample's antibody titers, manual functionalization, and target phenotypes, differential signals between the functionalized sensor and control were observed.

To further improve this blood typing system, thin-waveguide ring resonators [20] or sub-wavelength grating rings [308] would increase the native surface sensitivity of the biosensors. Additionally, zwitterionic polymer coatings that resist fouling from non-specific adsorption [40] would help increase the operational range, especially for samples with low titers. Finally, continuing to evolve the repertoire of highly specific conjugate antibodies and antigens for the various phenotypes that exist will ensure a robust platform that works across a wide range of samples. We believe this work clearly demonstrates the potential for the silicon photonic biosensors to be used in blood typing applications, helping improve the efficiency and reliability of blood collection, and reduce costly transfusion errors.

6.5 Acknowledgements

We gratefully acknowledge Dr. Sahba Talebi-Fard for her previous work on thin waveguide TE and TM mode ring resonators, Dr. James T. Kirk and Dr. Jing Shang for developing

the direct and indirect typing assay protocols, Dr. Jill Johnsen at BloodWorks Northwest for providing patient samples, Dr. Andrew Lingley and Duane Irish for cladding chips with CYTOP, and Dr. Nicholas Jaeger for the use of his laser in these experiments.

This work was supported by the University of Washington (UW) Royalty Research Fund, NSF CBET (Award no. 0930411), and the Washington Research Foundation. We gratefully acknowledge Lumerical Solutions, Inc. for providing the simulation software. Fabrication support was provided via the Natural Sciences and Engineering Research Council of Canada (NSERC) Silicon Electronic-Photonic Integrated Circuits (SiEPIC) Program. The devices were fabricated by Richard Bojko at the University of Washington Nanofabrication Facility, part of the National Science Foundation's National Nanotechnology Infrastructure Network (NNIN).

Chapter 7

CONCLUSION

7.1 Summary

In vitro diagnostics will play a significant role in the healthcare transformation currently underway in the United States. To realize their potential impact on improving healthcare delivery, diagnostic capabilities currently confined to well equipped laboratories must be developed for the POC setting. While many emerging biosensing platform technologies show promise to achieve such a goal, silicon photonic biosensors offer many advantages, including biosensing performance approaching clinically-relevant levels, integration of hundreds of sensors on a millimeter sized chip, and fabrication compatibility with existing CMOS foundries [17, 41, 210]. These elements provide the potential for silicon photonic lab-on-chip systems to be developed at economies of scale and cost of consumer electronics. Yet some diagnostic assays, like the PSA test or cancer detection, require performance beyond what can be achieved with a silicon photonic biosensor label-free [1, 43]. In addition, today's commercially available silicon photonic platforms require conventional gaskets, flow cells, and pumps to sequence samples across the sensors, adding cost and complexity to the overall system. Finally, while some tests have been demonstrated [23], expanding the repertoire of assays will expand its use as a diagnostic platform.

The research efforts described in this dissertation aim to improve the native performance of silicon photonics biosensors, simplify the system integration, and demonstrate new diagnostic applications that expand the use of silicon photonic biosensors for clinical applications.

7.1.1 Development tools

To reduce the barrier to entry for creating novel silicon photonic biosensors and improve the efficiency of silicon photonic biosensor development, a probe station that automates device characterization and assay orchestration was created. A PDK with an alignment framework and the probe station software have been open-sourced [48, 216] to support efforts of the broader scientific and industrial communities. The probe station is currently in use at more than a dozen institutions and companies worldwide and the PDK is routinely used for multi-project ebeam runs at the University of Washington organized by SiEPIC.

7.1.2 Improved sensors

Accomplishments toward improving the sensitivity and detection limit of silicon photonic biosensors by an order of magnitude over today's commercially available platforms were presented in chapter 4. Ring resonators (thin and SWG), disk resonators, and Bragg grating (on slab and suspended) biosensors designed using different waveguide geometries, polarizations, and operating wavelengths were fabricated and characterized. TE mode SWG rings with a bulk sensitivity of 500 nm/RIU and slot-waveguide Bragg gratings with a bulk sensitivity of 340 nm/RIU were demonstrated. Detection limit improvements of TM mode Bragg gratings for 1.31 μm wavelengths were shown to exceed the theoretical limits of their 1.55 μm counterparts. These achievements, when combined with non-fouling chemistries, will help silicon photonic biosensors achieve a clinically-relevant range (e.g. 1 ng/mL to 10 pg/mL) label-free.

7.1.3 Simplified systems

Chapter 5 showed how the overall system complexity can be improved by replacing traditional flow cells, gaskets and pumps with porous membranes. These membranes, that operate using capillary action, were shown to deliver undiluted human plasma for alloantibody detection (indirect blood typing) with similar performance to their conventional counterparts. With

the recent advances in porous membrane networks [297], integrating sample filtration, reagent sequencing, and waste containment with silicon photonic sensors would help facilitate a complete lab-on-chip system without pumps. With the advent of integrated lasers and on-chip detectors for highly multiplexed silicon photonic biosensor systems, porous membranes offer a welcome simplification to realize an integrated, lab-on-chip diagnostic device.

7.1.4 New applications

Many different resonant photonic devices have been investigated as label-free sensors for applications ranging from environmental monitoring [213] and basic science research [214] to bio threat detection [215] and medical diagnostics [26, 43, 90]. Blood typing has yet to be demonstrated using the silicon photonic biosensor platform and broadly published. Chapter 6 describes the use of silicon photonic ring resonators for red blood phenotyping (direct typing) as well as alloantibody detection (indirect typing) in undiluted human plasma. While the TE rings offer better limits of detection, they are more susceptible to thermal noise. Conversely, TM mode rings offer higher sensitivity resulting from a large evanescent field overlap with the aqueous cladding, but suffer from absorption loss to the sample.

To further improve this blood typing system, thin-waveguide ring resonators [20] or sub-wavelength grating rings [308] would increase the native surface sensitivity of the biosensors. Zwitterionic polymer coatings that resist fouling from non-specific adsorption [40] would help increase the operational range, especially for samples with low titers. This work clearly demonstrated the potential for silicon photonic biosensors to be used for blood typing applications, helping to improve the efficiency of blood collection and reduce costly transfusion errors.

7.2 Future directions

As silicon photonic biosensors mature, focus will shift toward lab-on-chip devices with integrated fluidics, lasers, detectors, and electronic control and readout. While a few groups have already demonstrated on-chip lasers and detectors [34, 42, 65, 66, 294, 295], most flu-

idic integration solutions require external pumps, tubing, valves and flow cells for silicon photonic biosensing systems [25, 67, 309, 310]. The addition of these components adds cost and complexity to the overall system.

Currently, the overall system cost of a silicon photonic biosensing platform is dominated by the laser (and detector) in comparison to the pumps, flow cell and tubing. However, there is growing evidence that chip-bonded lasers and integrated detectors will be affordable at the chip-scale in the near future [34, 42, 65, 66, 207, 293–295]. The experimental data presented throughout the document was measured using an expensive tunable laser source. While that might be ok for a bench top instrument (like the commercially available Genalyte Maverick system), a low cost light source would have to be implemented for a portable device (either external source or a Si/III-V hybrid implementation). The limitations by a low cost source may be overcome by compensating with additional passive or active optical components.

Improvements could be made that further enhance sensor performance by optimizing the waveguide geometry to maximize the sensing field at the waveguide's surface, i.e. choosing a different standard waveguide height (currently most MPW runs are offered with $h = 220$ nm). Designing sensors for 1310 nm wavelengths reduces absorptive losses to the aqueous cladding by 10 fold, enhancing detection limits [20]. Our system required secondary amplification to detect the bound target amidst the fouling from the complex sample. This additional step might be eliminated by employing strategies that resist fouling [40] and allow the detection of the target molecule in a label-free fashion. Finally, the porous membrane network offers many additional optimizations that could further simplify and integrate the overall system. Membranes could be used to filter or separate blood constituents [296] eliminating the need for any sample prep. Membranes with larger pores could be employed to operate in samples with cells, such as typing erythrocyte antigens directly. Finally, complex 2D and 3D networks could facilitate the sequencing of the sample, rinse buffers, and any additional amplification chemistries to eliminate the need for user intervention [137, 297].

There remains significant challenges to developing a new generation of IVD POC technologies, most notably compatibility with unprocessed, complex clinical samples. To enable

silicon photonic devices to detect certain biomolecules in clinically-relevant samples (e.g. plasma, cerebrospinal fluid), the silicon chip must possess both specificity towards target biomolecules within those complex matrices and the ability to prevent a nonspecific binding of biological interferants. When exposed to complex media, the surface of the sensing chip can be fouled by proteins (e.g., high abundance species such as serum albumin, fibrinogen, fibronectin, and circulating immunoglobulins) found at concentrations that dwarf most target analytes by several orders of magnitude. This 'biological noise' can substantially degrade the chip's sensitivity. However, advanced interfacial science and polymer chemistry are providing novel solutions to this challenge. For instance, layers of electrostatically neutral zwitterionic polymers have been shown to produce ultra-low fouling surfaces capable of resisting nonspecific protein interactions in clinical samples [174, 311, 312]. Our group has demonstrated that these zwitterionic polymers can be implemented on these silicon photonic chips to yield biosensing devices capable of performing with ELISA-like sensitivity in real-time in undiluted human plasma [40].

7.3 Contributions

7.3.1 Significance and impact of research activities and results

The list below highlights my personal contributions to the field based on the work presented in this dissertation.

- **Thin waveguide TE mode ring resonators** After learning that manipulating waveguide geometries (wide and thin waveguides specifically) can increase mode evanescent field overlap with the cladding, I suggested to Dr. Talebi Fard that we investigate thin waveguide TE and TM mode ring resonators. Dr. Talebi Fard and Dr. Valentina Donzella provided the design and layout. I managed their fabrication using ebeam lithography at the WNF. I also performed all the experimental characterization and analysis. This work demonstrated that foundry-compatible, 90 nm thick, TE mode rings provide 5x improved sensitivity over today's commercially available platforms

[25]. In addition, the 150 nm thick TM mode rings provide a 62% bulk sensitivity improvement over their 220 nm counterpart (see Table 4.3). These results have been published [57, 313, 314] and demonstrate how the performance of existing biosensing systems can be enhanced through the sensor alone.

- **Sub-wavelength TE mode ring resonators** Prof. Lukas Chrostowksi conceived the idea. Dr. Valentina Donzella demonstrated its use in air. Jonas Flueckiger leveraged this work and provided a design and layout for biosensing applications. I managed their fabrication using ebeam lithography at the WNF and conceived and conducted the experimental characterization and bio assays. These TE mode ring resonators were the first-of-their-kind and offered an order of magnitude sensitivity improvement over the best commercially available silicon photonic biosensors and a 2x improvement over the best reported TM mode ring resonators. This work was recently accepted for publication and its significance resides in its novelty. As such, the University of Washington filed a provisional patent [64]. Its performance enables new diagnostic applications for silicon photonic devices label-free that could only be achieved previously using secondary amplification. The next steps should be to make these structures CMOS-foundry compatible and assess any performance advantage of using 1310 nm wavelengths.

- **Suspended waveguide TE and TM mode Bragg gratings for biosensing** When taking Prof. Bohringer's MEM's class at the University of Washington, I learned that suspended silicon structures could be fabricated easily, a feature exploited for modern day MEMs-based sensors. After simulating TM mode profiles and seeing that more than half of the evanescent field energy exists in the substrate, I suggested we suspend TM mode Bragg gratings to improve their sensitivity. Jonas Flueckiger provided the TE and TM mode Bragg grating designs and layout. I managed their fabrication using ebeam lithography and suspension at the WNF. I also performed all the experimental characterization, biosensing assays, and analysis. These devices were first-of-their kind

in this suspended configuration and demonstrated marked performance improvements of Bragg gratings for biosensing applications, with the highest reported sensitivity for TM mode Bragg gratings. Because of their smaller footprint (compared to rings), these devices can be used for biosensing applications that require better performance and higher integration than what can be achieved by commercially available systems today. An invention disclosure was filed with the University of Washington for this structure and the work was published [61]. Further work on suspended waveguide biosensors should include a comparative performance assessment at 1310 nm wavelengths.

- **Open-sourced, low-cost automated probe station for silicon photonic circuit development** I architected the hardware and software, and managed the overall development of the system. Both Jonas Flueckiger and Wenxuan Wu contributed equally to this work [48]. Alex Wang provided mechanical drawings for parts I fabricated in the machine shop at the University of Washington for the hardware sub-assemblies. I developed much of the software and all the algorithms used to orchestrate biosensing assays. While some may argue as to the scientific merit of the work itself, this effort has enabled other research efforts worldwide, accelerating both knowledge and devices for the field of silicon photonics. The probe station has been used to generate scores of publications [49] and I co-founded a company with Jonas Flueckiger, *Maple Leaf Photonics* [315], to commercialize it beyond academic environments. It is currently in use at more than a dozen industrial and academic research labs. Future work should involve adding more features and further reducing hardware costs to accelerate its adoption and standardization throughout the field.

- **Integration of porous membranes and silicon photonic biosensors** My appreciation for porous membranes originated from my first research experience in Prof. Paul Yager's group. I realized that replacing the gaskets, flow cells and pumps used for silicon photonic biosensing would be a significant step toward simplifying an integrated system. The sensors used in the experiments, a set of TE and TM mode rings, were

designed by Jonas Flueckiger. I developed and fabricated the apparatus that integrated the chip and porous membranes, evaluated different porous membrane materials, determined lengths for optimal flow rates, performed the assays, analyzed the data, and wrote the manuscript. The results have been submitted for publication [69]. The significance of this accomplishment resides in its novelty. As such, the University of Washington has filed a provisional patent [68]. The next steps should be to integrate sample preparation required to use whole blood directly instead of undiluted human plasma.

7.3.2 Publications

The list below highlights published refereed and non-refereed works during my tenure as a graduate student.

Refereed publications:

1. **S. Schmidt**, J. Flueckiger, W.X. Wu, A. Lingley, K. Bohringer, K.C. Cheung, L. Chrostowski, D.M. Ratner, 'Enhancing Silicon Photonic Bragg Grating Performance for Biosensing Applications', *Ready for submission*, 2016.

2. **S. Schmidt**, J. Flueckiger, P. Khumwan, J. Shang, A. Wende, Z. Khaleel, H. Holmes, L. Chrostowski, D. Ratner, 'Erythrocyte and Serologic Phenotype Detection using Silicon Photonic Ring Resonators', *Ready for submission*, 2016.

3. **S. Schmidt**, J. Flueckiger, W.X. Wu, M. Reis, P. Kulik, L. Chrostowski, D. Ratner, 'Automated Probe Station and PDK for Silicon Photonic Biosensors', *Ready for submission*, 2016.

4. **S. Schmidt**, J. Flueckiger, J. Buser, A. Wende, A. Bleem, L. Chrostowski, K.C. Cheung, D.M. Ratner, 'Serologic phenotyping using silicon photonic biosensors and capillary driven networks', *Ready for submission*, 2016.

5. **S. Schmidt**, S. Grist, J. Flueckiger, V. Donzella, W. Shi, S. T. Fard, J. T. Kirk, D. Ratner, K. Cheung, and L. Chrostowski, 'Silicon photonic micro-disk resonators for label-free biosensing,' Optics Express, 2013.

6. **S. Schmidt**, J. Flueckiger, W. Wu, S.M. Grist, S. Talebi-Fard, V. Donzella, P. Khumwan, E.R. Thompson, Q. Wang, P. Kulik, X. Wang, A. Sherwali, J. Kirk, K.C. Cheung, L. Chrostowski, D. Ratner. 'Improving the performance of silicon photonic rings, disks, and Bragg gratings for use in label-free biosensing.' SPIE NanoScience Engineering VII. International Society for Optics and Photonics, 2014.

7. J. Flueckiger, **S. Schmidt**, V. Donzella, A. Sherwali, D.M. Ratner, L. Chrostowski, K.C. Cheung, 'Sub-wavelength grating for enhanced ring resonator biosensors', *Accepted in Optics Express*, 2016.

8. J. Flueckiger, **S. Schmidt**, Z. Chen, X. Wang, A. Liu, L. Chrostowski, D.M. Ratner, K.C. Cheung, 'TM polarized Silicon Photonic Bragg Gratings for Biosensing', *Ready for submission*, 2016.

9. S. Talebi Fard, K. Murray, M. Caverley, V. Donzella, J. Flueckiger, S. M. Grist, E. Huante-Ceron, **S. A. Schmidt**, E. Kwok, N. A. F. Jaeger, A. P. Knights, and L. Chrostowski, 'Silicon-on-insulator sensors using integrated resonance-enhanced defect-mediated photodetectors', Opt. Express, vol. 22, no. 23: OSA, pp. 28517-28529, 2014.

10. X. Wang, J. Flueckiger, **S. Schmidt**, S. Grist, S. T. Fard, J. T. Kirk, M. Doerfler, K. Cheung, L. Chrostowski, 'A silicon photonic biosensor using phase-shifted Bragg gratings in slot waveguide,' Journal Biophotonics, vol. 6, issue 10, pp. 821–828, 04/2013.

11. S. Talebi Fard, V. Donzella, **S. Schmidt**, J. Flueckiger, S.M. Grist, P. Talebi Fard, Y.

Wu, R. Bojko, E. Kwok, N.A.F. Jaeger, D.M Ratner, L. Chrostowski, 'Performance of ultra-thin SOI-based resonators for sensing applications', Opt. Express, vol. 22, no. 12: OSA, pp. 14166-14179, 06/2014.

12. S. Talebi Fard, **S. Schmidt**, W. Shi, W. Wu, N. A. F. Jaeger, E. Kwok, D. M. Ratner, and L. Chrostowski, 'Optimized Sensitivity of Silicon-on-Insulator Strip Waveguide Resonator Sensor', *In preparation*, 2016.

13. J. Kirk, **S. Schmidt**, P. Khumwan, J. Flueckiger, S. Talebi Fard, K. Lannert, J. Johnson, L. Chrostwoski, D. Ratner, 'Comparison of TE and TM microring resonators for red blood cell phenotyping', *In preparation*, 2016.

Non-refereed (conference abstracts, posters, software, and patents) publications:

1. **S. Schmidt**, L. Chrostowski, J. Flueckiger, 'Sub-wavelength grating for enhanced ring resonator biosensor', U.S. Provisional Patent Application No. 62/206,165 filed 8/17/2015.

2. **S. Schmidt**, J. Flueckiger, J. Kirk, D. Ratner, 'Capillary driven porous membrane integration with silicon photonic biosensors', U.S. Provisional Patent. *Ready for submission.*

3. **S. Schmidt**, J. Flueckiger, D. Ratner, 'Suspended waveguides for biosensing applications', U.S. Provisional Patent. *Ready for submission.*

4. **S. Schmidt**, J. Flueckiger, W.X. Wu, M. Reis, P. Kulik. (2015). Silicon Photonic Test Bench [Computer software]. https://github.com/shonschmidt/SiPhoTestBench.

5. **S. Schmidt**, J. Flueckiger, W.X. Wu. (2015). Silicon Photonic Test Bench for Biosensing [Computer software]. https://github.com/shonschmidt/SiPhoTestBenchBio.

6. **S. Schmidt**, J. Flueckiger, W.X. Wu. (2015). Silicon Photonic Analysis Tool [Computer software]. https://github.com/shonschmidt/SiPhoAnalysisTool.

7. **S. Schmidt**, J. Flueckiger, W. Wu, S.M. Grist, S. Talebi-Fard, V. Donzella, P. Khumwan, E.R. Thompson, Q. Wang, P. Kulik, X. Wang, A. Sherwali, J. Kirk, K.C. Cheung, L. Chrostowski, D. Ratner. Talk. 'Improving the performance of silicon photonic rings, disks, and Bragg gratings for use in label-free biosensing.' SPIE NanoScience Engineering VII. International Society for Optics and Photonics, 2014.

8. **S. Schmidt**, W. Shi, O. Wang, S. Grist, J. Kirk, M. Hochberg, R. Bjoko, L. Chrostowski, D. M. Ratner, Talk. 'Rapid prototyping of silicon photonic devices for label-free biosensing', BMES, Atlanta, October 2012.

9. **S. Schmidt**, X. Wang, J. Flueckiger, S.M. Grist, J. Kirk, K.C. Cheung, L. Chrostowski, D. Ratner. Abstract. Silicon Photonic Phase-shifted Bragg Gratings For Use In Label-free Biosensing. Poster session presented at: 2013 BMES Annual Meeting, Biomedical Engineering Society, 2013 September 25-28; Seattle, WA.

10. **S. Schmidt**, J. Flueckiger, V. Donzella, L. Chrostowski, D. Ratner, Talk. 'Sub-Wavelength Gratings For Label-Free Biological Sensing' BMES, Tampa, FL, October 2015.

11. **S. Schmidt**, A. Wende, J. Flueckiger, B. Lutz, L. Chrostowski, D. Ratner, Abstract. 'Capillary-driven fluidic networks for blood typing using silicon photonic biosensors', *Accepted*, BMES, Minneapolis, October 2016.

12. P. Kulik, W. Wu, Q. Wang, **S. Schmidt**, J. Flueckiger, L. Chrostowski, D. Ratner. Abstract. Open-Sourced Optical Test Setup for Rapid and Affordable Silicon Photonic Biosensor Development. Poster session presented at: 2013 BMES Annual Meeting, Biomedical Engineering Society, 2013 September 25-28; Seattle, WA.

13. V. Donzella, S.T. Fard, **S.A. Schmidt**, D.M. Ratner, Y. Wu, R.J. Bojko, and L. Chrostowski, Abstract. 'Sensitivity analysis of thin and ultra-thin SOI rings for sensing applications', IEEE Photonics Conference (IPC), Bellevue, WA, 8-12 September 2013.

14. S. T. Fard, V. Donzella, S. Grist, **S. Schmidt**, J. Flueckiger, X. Wang, W. Shi, A. Millspaugh, M. Webb, D. Ratner, K. C. Cheung, L. Chrostowksi, Talk. 'Label-free silicon photonic biosensors for use in clinical diagnostics,' presented at the SPIE Lase, San Francisco, CA, 2013.

15. **S. Schmidt**, A. Wende, J. Flueckiger, Q. Wang, Z. Kahleel, B. Lutz, L. Chrostowski, D. Ratner, Abstract. 'Integrating Paper-based Fluidics for Label-Free Blood Phenotyping via Silicon Photonics', *Accepted* MicroTAS 2016 Conference, Dublin, Ireland, 9-13 October 2016.

16. L. Chrostowski, S. M. Grist, **S. Schmidt**, and D. Ratner, 'Assessing silicon photonic biosensors for home healthcare,' Abstract. SPIE Newsroom, p. 3, Mar. 1, 2012.

17. L. Chrostowski, S. Grist, J. Flueckiger, W. Shi, X. Wang, E. Ouellet, H. Yun, M. Webb, B Nie, Z. Liang, K. Chung, **S. Schmidt**, D. Ratner, N. Jaeger, Abstract. 'Silicon photonic resonator sensors and devices,' in SPIE LASE, Jan 2012.

BIBLIOGRAPHY

[1] JL Arlett, EB Myers, and ML Roukes. Comparative advantages of mechanical biosensors. *Nature nanotechnology*, 6(4):203–215, 2011. 2, 3, 218

[2] Pierce protein biology products: Elisa and target-specific assay kits. URL http://www.piercenet.com/browse.cfm?fldID=BD0EF065-AD36-4337-B36B-A8000058840E. accessed: June 27, 2016.

[3] John R Crowther. *The ELISA guidebook*, volume 149. Springer Science & Business Media, 2000. 13

[4] G Ya Wiederschain. The elisa guidebook. *Biochemistry (Moscow)*, 74(9):1058–1058, 2009. 2

[5] Vladimir Gubala, Leanne F Harris, Antonio J Ricco, Ming X Tan, and David E Williams. Point of care diagnostics: status and future. *Analytical chemistry*, 84(2): 487–515, 2011. 2

[6] Curtis D Chin, Vincent Linder, and Samuel K Sia. Commercialization of microfluidic point-of-care diagnostic devices. *Lab on a Chip*, 12(12):2118–2134, 2012. 2

[7] John Toussaint, David Krueger, Stephen M Shortell, Arnold Milstein, and David M Cutler. Aco model should encourage efficient care delivery. In *Healthcare*, volume 3, pages 150–152. Elsevier, 2015. 2

[8] Shara Rosen. *Worldwide Market for IVD Tests*. Kalorama Information, New York, 2012. 2

[9] The Lewin Group Inc. The value of diagnosis, 2009, report commissioned by advameddx. 2009. accessed: June 27, 2016. 2

[10] Piia Von Lode. Point-of-care immunotesting: approaching the analytical performance of central laboratory methods. *Clinical biochemistry*, 38(7):591–606, 2005. 2

[11] Jen Kok, Jimmy Ng, Stephen C Li, John Giannoutsos, Vineet Nayyar, Jonathan R Iredell, Dominic E Dwyer, and Sharon CA Chen. Evaluation of point-of-care testing in critically unwell patients: comparison with clinical laboratory analysers and applicability to patients with ebolavirus infection. *Pathology*, 47(5):405–409, 2015. 2

[12] Xudong Fan, Ian M. White, Siyka I. Shopova, Hongying Zhu, Jonathan D. Suter, and Yuze Sun. Sensitive optical biosensors for unlabeled targets: A review. *Analytica Chimica Acta*, 620(1-2):8–26, 2008. URL http://www.sciencedirect.com/science/article/pii/S0003267008009343. 2, 3, 13, 14, 66, 190

[13] M.C. Estevez, M. Alvarez, and L.M. Lechuga. Integrated optical devices for labonachip biosensing applications. *Laser & Photonics Reviews*, 2012.

[14] Adrián Fernández Gavela, Daniel Grajales Garcia, Jhonattan C Ramirez, and Laura M Lechuga. Last advances in silicon-based optical biosensors. *Sensors*, 16(3):285, 2016. 66, 168, 190

[15] Adam L. Washburn and Ryan C. Bailey. Photonics-on-a-chip: recent advances in integrated waveguides as enabling detection elements for real-world, lab-on-a-chip biosensing applications. *Analyst*, 136(2):227–236, 2011. URL http://dx.doi.org/10.1039/C0AN00449A.

[16] AB González-Guerrero, S Dante, Daphné Duval, J Osmond, and Laura M Lechuga. Advanced photonic biosensors for point-of-care diagnostics. *Procedia Engineering*, 25:71–75, 2011.

[17] Ryan C Bailey, Adam L Washburn, Abraham J Qavi, Muzammil Iqbal, Martin Gleeson, Frank Tybor, and L Cary Gunn. A robust silicon photonic platform for multiparameter biological analysis. In *SPIE OPTO: Integrated Optoelectronic Devices*, pages 72200N–72200N. International Society for Optics and Photonics, 2009. 2, 218

[18] James T Kirk, Gina E Fridley, Jeffrey W Chamberlain, Elijah D Christensen, Michael Hochberg, and Daniel M Ratner. Multiplexed inkjet functionalization of silicon photonic biosensors. *Lab on a Chip*, 11(7):1372–1377, 2011. 3

[19] Katrien De Vos, Irene Bartolozzi, Etienne Schacht, Peter Bienstman, and Roel Baets. Silicon-on-insulator microring resonator for sensitive and label-free biosensing. *Optics express*, 15(12):7610–7615, 2007. 4, 156

[20] Shon Schmidt, Jonas Flueckiger, WenXuan Wu, Samantha M Grist, Sahba Talebi Fard, Valentina Donzella, Pakapreud Khumwan, Emily R Thompson, Qian Wang, and Pavel Kulik. Improving the performance of silicon photonic rings, disks, and bragg gratings for use in label-free biosensing. In *SPIE NanoScience+ Engineering*, pages 91660M–91660M. International Society for Optics and Photonics, 2014. 3, 8, 29, 47, 67, 102, 121, 171, 177, 186, 190, 191, 199, 201, 203, 204, 216, 220, 221

[21] Samantha M Grist, Shon A Schmidt, Jonas Flueckiger, Valentina Donzella, Wei Shi, Sahba Talebi Fard, James T Kirk, Daniel M Ratner, Karen C Cheung, and Lukas Chrostowski. Silicon photonic micro-disk resonators for label-free biosensing. *Optics express*, 21(7):7994–8006, 2013. 3, 8, 67, 91, 123, 124, 158

[22] Mindy R Lee and Philippe M Fauchet. Two-dimensional silicon photonic crystal based biosensing platform for protein detection. *Optics Express*, 15(8):4530–4535, 2007. 3

[23] IA Estrada, RW Burlingame, AP Wang, K Chawla, T Grove, J Wang, SO Southern, M Iqbal, LC Gunn, and MA Gleeson. Multiplex detection of pathogen biomarkers in human blood, serum, and saliva using silicon photonic microring resonators. In

SPIE Sensing Technology+ Applications, pages 94900E–94900E. International Society for Optics and Photonics, 2015. 4, 13, 180, 190, 218

[24] Matthew S Luchansky, Adam L Washburn, Teresa A Martin, Muzammil Iqbal, L Cary Gunn, and Ryan C Bailey. Characterization of the evanescent field profile and bound mass sensitivity of a label-free silicon photonic microring resonator biosensing platform. *Biosensors and Bioelectronics*, 26(4):1283–1291, 2010. 4, 8, 124, 139, 140, 157, 172, 178, 195

[25] Muzammil Iqbal, Martin A Gleeson, Bradley Spaugh, Frank Tybor, William G Gunn, Michael Hochberg, Tom Baehr-Jones, Ryan C Bailey, and L Cary Gunn. Label-free biosensor arrays based on silicon ring resonators and high-speed optical scanning instrumentation. *Selected Topics in Quantum Electronics, IEEE Journal of*, 16(3):654–661, 2010. 4, 6, 8, 9, 13, 105, 121, 135, 165, 169, 221, 223

[26] Adam L Washburn, Matthew S Luchansky, Adrienne L Bowman, and Ryan C Bailey. Quantitative, label-free detection of five protein biomarkers using multiplexed arrays of silicon photonic microring resonators. *Analytical chemistry*, 82(1):69–72, 2009. 4, 8, 67, 99, 220

[27] Gilberto A Rodriguez, Shuren Hu, and Sharon M Weiss. Porous silicon ring resonator for compact, high sensitivity biosensing applications. *Optics express*, 23(6):7111–7119, 2015. 4

[28] Tomoya Taniguchi, Anna Hirowatari, Takeshi Ikeda, Masataka Fukuyama, Yoshiteru Amemiya, Akio Kuroda, and Shin Yokoyama. Detection of antibody-antigen reaction by silicon nitride slot-ring biosensors using protein g. *Optics Communications*, 365: 16–23, 2016. 4

[29] Tom Claes, J Girones Molera, Katrien De Vos, E Schachtb, Roel Baets, and Peter

Bienstman. Label-free biosensing with a slot-waveguide-based ring resonator in silicon on insulator. *Photonics Journal, IEEE*, 1(3):197–204, 2009. 4, 63, 134, 135, 137, 154

[30] Katrien De Vos, Jordi Girones, Stepan Popelka, Etienne Schacht, Roel Baets, and Peter Bienstman. Soi optical microring resonator with poly (ethylene glycol) polymer brush for label-free biosensor applications. *Biosensors and Bioelectronics*, 24(8):2528–2533, 2009. 4, 41, 47, 100, 106

[31] Carl Fredrik Carlborg, Kristinn Björgvin Gylfason, A Kaźmierczak, Fabian Dortu, MJ Banuls Polo, A Maquieira Catala, GM Kresbach, Hans Sohlström, Thomas Moh, Laurent Vivien, et al. A packaged optical slot-waveguide ring resonator sensor array for multiplex label-free assays in labs-on-chips. *Lab on a Chip*, 10(3):281–290, 2010. 4

[32] Mi Kyoung Park, Jack Sheng Kee, Jessie Yiying Quah, Vivian Netto, Junfeng Song, Qing Fang, Eric Mouchel La Fosse, and Guo-Qiang Lo. Label-free aptamer sensor based on silicon microring resonators. *Sensors and Actuators B: Chemical*, 176:552–559, 2013. 4

[33] Shuren Hu, Yiliang Zhao, Kun Qin, Scott T Retterer, Ivan I Kravchenko, and Sharon M Weiss. Enhancing the sensitivity of label-free silicon photonic biosensors through increased probe molecule density. *ACS Photonics*, 1(7):590–597, 2014. 4

[34] Rene Heideman, Marcel Hoekman, and Erik Schreuder. Triplex-based integrated optical ring resonators for lab-on-a-chip and environmental detection. *Selected Topics in Quantum Electronics, IEEE Journal of*, 18(5):1583–1596, 2012. 4, 186, 220, 221

[35] Carlos A Barrios, Maria Jose Banuls, Victoria Gonzalez-Pedro, Kristinn B Gylfason, Benito Sanchez, Amadeu Griol, Angel Maquieira, Hans Sohlström, Miquel Holgado, and R Casquel. Label-free optical biosensing with slot-waveguides. *Optics letters*, 33 (7):708–710, 2008. 4, 63, 135

[36] Shinyoung Lee, Seok Chan Eom, Jee Soo Chang, Chul Huh, Gun Yong Sung, and Jung H Shin. Label-free optical biosensing using a horizontal air-slot sinx microdisk resonator. *Optics express*, 18(20):20638–20644, 2010. 4

[37] Yi Zou, Swapnajit Chakravarty, David N Kwong, Wei-Cheng Lai, Xiaochuan Xu, Xiaohui Lin, Amir Hosseini, and Ray T Chen. Cavity-waveguide coupling engineered high sensitivity silicon photonic crystal microcavity biosensors with high yield. *Selected Topics in Quantum Electronics, IEEE Journal of*, 20(4):171–180, 2014. 4

[38] Lijun Huang, Huiping Tian, Jian Zhou, Qi Liu, Pan Zhang, and Yuefeng Ji. Label-free optical sensor by designing a high-q photonic crystal ring–slot structure. *Optics Communications*, 335:73–77, 2015. 4

[39] Kiana Malmir, Hamidreza Habibiyan, and Hassan Ghafoorifard. An ultrasensitive optical label-free polymeric biosensor based on concentric triple microring resonators with a central microdisk resonator. *Optics Communications*, 365:150–156, 2016. 4

[40] James T Kirk, Norman D Brault, Tom Baehr-Jones, Michael Hochberg, Shaoyi Jiang, and Daniel M Ratner. Zwitterionic polymer-modified silicon microring resonators for label-free biosensing in undiluted humanplasma. *Biosensors and Bioelectronics*, 42: 100–105, 2013. 3, 6, 8, 41, 48, 99, 121, 186, 190, 216, 220, 221, 222

[41] Nan Jokerst, Matthew Royal, Sabarni Palit, Lin Luan, Sulochana Dhar, and Talmage Tyler. Chip scale integrated microresonator sensing systems. *Journal of biophotonics*, 2(4):212–226, 2009. 3, 12, 66, 190, 218

[42] Nan M Jokerst, Luan Lin, Sabarni Palit, Matthew Royal, Sulochana Dhar, M Brooke, and Talmage Tyler. Progress in chip-scale photonic sensing. *IEEE transactions on biomedical circuits and systems*, 3(4):202–211, 2009. 3, 9, 12, 66, 169, 186, 190, 220, 221

[43] Matthew S Luchansky and Ryan C Bailey. Silicon photonic microring resonators for quantitative cytokine detection and t-cell secretion analysis. *Analytical chemistry*, 82 (5):1975–1981, 2010. 6, 8, 13, 57, 67, 99, 190, 191, 218, 220

[44] Fea Vollmer, D Braun, A Libchaber, M Khoshsima, I Teraoka, and S Arnold. Protein detection by optical shift of a resonant microcavity. *Applied Physics Letters*, 80(21): 4057–4059, 2002. 6, 57, 191

[45] Jonathan D Suter, Ian M White, Hongying Zhu, Huidong Shi, Charles W Caldwell, and Xudong Fan. Label-free quantitative dna detection using the liquid core optical ring resonator. *Biosensors and Bioelectronics*, 23(7):1003–1009, 2008. 6, 191

[46] F Vollmer, S Arnold, and D Keng. Single virus detection from the reactive shift of a whispering-gallery mode. *Proceedings of the National Academy of Sciences*, 105(52): 20701–20704, 2008. 6, 57, 190, 191

[47] A Ramachandran, S Wang, J Clarke, SJ Ja, D Goad, L Wald, EM Flood, E Knobbe, JV Hryniewicz, ST Chu, et al. A universal biosensing platform based on optical microring resonators. *Biosensors and Bioelectronics*, 23(7):939–944, 2008. 6, 57, 190, 191

[48] Silicon photonic test bench, . URL https://github.com/shonschmidt/SiPhoTestBench. accessed: June 27th, 2016. 7, 68, 219, 224

[49] Lukas Chrostowski. Lukas chrostowski mina faculty member webpage. URL http://www.mina.ubc.ca/lukasc. 7, 224

[50] Edx silicon photonic design and fabrication. URL https://www.edx.org/course/silicon-photonics-design-fabrication-ubcx-phot1x-1. accessed: June 27th, 2016. 8, 68

[51] S. Schmidt, J. Flueckiger, W. Wu, M. Reis, P. Kulik, L. Chrostowski, and D. Ratner. Automated probe station and pdk for silicon photonic biosensors. *Manuscript in preparation*, 2016. 8

[52] Lukas Chrostowski and Michael Hochberg. *Silicon Photonics Design: From Devices to Systems*. Cambridge University Press, 2015. 8, 18, 31, 35, 69, 110, 113, 131, 162, 171, 204

[53] Richard Soref. Silicon photonics: a review of recent literature. *Silicon*, 2(1):1–6, 2010. 8, 66, 99, 190

[54] Adam L Washburn, Matthew S Luchansky, Melinda S McClellan, and Ryan C Bailey. Label-free, multiplexed biomolecular analysis using arrays of silicon photonic microring resonators. *Procedia Engineering*, 25:63–66, 2011. 8, 99

[55] Valentina Donzella, Ahmed Sherwali, Jonas Flueckiger, Samantha M Grist, Sahba Talebi Fard, and Lukas Chrostowski. Design and fabrication of soi micro-ring resonators based on sub-wavelength grating waveguides. *Optics Express*, 23(4):4791–4803, 2015. 8

[56] Xu Wang, Jonas Flueckiger, Shon Schmidt, Samantha Grist, Sahba T. Fard, James Kirk, Matt Doerfler, Karen C. Cheung, Daniel M. Ratner, and Lukas Chrostowski. A silicon photonic biosensor using phase-shifted bragg gratings in slot waveguide. *Journal of Biophotonics*, 6(10):821–828, 2013. URL http://dx.doi.org/10.1002/jbio.201300012. 67, 138, 163

[57] Sahba Talebi Fard, Valentina Donzella, Shon A Schmidt, Jonas Flueckiger, Samantha M Grist, Pouria Talebi Fard, Yichen Wu, Rick J Bojko, Ezra Kwok, Nicolas AF Jaeger, et al. Performance of ultra-thin soi-based resonators for sensing applications. *Optics Express*, 22(12):14166–14179, 2014. 108, 116, 119, 223

[58] Sahba Talebi Fard, Samantha M Grist, Valentina Donzella, Shon A Schmidt, Jonas Flueckiger, Xu Wang, Wei Shi, Andrew Millspaugh, Mitchell Webb, Daniel M Ratner, et al. Label-free silicon photonic biosensors for use in clinical diagnostics. In *SPIE OPTO*, pages 862909–862909. International Society for Optics and Photonics, 2013.

[59] Jonas Flueckiger, Shon Schmidt, Valentina Donzella, Ahmed Sherwali, Daniel M. Ratner, Lukas Chrostowski, and Karen C. Cheung. Sub-wavelength grating for enhanced ring resonator biosensor. *Opt. Express*, 24(14):15672–15686, Jul 2016. doi: 10.1364/OE.24.015672. URL http://www.opticsexpress.org/abstract.cfm?URI=oe-24-14-15672. 8

[60] S. Schmidt, J. Flueckiger, W. Wu, A. Lingley, K. Bohringer, K. Chrostowski, and D. Ratner. Enhancing silicon photonic bragg gratings for biosensing applications. *Manuscript in preparation*, 2016. 8

[61] Shon Schmidt, Jonas Flueckiger, Wenxuan Wu, Andrew Lingley, Karl Bohringer, Karen C. Cheung, Lukas Chrostowski, and Daniel M. Ratner. Enhancing silicon photonic bragg gratings for biosensing. *Manuscript in preparation*, 2016. 224

[62] W. Shi W. Wu N. Jaeger E. Kwok D. Ranter L. Chrostowski S. Talebi Fard, S. Schmidt. Optimized sensitivity of silicon-on-insulator strip waveguide resonator sensor. *Submitted*, 2016.

[63] J. Flueckiger, S. Schmidt, Z. Chen, X. Wang, A. Liu, L. Chrostowski, D. Ratner, and K. Cheung. Tm polarized silicon photonic bragg gratings for biosensing. *Manuscript in preparation*, 2016. 8

[64] Shon Schmidt, Jonas Flueckiger, Valentina Donzella, Lukas Chrostowski, and Daniel Ratner. Sub-wavelength gratings for label-free biological sensing. In *Biomedical Engineering Socity*, 2015. 8, 223

[65] MJ Heck, Jared F Bauters, Michael L Davenport, Jonathan K Doylend, Siddharth Jain, Geza Kurczveil, Sudharsanan Srinivasan, Yongbo Tang, and John E Bowers. Hybrid silicon photonic integrated circuit technology. *IEEE Journal of Selected Topics in Quantum Electronics*, 19(4), 2013. 9, 169, 186, 220, 221

[66] Sahba Talebi Fard, Kyle Murray, Michael Caverley, Valentina Donzella, Jonas Flueckiger, Samantha M Grist, Edgar Huante-Ceron, Shon A Schmidt, Ezra Kwok, Nico-

las AF Jaeger, et al. Silicon-on-insulator sensors using integrated resonance-enhanced defect-mediated photodetectors. *Optics express*, 22(23):28517–28529, 2014. 9, 169, 186, 220, 221

[67] Catherine Rivet, Hyewon Lee, Alison Hirsch, Sharon Hamilton, and Hang Lu. Microfluidics for medical diagnostics and biosensors. *Chemical Engineering Science*, 66 (7):1490–1507, 2011. 9, 169, 221

[68] Shon Schmidt, Alex Wende, Jonas Flueckiger, Barry Lutz, Lukas Chrostowski, and Daniel M. Ratner. Capillary-driven fluidic networks for blood typing using silicon photonic biosensors. In *Biomedical Engineering Society*, 2016. 9, 225

[69] Shon Schmidt, Jonas Flueckiger, Alex Wende, Josh Buser, Alissa Bleem, Lukas Chrostowski, and Daniel M. Ratner. Serilogic phenotyping using silicon photonic biosensors and capillary driven networks. *Manuscript in preparation*, 2016. 9, 225

[70] Koo-Whang Chung, Sridhar V Basavaraju, Yi Mu, Katharina L van Santen, Kathryn A Haass, Richard Henry, James Berger, and Matthew J Kuehnert. Declining blood collection and utilization in the united states. *Transfusion*, 2016. 9, 52, 189

[71] Wim Malomgré and Birgid Neumeister. Recent and future trends in blood group typing. *Analytical and bioanalytical chemistry*, 393(5):1443–1451, 2009. 9, 55, 188, 189

[72] Eleftherios C Vamvakas and Morris A Blajchman. Blood still kills: six strategies to further reduce allogeneic blood transfusion-related mortality. *Transfusion medicine reviews*, 24(2):77–124, 2010. 10, 54, 188

[73] S. Schmidt, J. Flueckiger, P. Khumwan, J. Shang, A. Wende, Z. Khaleel, H. Holmes, L. Chrostowski, and D. Ratner. Erythrocyte and serologic phenotyping using silicon photonic ring resonators. *Manuscript in preparation*, 2016. 10

[74] Anthony PF Turner. Biosensors: sense and sensibility. *Chemical Society Reviews*, 42 (8):3184–3196, 2013. 11

[75] Leland C Clark and Champ Lyons. Electrode systems for continuous monitoring in cardiovascular surgery. *Annals of the New York Academy of sciences*, 102(1):29–45, 1962. 11

[76] Elain Fu, Timothy Chinowsky, Kjell Nelson, Kyle Johnston, Thayne Edwards, Kristen Helton, Michael Grow, John W Miller, and Paul Yager. Spr imaging-based salivary diagnostics system for the detection of small molecule analytes. *Annals of the New York Academy of Sciences*, 1098(1):335–344, 2007. 12

[77] Curtis D Chin, Vincent Linder, and Samuel K Sia. Lab-on-a-chip devices for global health: Past studies and future opportunities. *Lab Chip*, 7(1):41–57, 2006.

[78] Jiri Homola, Ivo Koudela, and Sinclair S Yee. Surface plasmon resonance sensors based on diffraction gratings and prism couplers: sensitivity comparison. *Sensors and Actuators B: Chemical*, 54(1):16–24, 1999. 12

[79] Jiri Homola. Present and future of surface plasmon resonance biosensors. *Analytical and bioanalytical chemistry*, 377(3):528–539, 2003. 12

[80] Bo Liedberg, Claes Nylander, and Ingemar Lundström. Biosensing with surface plasmon resonance - how it all started. *Biosensors and Bioelectronics*, 10(8):i–ix, 1995. 12

[81] U Jonson and M Malmqvist. Real time biospecific interaction analysis. *Adv. Biosens*, 2:291–336, 1992. 12

[82] Jiri Homola. Surface plasmon resonance sensors for detection of chemical and biological species. *Chemical reviews*, 108(2):462, 2008. 12

[83] Timothy M Chinowsky, Scott D Soelberg, Paul Baker, Nathaneal R Swanson, Peter Kauffman, Anthony Mactutis, Michael S Grow, Robert Atmar, Sinclair S Yee, and Clement E Furlong. Portable 24-analyte surface plasmon resonance instruments for rapid, versatile biodetection. *Biosensors and Bioelectronics*, 22(9):2268–2275, 2007. 12

[84] Richard A Soref, Joachim Schmidtchen, and Klaus Petermann. Large single-mode rib waveguides in gesi-si and si-on-sio 2. *Quantum Electronics, IEEE Journal of*, 27(8): 1971–1974, 1991. 13

[85] Richard A Soref and Brian R Bennett. Kramers-kronig analysis of electro-optical switching in silicon. In *Cambridge Symposium-Fiber/LASE'86*, pages 32–37. International Society for Optics and Photonics, 1987. 13

[86] Richard Soref. Silicon photonics technology: past, present, and future. In *Integrated Optoelectronic Devices 2005*, pages 19–28. International Society for Optics and Photonics, 2005. 13, 18

[87] María-José Bañuls, Rosa Puchades, and Ángel Maquieira. Chemical surface modifications for the development of silicon-based label-free integrated optical (io) biosensors: A review. *Analytica chimica acta*, 777:1–16, 2013. 13, 41, 45, 48

[88] Andy Eu-Jin Lim, Junfeng Song, Qing Fang, Chao Li, Xiaoguang Tu, Ning Duan, Kok Kiong Chen, Roger Poh-Cher Tern, and Tsung-Yang Liow. Review of silicon photonics foundry efforts. *Selected Topics in Quantum Electronics, IEEE Journal of*, 20(4):405–416, 2014. 13

[89] Jiri Homola, Sinclair S Yee, and Günter Gauglitz. Surface plasmon resonance sensors: review. *Sensors and Actuators B: Chemical*, 54(1):3–15, 1999. 14

[90] Matthew S Luchansky, Adam L Washburn, Melinda S McClellan, and Ryan C Bailey. Sensitive on-chip detection of a protein biomarker in human serum and plasma over an extended dynamic range using silicon photonic microring resonators and sub-micron beads. *Lab on a Chip*, 11(12):2042–2044, 2011. 15, 67, 99, 220

[91] Wim Bogaerts, Peter De Heyn, Thomas Van Vaerenbergh, Katrien De Vos, Shankar Kumar Selvaraja, Tom Claes, Pieter Dumon, Peter Bienstman, Dries Van Thourhout,

and Roel Baets. Silicon microring resonators. *Laser & Photonics Reviews*, 6(1):47–73, 2012. 16, 30, 67, 108, 168, 171, 191, 192

[92] Katrin Schmitt and Christian Hoffmann. High-refractive-index waveguide platforms for chemical and biosensing. In *Optical Guided-wave Chemical and Biosensors I*, pages 21–54. Springer, 2009. 18

[93] Mode solutions - fde mode solver. URL https://www.lumerical.com/tcad-products/mode/. accessed: June 27, 2016. 19

[94] Zhaoming Zhu and Thomas Brown. Full-vectorial finite-difference analysis of microstructured optical fibers. *Optics Express*, 10(17):853–864, 2002. 19

[95] Allan W Snyder and J Love. *Optical waveguide theory*, volume 190. Springer, 1983. 22, 24

[96] Malvin Carl Teich and BEA Saleh. *Fundamentals of photonics*. John Wiley and Sons, Inc., 1991.

[97] Amnon Yariv and Pochi Yeh. *Photonics: Optical Electronics in Modern Communications (the Oxford Series in Electrical and Computer Engineering)*. Oxford University, 2006. 22, 24, 66, 109, 129

[98] F Höök, J Vörös, M Rodahl, R Kurrat, P Böni, JJ Ramsden, M Textor, ND Spencer, Pentti Tengvall, J Gold, et al. A comparative study of protein adsorption on titanium oxide surfaces using in situ ellipsometry, optical waveguide lightmode spectroscopy, and quartz crystal microbalance/dissipation. *Colloids and Surfaces B: Biointerfaces*, 24(2):155–170, 2002. 23, 34, 49, 157, 195, 201

[99] Janos Vörös. The density and refractive index of adsorbing protein layers. *Biophysical journal*, 87(1):553–561, 2004. 34, 41, 43, 49, 103, 150, 157, 186, 191, 195, 201, 209

[100] H. Arwin. Optical properties of thin layers of bovine serum albumin, globulin, and hemoglobin. *Applied Spectroscopy*, 40(3):313–318, 1986-03-01T00:00:00. doi: doi:10.1366/0003702864509204. URL http://www.ingentaconnect.com/content/sas/sas/1986/00000040/00000003/art00005.

[101] Vincent Ball and Jeremy J Ramsden. Buffer dependence of refractive index increments of protein solutions. *Biopolymers*, 46(7):489–492, 1998. 23, 49, 157

[102] S Arnold, M Khoshsima, I Teraoka, S Holler, and F Vollmer. Shift of whispering-gallery modes in microspheres by protein adsorption. *Optics letters*, 28(4):272–4, Feb 2003. 27

[103] Lukas Chrostowski, Samantha Grist, Jonas Flueckiger, Wei Shi, Xu Wang, Eric Ouellet, Han Yun, Mitch Webb, Ben Nie, and Zhen Liang. Silicon photonic resonator sensors and devices. In *SPIE LASE*, pages 823620–823620. International Society for Optics and Photonics, 2012. 31, 36, 37, 61, 62, 121, 123, 124, 137, 150, 153, 159, 162, 177, 200, 203

[104] Tom Baehr-Jones, Michael Hochberg, Chris Walker, Eric Chan, Dennis Koshinz, William Krug, and Axel Scherer. Analysis of the tuning sensitivity of silicon-on-insulator optical ring resonators. *Journal of lightwave technology*, 23(12):4215, 2005. 27

[105] K Tiefenthaler and W Lukosz. Sensitivity of grating couplers as integrated-optical chemical sensors. *JOSA B*, 6(2):209–220, 1989. 27

[106] Shankar Kumar Selvaraja. *Wafer-scale fabrication technology for silicon photonic integrated circuits*. PhD thesis, PhD thesis, Ghent University, 2011. 30, 31

[107] Pieter Dumon. Ultra-compact integrated optical filters in silicon-on-insulator by means of wafer-scale technology. *University of Ghent, Ph. D. Thesis*, 2007. 30, 31

[108] Kevin K. Lee, Desmond R. Lim, Hsin-Chiao Luan, Anuradha Agarwal, James Foresi, and Lionel C. Kimerling. Effect of size and roughness on light transmission in a si/sio2 waveguide: Experiments and model. *Applied Physics Letters*, 77(11):1617–1619, 2000. doi: http://dx.doi.org/10.1063/1.1308532. URL http://scitation.aip.org/content/aip/journal/apl/77/11/10.1063/1.1308532. 30

[109] Steven G Johnson, ML Povinelli, M Soljačić, Aristeidis Karalis, S Jacobs, and JD Joannopoulos. Roughness losses and volume-current methods in photonic-crystal waveguides. *Applied Physics B*, 81(2-3):283–293, 2005. 30

[110] Shankar Kumar Selvaraja, Patrick Jaenen, Wim Bogaerts, Dries Van Thourhout, Pieter Dumon, and Roel Baets. Fabrication of photonic wire and crystal circuits in silicon-on-insulator using 193-nm optical lithography. *Lightwave Technology, Journal of*, 27(18):4076–4083, 2009. 30

[111] Juejun Hu, Xiaochen Sun, Anu Agarwal, and Lionel C Kimerling. Design guidelines for optical resonator biochemical sensors. *JOSA B*, 26(5):1032–1041, 2009. 31, 177, 200

[112] Ian M White and Xudong Fan. On the performance quantification of resonant refractive index sensors. *Optics Express*, 16(2):1020–1028, 2008. 31, 36, 161, 162, 177, 200, 204

[113] GJ Veldhuis, O Parriaux, HJWM Hoekstra, and PV Lambeck. Sensitivity enhancement in evanescent optical waveguide sensors. *Journal of lightwave technology*, 18(5):677, 2000. 32

[114] Olivier Parriaux and GJ Veldhuis. Normalized analysis for the sensitivity optimization of integrated optical evanescent-wave sensors. *Journal of lightwave technology*, 16(4): 573, 1998. 33

[115] Olivier Parriaux and P Dierauer. Normalized expressions for the optical sensitivity of evanescent wave sensors. *Optics letters*, 19(7):508–510, 1994. 32

[116] De-Kui Qing and Ichirou Yamaguchi. Analysis of the sensitivity of optical waveguide chemical sensors for tm modes by the group-index method. *JOSA B*, 16(9):1359–1369, 1999. 33

[117] Bradley J Frey, Douglas B Leviton, and Timothy J Madison. Temperature-dependent refractive index of silicon and germanium. In *SPIE Astronomical Telescopes+ Instrumentation*, pages 62732J–62732J. International Society for Optics and Photonics, 2006. 35

[118] G Cocorullo and I Rendina. Thermo-optical modulation at 1.5 μm in silicon etalon. *Electronics Letters*, 28(1):83–85, 1992.

[119] JA McCaulley, VM Donnelly, M Vernon, and I Taha. Temperature dependence of the near-infrared refractive index of silicon, gallium arsenide, and indium phosphide. *Physical Review B*, 49(11):7408, 1994. 35

[120] Zeqin Lu, Kyle Murray, Hasitha Jayatilleka, and Lukas Chrostowski. Michelson interferometer thermo-optic switch on soi with a 50-μw power consumption. *Photonics Technology Letters, IEEE*, 27(22):2319–2322, 2015. 35

[121] Kyle Murray, Zeqin Lu, Hasitha Jayatilleka, and Lukas Chrostowski. Dense dissimilar waveguide routing for highly efficient thermo-optic switches on silicon. *Optics express*, 23(15):19575–19585, 2015. 35

[122] Kishore Padmaraju and Keren Bergman. Resolving the thermal challenges for silicon microring resonator devices. *Nanophotonics*, 3(4-5):269–281, 2014. 35

[123] Jie Teng, Pieter Dumon, Wim Bogaerts, Hongbo Zhang, Xigao Jian, Xiuyou Han, Mingshan Zhao, Geert Morthier, and Roel Baets. Athermal silicon-on-insulator ring resonators by overlaying a polymer cladding on narrowed waveguides. *Optics express*, 17(17):14627–14633, 2009. 35

[124] Jong-Moo Lee, Duk-Jun Kim, Hokyun Ahn, Sang-Ho Park, and Gyungock Kim. Temperature dependence of silicon nanophotonic ring resonator with a polymeric overlayer. *Journal of lightwave technology*, 25(8):2236–2243, 2007.

[125] Jong-Moo Lee, Duk-Jun Kim, Gwan-Ha Kim, O-Kyun Kwon, Kap-Joong Kim, and Gyungock Kim. Controlling temperature dependence of silicon waveguide using slot structure. *Optics express*, 16(3):1645–1652, 2008.

[126] N Ye Winnie, Rong Sun, Jurgen Michel, Louay Eldada, Deepti Pant, and Lionel C Kimerling. Thermo-optical compensation in high-index-contrast waveguides. 2008.

[127] Linjie Zhou, Ken Kashiwagi, Katsunari Okamoto, RP Scott, NK Fontaine, Dan Ding, Venkatesh Akella, and SJB Yoo. Towards athermal optically-interconnected computing system using slotted silicon microring resonators and rf-photonic comb generation. *Applied Physics A*, 95(4):1101–1109, 2009.

[128] Mutsunori Uenuma and Teruaki Motooka. Temperature-independent silicon waveguide optical filter. *Optics letters*, 34(5):599–601, 2009. 35

[129] Alexey N Bashkatov and Elina A Genina. Water refractive index in dependence on temperature and wavelength: a simple approximation. In *Saratov Fall Meeting 2002: Optical Technologies in Biophysics and Medicine IV*, pages 393–395. International Society for Optics and Photonics, 2003. 35

[130] G Abbate, U Bernini, E Ragozzino, and F Somma. The temperature dependence of the refractive index of water. *Journal of Physics D: Applied Physics*, 11(8):1167, 1978. 35

[131] S. J. Carlisle R. J. Davies, S. S. Eapen. 74 lateral-flow immunochromatographic assays. *Handbook of Biosensors and Biochips*, 2008. DOI: 10.1002/9780470061565.hbb110. 38

[132] Andres W Martinez, Scott T Phillips, George M Whitesides, and Emanuel Carrilho. Diagnostics for the developing world: microfluidic paper-based analytical devices. *Analytical chemistry*, 82(1):3–10, 2009. 38, 170

[133] Ali Kemal Yetisen, Muhammad Safwan Akram, and Christopher R Lowe. Paper-based microfluidic point-of-care diagnostic devices. *Lab on a Chip*, 13(12):2210–2251, 2013.

[134] Samantha Byrnes, Gregory Thiessen, and Elain Fu. Progress in the development of paper-based diagnostics for low-resource point-of-care settings. *Bioanalysis*, 5(22): 2821–2836, 2013. 38

[135] Rapid Lateral Flow Test Strips. Considerations for product development. *Bedford, MA: Millipore Corporation*, 2001. 38, 39

[136] Sergio Mendez, Erin M Fenton, Gil R Gallegos, Dimiter N Petsev, Scott S Sibbett, Howard A Stone, Yi Zhang, and Gabriel P López. Supplemental info: Imbibition in porous membranes of complex shape: quasi-stationary flow in thin rectangular segments. *Langmuir*, 2009. 39

[137] E. Fu, S.A. Ramsey, P. Kauffman, B. Lutz, and P. Yager. Transport in two-dimensional paper networks. *Microfluidics and nanofluidics*, 10(1):29–35, 2011. 40, 170, 178, 186, 221

[138] Barry R Lutz, Philip Trinh, Cameron Ball, Elain Fu, and Paul Yager. Two-dimensional paper networks: programmable fluidic disconnects for multi-step processes in shaped paper. *Lab on a Chip*, 11(24):4274–4278, 2011. 40, 178

[139] Todd M Squires, Robert J Messinger, and Scott R Manalis Manalis. Making it stick: convection, reaction and diffusion in surface-based biosensors. *Nature biotechnology*, 26(4):417–426, 2008. 40

[140] Amgad R Rezk, Aisha Qi, James R Friend, Wai Ho Li, and Leslie Y Yeo. Uniform mixing in paper-based microfluidic systems using surface acoustic waves. *Lab on a Chip*, 12(4):773–779, 2012. 40

[141] Jing Shang, Fang Cheng, Manish Dubey, Justin M Kaplan, Meghana Rawal, Xi Jiang, David S Newburg, Philip A Sullivan, Rodrigo B Andrade, and Daniel M Ratner. An organophosphonate strategy for functionalizing silicon photonic biosensors. *Langmuir*, 28(6):3338–3344, 2012. 41, 45

[142] Ayelet Vilan, Omer Yaffe, Ariel Biller, Adi Salomon, Antoine Kahn, and David Cahen. Molecules on si: electronics with chemistry. *Advanced materials*, 22(2):140–159, 2010.

[143] Rory Stine, Christina L Cole, Kristy M Ainslie, Shawn P Mulvaney, and Lloyd J Whitman. Formation of primary amines on silicon nitride surfaces: a direct, plasma-based pathway to functionalization. *Langmuir*, 23(8):4400–4404, 2007. 41

[144] Y Ikada. Surface modification of polymers for medical applications. *Biomaterials*, 15 (10):725–736, 1994. 41

[145] Claudia Haensch, Stephanie Hoeppener, and Ulrich S Schubert. Chemical modification of self-assembled silane based monolayers by surface reactions. *Chemical Society Reviews*, 39(6):2323–2334, 2010. 45

[146] Dohyun Kim and Amy E Herr. Protein immobilization techniques for microfluidic assays. *Biomicrofluidics*, 7(4):041501, 2013. 45

[147] LT Zhuravlev. The surface chemistry of amorphous silica. zhuravlev model. *Colloids and Surfaces A: Physicochemical and Engineering Aspects*, 173(1):1–38, 2000.

[148] Arthur W Adamson, Alice Petry Gast, et al. *Physical chemistry of surfaces*. Interscience publishers New York, 1967. 41

[149] Julie Melissa Goddard and JH Hotchkiss. Polymer surface modification for the attachment of bioactive compounds. *Progress in polymer science*, 32(7):698–725, 2007. 41, 43

[150] H. Elwing. Protein absorption and ellipsometry in biomaterial research. *Biomaterials*, 19(4-5):397–406, 1998. 41, 104, 148, 202

[151] K.P.S. Dancil, D.P. Greiner, and M.J. Sailor. A porous silicon optical biosensor: detection of reversible binding of igg to a protein a-modified surface. *Journal of the American Chemical Society*, 121(34):7925–7930, 1999. 41, 104, 148, 202

[152] Erwin A Vogler. Structure and reactivity of water at biomaterial surfaces. *Advances in colloid and interface science*, 74(1):69–117, 1998. 42

[153] Chung-Jung Tsai, Jacob V Maizel, and Ruth Nussinov. The hydrophobic effect: a new insight from cold denaturation and a two-state water structure. *Critical reviews in biochemistry and molecular biology*, 37(2):55–69, 2002.

[154] Michael A Henderson. The interaction of water with solid surfaces: fundamental aspects revisited. *Surface Science Reports*, 46(1):1–308, 2002. 42

[155] Marc Graille, Enrico A Stura, Adam L Corper, Brian J Sutton, Michael J Taussig, Jean-Baptiste Charbonnier, and Gregg J Silverman. Crystal structure of a staphylococcus aureus protein a domain complexed with the fab fragment of a human igm antibody: structural basis for recognition of b-cell receptors and superantigen activity. *Proceedings of the National Academy of Sciences*, 97(10):5399–5404, 2000. 43, 103

[156] Harold Erickson. Size and shape of protein molecules at the nanometer level determined by sedimentation, gel filtration, and electron microscopy. *Biological Procedures Online*, 11(1):32 – 51, 2009. URL http://www.biologicalproceduresonline.com/content/11/1/32. 43, 103, 150, 186, 202, 209, 214

[157] I.; Sjöquist; J.; Mota, Gabriela; Moraru and V. Ghetie. Protein a as a molecular probe for the detection of antigen induced conformational change in fc region of rabbit antibody. *Molecular immunology*, 18(5):373–378, 1981. 43, 148

[158] W.L. DeLano, M.H. Ultsch, and J.A. Wells. Convergent solutions to binding at a protein-protein interface. *Science*, 287(5456):1279–1283, 2000. 43, 148

[159] Martine Collaud Coen, Roland Lehmann, Pierangelo Gröning, Michael Bielmann, Carine Galli, and Louis Schlapbach. Adsorption and bioactivity of protein a on silicon surfaces studied by afm and xps. *Journal of colloid and interface science*, 233(2): 180–189, 2001. 43, 44, 104, 122, 127, 142, 150, 158, 202, 214

[160] S. A. Darst, M. Ahlers, P. H. Meller, E. W. Kubalek, R. Blankenburg, H. O. Ribi, H. Ringsdorf, and R. D. Kornberg. Two-dimensional crystals of streptavidin on biotinylated lipid layers and their interactions with biotinylated macromolecules. *Biophys J*, 59(2):387–96, 1991. URL http://www.ncbi.nlm.nih.gov/pubmed/1901232. 43, 125, 137, 150, 203

[161] AL Weisenhorn, F.J. Schmitt, W. Knoll, and PK Hansma. Streptavidin binding observed with an atomic force microscope. *Ultramicroscopy*, 42:1125–1132, 1992. 43, 125, 137, 150, 203, 214

[162] Kazuhiro Nakanishi, Takaharu Sakiyama, Yoichi Kumada, Koreyoshi Imamura, and Hiroyuki Imanaka. Recent advances in controlled immobilization of proteins onto the surface of the solid substrate and its possible application to proteomics. *Current Proteomics*, 5(3):161–175, 2008. 44

[163] Federica Rusmini, Zhiyuan Zhong, and Jan Feijen. Protein immobilization strategies for protein biochips. *Biomacromolecules*, 8(6):1775–1789, 2007. 44

[164] Stephan Laib and Brian D MacCraith. Immobilization of biomolecules on cycloolefin polymer supports. *Analytical chemistry*, 79(16):6264–6270, 2007. 44

[165] Abraham Ulman. Formation and structure of self-assembled monolayers. *Chemical reviews*, 96(4):1533–1554, 1996. 46

[166] Greg T Hermanson. *Bioconjugate techniques*. Academic press, 2013. 46, 47

[167] Christina Jönsson, Magnus Aronsson, Gerd Rundström, Christer Pettersson, Ib Mendel-Hartvig, Jimmy Bakker, Erik Martinsson, Bo Liedberg, Brian MacCraith, Ove Öhman, et al. Silane–dextran chemistry on lateral flow polymer chips for immunoassays. *Lab on a Chip*, 8(7):1191–1197, 2008. 47

[168] Jung Jin Park, Xiaolong Luo, Hyunmin Yi, Theresa M Valentine, Gregory F Payne, William E Bentley, Reza Ghodssi, and Gary W Rubloff. Chitosan-mediated in situ biomolecule assembly in completely packaged microfluidic devices. *Lab on a Chip*, 6 (10):1315–1321, 2006. 47

[169] Guodong Sui, Jinyi Wang, Chung-Cheng Lee, Weixing Lu, Stephanie P Lee, Jeffrey V Leyton, Anna M Wu, and Hsian-Rong Tseng. Solution-phase surface modification in intact poly (dimethylsiloxane) microfluidic channels. *Analytical chemistry*, 78(15): 5543–5551, 2006. 47

[170] Katrien De Vos, Jordi Girones, Tom Claes, Yannick De Koninck, Stepan Popelka, Etienne Schacht, Roel Baets, and Peter Bienstman. Multiplexed antibody detection with an array of silicon-on-insulator microring resonators. *Photonics Journal, IEEE*, 1(4):225–235, 2009. 47

[171] Sonia Grego, Jonathan R McDaniel, and Brian R Stoner. Wavelength interrogation of grating-based optical biosensors in the input coupler configuration. *Sensors and Actuators B: Chemical*, 131(2):347–355, 2008. 47

[172] Sudeshna Pal, Elisa Guillermain, Rashmi Sriram, Benjamin L Miller, and Philippe M Fauchet. Silicon photonic crystal nanocavity-coupled waveguides for error-corrected optical biosensing. *Biosensors and Bioelectronics*, 26(10):4024–4031, 2011. 47

[173] Norman D Brault, Changlu Gao, Hong Xue, Marek Piliarik, Jiří Homola, Shaoyi Jiang, and Qiuming Yu. Ultra-low fouling and functionalizable zwitterionic coatings grafted onto sio 2 via a biomimetic adhesive group for sensing and detection in complex media. *Biosensors and Bioelectronics*, 25(10):2276–2282, 2010. 48

[174] Zheng Zhang, Shengfu Chen, Yung Chang, and Shaoyi Jiang. Surface grafted sulfobetaine polymers via atom transfer radical polymerization as superlow fouling coatings. *The Journal of Physical Chemistry B*, 110(22):10799–10804, 2006. 48, 222

[175] B Lillis, M Manning, H Berney, E Hurley, A Mathewson, and MM Sheehan. Dual polarisation interferometry characterisation of dna immobilisation and hybridisation detection on a silanised support. *Biosensors and Bioelectronics*, 21(8):1459–1467, 2006. 49, 157

[176] JAd De Feijter, d J Benjamins, and FA Veer. Ellipsometry as a tool to study the adsorption behavior of synthetic and biopolymers at the air–water interface. *Biopolymers*, 17(7):1759–1772, 1978. 49

[177] L Guemouri, J Ogier, and JJ Ramsden. Optical properties of protein monolayers during assembly. *The Journal of chemical physics*, 109(8):3265–3268, 1998. 49

[178] Ulf Jönsson, Magnus Malmqvist, and Inger Ronnberg. Adsorption of immunoglobulin g, protein a, and fibronectin in the submonolayer region evaluated by a combined study of ellipsometry and radiotracer techniques. *Journal of colloid and interface science*, 103(2):360–372, 1985. 49

[179] Huaying Zhao, Patrick H Brown, and Peter Schuck. On the distribution of protein refractive index increments. *Biophysical journal*, 100(9):2309–2317, 2011. 49

[180] Lorena Diéguez, N Darwish, M Mir, E Martínez, M Moreno, and J Samitier. Effect of the refractive index of buffer solutions in evanescent optical biosensors. *Sensor Letters*, 7(5):851–855, 2009. 49

[181] Petr I Nikitin, BG Gorshkov, EP Nikitin, and TI Ksenevich. Picoscope, a new label-free biosensor. *Sensors and Actuators B: Chemical*, 111:500–504, 2005. 50, 157

[182] Emre Özkumur, Ayça Yalçın, Marina Cretich, Carlos A Lopez, David A Bergstein, Bennett B Goldberg, Marcella Chiari, and M Selim Ünlü. Quantification of dna and protein adsorption by optical phase shift. *Biosensors and Bioelectronics*, 25(1):167–172, 2009.

[183] Jacob Piehler, Andreas Brecht, and Guenter Gauglitz. Affinity detection of low molecular weight analytes. *Analytical Chemistry*, 68(1):139–143, 1996.

[184] Lev Moiseev, M Selim Ünlü, Anna K Swan, Bennett B Goldberg, and Charles R Cantor. Dna conformation on surfaces measured by fluorescence self-interference. *Proceedings of the National Academy of Sciences of the United States of America*, 103(8):2623–2628, 2006. 50, 157

[185] N Leigh Anderson and Norman G Anderson. The human plasma proteome history, character, and diagnostic prospects. *Molecular & cellular proteomics*, 1(11):845–867, 2002. 50, 183

[186] Blood safety basics. URL http://www.cdc.gov/bloodsafety/basics.html. accessed: June 27, 2016. 50, 57, 189

[187] Paul LF Giangrande. The history of blood transfusion. *British Journal of Haematology*, 110(4):758–767, 2000. 51

[188] Eduardo Fastag, Joseph Varon, and George Sternbach. Richard lower: the origins of blood transfusion. *The Journal of emergency medicine*, 44(6):1146–1150, 2013. 51

[189] Holly Tucker. *Blood work: A tale of medicine and murder in the scientific revolution*. WW Norton & Company, 2011. 51, 52

[190] World health organization. blood safety: Key global fact and figures in 2011. URL http://www.who.int/worldblooddonorday/media/who_blood_safety_factsheet_2011.pdf. 52

[191] JR Storry and Martin L Olsson. The abo blood group system revisited: a review and update. *Immunohematology*, 25(2):48–59, 2009. 52, 53, 57, 179, 180, 185, 188, 189, 206, 210

[192] Robert Russell Race and Ruth Sanger. *Blood groups in man*. Blackwell scientific publications, 1965. 52

[193] Ajit Varki. Biological roles of oligosaccharides: all of the theories are correct. *Glycobiology*, 3(2):97–130, 1993. 53

[194] F Yamamoto. Review: Abo blood group system–abh oligosaccharide antigens, anti-a and anti-b, a and b glycosyltransferases, and abo genes. *Immunohematology/American Red Cross*, 20(1):3–22, 2003. 53, 54

[195] Axel Seltsam, Daniela Grüger, Burkhard Just, Constança Figueiredo, Christa Das Gupta, David S DeLuca, and Rainer Blasczyk. Aberrant intracellular trafficking of a variant b glycosyltransferase. *Transfusion*, 48(9):1898–1905, 2008. 53

[196] DJ Anstee. The nature and abundance of human red cell surface glycoproteins. *International Journal of Immunogenetics*, 17(4-5):219–225, 1990. 54

[197] Miriam Cohen, Nancy Hurtado-Ziola, and Ajit Varki. Abo blood group glycans modulate sialic acid recognition on erythrocytes. *Blood*, 114(17):3668–3676, 2009. 54, 185, 188

[198] DM Harmening. Modern blood banking and transfusion medicine, 2005. 56

[199] Susan L Stramer, F Blaine Hollinger, Louis M Katz, Steven Kleinman, Peyton S Metzel, Kay R Gregory, and Roger Y Dodd. Emerging infectious disease agents and their potential threat to transfusion safety. *Transfusion*, 49(s2):1S–29S, 2009. 57, 189

[200] Richard J Benjamin, Carl P McDonald, et al. The international experience of bacterial screen testing of platelet components with an automated microbial detection system: a need for consensus testing and reporting guidelines. *Transfusion medicine reviews*, 28(2):61–71, 2014. 57, 189

[201] Eleftherios C Vamvakas and Morris A Blajchman. Transfusion-related mortality: the ongoing risks of allogeneic blood transfusion and the available strategies for their prevention. *Blood*, 113(15):3406–3417, 2009. 58

[202] AS Jugessur, J Dou, JS Aitchison, RM De La Rue, and M Gnan. A photonic nanobragg grating device integrated with microfluidic channels for bio-sensing applications. *Microelectronic Engineering*, 86(4):1488–1490, 2009. 63, 128, 132

[203] P Prabhathan, VM Murukeshan, Zhang Jing, and Pamidighantam V Ramana. Compact soi nanowire refractive index sensor using phase shifted bragg grating. *Optics express*, 17(17):15330–15341, 2009. 64, 128, 132, 137, 159

[204] Xu Wang, Samantha Grist, Jonas Flueckiger, Nicolas A. F. Jaeger, and Lukas Chrostowski. Silicon photonic slot waveguide bragg gratings and resonators. *Optics Express*, 21(16):19029–19039, 2013. URL http://www.opticsexpress.org/abstract.cfm?URI=oe-21-16-19029. 64, 128

[205] Wim Bogaerts, Dirk Taillaert, Bert Luyssaert, Pieter Dumon, Joris Van Campenhout, Peter Bienstman, Dries Van Thourhout, Roel Baets, V Wiaux, and S Beckx. Basic structures for photonic integrated circuits in silicon-on-insulator. *Opt. Express*, 12(8): 1583–1591, 2004. 66

[206] Trevor J Hall, Sergey V Gaponenko, and Sofia A Paredes. *Extreme photonics and applications*. Springer, 2010.

[207] Global silicon photonics market, 2010. 66, 186, 221

[208] James Pond, Chris Cone, Lukas Chrostowski, Jackson Klein, Jonas Flueckiger, Amy Liu, Dylan McGuire, and Xu Wang. A complete design flow for silicon photonics. In *SPIE Photonics Europe*, pages 913310–913310. International Society for Optics and Photonics, 2014. 66

[209] Lukas Chrostowski, Jonas Flueckiger, Charlie Lin, Michael Hochberg, James Pond, Jackson Klein, John Ferguson, and Chris Cone. Design methodologies for silicon photonic integrated circuits. In *SPIE OPTO*, pages 89890G–89890G. International Society for Optics and Photonics, 2014.

[210] Matthew W Royal, Richard B Fair, and Nan M Jokerst. Integrated sample preparation and sensing: Microresonator optical sensors embedded in digital electrowetting microfluidics systems. In *Sensors, 2011 IEEE*, pages 2050–2053. IEEE, 2011. 66, 218

[211] Yurii Vlasov. Silicon photonics for next generation computing systems. 2008. 66, 190

[212] Andrew Rickman. The commercialization of silicon photonics. *Nature Photonics*, 8(8): 579–582, 2014. 66, 190

[213] Benedetto Troia, Antonia Paolicelli, Francesco De Leonardis, and Vittorio MN Passaro. Photonic crystals for optical sensing: A review. 2013. 67, 220

[214] Frank Vollmer and Lan Yang. Review label-free detection with high-q microcavities: a review of biosensing mechanisms for integrated devices. *Nanophotonics*, 1(3-4):267–291, 2012. 67, 220

[215] Jeffrey Kirsch, Christian Siltanen, Qing Zhou, Alexander Revzin, and Aleksandr Simonian. Biosensor technology: recent advances in threat agent detection and medicine. *Chemical Society Reviews*, 42(22):8733–8768, 2013. 67, 220

[216] Siepic ebeam pdk. URL https://github.com/lukasc-ubc/SiEPIC_EBeam_PDK. accessed: June 27, 2016. 68, 219

[217] Xu Wang, James Pond, Chris Cone, Lukas Chrostowski, Jackson Klein, Jonas Flueckiger, Amy Liu, and Dylan McGuire. Large-scale silicon photonics circuit design. In *SPIE/COS Photonics Asia*, pages 927706–927706. International Society for Optics and Photonics, 2014. 69, 71

[218] Jeol jbx-6300fs e-beam lithography at the washington nanofabrication facility, . URL https://ebeam.mff.uw.edu/ebeamweb/. accessed: June 27th, 2016. 69

[219] Singapore A-Star IME foundry. Foundry, singapore a-star ime. URL https://www.a-star.edu.sg/ime/. accessed: June 27th, 2016. 69, 100

[220] epix foundry. URL http://www.epixfab.eu/. accessed: June 27th, 2016. 171, 193

[221] Europractice silicon photonics mpw. URL http://www.europractice-ic.com/SiPhotonics_general.php. accessed: June 27th, 2016.

[222] Moses silicon photonics mpw. URL https://www.mosis.com/vendors/view/imec. accessed: June 27th, 2016.

[223] Michael Hochberg and Tom Baehr-Jones. Towards fabless silicon photonics. *Nature Photonics*, 4(8):492–494, 2010. 69, 100

[224] Yun Wang, Xu Wang, Jonas Flueckiger, Han Yun, Wei Shi, Richard Bojko, Nicolas AF Jaeger, and Lukas Chrostowski. Focusing sub-wavelength grating couplers with low back reflections for rapid prototyping of silicon photonic circuits. *Optics express*, 22 (17):20652–20662, 2014. 71

[225] Lukas Chrostowski, Xu Wang, Jonas Flueckiger, Yichen Wu, Yun Wang, and Sahba Talebi Fard. Impact of fabrication non-uniformity on chip-scale silicon photonic integrated circuits. In *Optical Fiber Communication Conference*, pages Th2A–37. Optical Society of America, 2014. 73

[226] Frank Vollmer and Stephen Arnold. Whispering-gallery-mode biosensing: label-free detection down to single molecules. *Nature methods*, 5(7):591–596, 2008. 99, 158

[227] Andrea M Armani, Rajan P Kulkarni, Scott E Fraser, Richard C Flagan, and Kerry J Vahala. Label-free, single-molecule detection with optical microcavities. *Science*, 317 (5839):783–787, 2007. 99

[228] Dongliang Yin, David W Deamer, Holger Schmidt, John P Barber, and Aaron R Hawkins. Single-molecule detection sensitivity using planar integrated optics on a chip. *Optics letters*, 31(14):2136–2138, 2006. 99

[229] Jan-Willem Hoste, Sam Werquin, Tom Claes, and Peter Bienstman. Conformational analysis of proteins with a dual polarisation silicon microring. *Optics express*, 22(3): 2807–2820, 2014. 100, 106, 191

[230] Silicon photonics group at cornell, . URL http://nanophotonics.ece.cornell.edu/research/silicon-photonics.cfm. accessed: June 27th, 2016. 100

[231] Silicon photonics at ucsb, . URL http://siliconphotonics.ece.ucsb.edu/. accessed: June 27th, 2016.

[232] Uw nnin washington nanofabrication facility, . URL https://www.wnf.washington.edu/. accessed: June 27th, 2016. 100

[233] Stefano Sardo, Fabrizio Giacometti, Sergio Doneda, Umberto Colombo, Melissa Di Muri, Anna Donghi, Romano Morson, Giorgio Mutinati, Alessandro Nottola, Massimo Gentili, et al. Line edge roughness (ler) reduction strategy for soi waveguides fabrication. *Microelectronic Engineering*, 85(5):1210–1213, 2008. 100

[234] M Gnan, DS Macintyre, M Sorel, RM De La Rue, and S Thoms. Enhanced stitching for the fabrication of photonic structures by electron beam lithography. *Journal of Vacuum Science & Technology B*, 25(6):2034–2037, 2007. 138

[235] Yao Chen, Junbo Feng, Zhiping Zhou, ChristopherJ Summers, DavidS Citrin, and Jun Yu. Simple technique to fabricate microscale and nanoscale silicon waveguide devices. *Frontiers of Optoelectronics in China*, 2(3):308–311, 2009. URL http://dx.doi.org/10.1007/s12200-009-0049-1.

[236] Richard J Bojko, Jing Li, Li He, Tom Baehr-Jones, Michael Hochberg, and Yukinori Aida. Electron beam lithography writing strategies for low loss, high confinement silicon optical waveguides. *Journal of Vacuum Science & Technology B*, 29(6):06F309, 2011. 100, 101, 138, 145

[237] Yao Chen, Junbo Feng, Zhiping Zhou, Jun Yu, Christopher J Summers, and David S Citrin. Fabrication of silicon microring resonator with smooth sidewalls. *Journal of Micro/Nanolithography, MEMS, and MOEMS*, 8(4):043060–043060, 2009. 101

[238] Asahi Glass Co. Ltd. Cytop. Technical report, AGC Chemicals, 2009. 101, 139, 171, 193

[239] Raza Hanif. *Microfabrication of Plasmonic Biosensors in CYTOP Integrating a Thin SiO2 Diffusion and Etch-barrier Layer*. PhD thesis, University of Ottawa, 2011. 101, 139, 171, 193

[240] Cheng Zhenzhou, Wong Chi Yan, Chen Xia, Xu Ke, Y. M. Chen, and Tsang Hon Ki. Monolithic suspended membrane ring resonator for mid-infrared applications. pages 87–89, 2012. 101, 143

[241] Cheng Zhenzhou, Chen Xia, C. Y. Wong, Xu Ke, C. K. Y. Fung, Y. M. Chen, and Tsang Hon Ki. Mid-infrared suspended membrane waveguides on silicon-on-insulator. pages 257–258, 2012.

[242] Christopher Batten, Ajay Joshi, Jason Orcutt, Anatoly Khilo, Benjamin Moss, Charles W Holzwarth, Milo A Popovic, Hanqing Li, Henry I Smith, and Judy L

Hoyt. Building many-core processor-to-dram networks with monolithic cmos silicon photonics. *Micro, IEEE*, 29(4):8–21, 2009.

[243] Shankar Kumar Selvaraja, Patrick Jaenen, Wim Bogaerts, Dries Van Thourhout, Pieter Dumon, and Roel Baets. Fabrication of photonic wire and crystal circuits in silicon-on-insulator using 193-nm optical lithography. *Lightwave Technology, Journal of*, 27(18):4076–4083, 2009. 101, 143

[244] RL Sokoloff, KC Norton, CL Gasior, KM Marker, and LS Grauer. A dualmonoclonal sandwich assay for prostatespecific membrane antigen: Levels in tissues, seminal fluid and urine. *The Prostate*, 43(2):150–157, 2000. 103

[245] U.B. Nielsen and B.H. Geierstanger. Multiplexed sandwich assays in microarray format. *Journal of immunological methods*, 290(1):107–120, 2004. 103, 142

[246] Wei Shi, Han Yun, Charlie Lin, Jonas Flueckiger, Nicolas AF Jaeger, and Lukas Chrostowski. Coupler-apodized bragg-grating adddrop filter. *Optics letters*, 38(16): 3068–3070, 2013. 105

[247] Wei Shi, Xu Wang, Wen Zhang, Han Yun, Charlie Lin, Lukas Chrostowski, and Nicolas AF Jaeger. Grating-coupled silicon microring resonators. *Applied Physics Letters*, 100(12):121118, 2012. 105

[248] D. G. Rabus. *Integrated Ring Resonators*. Number 127. Springer, 2007. 107

[249] Wei-Ping Huang. Coupled-mode theory for optical waveguides: an overview. *JOSA A*, 11(3):963–983, 1994. 109

[250] Amnon Yariv. Coupled-mode theory for guided-wave optics. *Quantum Electronics, IEEE Journal of*, 9(9):919–933, 1973. 109

[251] Nicolas Rouger, Lukas Chrostowski, and Raha Vafaei. Temperature effects on silicon-on-insulator (soi) racetrack resonators: A coupled analytic and 2-d finite difference approach. *Journal of Lightwave Technology*, 28(9):1380–1391, 2010. 111

[252] Adam Densmore, D-X Xu, Philip Waldron, Siegfried Janz, Pavel Cheben, J Lapointe, André Delâge, Boris Lamontagne, JH Schmid, and Edith Post. A silicon-on-insulator photonic wire based evanescent field sensor. *Photonics Technology Letters, IEEE*, 18 (23):2520–2522, 2006. 112, 186

[253] Valery V Tuchin, Irina L Maksimova, Dmitry A Zimnyakov, Irina L Kon, Albert H Mavlyutov, and Alexey A Mishin. Light propagation in tissues with controlled optical properties. *Journal of biomedical optics*, 2(4):401–417, 1997. 118

[254] Przemek J. Bock, Pavel Cheben, Jens H. Schmid, Jean Lapointe, André Delâge, Dan-Xia Xu, Siegfried Janz, Adam Densmore, and Trevor J. Hall. Subwavelength grating crossings for silicon wire waveguides. *Optics Express*, 18(15):16146–16155, 2010. URL http://www.opticsexpress.org/abstract.cfm?URI=oe-18-15-16146. 119

[255] Robert Halir, Przemek J Bock, Pavel Cheben, Alejandro Ortega-Moñux, Carlos Alonso-Ramos, Jens H Schmid, Jean Lapointe, Dan-Xia Xu, J Gonzalo Wangüemert-Pérez, and Íñigo Molina-Fernández. Waveguide sub-wavelength structures: a review of principles and applications. *Laser and Photonics Reviews*, 9(1):25–49, 2015.

[256] P Cheben, PJ Bock, JH Schmid, J Lapointe, S Janz, D-X Xu, R Ma, A Densmore, A Delâge, and B Lamontagne. Subwavelength and diffractive waveguide structures and their applications in nanophotonics and sensing. In *SPIE OPTO*, pages 794111–794111. International Society for Optics and Photonics, 2011. 119

[257] Valentina Donzella, Ahmed Sherwali, Jonas Flueckiger, Sahba Talebi Fard, Samantha M Grist, and Lukas Chrostowski. Sub-wavelength grating components for integrated optics applications on soi chips. *Optics express*, 22(17):21037–21050, 2014. 120

[258] Marko Lončar, Theodor Doll, Jelena Vučković, and Axel Scherer. Design and fabrication of silicon photonic crystal optical waveguides. *J. Lightwave Technol.*, 18(10):1402, Oct 2000. URL http://jlt.osa.org/abstract.cfm?URI=jlt-18-10-1402. 120

[259] Kazuaki Sakoda. *Optical properties of photonic crystals*, volume 80. Springer Science & Business Media, 2004. 120

[260] Xu Wang, Yun Wang, Jonas Flueckiger, Richard Bojko, Amy Liu, Adam Reid, James Pond, Nicolas AF Jaeger, and Lukas Chrostowski. Precise control of the coupling coefficient through destructive interference in silicon waveguide bragg gratings. *Optics letters*, 39(19):5519–5522, 2014. 120, 129, 131, 138

[261] Robert W Boyd and John E Heebner. Sensitive disk resonator photonic biosensor. *Applied Optics*, 40(31):5742–5747, 2001. 123

[262] Aaron Schweinsberg, Sandrine Hocdé, Nick N. Lepeshkin, Robert W. Boyd, Christopher Chase, and Julie E. Fajardo. An environmental sensor based on an integrated optical whispering gallery mode disk resonator. *Sensors and Actuators B: Chemical*, 123(2):727–732, 2007. 123

[263] Carlos Angulo Barrios, Benito Sánchez, Kristinn Bjrgvin Gylfason, Amadeu Griol, Hans Sohlstrm, Miquel Holgado, and Raphael Casquel. Demonstration of slot-waveguide structures on silicon nitride/silicon oxide platform. *Optics express*, 15(11): 6846–6856, 2007. 123, 134

[264] Jonas Flueckiger, Samantha M Grist, Gurpal Bisra, Lukas Chrostowski, and Karen C Cheung. Cascaded silicon-on-insulator microring resonators for the detection of biomolecules in pdms microfluidic channels. In *SPIE MOEMS-MEMS*, pages 79290I–79290I. International Society for Optics and Photonics, 2011. 125

[265] Kirill Zinoviev, Laura G. Carrascosa, José Sánchez del Río, Borja Sepúlveda, Car-

los Domínguez, and Laura M. Lechuga. Silicon photonic biosensors for lab-on-a-chip applications. 2008. URL http://www.hindawi.com/journals/aot/2008/383927/. 128

[266] Xu Wang, Wei Shi, Raha Vafaei, Nicolas AF Jaeger, and Lukas Chrostowski. Uniform and sampled bragg gratings in soi strip waveguides with sidewall corrugations. *IEEE Photonics Technology Letters*, 23(5):290, 2011. 128, 138

[267] Zhitian Chen, Jonas Flueckiger, Xu Wang, Fan Zhang, Han Yun, Zeqin Lu, Michael Caverley, Yun Wang, Nicolas AF Jaeger, and Lukas Chrostowski. Spiral bragg grating waveguides for tm mode silicon photonics. *Optics Express*, 23(19):25295–25307, 2015. 129, 131, 138

[268] Alexandre D Simard, Nezih Belhadj, Yves Painchaud, and Sophie LaRochelle. Apodized silicon-on-insulator bragg gratings. *Photonics Technology Letters, IEEE*, 24(12):1033–1035, 2012. 129

[269] Xu Wang. *Silicon photonic waveguide Bragg gratings*. PhD thesis, University of British Columbia, 2013. 129, 131

[270] DC Flanders, H Kogelnik, RV Schmidt, and CV Shank. Grating filters for thin-film optical waveguides. *Applied Physics Letters*, 24(4):194–196, 1974. 129

[271] James Pond, Xu Wang, Jonas Flückiger, Adam Reid, Jens Niegemann, Amy Liu, and Lukas Chrostowski. Design and optimization of photolithography friendly photonic components. In *SPIE OPTO*, pages 97510V–97510V. International Society for Optics and Photonics, 2016. 131

[272] Xu Wang, Wei Shi, Han Yun, Samantha Grist, Nicolas A. F. Jaeger, and Lukas Chrostowski. Narrow-band waveguide bragg gratings on soi wafers with cmos-compatible fabrication process. *Opt. Express*, 20(14):15547–15558, 2012. URL http://www.opticsexpress.org/abstract.cfm?URI=oe-20-14-15547. 133, 137

[273] Xu Wang, Wei Shi, Michael Hochberg, Kostas Adam, Ellen Schelew, Jeff F Young, Nicolas AF Jaeger, and Lukas Chrostowski. Lithography simulation for the fabrication of silicon photonic devices with deep-ultraviolet lithography. In *IEEE Group IV Photonics Conference (San Diego, CA, USA 2012), paper ThP17*, 2012. 133, 138

[274] Carlos A Barrios, Kristinn B Gylfason, Benito Sánchez, Amadeu Griol, Hans Sohlstrm, Miquel Holgado, and Raphael Casquel. Slot-waveguide biochemical sensor. *Optics letters*, 32(21):3080–3082, 2007. 134

[275] Francesco DellOlio and Vittorio MN Passaro. Optical sensing by optimized silicon slot waveguides. *Opt. Express*, 15(8):4977–4993, 2007. 134

[276] Joseph A Curcio and Charles C Petty. The near infrared absorption spectrum of liquid water. *JOSA*, 41(5):302–302, 1951. 138, 150, 186

[277] Wim Bogaerts, Roel Baets, Pieter Dumon, Vincent Wiaux, Stephan Beckx, Dirk Taillaert, Bert Luyssaert, Joris Van Campenhout, Peter Bienstman, and Dries Van Thourhout. Nanophotonic waveguides in silicon-on-insulator fabricated with cmos technology. *Lightwave Technology, Journal of*, 23(1):401–412, 2005. 139, 159, 162

[278] Min Huang, Ahmet Ali Yanik, Tsung-Yao Chang, and Hatice Altug. Sub-wavelength nanofluidics in photonic crystal sensors. *Optics express*, 17(26):24224–24233, 2009. 143

[279] Taechung Yi, Lu Li, and Chang-Jin Kim. Microscale material testing of single crystalline silicon: process effects on surface morphology and tensile strength. *Sensors and Actuators A: Physical*, 83(1):172–178, 2000. 144

[280] Linhong Kou, Daniel Labrie, and Petr Chylek. Refractive indices of water and ice in the 0.65-to 2.5-m spectral range. *Applied Optics*, 32(19):3531–3540, 1993. 150

[281] Matthew S Luchansky and Ryan C Bailey. High-q optical sensors for chemical and biological analysis. *Analytical chemistry*, 84(2):793–821, Jan 2012. doi: 10.1021/ac2029024. 156, 158, 159, 164

[282] J Gonzalo Wangüemert-Pérez, Pavel Cheben, Alejandro Ortega-Moñux, Carlos Alonso-Ramos, Diego Pérez-Galacho, Robert Halir, Iñigo Molina-Fernández, Dan-Xia Xu, and Jens H Schmid. Evanescent field waveguide sensing with subwavelength grating structures in silicon-on-insulator. *Optics letters*, 39(15):4442–4445, 2014. 158

[283] Daniel K Sparacin, Steven J Spector, and Lionel C Kimerling. Silicon waveguide sidewall smoothing by wet chemical oxidation. *Journal of lightwave technology*, 23(8): 2455, 2005. 159

[284] F Grillot, L Vivien, S Laval, D Pascal, and E Cassan. Size influence on the propagation loss induced by sidewall roughness in ultrasmall soi waveguides. *Photonics Technology Letters, IEEE*, 16(7):1661–1663, 2004. 159, 162

[285] Jared T Kindt, Matthew S Luchansky, Abraham J Qavi, So-Hyun Lee, and Ryan C Bailey. Subpicogram per milliliter detection of interleukins using silicon photonic microring resonators and an enzymatic signal enhancement strategy. *Analytical chemistry*, 85(22):10653–10657, 2013. 160

[286] Niels Asger Mortensen, Sanshui Xiao, and Jesper Pedersen. Liquid-infiltrated photonic crystals: enhanced light-matter interactions for lab-on-a-chip applications. *Microfluidics and Nanofluidics*, 4(1-2):117–127, 2008. 160

[287] Katrien De Vos. *Label-free silicon photonics biosensor platform with microring resonators*. PhD thesis, 2010. 165

[288] Sergio Mendez, Erin M Fenton, Gil R Gallegos, Dimiter N Petsev, Scott S Sibbett, Howard A Stone, Yi Zhang, and Gabriel P López. Imbibition in porous membranes of complex shape: quasi-stationary flow in thin rectangular segments. *Langmuir*, 26(2): 1380–1385, 2009. 170

[289] Lumerical solutions, inc. URL http://www.lumerical.com. accessed: June 27, 2016. 171, 192, 201

[290] Shon Schmidt. *Enhancing the performance of silicon photonic biosensors for clinical applications*. PhD thesis, University of Washington, 3720 15th Ave NE, July 2016. 184, 185

[291] M Alan Chester and Martin L Olsson. The abo blood group gene: a locus of considerable genetic diversity. *Transfusion medicine reviews*, 15(3):177–200, 2001. 185, 189

[292] EA Munn, L Bachmann, and A Feinstein. Structure of hydrated immunoglobulins and antigen-antibody complexes. electron microscopy of spray-freeze-etched specimens. *Biochimica et Biophysica Acta (BBA)-Protein Structure*, 625(1):1–9, 1980. 186, 203, 209

[293] Dan-Xia Xu, Jens H Schmid, Graham T Reed, Goran Z Mashanovich, David J Thomson, Milos Nedeljkovic, Xia Chen, Dries Van Thourhout, Shahram Keyvaninia, and Shankar K Selvaraja. Silicon photonic integration platform-have we found the sweet spot? *IEEE Journal of Selected Topics in Quantum Electronics*, 20(4):189–205, 2014. 186, 221

[294] Rongjin Yan, Santano P Mestas, Guangwei Yuan, Rashid Safaisini, David S Dandy, and Kevin L Lear. Label-free silicon photonic biosensor system with integrated detector array. *Lab on a Chip*, 9(15):2163–2168, 2009. 220

[295] Günther Roelkens, Joris Van Campenhout, Joost Brouckaert, Dries Van Thourhout, Roel Baets, P Rojo Romeo, P Regreny, A Kazmierczak, C Seassal, X Letartre, et al. Iii-v/si photonics by die-to-wafer bonding. *Materials Today*, 10(7):36–43, 2007. 186, 220, 221

[296] Temsiri Songjaroen, Wijitar Dungchai, Orawon Chailapakul, Charles S Henry, and Wanida Laiwattanapaisal. Blood separation on microfluidic paper-based analytical devices. *Lab on a Chip*, 12(18):3392–3398, 2012. 186, 221

[297] David M Cate, Jaclyn A Adkins, Jaruwan Mettakoonpitak, and Charles S Henry. Recent developments in paper-based microfluidic devices. *Analytical chemistry*, 87(1): 19–41, 2014. 186, 220, 221

[298] Moussa Kourout, Carolyn Fisher, Anjan Purkayastha, Clark Tibbetts, Valerie Winkelman, Phillip Williamson, Hira L Nakhasi, and Robert Duncan. Multiplex detection and identification of viral, bacterial, and protozoan pathogens in human blood and plasma using a high-density resequencing pathogen microarray platform. *Transfusion*, 2016. 189

[299] John G Quinn, Richard O'Kennedy, Malcolm Smyth, John Moulds, and Tom Frame. Detection of blood group antigens utilising immobilised antibodies and surface plasmon resonance. *Journal of immunological methods*, 206(1):87–96, 1997.

[300] Oleksiy Krupin, Chen Wang, and Pierre Berini. Selective capture of human red blood cells based on blood group using long-range surface plasmon waveguides. *Biosensors and Bioelectronics*, 53:117–122, 2014.

[301] Nongluck Houngkamhang, Apirom Vongsakulyanon, Patjaree Peungthum, Krisda Sudprasert, Pimpun Kitpoka, Mongkol Kunakorn, Boonsong Sutapun, Ratthasart Amarit, Armote Somboonkaew, and Toemsak Srikhirin. Abo blood-typing using an antibody array technique based on surface plasmon resonance imaging. *Sensors*, 13(9):11913–11922, 2013. 189

[302] Zhugong Liu, Meihong Liu, Teresita Mercado, Orieji Illoh, and Richard Davey. Extended blood group molecular typing and next-generation sequencing. *Transfusion medicine reviews*, 28(4):177–186, 2014. 189

[303] SA Boccoz, LJ Blum, and CA Marquette. Dna biosensor/biochip for multiplex blood group genotyping. *Methods*, 64(3):241–249, 2013. 189

[304] Mohammad Al-Tamimi, Wei Shen, Rania Zeineddine, Huy Tran, and Gil Garnier. Validation of paper-based assay for rapid blood typing. *Analytical chemistry*, 84(3): 1661–1668, 2012. 189

[305] WL Then, Miaosi Li, Heather McLiesh, Wei Shen, and Gil Garnier. The detection of blood group phenotypes using paper diagnostics. *Vox sanguinis*, 108(2):186–196, 2015.

[306] Julaluk Noiphung, Kwanrutai Talalak, Irin Hongwarittorrn, Naricha Pupinyo, Pannawich Thirabowonkitphithan, and Wanida Laiwattanapaisal. A novel paper-based assay for the simultaneous determination of rh typing and forward and reverse abo blood groups. *Biosensors and Bioelectronics*, 67:485–489, 2015. 189

[307] Carlos Angulo Barrios. Integrated microring resonator sensor arrays for labs-on-chips. *Analytical and bioanalytical chemistry*, 403(6):1467–1475, 2012. 190

[308] Soha Yousuf, Mahmoud M. Shahin, Hayk Gevorgyan, Bob Voort, Ayat Taha, Clara Dimas, Marcus Dahlem, and Anatol Khilo. Suspended microring resonator sensor using internal sub-wavelength grating. In *Advanced Photonics 2015*, page SeS4C.4. Optical Society of America, 2015. doi: 10.1364/SENSORS.2015.SeS4C.4. URL http://www.osapublishing.org/abstract.cfm?URI=Sensors-2015-SeS4C.4. 216, 220

[309] Long-Fang Tsai, William C Dahlquist, Seunghyun Kim, and Gregory P Nordin. Bonding of polydimethylsiloxane microfluidics to silicon-based sensors. *Journal of Micro/-Nanolithography, MEMS, and MOEMS*, 10(4):043009–043009, 2011. 221

[310] George M Whitesides. The origins and the future of microfluidics. *Nature*, 442(7101): 368–373, 2006. 221

[311] Norman D. Brault, Changlu Gao, Hong Xue, Marek Piliarik, Jií Homola, Shaoyi Jiang, and Qiuming Yu. Ultra-low fouling and functionalizable zwitterionic coatings grafted onto sio2 via a biomimetic adhesive group for sensing and detection in complex media.

Biosensors and Bioelectronics, 25(10):2276–2282, 2010. URL http://www.sciencedirect.com/science/article/pii/S0956566310001302. 222

[312] Zheng Zhang, Timothy Chao, Shengfu Chen, and Shaoyi Jiang. Superlow fouling sulfobetaine and carboxybetaine polymers on glass slides. *Langmuir*, 22(24):10072–10077, 2006. 222

[313] Sahba Talebi Fard, Valentina Donzella, Shon Schmidt, Wenxuan Wu, Rick Bojko, and Lukas Chrostowski. Sensitivity analysis of thin and ultra-thin soi rings for sensing applications. In *IEEE Photonics Conference*, 2013. 223

[314] Sahba Talebi Fard, Shon Schmidt, Wei Shi, Wenxuan Wu, Nick Jaeger, Ezra Kwok, Daniel M. Ratner, and Lukas Chrostwoski. Optimized sensitivity of silicon-on-insulator strip waveguide resonator sensor. *Submitted*, 2016. 223

[315] Maple leaf photonics. URL wwww.mapleleafphotonics.com. 224

[316] Project and bug tracking in jira. URL https://biobench.atlassian.net/secure/Dashboard.jspa. accessed: June 27, 2016. 291

[317] Silicon photonic analysis tool, . URL https://github.com/shonschmidt/SiPhoAnalysisTool. accessed: June 27th, 2016. 291

Appendix A

TESTBENCH SOFTWARE

A.1 Control Software

The test platform control software is written in MATLAB (Natick, MA). This language choice was largely motivated by the need for maintainability and extensibility since most bioengineering students learn and use MATLAB sometime during their academic tenure. GitHub (San Francisco, CA) and Atlassian's Jira (Sydney, Australia) are used for source code version control and bug tracking. The software architecture follows the industry standard

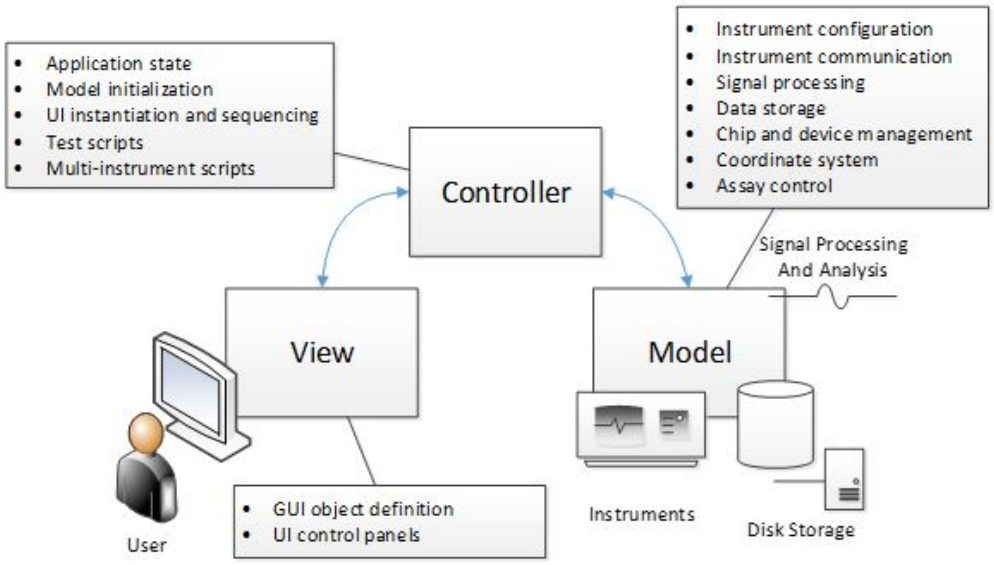

Figure A.1: Platform Control Application Model-View-Controller Overview. The View defines UI objects used to interpret commands from the user and provide status. The Controller executes command sequences, manages the application state, and controls the test processes. The Models communicate with the instruments and structures that store data.

model-view-controller partitioning as much as possible among the MATLAB objects, scripts, and UI elements (as shown in Fig. A.1). The models define objects that interact with a data source like the hard disk or an instrument. The view defines the user interaction experience (shows output and manages user input) through MATLAB's built-in GUI elements. The controller interprets the user's commands and orchestrates steps using the models to provide the result. While the controller could be implemented as a class, it largely exists as MATLAB scripts with global access to every object and GUI element in the application's namespace.

Table A.1: Platform control application class definition

Name (in source)	Description	Purpose
TestBenchClass	Testbench application class	Manage initialization, application state and settings, and sequenced flow
AssayCtl	Assay control class	Orchestrates assays, controls the instruments, and updates GUI
CoordSysClass	Coordinate system class	Configures coordinate system and translates position/coordinate pairs
InstrClass	Instrument class	Properties and methods to interface and control instruments
DeviceClass	Device class	Manages the data for each sensor, i.e. 'device', within a chip
ChipClass	Chip class	Manages chip-level data common to all devices, e.g. coordinate file, assay params, etc.

Due to historical reasons, the GUI is not a class but handles to its object are accessible throughout the application via a testbench class property. Other classes implemented in the control software are listed in Table A.1 with brief explanations of their purpose. Care was taken keep classes and objects as independent as possible to facilitate re-use and maintainability.

A.1.1 Program Flow (Sequencing)

Since testing devices or performing assays involve many sequenced steps, the application guides the user through the process shown in Fig. A.2.

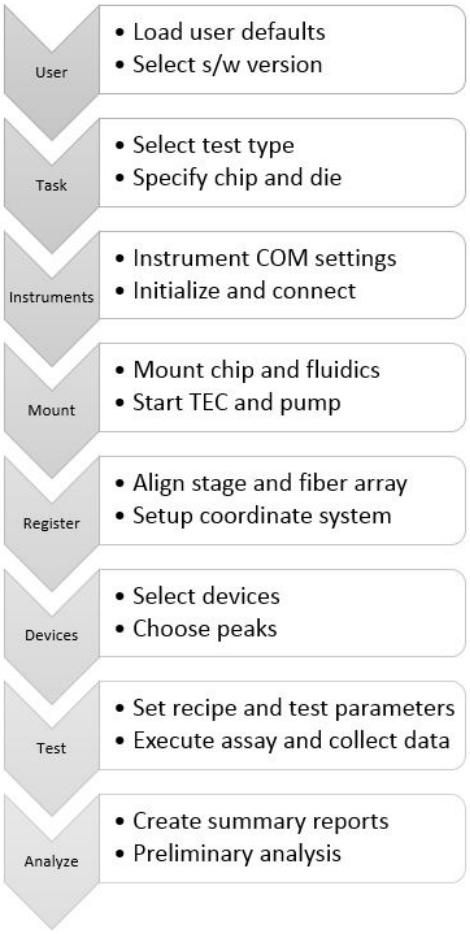

Figure A.2: Control application flow and sequenced tasks. The software is designed to step the user through the required steps necessary to fully test and characterize biosensing devices.

The GUI has eight sequenced panels which host smaller UI control panels for instrument or object controls (like coordinate system). Panels are hidden or visible based on the user's progress through the required sequence and the control UI windows are often replicated

across panels depending on the functionality required. The panel sequence is shown in Fig. A.2 with a brief description of tasks performed at that step.

Initializing the application (Users, Task, and Instrument panels)

The application opens to the user panel allowing the user to load their previous settings, specify an email address for automated alerts, and select a specific version tailored for their specific hardware or group. Pressing the next button will advance to the task panel where the user selects the test type (DryTest, WetTest, SaltSteps, BioAssay, or VirtualTestMode) and specifies the test data location on disk, the chip architecture (coordinate file), and unique die identifier (string). The next panel is the instrument panel where the user selects specific instruments and connects to them. The next button will remain disabled until all the selected instruments have successfully initialized. If an instrument is not loaded, its control UI will not appear on the subsequent panels.

Setting up the device under test (Mount and Resister panels)

The mount and register panels help the user align the chip and begin the equilibrium process for the chip in its thermally tuned, aqueous environment. During this step, the user loads a chip, enables the vacuum to immobilize it and then mounts a fluidic gasket before seating the flow cell over it. The user can then begin the alignment with the chip and flow cell securely mounted.

An overhead USB camera connected to a monocular zoom lens provides the necessary resolution to rotationally align the chip to the fiber array. To accomplish this, the user physically marks an on-chip alignment farm or fiducial at one of the chip on the display with a small piece of tape and traverses the chip to the complementary alignment feature (see Figs. A.3(a) and A.3(b). The rotation stage aligns the x and y axes. This process is repeated until the two features align perfectly with the tape. The user then lowers the fiber array until its reflection off the chip's surface can be seen from the second alignment camera (see Fig. A.3(c)). At this point, the fiber array is typically within a few hundred microns of

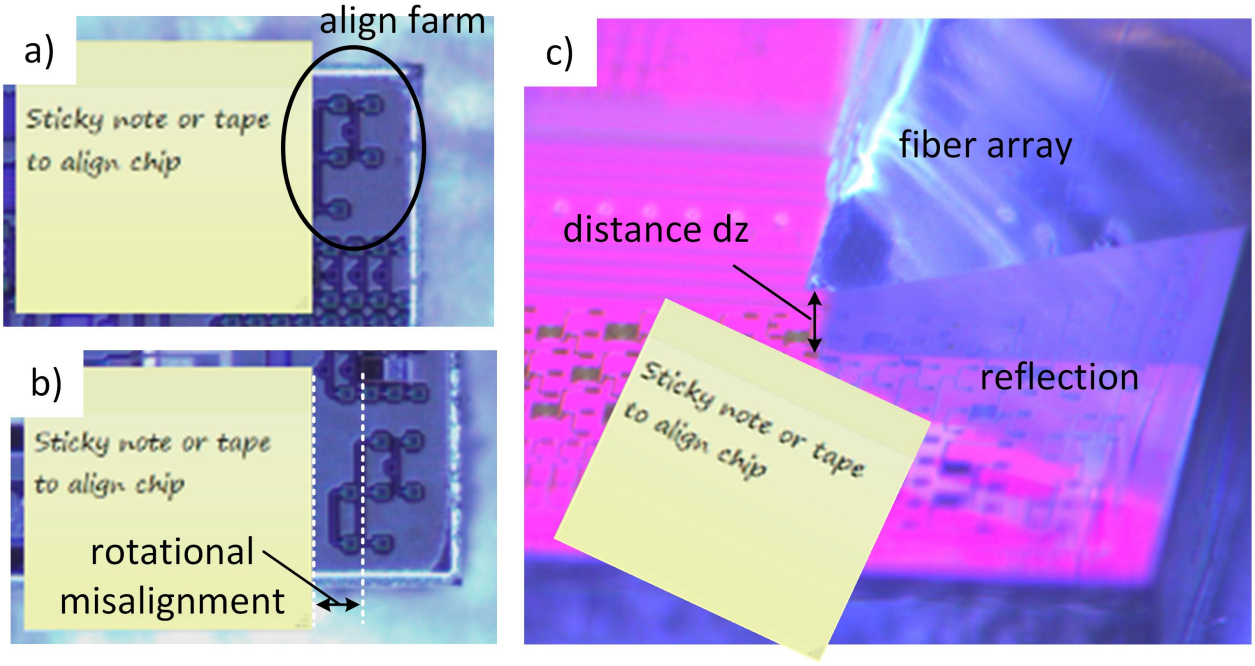

Figure A.3: The chip must be rotationally aligned to the fiber array prior to setting up a coordinate system for automated testing. (a) Any feature can provide a reference to rotationally align the chip but it must have a complementary, in-line marking on the other side of the chip (in this case, the loop backed alignment grating couplers are used). The user moves to the other end of the chip and checks for rotational misalignment (b). This process is repeated until the misalignment is gone. (c) The tip-tilt stage is used to ensure a fully parallel plane between the chip and fiber array. The corner of the fiber array's reflection is marked and the user moves the chip to each corner, ensuring the marked gap is consistent at all locations.

the chip's surface. Again, the user places the piece of tape along a reflected edge traverses the chip in both the X and Y directions. If the chip and fiber array are not in the same plane then the distance between the fiber array and chip (dz) changes and so does the location of the shadow. The tip-tilt stage can be adjusted until the marked edge used for alignment is consistently coincident with the marker. With the chip know appropriately aligned, the

fiber array can be moved within 30-50 µm's of the surface to begin the registration process.

If a TEC is connected, the user can thermally tune the stage. For wet and bio assays, the user loads the fluidic tray and specifies the well plate configurations (any combination of two 6, 24, and 96 well plates is currently supported). To continue from a previous assay, the user can also specify the current well for previously loaded trays. If a pump is connected, the user can set the flow rate and start the pump to establish a signal baseline prior to the assay. With the completion of these tasks, the user advances to the registration panel to setup a coordinate system. The registration panel is designed with the intent to use image processing provided by the overhead alignment camera to automatically align and register the chip. Since this feature has not been implemented fully, the user creates the coordinate system manually. Clicking on the Start button will pop-up a new window with all the controls necessary to start the process. The user begins setting up a coordinate system by aligning the fiber array over the first grating coupler alignment farm and starting a 'Map GC'. This feature enables lasing and captures any reflected power as the optical stage rasters a user-defined area. The results are shown in a window (Fig. 3.16) where the looped-back grating couplers will have a distinct signature since they reflect back a majority of the power. The user then clicks the 'Snap to GC' button. A cross-hair appears that allows the user to click on a GC in the results window. The stage moves to that position and the user executes a 'Fine Align' to optimize the fiber array's position to the on-chip grating coupler. The user then selects the device from the pull down window in the 'Coordinates' sub-panel and clicks the 'set' radial button to specify a stage location and gds coordinate pair. The user then moves to the next alignment structure and repeats the process. The application computes the coordinate system mapping function automatically after three valid assignments have been set and displays the goodness of fit. As an aside, the Laser UI panel is also included in the window so the user can change the lasing wavelength if need be or execute sweeps to optimize the fiber array's rotation (and angle of incidence) to maximize bandwidth and minimize insertion loss at the required wavelengths.

Selecting devices (Devices Panel)

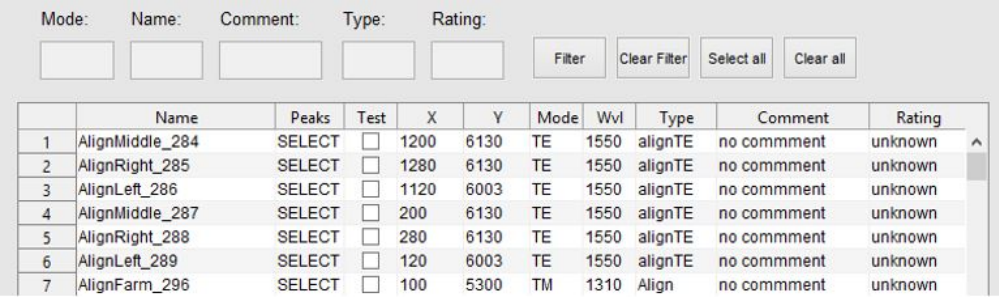

	Name	Peaks	Test	X	Y	Mode	Wvl	Type	Comment	Rating
1	AlignMiddle_284	SELECT	☐	1200	6130	TE	1550	alignTE	no commment	unknown
2	AlignRight_285	SELECT	☐	1280	6130	TE	1550	alignTE	no commment	unknown
3	AlignLeft_286	SELECT	☐	1120	6003	TE	1550	alignTE	no commment	unknown
4	AlignMiddle_287	SELECT	☐	200	6130	TE	1550	alignTE	no commment	unknown
5	AlignRight_288	SELECT	☐	280	6130	TE	1550	alignTE	no commment	unknown
6	AlignLeft_289	SELECT	☐	120	6003	TE	1550	alignTE	no commment	unknown
7	AlignFarm_296	SELECT	☐	100	5300	TM	1310	Align	no commment	unknown

Figure A.4: Platform Control Application Selecting Devices Panel. The user is able to filter the hundreds of devices on a chip based on the mode, name, type (bio, test, etc.), or rating. Devices can be selected for testing. Selecting a device automatically initiates a fine alignment and pops-up a window to select peaks to track. This is unnecessary for dry testing.

The list of devices on the chip will remain unselectable until a valid coordinate system exists or the user has specified the fiber array's current location (if already on a device). The devices panel allows the user to filter the list of devices and selects which ones will be tested. For characterization or bio assays, the user can specify which peaks to track during the test. Clicking on the SELECT button will perform a fine align and pop-up a new window to select peaks. Settings and ranges can be configured before performing a sweep. Scan results are displayed for each enabled detector and the user clicks the start button to select the resonant peaks or nulls in the waveform. Multiple peaks can be selected. The Save and Close button returns the user to the devices list to continue a similar process for other devices to test. When all the devices have been selected, the next button advances the application to the test control panel.

Test orchestration and control (Test Panel)

In the case of a dry or wet test, the user simply clicks 'Start' and the application sequences through the list of devices, performing a fine align and sweep for each device and saving the

results to the specified data repository. For a SaltSteps test, clicking 'Start' briefly pops-up a window that allows the user to specify well numbers for a pre-specified number of titrations. The user can edit the `<path>/defaultSaltSteps.txt` file directly to change reagents or temperature settings if necessary. Selecting the BioAssay test will initiate two pop-ups before the user can begin testing. The first window allows the user to specify the recipe file for the assay. The second window allows the user to set configuration switches for the assay. The most significant configurable parameters include: temperature stabilization precision and timeout periods, inlet tubing size for auto-priming and correctly marking reagents with acquired scans, manual or automated sequencing of reagents, tube relaxation periods to minimize air bubbles during reagent changes, how many scans to perform before executing a fine align, and the number of iterations through the recipe for the selected devices.

Recipe File The recipe file allows the user to automate multi-step assays easily. The first line in this simple text file is a comment representing the appropriate format (shown below) and a comma separates the parameters.

```
%<well>,<time(min)>,<reagent>,<ri>,<velocity>,<temp>,<comment>
```

The parameters include: the well number ($\# > 0$), the dwell time in the well ($\# > 0$) which can also be translated into number of sweeps using an assay configuration setting), the reagent name (string of any length), the refractive index of the reagent can be any number and is most useful for automated salt-step characterization used to determine sensitivity, pump flow rate in uL/min (> 0), the target stage temperature in Celsius (number), and a comment (string of any length). An example recipe file is included the GitHub repository with the source code.

Real-time Assay Control Bio assays often need user intervention. Extra time might be required to achieve a binding equilibrium, the user might want to immediately advance to the next step, or an air bubble may be trapped over the sensor under test. Whatever

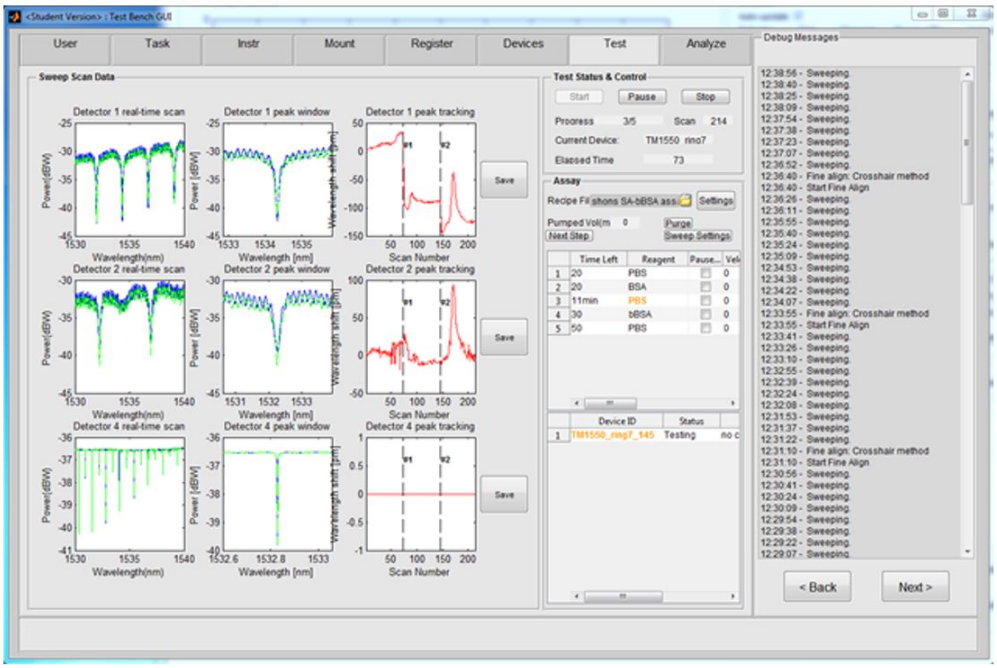

Figure A.5: Platform Control Application Assay Panel. In this example, three detector channels are active (top to bottom), showing the entire spectra for one scan (on left), the selected peak within the tracking window (center), and the tracked peak over the course of the assay (right). The recipe window indicates the current assay step and remaining time. Status messages are provided to the user in the debug window along the left-side.

the case, pressing the 'cancel' button in the 'Sweeping' waitbar popup pauses the assay and allows the user to intervene mid-way through the test. The user can add time to the current step, skip to the next step, edit the recipe, and interact with the pump directly to remove air bubbles. Clicking the 'Resume' button returns control to the application continuing programmed execution.

Automated analysis and reporting (Analyze Panel)

When the test finishes, advancing to the analyze panel provides options to generate automated reports and analysis for dry, wet, and salt step test. For dry and wet tests, the user

can generate a single report (pdf) which includes scanline plots for the enabled detectors for all the devices tested. This is useful to quickly assess which devices worked well enough to invest the additional time and effort to characterize. To analyze salt step results, the user selects the device, detector number, and then clicks 'Analyze'. The application automatically calculates and plots the sensitivity (nm/RIU) based on the refractive index value specified in the recipe file. Bio assays and other specialized tests can be analyzed using the stand-alone analysis tool described in the next major section below.

A.1.2 Adding new Instruments

Flexibility and extensibility were key design requirements when developing the application. Adding a new instrument involves modifying a few lines of code and creating the instrument object (class) with the appropriate parameters and methods.

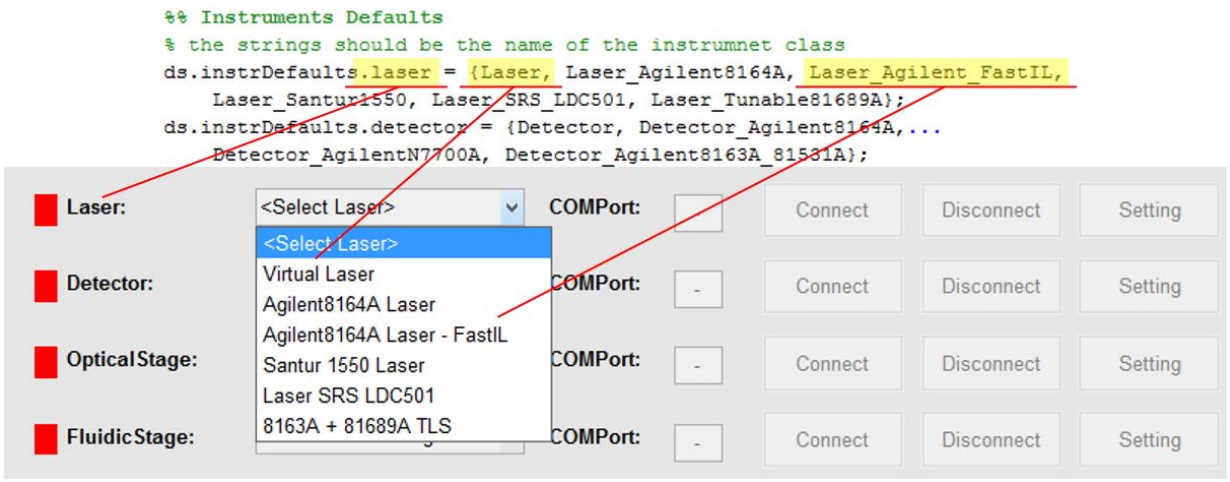

Figure A.6: Initializing and connecting instruments panel. The application automatically populates a pull down menu with available class models. The user selects an instrument model, modifies any connections if needed, and connects to initialize communication with the instrument.

To add a new instrument to an existing instrument group, a new entry must be made

in the ds.instrDefaults struct in the applicationDefaults.m file. The entry name must match the class name. To add a new group of instruments, a new fieldname must be created for the group in the applicationDefaults.m file. The code will parse the applicationDefaults.m file and generate an instrument class entry for each fieldname. Specific instrument options for each class get populated with the instrument description from the class (property). The very first entry in the list is used as the string for the class as well as the virtual instrument (which is always listed first) as shown in Fig. A.6.

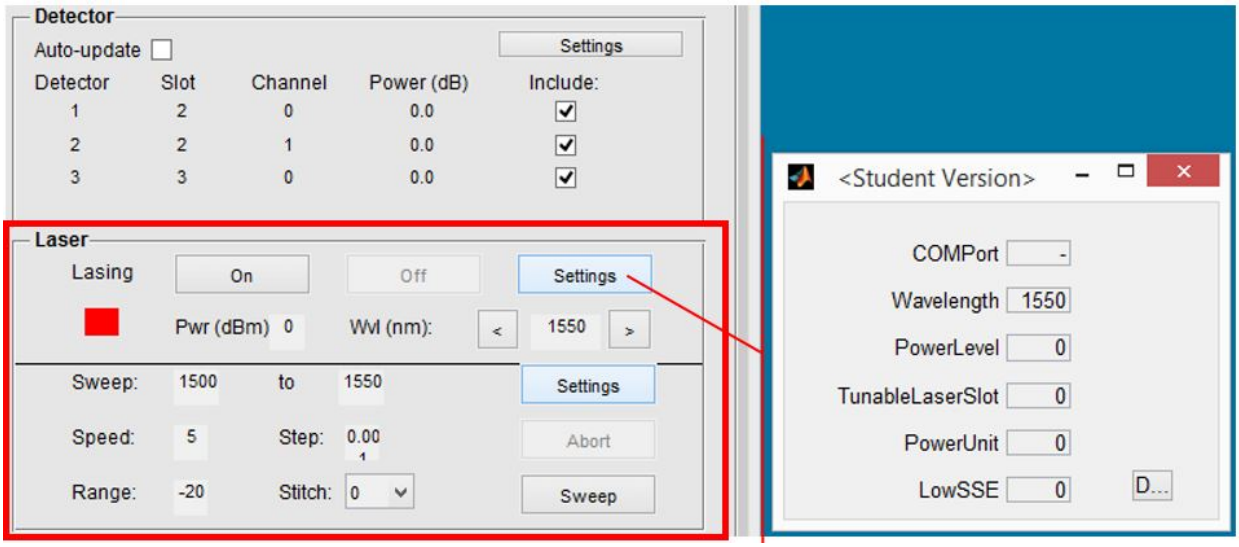

Figure A.7: Laser control UI with settings pop-up. The instrument class provides inherited properties and methods (like the settings pop-up shown) for all instruments added to the test platform.

The other requirement for adding an instrument is to create a UI control element instantiated in the view. Figure A.7 shows an example of the laser and detector UI control panels. If a new instrument is being added to an existing instrument group, the class methods named similar to the existing methods to ensure compatibility with the callback functions from the control UI. When creating a new instrument group, a new UI control panel will be needed and integrated with the existing GUI panels. Since all the instruments share a

somewhat common framework and function (configuration parameters and providing data of some kind), an instrument superclass provides some methods common to each instrument. For example, if a new instrument class contains a property struct called 'params', clicking on the settings button will generate a pop-up window and create editable elements for every param struct entry as shown in the popup window on the right hand side of Fig. A.7.

A.1.3 Adding New Features to an Existing Test

Changing existing features or adding new ones to existing test modes may be needed. New parameters easily be added to existing test modes by first adding the parameter name and value to the `ds.AppSettings.<testType>` structure in the `applicationsDefaults.m` file. When the application first starts, all the settings in the `applicationsDefaults.m` file are read into a public TestBenchClass property called 'AppSettings. 'AppSettings' stores all the active settings in the entire application. To use the new parameter for the dry or wet test, new code needs to be added to the `scripts/dry_test.m` script. To use a new parameter for a bio assay or salt-step test, the file `models/@AssayCtlClass/AssayCtlClass.m` needs to be modified to support the new functionality.

A.1.4 Software Testing

Software functions and features were progressively tested in both virtual and physical environments. Virtual instrument models were created to mimic their real-life counterparts and can be integrated into the application like any physical instrument for verification before using real hardware. For example, a user can select a 'Virtual laser', 'Agilent laser', or 'Santur laser' as the laser component during instrument connection and initialization. This way, the software's programmatic flow, user interaction, and interfaces could be verified independent of the hardware. This not only facilitated the rapid development of the GUI and application flow, but also an initial verification before validating the code on the actual hardware components. The virtual environment was especially useful once the setup up was up and running and used in actual assays. Adding features and debugging is time consuming and

takes time away from applied research. In addition, experiments with wet chemistries and multiple steps often take more than 24h to run and it is expensive (time and money) to discover that the acquired dataset is invalid because of an undiscovered software bug in the latest feature.

A.2 Analysis Tool

While the platform control software provides a mechanism to select and track peaks during an assay, circumstances often arise when the peak may be lost and the only way to recover the true sensogram is post-acquisition. For example, the unfortunate introduction of an air bubble may move the resonant peak out of the tracking window or the slow (laser-dependent) scan rate may miss a quickly shifting peak during a significant bulk refractive index change resulting in an anomalous result. This section describes a custom analysis tool which complements the platform control application described previously.

The analysis tool allows a user to import an acquired dataset and remove unwanted scans, select and track different peaks, curve fit peaks using a poly or a loretz function, subtract reference channels, compare a functional sensor's drift to the system temperature, correlate entire scans or the peak window with previous ones, measure y-offsets on the sensorgram, and most importantly, export the analyzed data and figure. Lastly, the user can save all the fit parameters and excluded scans to an analysis file that can be reloaded when the dataset is selected again at a future time.

The analysis tool has become an invaluable aspect of the overall development methodology providing an efficient means to assess large datasets and generate publication worthy plots. The remainder of this section describes the software architecture and partitioning, a high level overview of the key features and user interaction model, how the tool was validated, and how it can be accessed as part of our open source effort.

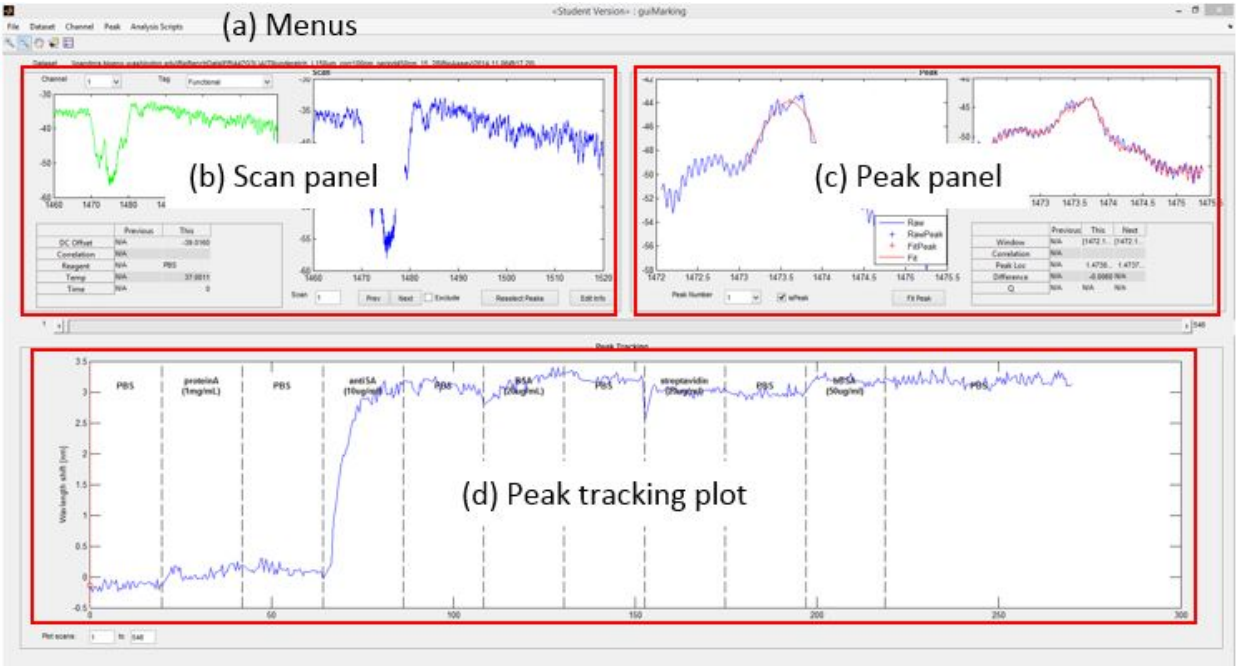

Figure A.8: Analysis Tool Application Overview. (a) Standard menu options allow the user to open datasets, preprocess datasets, run custom analysis scripts, or set specific configuration parameters. (b) Scan panel window allows the user to select different detector channels. (c) Peak panel provides fitting features and allows the user to select tracked peaks within the scan. (d) shows all the tracked peaks for the active detector and peak.

A.2.1 Application overview

The analysis tool's main window with a loaded sample dataset is shown in Fig. A.8. Datasets are loaded or preprocessed through the Dataset menu (Fig. A.8(a) in the upper left corner of the application. The tool supports a preprocessing function that can modify older datasets with the necessary parameters to ensure compatibility with its latest features. The scan panel (Fig. A.8(b) allows the user to interact with one scan at a time from the dataset and the peak panel (Fig. A.8(c) provides additional tools to fit and compare the tracked peaks. Finally, all the tracked peaks are plotted in the peak tracking window (Fig. A.8(d)

Scan panel

Even though the entire dataset is loaded, the user only views one detector channel at a time. The Scan window (Fig. A.9) allows the user to select other channels through a drop-down menu and tag the channel as either a functional or reference dataset. Reference channels can be subtracted from functional channels in the tracked peak plots figure (Fig. A.8(d). The selected peaks are shown as a small red cross-hair in the main plot window on the right side of the panel. The user can exclude scans from the dataset (checkbox) and reselect peaks within this window. The smaller green plot on the right side shows the user the previous scan for reference only. The table below the previous scan window (in Fig. A.9) shows comparative information between the two adjacent scans including: DC offset or shift for each scan, correlation between the scans, reagent currently in the channel, recorded temperature, and the time stamp of the acquisition.

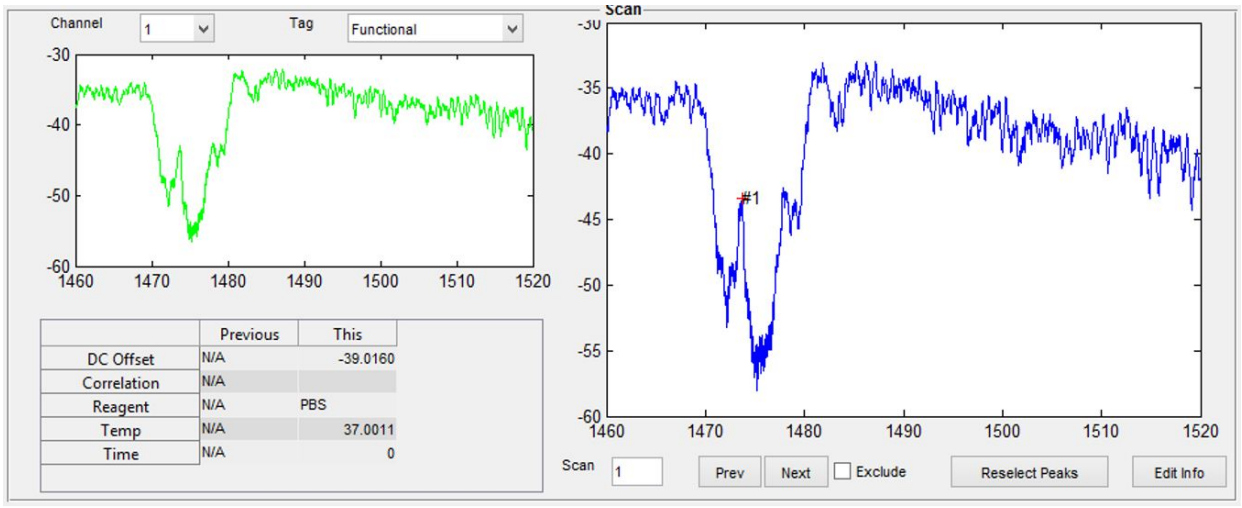

Figure A.9: Analysis tool scan panel. The user can select different detector channels, specify the channel's purpose (eg: functional, reference, acetylene, etc.), the exclude a peak from the tracking if necessary.

Peak panel

The peak panel compliments the scan panel and resides in the upper right hand corner of the application window (Fig. A.10).

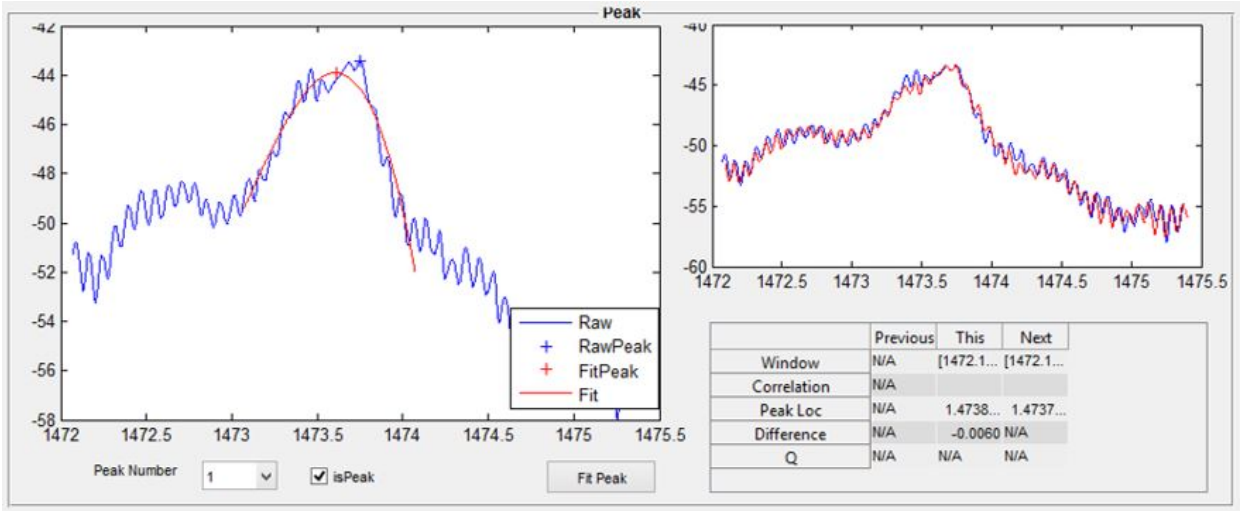

Figure A.10: Analysis Tool Peak Panel. The peak panel allows the user to select different peaks tracked within the scan. It also provides statistics on the active peak and allows the user to fit the peak through a separate pop-up window.

A small pull-down menu beneath the main peak window allows the user to select different peaks that were tracked within the scan. One of the most powerful features of the analysis tool is the peak fitting function. When the Fit Peak button is clicked, another popup window appears allowing the user to perform a fitting function around the selected peak (Fig. A.11). Currently, both poly and Lorentz fitting functions are supported and the fit result is plotted in red between the two, vertical dashed lines that represent the fit window boundaries. The user can specify the fit order, fit window size, and fit window center. Results such as the fitted and raw peak location difference and the goodness of fit are shown in the lower left hand corner of the window. By right clicking the mouse, a context menu appears allowing the user to add the calculated Q or export the figure to its own file. Once the fit has been

optimized, the user is provided the option to apply the same fitting parameters to all the other peaks when closing the peaking fitting window.

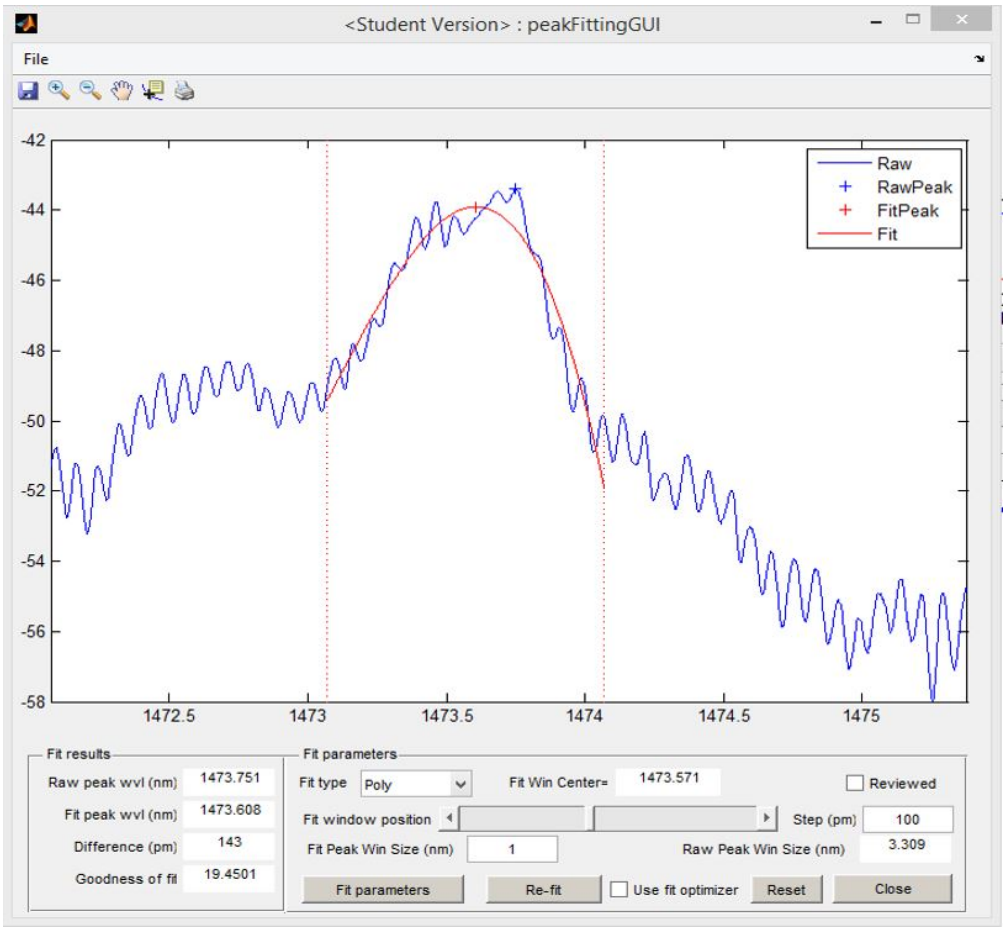

Figure A.11: Analysis Tool Peak Fitting Popup. The peak fitting tool allows the user to set the fit window size and fit type. Upon closing the window, the user can choose to apply similar fitting parameters to the rest of the peaks in the scan.

Peak tracking panel

The tracked peak results for all the scans in the dataset is shown in the peak tracking plot panel (Fig. A.8(d). The application does not plot excluded scans and different channels or

peaks can be plotted by simply making them active by selecting them from the drop-down menus in the scan and peak panels. The peak tracking plot has a context menu as well with many features to further process the dataset. The main features include: normalization, subtracting a reference, measuring a y-difference on the plot, adding vertical markers and text to highlight specific events, overlaying the system's temperature, and showing the various reagents sequenced during the assay. Most importantly, the figure and its underlying data arrays can be exported to a .csv or .fig file for further processing or publication.

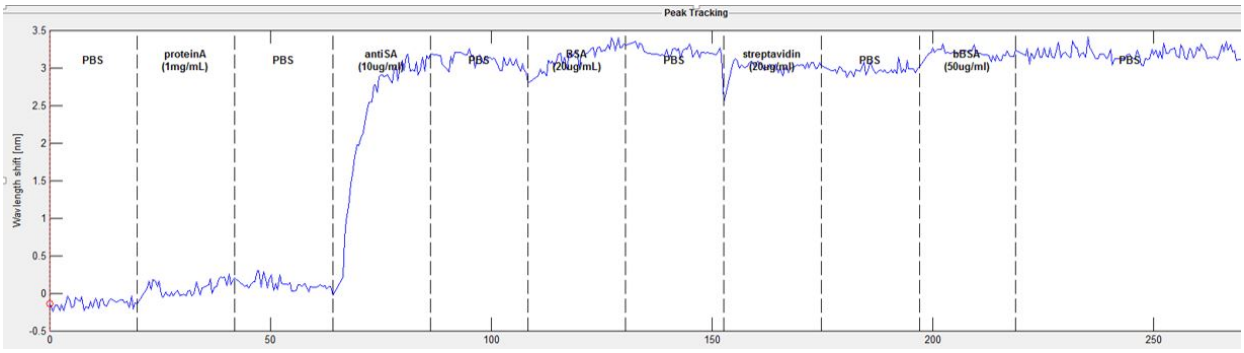

Figure A.12: Analysis Tool Peak Tracking Plot. The user enable special processing features (normalization, reagent labeling, etc.) and add markings to the plot user a context menu accessed using the right-mouse-button.

Custom scripting and analysis

The tool also supports the facile development and integration of custom analysis scripts. Using the provided scripting template that has access to all the active data in application's namespace, the user can quickly develop custom analysis routines and invoke them from within the tool (Analysis Scripts menu shown in Fig. A.8(a) by simply adding them to the analysisScripts directory.

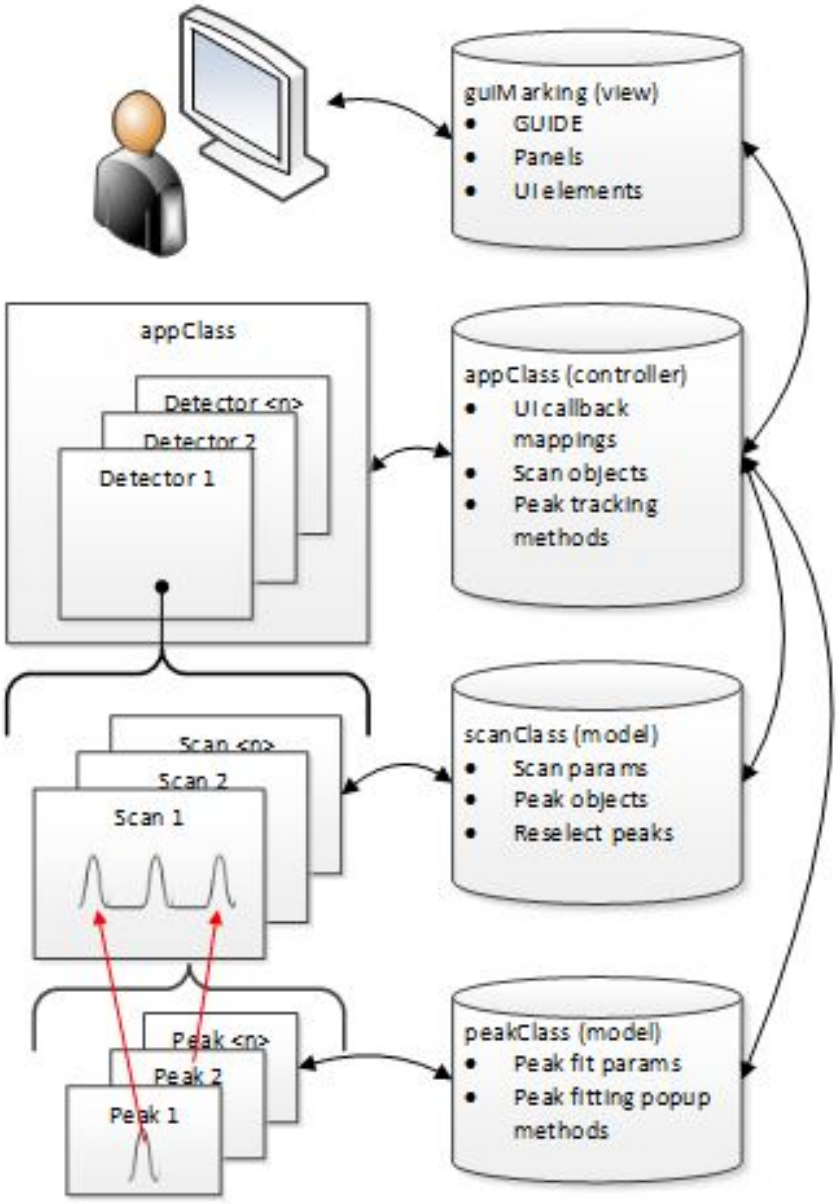

Figure A.13: Analysis tool class and data model architecture. This schematic shows the interaction model for the various classes that comprise the analysis tool. A MATLAB generate figure is used as the View, the appClass acts as the Controller, and the scanClass and peakClass act as Models manipulating the data stores.

A.2.2 Software architecture

Similar to the platform control application described previously, the analysis tool follows a model-view-controller partitioning scheme. Three custom classes form the foundation of the tool. The appClass acts as the controller and invokes the view, a figure and m-file pair (guiMarking.fig and guiMarking.m) generated using MATLAB's GUIDE. The scanClass and peakClass act as models, manipulating and storing the scan line and peak data respectively.

AppClass

The appClass acts as the application's controller, instantiating the other objects and mapping GUI callbacks to its methods. The classes' constructor sets default values for the applications parameters and unlike the platform control application, a specific user's preferences and settings are not stored and must be set during each use. When loading a dataset, the appClass instantiates a scanClass object for the data read from each scan file. One scan object is created for each channel, or detector that exists in the scan file on disk. The appClass keeps track of all the scan sets in a dataset and performs many of the scan-to-scan comparative analysis. After the dataset has been loaded, the class methods primarily execute the service routines invoked by the user's interaction with the UI. And while the scan class and peak class primarily manipulate and store the waveform data, the appClass combines all the data elements and manages the plotting of the tracked peaks. With all the plotting and analysis features provided through the peak tracking figure's context menu, these methods result in a large portion of what constitutes the class.

ScanClass

The scanClass acts as the model for a single scan, storing parameters pertinent to the scan like temperature, reagent, inclusion or exclusion state, the wavelength and power vectors for all the channels, and all the peaks selected for each channel in the scan. Based on the number of peaks selected, the scan class instantiates the peak objects (one per peak) and

keeps track of them in a class property. Of all the classes in the application, the scan class is the simplest, providing support for the reselect peak feature-which includes the tracking window size and methods that refind the peak within that window.

PeakClass

The peakClass contains all the necessary properties and methods to fit peaks and manage their data. Peak objects are instantiated and invoked through the scan object, which is managed by the appClass. The majority of the peakClass properties relate to the necessary fitting parameters to support poly and Lorentz fitting functions. The peakClass also has methods to estimate the Q of a peak and provides all the callback methods for the peak fitting window pop-up invoked from the application's scan panel.

Scripts

Two directories exist with scripts that support the analysis tool. The first set provides support through specialized analysis routines for certain biosensors, like calculating propagation loss from the chip framework's test cells provided in the PDK, or the backwards-compatibility scripts to modify older datasets. The other script directory, analysisScripts, contains user generated analysis scripts to further analyze datasets cleaned up with the tool. To add a new script, the user simply starts with the provided script template that contains the code and variable formats to access data from the analysis tool directly. Each time the user clicks on the Analysis Scripts menu from the main application window, the appClass builds a list of all the scripts in that directory as a pop-up for selection. This feature has been used extensively to analyze the test platform characterization data and sensor characterization routines not supported in the platform control application directly.

A.2.3 Validation

Initial software validation was accomplished by loading datasets and manually testing all the features and methods. Results were compared with many of the one-off scripts that had been developed previously to analyze datasets. Software bugs and required new features were tracked using Atlassian's online issue and project tracking software, JIRA [316].

The tool has also been used to analyze datasets and provide figures for the following publications: (1) Optimal design parameters for TM ring resonator biosensors, (2) SWG ring resonators for biosensing, and (3) TM Bragg gratings for use in label-free biosensing. The tool has also been used exclusively in analyzing the test platform characterization data described below.

A.2.4 Access and future work

The analysis tool can be freely downloaded, modified, and used from the SiPhoAnalysisTool project on GitHub [317] under the Gnu Lesser General Public License Version 3 license. Our hope is that other silicon photonic research groups would find our tool as useful as we do, helping to accelerate the development of devices that will be commercialized and realize the impact we believe they can have on society.

Performing bio assays and testing devices is expensive. Lots of time and effort is required to setup devices, purchase and prepare reagents, and then run assays which often times do not have the expected results. One nice feature analyzing datasets post-acquisition is the ability to develop useful real-time features off-line. We have started refining an air-bubble detection feature that will halt the assay and alert the user, allowing intervention and (hopefully) salvaging the experiment. The tool could also benefit from other enhancements including saving user preferences, loading multiple datasets sequentially without having to restart the tool, and most importantly, providing dataset comparisons and statistical analysis across many different chips, devices, and experiments.